# Numerical Modelling of Tyre-Derived Geo-Composites

**Can Wang**

A thesis submitted in fulfilment of the requirements for the degree of
Doctor of Philosophy

The University of Adelaide

Faculty of Engineering, Computer and Mathematical Sciences

School of Civil, Environmental and Mining Engineering

This thesis is dedicated to my beloved parents

# Numerical Modelling of Tyre-Derived Geo-Composites

By:


Can Wang

Supervised by:

Senior Lecturer An Deng, *Ph.D.*
*School of Civil, Environmental & Mining Engineering,*
*The University of Adelaide*



Senior Lecturer Abbas Taheri, *Ph.D.*
*School of Civil, Environmental & Mining Engineering,*
*The University of Adelaide*

Thesis submitted in fulfilment of the requirements for the degree of

**Doctor of Philosophy**

School of Civil, Environmental & Mining Engineering

Faculty of Engineering, Computer and Mathematical Sciences

The University of Adelaide

North Terrace, Adelaide, SA 5005, Australia

Tel:  +61(8) 8303 4323

Fax:  +61(8) 8303 4359
Email: c.wang@adelaide.edu.au, samwang0518@gmail.com

# Abstract

This thesis aims to study the property of rubber–sand mixtures as a geotechnical alternative. Previous studies have shown superior properties of this artificial composite such as high resiliency, light weight, and improved skin-resistance. Also, when mixed with conventional geotechnical materials, the composite often exhibits adjusted void ratio, high compressibility, high compression, high friction angle, and high attenuation of vibration.

In the past, the major efforts were focused on the laboratory tests. There is limited research in numerical domain performed to predict the mechanical behaviour of rubber–soil. In these numerical studies, approximations are unsatisfactory because the past studies usually treat the compressible rubble granule as a rigid material. To address these research gaps, this study in this thesis develops and applies a series of numerical models to replicate the compressible nature of the rubber material and to examine the behaviour of the rubber-derived composite materials. The behaviour includes the shear strength, dynamic damping, mixture segregation, contact asperity, and contact deformation, from the macro- to microscale.

The aims of this thesis contain the following aspects: 1) investigating the shear strength of rubber–sand mixture obtained in direct shear test; 2) assessing the segregation occurred when rubber–sand mixture is placed; 3) developing a coupled numerical method to replicate rigid–soft matters interaction; and 4) examining the influence of material surface asperity on energy dissipation. To attain these aims, the discrete element method (DEM), a numerical modelling tool, is employed to develop a series of modelling framework. The framework is

validated, verified and applied through a blend of solutions, including test setups, analytical solutions, example problems and case studies.

The DEM is used to replicate the discrete natural of rubber granules. Using this method, the macroscopic material response and particle flow can be monitored by determining granular properties such as contact stiffness, friction and damping coefficient. As a significant numerical tool, the commercial software package PFC is used to investigate the rubber and soil granular interactions.

# Declaration

I, **Can Wang**, certify that this work contains no material which has been accepted for the award of any other degree or diploma in my name, in any university or other tertiary institution and, to the best of my knowledge and belief, contains no material previously published or written by another person, except where due reference has been made in the text. In addition, I certify that no part of this work will, in the future, be used in a submission in my name, for any other degree or diploma in any university or other tertiary institution without the prior approval of the University of Adelaide and where applicable, any partner institution responsible for the joint-award of this degree. I acknowledge that copyright of published works contained within this thesis resides with the copyright holder(s) of those works. I also give permission for the digital version of my thesis to be made available on the web, via the University's digital research repository, the Library Search and also through web search engines, unless permission has been granted by the University to restrict access for a period of time. I acknowledge the support I have received for my research through the provision of an Australian Government Research Training Program Scholarship.

Signed: ……………                        …………Date: …..11/08/2018……..

# Statement of Originality

I, **Can Wang**, hereby declare that this work contains no material which has been accepted for the award of any other degree or diploma in any university or other tertiary institution in my name and, to the best of my knowledge and belief, contains no material previously published or written by another person, except where due reference has been made in the text. In addition, I certify that no part of this work will, in the future, be used in a submission in my name, for any other degree or diploma in any university or other tertiary institution without the prior approval of the University of Adelaide and, where applicable, any partner institution responsible for the joint award of this degree.

I give consent to this copy of my thesis when deposited in the University Library, being made available for loan and photocopying, subject to the provisions of the Copyright Act 1968.

The author acknowledges that copyright of published works contained within this thesis resides with the copyright holder(s) of those works.

I also give permission for the digital version of my thesis being made available on the web, via the University's digital research repository, the Library catalogue, the Australian Digital Thesis Program (ADTP) and also through web search engines, unless permission has been granted by the University to restrict access for a period of time.

Signed: …………            ….Date: ………11/08/2018…………..

# Acknowledgments

# **Table of Contents**

# Table of Contents

*Table of Contents*

# List of Figures

# List of Tables

# Chapter 1

# Introduction

## 1.1    Background

In Australia, it is estimated that there are around 48 million waste tyres generated each year, but less than 16% of these waste materials are recycled and properly managed. A large percentage of waste tyres are either dumped in overcrowded landfills or discarded illegally, indicating potential fire hazards and other environmental and health problems, e.g., breeding mosquitos and rodents, resulting in great demand for storage spaces and other associated cost.

On the other hand, waste tyres are not desired at landfills because of their large volume, high void space which occupies limiting and valuable landfill space. Currently, the main methods of dealing with discarded tyres are burning them to produce electricity or for other purposes such as run pulp or paper mills. However, according to Masad et al. (1996b), by using these methods, waste tyres are still stockpiled, landfilled or even illegally dumped. Thus, trying to reuse and recycle waste tyres and incorporating them into engineering materials could be an alternative method.

*Chapter 2*

A rising interest in industry of using rubber composite or rubber chips alone has been found in recent years. This includes the application in reinforcing road construction (Bosscher et al., 1997, Heimdahl and Drescher, 1999, Nightingale and Green, 1997), controlling erosion of ground (Poh and Broms, 1995), slope stabilization (Poh and Broms, 1995, Garga and O'shaughnessy, 2000), backfilling retaining structures (Basheer et al., 1996, Bosscher et al., 1997, Garga and O'shaughnessy, 2000, Humphrey and Manion, 1992, Humphrey et al., 1993, Lee et al., 1999, O'Shaughnessy and Garga, 2000), subsurface drainage system (Nagasaka et al., 1996) and vibration isolation system (Eldin and Senouci, 1993, Tsang et al., 2012).

The superior properties of waste rubber tyre shreds have been identified through a large number of laboratory tests. Generally they are resilient, lightweight, skin-resistive and rubber-sand mixtures often exhibit low void ratio, high compressibility, high compression, high friction angle and high attenuation (Edil and Bosscher, 1994, Feng and Sutter, 2000, Foose et al., 1996, Gebhardt, 1997, Humphrey et al., 1993, Kim and Santamarina, 2008, Masad et al., 1996a, Pamukcu and Akbulut, 2006, Wu et al., 1997, Yanagida et al., 2002, Zornberg et al., 2004) which makes rubber particles a wide application in civil fields. Also, mechanical properties of rubber-sand mixture such as integrity, strength, ductility and damping ratio could be improved if incorporating cement matrix (Lee and Lui 2000, Shahin et al 2011, Tsoi and Lee 2010, Anastasiadis et al 2012).

However, there are insufficient numerical studies undertaken to investigate the granular flow behaviour of sand–rubber mixtures. Most existing numerical studies adopt a discrete element method (DEM) as a simulation tool. Comparing

to other numerical methods such as a finite element method (FEM), the DEM treats geotechnical material as a group of individual particles due to system's granular nature. Each particle would be governed by physical laws as it has its own physical properties so that the material deformation, failure mode, bifurcation behaviour and significant non–linear deformation can be successfully captured (Ting et al., 1989).

Despite the advantages of using the DEM, it should further investigate the behaviour of deformable rubber material in the framework of rigid – body but soft – contact assumption. This is because in the DEM, the material deformation is assumed as a finite overlap at material boundaries, and how to best calibrate the deformable soft material in DEM still remains to be a numerical difficulty.

## 1.2    Research aims

The research aims of the study include:

- Numerically investigating the shear properties of sand–rubber mixture and assessing the packing influence to shearing resistance from a microscale view.
- Investigating material segregation by adopting a digital image method combined with the DEM and identifying the most significant parameter to composite segregation.
- Proposing a theoretical based model to estimate the influence of surface roughness to energy dissipation.

- Proposing a numerical algorithm to couple the DE and EF (element free) methods where the material behaviour in rigid and soft domain can be simulated respectively.

## 1.3    Layout of the thesis

This thesis contains seven chapters in the public format. Chapter 1 presents a general introduction of research. A literature review related to the numerical methodologies and theories is presented in Chapter 2. This includes a brief review of existing studies on rubber—sand composites; an introduction of discrete element method (DEM); the using of digital image processing (DIP) to distinguish colour difference; and theories in element free Galerkin method. Chapter 3, 4, 5 and 6 present the four published and/or submitted journal papers, which are the core outcomes of the research program.

Chapter 3 contains a journal paper published in *Computers and Geotechnics*. This paper presents a numerical 3D DE model of sand—rubber mixture subjected to direct shear test. This numerical model is verified with the laboratory test under various rubber contents and loading stresses, showing great capacity and accuracy of the model. Interparticle contact forces, displacement, rotation and their variation with rubber content were investigated at a microscale. From a particulate-level, it demonstrates the composite stiffness, grading and packing greatly influenced by rubber inclusion, resulting in shear resistance variations. Some interesting phenomenon were further studied using the DEM tool.

*Chapter 2*

Chapter 4 includes a journal paper published in *International Journal of Geomechanics*. This paper presents a study on sand–rubber segregation by using a digital image processing (DIP) method.  By converting a colour image into a binary picture, it enables material ingredients identification through determining a threshold grey level. Several important material properties including friction, rolling friction, damping and stiffness were calibrated through a range of laboratory tests. This research reveals a deeper understanding of composite heterogeneity when incorporating artificial material in conventional geotechnical materials. The discrete element studies further estimated the influence of micro–mechanical properties to mixture segregation and identified the most influential factor to be density difference. The bigger the density difference is, the more likely that segregation can occur but restricted by material surface roughness.

Chapter 5 includes a journal paper submitted to *Granular Mechanics*. This paper presents a numerical and theoretical study on single particle moving along a bumpy surface made by discs. The theoretical study is based on the collision model in order to verify the limitations of the DEM due to contact overlap. To estimate the roughness of the surface, the disc's gap and radius were used to describe the surface geometric properties. In the numerical and theoretical models, inter–particle friction is not considered due to a perfect geometric shape. An initial horizontal velocity is given to an object so that its moving trajectory is recorded against the loss of energy. It is observed a viscous behaviour of energy dissipation due to collisions. To better quantify the surface roughness, the collision angle is found to be more accurate over surface asperity average height and height variance as a monotonic relationship was observed between energy loss and collision angle. In the numerical studies, the surface roughness is increased by using a clump

method and a significantly influence to energy dissipation is found due to multiple collisions.

Chapter 6 includes a journal paper submitted to *International Journal for Numerical Methods in Engineering.* This paper presents an algorithm to couple DEM (discrete element method) and EFGM (element free Galerkin method) to solve dynamic interaction between soft and rigid domains. In both DE and EFG domains, an implicit Newmark-$\beta$ time integration scheme is adopted in the step–to–step analysis, coded in Matlab. The exchange of the contact force from DE to EFG is enforced as the form of point loads at domain interface using the Dirac delta function. To prevent the ill–conditioned problems, a weighted orthogonal base function is used to compute shape functions. Also, a penalty method is enforced to ensure essential boundary problem. It is also demonstrated that DEM and EFGM work compatibility in the self-developed Matlab codes. Several numerical cases illustrate great accuracy and efficiency is can be obtained.

The above studies are summarised in Chapter 7 where the contributions and outcomes are discussed. Limitations of the research and recommendation to the future work are also discussed.

# Chapter 2

# Literature review

This chapter presents a literature review containing different parts relevant to the research study, including the existing studies on rubber—sand material; discussion of the numerical tools such as DEM and DIP used to study mixture properties and segregation respectively; the theories of using element free Galerkin method.

## 2.1　Existing studies on rubber—sand mixture

### 2.1.1　Experimental studies

The existing studies mainly focus on investigating the mechanical properties of the mixtures experimentally or numerically. As a guidance to the design of the structures, multiple composite properties are investigated, which can be categorized into two groups: the static and dynamic properties of the material.

One of the most important static properties of rubber sand mixture is its shearing resistance. A common research interest of using rubber soil is to determine the optimal rubber content where the maximum shearing properties can be reached (Ghazavi, 2004b, Zornberg et al., 2004). In the static test of soil—sand material, direct shear test (Foose et al., 1996, Ghazavi, 2004a, Ghazavi and Sakhi, 2005) and triaxial test (Airey, 1993, Lee et al., 1999, Wu et al., 1997, Zornberg et al., 2004) are most commonly used in investigating mixture mechanical properties.

In the triaxial test, pure rubber chips, sand—rubber mixtures and slightly cemented sand rubber mixtures can be found in the literature. It is unanimously agreed that the shearing properties are mostly related to loading stress, mixture unit weight and rubber dosage. Other factors such as rubber aspect ratio also have a positive influence on shearing resistance of the mixture.

The dynamic properties of sand—rubber mixture were investigated by a number of previous studies. These are often carried out by torsional resonant test (Anastasiadis et al., 2012a, Anastasiadis et al., 2012b, Feng and Sutter, 2000, Senetakis et al., 2012), cyclic triaxial test (Nakhaei et al., 2012) and modified odemetor test (Kim and Santamarina, 2008) in order to determine material shear modulus and damping ratio. Confining pressure, rubber content, grain sizes and relative size ratio are believed to be the most important characteristics of the mixture dynamic properties.

## 2.1.2    Numerical studies

The numerical studies are mainly conducted by using the discrete element method. Comparing to the conventional finite element method, the material behaviour can be investigated up to particulate level and in the binary mixture, the granular interaction is often of great interest to the researchers. For sand—rubber mixture, a range of numerical tests have been performed validating the laboratory results, including odemetor test  (Lee et al., 2014, Patil et al., 2010) and 1D compression test (Evans and Valdes, 2011, Lee et al., 2010, Valdes and Evans, 2008). The material stress—strain relationships were closely predicted by these numerical

simulations thorough calibrated material parameters. More importantly, an insight result into the particulate interaction can be revealed through DEM simulations.

The inclusion of rubber content has an important role in determining material behaviour in various strain levels. According to (Lee et al., 2014), the rubber material usually demonstrates low stiffness and high angularity, elasticity and irregularity. These unique properties finally determine the mixture behaviour especially at small strain level. As a heterogenous material, the mixture can generally behave as sand–like, rubber–like or at transition. The role of rubber granules can be illustrated in Table 2-1 where $\chi$ is the volume fraction of rubber ($\chi = V_{rubber}/V_{total}$):

**Table 2-1**.Transition and role of the rubber particles with the strain level

| Strain level | Small strain | Intermediate strain | Large strain |
|---|---|---|---|
| Sand-like | $\chi \leq 0.8$ | $\chi < 0.2$ | $\chi \leq 0.2$ |
| Transition | $\chi > 0.8$ | $0.4 < \chi < 0.6$ | $\chi > 0.2$ |
| Rubber like | | $\chi > 0.8$ | |

Role of rubber particle:

    (a)        (b)        (c)

(a) Increase coordination number; High elasticity and low stiffness
(b) Prevent buckling from force chain; Secondary particle
(c) Lead a contractive behaviour

White and black circles denote sand and rubber particles, respectively. Reproduced from Lee et al. (2014).

In a granular system, the material behaves anisotropic due to a discrete assembly and different stress levels. The inherent material anisotropy and stress induced anisotropy can be measured by fitting the contact force polar histogram with a truncated Fourier series. This method was first introduced by Bathurst and Rothenburg (1990). According to the authors, the micromechanical behaviour of the granular media can be quantified through introducing average chrematistics fabric anisotropy and statistics averages of contact forces.

The following numerical study illustrates mixture anisotropy changes before and after rubber—soil mixture swelling. The samples are initially

consolidated to an effective vertical stress of 100 kPa to validate the numerical results. The next stage is followed by the radii of the expansive soil expansion which multiplies an experimentally determined value. Different mixtures were compared based on different rubber inclusions and the mitigation of rubber inclusion is illustrated. In the different material matrix, the change of contact force anisotropy is illustrated as following:
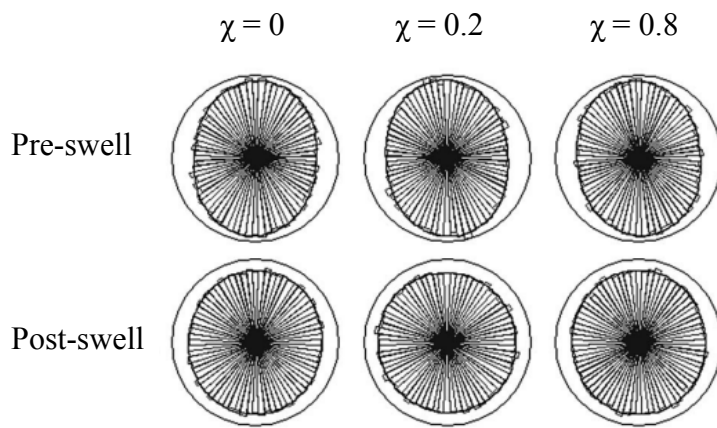


(a) Normal force diagrams
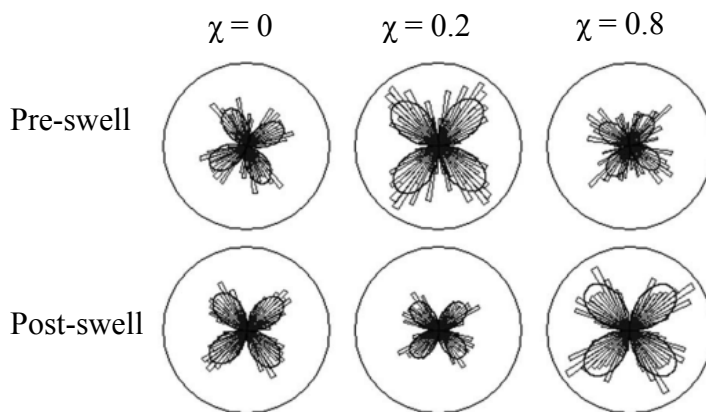


(b) Shear force diagrams

**Figure 2-1**. Contact force statistics: polar histograms of (a) contact normal force and (b) contact shear force normalized by mean contact normal force and plotted on equal scales, reproduced from Patil et al. (2010).

Table 2-1 illustrates the change of lock-in stress before and after swelling. According to Patil et al. (2010), a preferred vertical orientation can be identified in the three assemblies at pre-swell conditions and this is equivalent to a $K_0$ consolidation condition. The expansive material swells as the normal contact force dissipates, which is consistent in all the cases as shown in Figure 2-1(a). However, increasing granular rubber fraction increases the lock-in horizontal stress where swell mitigation is enhanced. Adding rubber additives in the sand matrix also reduces the rotational resistance after swelling as there is a smaller lock stress at shear direction.

The experimental and numerical studies illustrate a wide range of advantages of using rubber material in the conventional geotechnical materials. Apart from the alleviation on environmental hazards, the engineering properties of geotechnical foundation can be greatly improved. The most significant benefit of incorporating rubber material lies in the aspect of the friction angle enhancement and this usually comes with a benefit of reducing self-weight by adding light weight rubber material. The mitigation of expansive soil by including rubber components also demonstrates a practical and economical treatment.

The DEM simulations used in the literature review are capable to capture the contact force changes when rubber material is added the soil matrix. A great advantage of using DEM over FEM tool is the individual particle behaviour can be simulated, such as granular flows or particle rotation. Through a statistics analysis, an insight is also provided into the mechanical behaviour of large number of particles, such as observing the particle flow, the preferred orientation of contact or contact force. Generally, DEM is a more suitable tool used in the current

research program as to observe the microscale behaviour of sand—rubber mixture through a number of different tests.

## 2.2    The application of DEM in geotechnical studies

### 2.2.1    Introduction of DEM

The first program code based on DEM concept was introduced by Goodman et al. (1968) although his work cannot be strictly defined as discrete element method. A true discrete element method system was first established by Cundall (1971) in order to address the problems in rock mechanics. Later on, this method was adopted in soils by Cundall and Strack (1979).

Being the first granular dynamic technique adopting a soft—particle approach, this method received a great deal of attention as it provides detailed dynamic information of the granular assembly, which is nearly impossible to be captured in the laboratory test. After that, a number of other distinct element codes and software such as UDEC, DIBS, 2DSHEAR, 3DEC, $PFC^{2D}$ or $PFC^{3D}$ are established.

Since this method was developed, a large number of research has been published related to DEM. A survey of the literature review conducted by Zhu et al. (2007) shows a rapidly growing interest in the DEM related studies after 2 decades since the method was introduced. The summary of literature is shown in Figure 2-2.
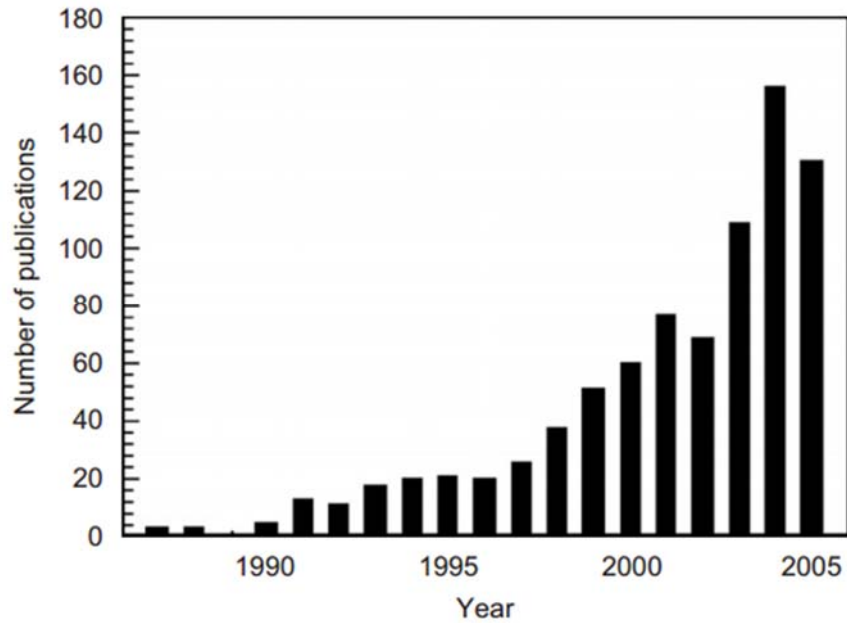
**Figure 2-2**. Number of publications related to discrete particle simulation in the recent 20 years, obtained from the Web of Science with the following keywords: discrete element method/model, distinct element method/model, discrete particle simulation/method/model, and granular dynamic simulation, reproduced from Zhu et al. (2007).

The DEM numerical calculation is based on the Newton's second Law at the particles and a force-displacement law at the contacts. Specifically, the calculation cycle adopts a time stepping algorithm, by firstly setting up particle and boundary positions and applying the law of motion to each particle, updating its velocity and position resulted from the contact force and moment. The calculations cycles performed in a DEM tool PFC3D are shown in Figure 2-3.
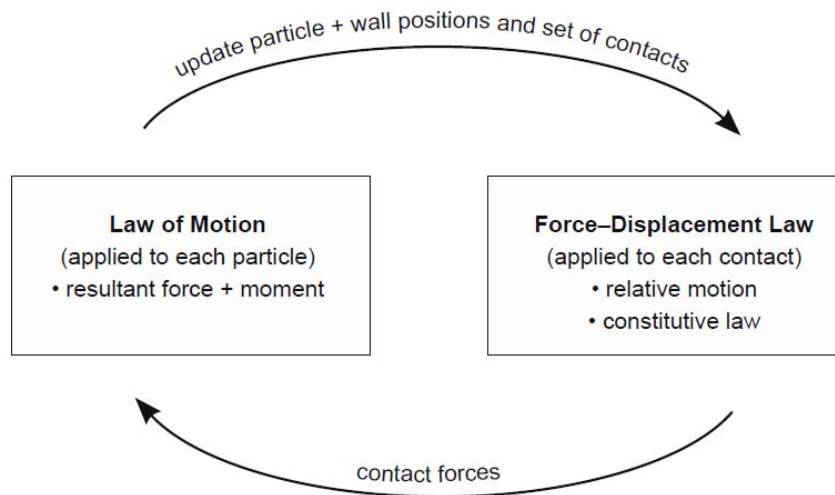
**Figure 2-3**. Calculation circle in DEM (ITASCA, 2008)

A wide range of geotechnical applications can be investigated by using DEM. In the past two decades, DEM or DEM coupled method has become a powerful tool in revealing the microscopic behaviour in soil dynamics. These research topics include studying typical soil behaviour such as cemented sand (Wang and Leung, 2008), sand creep and aging (Wang et al., 2008), various sand behaviour under $K_0$ condition (Gao and Wang, 2014), soil suction and hysteresis (Anandarajah and Amarasinghe, 2011), and cyclic liquefaction (Kuhn et al., 2014), soil—pile interaction such as monotonic pile penetration in crushable sand (Wang and Zhao, 2014), soil—pile failure problems (Khanal et al., 2017), validation of soil—pile interaction (Calvetti et al., 2004) and cone penetration test (Butlanska et al., 2013), slope stability such as earth pressure balance during excavation (Maynar and Rodríguez, 2005) and cohesive soil slope (Li et al., 2017), other topics related to hydraulic problems(El Shamy and Aydin, 2008, Nguyen and Indraratna, 2016) and discussions of geo-synthesis (Villard and Chareyre, 2004).

## 2.2.2    Theoretical development of DEM

The particulate assembly maybe bonded together like rock or un-bonded like sand or soil. Owning to the behaviour of assembly, different contact models may be used in different categories. The discrete element method uses a wide range of contact models to describe the mechanical behaviour of an un-bonded granular system, including linear spring—dashpot model (Cundall and Strack, 1979), simplified Hertz—Mindlin and Deresiewicz model (Langston et al., 1994), Walton and Braun's model (Walton, 1993, Walton and Braun, 1986) and other torque models (Ai et al., 2011, Iwashita and Oda, 1998, Iwashita and Oda, 2000, Zhou et al., 1999).

Of all the contact models described, the linear contact model is the most intuitive one and is renowned for its simplicity. This model adopts linear and dashpot components at the contact which provide linear elastic frictional behaviour and viscous behaviour respectively. The schematic drawing of the model is illustrated in Figure 2-4.
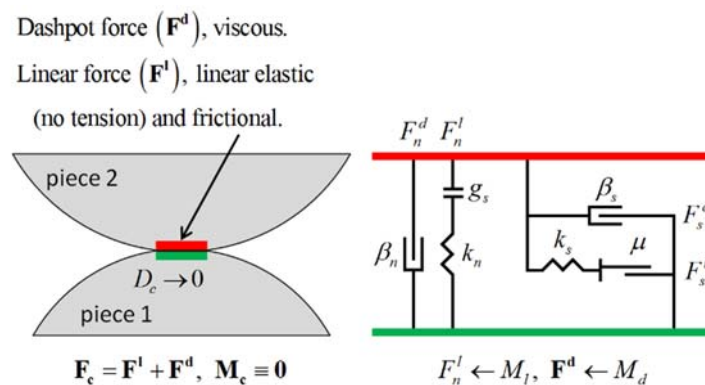


**Figure 2-4.** Behaviour and rheological components of the linear model, reproduced from (ITASCA, 2014)

In the original linear contact model developed by Cundall and Strack (1979), the contact does not resist rotation so that the contact moment is zero ($M_c \equiv 0$). The total contact force $F_c$ is resolved to linear and dashpot force:

$$F_c = F^l + F^d \tag{2.1}$$

where $F^d$ is the linear force and $F^l$ is the dashpot force.

The linear contact force $F^l$ can be resolved into normal and shear direction, which is produced by linear springs with constant normal and shear stiffness, $k_n$ and $k_s$ respectively. A coulomb limit is also enforced at the contact shear direction using a friction coefficient $\mu$. The linear force can be updated as:

$$F_n^l = k_n \times \Delta\delta_n \tag{2.2}$$

$$F_s^l = k_s \times \Delta\delta_s \tag{2.3}$$

$$F_s^l \leq \mu \times F_n^l \tag{2.4}$$

where $\Delta\delta_n$ and $\Delta\delta_s$ are the increment displacement during a time step $\Delta t$ at contact normal and shear directions respectively.

The linear stiffness inherits the properties of the particles,

$$\frac{1}{k_n} = \frac{1}{k_n^{\;1}} + \frac{1}{k_n^{\;2}} \tag{2.5}$$

$$\frac{1}{k_s} = \frac{1}{k_s^{\;1}} + \frac{1}{k_s^{\;2}} \tag{2.6}$$

$$\mu = \min(\mu_1, \mu_2) \tag{2.7}$$

where $k_n^{\;1}$, $k_n^{\;2}$ and $k_s^{\;1}$, $k_s^{\;2}$ are normal and shear stiffness for contact particles.

The dashpot normal and shear contact force between particles can be calculated as:

$$F_n^d = 2\beta_n \sqrt{m_c k_n} \, \dot{\delta}_n \qquad\qquad (2.8)$$

$$F_s^d = 2\beta_s \sqrt{m_c k_s} \, \dot{\delta}_s \qquad\qquad (2.9)$$

$$m_c = \frac{m^1 \times m^2}{m^1 + m^2} \qquad\qquad (2.10)$$

where $m^1$ and $m^2$ are the mass of the contact particles. $\beta_n$ and $\beta_s$ are damping ratio at normal and shear directions, respectively.

The contact force development comes from a dynamic process where velocities and acceleration are assumed to be constant during the time step. According to Cundall and Strack (1979), the time step is taken so small that disturbance is only restricted to the neighbour particles without propagating further. The resultant force and moment at the particle are calculated using a time-centred scheme where they updated from timestep $t_{N-1/2}$ to $t_{N+1/2}$. Generally, in an assembly of many particles, force-displacement law is enforced at any contact and the resultant force comes from a vectorial sum of the contact forces. Once the state is determined, the particles new acceleration can be determined. For a detailed description of a calculation cycle for a general particle assembly, one can refer to the work proposed by Cundall and Strack (1979).

## 2.3 An introduction to couple numerical methods between the element-free Galerkin (EFG) method and DEM

One would like to find the exact solutions analytically to the mechanical response of geotechnical material. But in fact, only a small proportion of the practical problems can be solved analytically due to the complex situation. Thanks to the rapid development of computer technology, numerical tools such as DEM has

become an important method to describe and simulate the behaviour of geotechnical material.

Using the numerical method, the complex problem is simplified by transforming into a discrete, mathematical form of description. This procedure usually requires the use of computer so that the physical process can be revealed virtually. Technically, no matter how complex the problem is, a numerical solution can often be found with an approximate result. Apart from the DEM, other numerical tools such as the finite element method (FEM), the finite difference method (FDM) or the boundary element method (BEM) are also used. In this section, a meshed free method is introduced which is known as the element-free Galerkin method (EFGM).

The purpose of introducing this method is mainly to couple it with DEM to solve the interaction between rigid material (such as rock or sand) and soft material such as rubber. Despite DEM has been introduced to study soft—rigid material behaviour such as rubber—sand simulation (Evans and Valdes, 2011, Lee et al., 2014, Lee et al., 2010, Valdes and Evans, 2008) or particle—membrane interaction (De Bono et al., 2012, Lu and McDowell, 2008)it often lacks a proper description of soft material deformation. This drawback is attributed to the fundamental principles of DEM as the material deformation is numerically described as an 'overlap' at contacts. In most cases, this principle works well when dealing with rock or sand materials; however, it cannot effectively describe the mechanical response of soft material. To this end, the EFGM is combined with DEM so that the rigid and soft material can be described in different domains.

**2.3.1       A multiscale analysis of a geotechnical system**

Simulating the nature of granular soils can be accurately achieved at a microscale level using DEM tools; however, with the current computing capability, constructing a geotechnical model entirely at this level is impossible, owning to the large number of particles in the spatial geotechnical domain.

At the current stage, geotechnical materials are mostly simulated by using FEM based techniques. As the most mature numerical method, continuum mechanics can be solved in various fields. A core component of this numerical technique is the constitutive relationship describing the material stress-strain behaviour (Elmekati and El Shamy, 2010). The drawbacks of this technique are described as follow:

- Constitutive laws and continuum techniques do not provide satisfactory results involving contact mechanics (Elmekati and El Shamy, 2010);

- Capturing the discontinuous soil nature is a challenge for this numerical tool (Lei and Zang, 2010);

- Limitations in some of the situations, such as under large deformation, crack growth and material breakage problems (Liu and Gu, 2005).

To take advantage of both DEM and FEM, an ideal of coupling these two methods emerged in the late 1980s (Munjiza et al., 1995) thanks to the computational power advancement. Despite the geotechnical problems maybe complex and extend to large spatial area, one would be only interested in limited area such as interfaces, boundaries or particulate geotechnical zones which can be investigated in a microscale while the rest of domain can be adequately modelled based on a macroscale continuous technique. An example of multi domains coupling between DEM-FEM can be illustrated below:
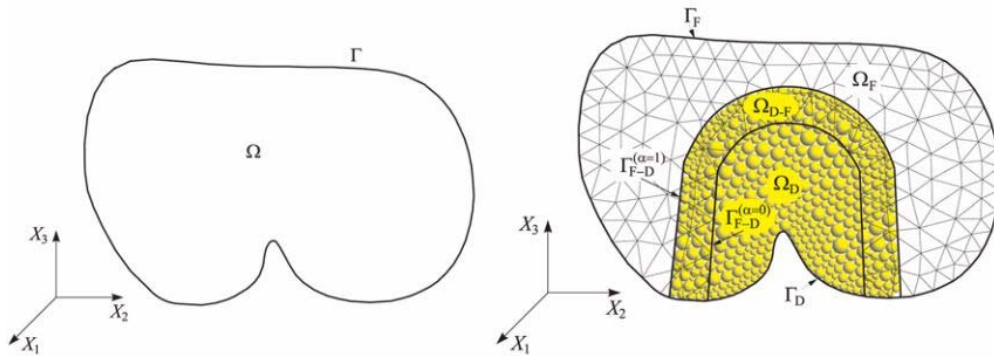


**Figure 2-5**. The ideal of the model: (a) deformable body, (b) multiscale finite-discrete element model (Rojek and Oñate, 2007).

Coupling DEM-FEM in different domains has been adopted to solve a wide range of engineering purposes. It is found that this method shows great efficiency in simulating the interaction between geo-grids and backfill materials, e.g., geosynthetic earth reinforced (Villard et al., 2009) structures, pile installation (Elmekati and El Shamy, 2010) and earth pressure on tunnel linings (Dang and Meguid, 2013).

It should be pointed out that using FEM based coupled method can still be time consuming, which mainly exists in the element meshing process. Usually the

problem domain needs to be meshed as a prerequisite for calculation. But in some particular cases, fully automatic meshing is not always possible which usually requires human intervention. Moreover, according to Liu and Gu (2005), in an FEM adaptive analysis, re-meshing the problem domain is often required which is computationally expensive.

To better address the issues discussed above, an element-free Galerkin (EFG) method was proposed by Belytschko et al. (1994). Comparing to the FEM, some advantages were identified in the studies by Belytschko et al. (1994):

- Volumetric locking is not observed even in a linear base function;

- It is faster in terms of convergence rate comparing to the FEM;

- High resolution of localised steep gradients can be achieved;

- High efficiency in linear elastic fracture problems.

Due to the advantages of the EFGM over the FEM, one of the targets in the thesis is to develop an algorithm to couple the EFGM and the DEM. The contact mechanics between the DEM and the EFG node is one the major tasks that needs to be solved. The research gap is identified that so far there is no existing method to couple the two numerical techniques. A detailed discussion will be presented in Chapter 6.

### 2.3.2    A multiscale analysis of a geotechnical system

As opposed to the FEM, the MFree method adopts a set of scattered nodes to represent the problem domain and boundary. The functions of the field variables

do not need to be pre-determined as the scattered nodes, also called as *field nodes*, do not need to form a mesh so that the relationship between the geometry points is unimportant. According to the definition of MFree methods (Liu, 2002), an MFree method is a method used to establish system algebraic equations for the whole problem domain without the use of predefined mesh for the domain discretization.

The FEM and element-free method differs in the problem domain representation. In the FEM, the mesh is used to discretise the problem domain and each mesh unit is called an element. The shape of the element has to be specific, such as triangles or quadrilaterals. The problem domain has to be properly meshed and the elements are connected. This process is usually a pre-process of FEM. In comparison, the element-free method adopts a number of scatter points to carry the material properties and they are called field nodes. The density of the nodes depends on the required accuracy and the fields nodes can be distributed arbitrarily. Figure 2-6 illustrates the different domain representation in the FEM and the element-free method.

FEM elements



(a) FEM

Field nodes



(b) element free method
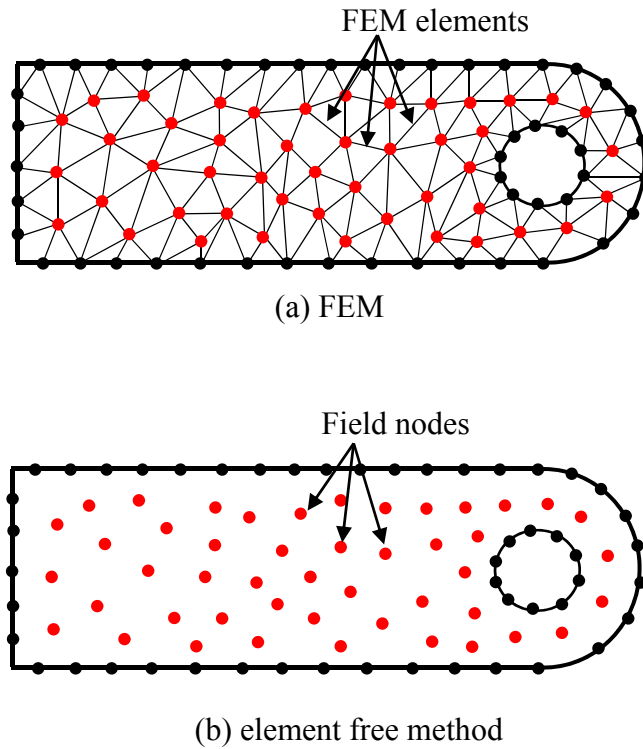
**Figure 2-6.** Domain representation in FEM and EFree method, reproduced from Liu and Gu (2005).

### 2.3.3    Basic theoretical development of MFree method

The general solution procedure of MFree methods follow the steps below:

- Domain representation: a set of nodes are selected scatting in the problem domain and boundary to represent problem domain and its boundary;

- Function interpolation/approximation: the field variable at any position is interpolated using an approximation procedure at a small local domain;

- Formation of system equations: based on shape function and strong/weak form equation

- Solve the global form MFree equation.

The meshless method adopts an approximation of displacement at domain coordinates, which can be written as:

$$u(x,t) = \sum_{I \in S} \Phi_I(x) u_I(t) \qquad (2.11)$$

where $\Phi_I$ is the shape function at problem domain $\Omega$ and $u_I$ is the nodal value at I, S is a set of nodes I for which $\Phi_I(x) \neq 0$. The discretization of the problem domain is illustrated in Figure 2-7,
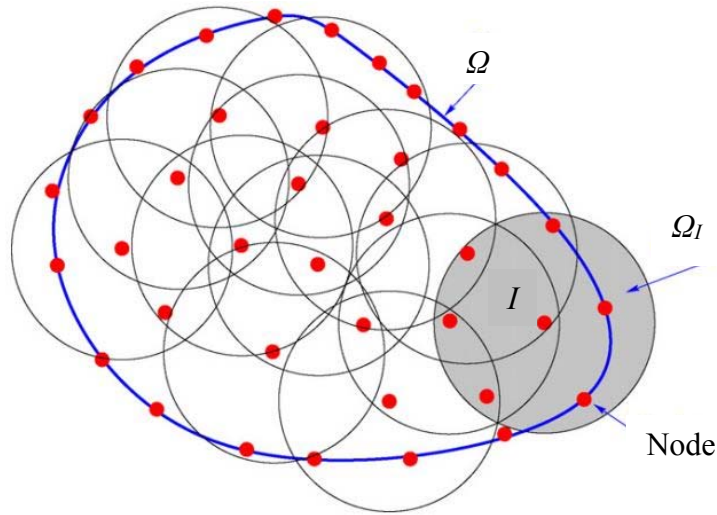


**Figure 2-7.** Domain discretization in meshless method: nodes, and domain influence, Nguyen et al. (2008)

The Moving Least-Square (MLS) is one the function approximation schemes. Other schemes such as smooth particle hydrodynamics (SPH) (Lucy, 1977), radical point interpolation method (RPIM) (Liu and Gu, 2001), *hp*-cloud (Liszka et al., 1996) etc. can be found in the relevant references. In this thesis, it is mainly focused on using the MLS approximation. Using the MLS, Eq.(2.11) can be written as:

$$u^h(x) = \sum_{j}^{m} p_j(x) a_j(x) \equiv p^t(x) a(x) \tag{2.12}$$

where $u^h(x)$ is the approximation of the function $u(x)$; $p_j(x)$ are the monomial in

the space coordinates $x^t=[x,y]$ constituting the basis function. The coefficients are

selected to reach a minimum weighted discrete form:

$$J = \sum_{i=1}^{n} \widehat{W}(x - x_i)[p^T(x_i)a(x) - u_i]^2 \tag{2.13}$$

where $n$ is the number of nodes in the support domain of $x$ satisfying the weight

function $\widehat{W}(x - x_i) \neq 0$ and $u_i$ is the nodal parameter of u at $x=x_i$. The relationship

between $u(x)$ and $u^h(x)$ can be illustrated as follow:
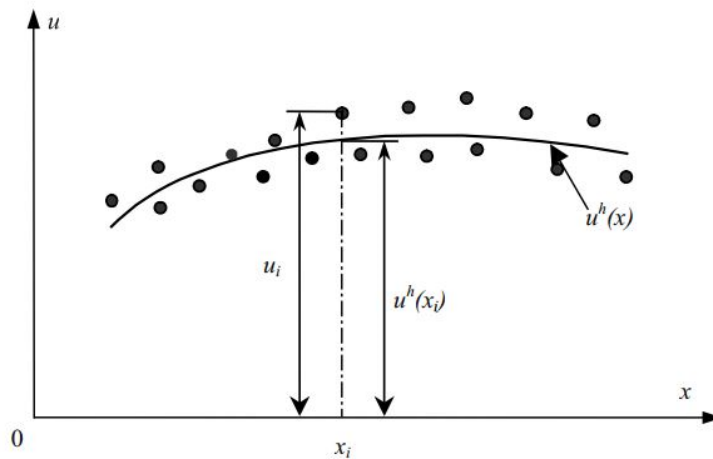


**Figure 2-8.** The approximate function $u^h(x)$ and the nodal parameters $u_i$ in the

MLS approximation (Liu and Gu, 2005).

Solving the global form of the MFree equation requires the partial

derivatives of the shape function and the selection of weight function where the

details will be given in Chapter 6**.** As the shape function approximation is the core

component of a MFree method, special attention should be placed. The properties

of a MLS approximation include, as summarised in (Liu and Gu, 2005) 1)

Consistency; 2) Reproduction;3) Partition of unity and 4) Lack of Kronecker delta

function property, which can be expressed as:

$$\phi_i(x_j) \neq \delta_{ij} = \begin{cases} 1 & i = j \\ 0 & i \neq j \end{cases} \tag{2.14}$$

which is due to the approximation curve not passing through the nodal values.

Because of this property, it requires special treatment to the coupling at the contact

between the MFree and the DEM. This will be further discussed in Chapter 6.

**2.4 References for Chapter 1 & 2**

AI, J., CHEN, J.-F., ROTTER, J. M. & OOI, J. Y. 2011. Assessment of rolling resistance models in discrete element simulations. *Powder Technology,* 206**,** 269-282.

AIREY, D. 1993. Triaxial testing of naturally cemented carbonate soil. *Journal of Geotechnical Engineering,* 119**,** 1379-1398.

ANANDARAJAH, A. & AMARASINGHE, P. M. 2011. Microstructural investigation of soil suction and hysteresis of fine-grained soils. *Journal of Geotechnical and Geoenvironmental Engineering,* 138**,** 38-46.

ANASTASIADIS, A., SENETAKIS, K. & PITILAKIS, K. 2012a. Small-strain shear modulus and damping ratio of sand-rubber and gravel-rubber mixtures. *Geotechnical and Geological Engineering,* 30**,** 363-382.

ANASTASIADIS, A., SENETAKIS, K., PITILAKIS, K., GARGALA, C. & KARAKASI, I. 2012b. Dynamic behavior of sand/rubber mixtures. Part I: Effect of rubber content and duration of confinement on small-strain shear modulus and damping ratio. *Testing and Specification of Recycled Materials for Sustainable Geotechnical Construction.* ASTM International.

BASHEER, I. A., NAJJAR, Y. M., DAY, R. W., POH, P. S. & BROMS, B. B. 1996. Discussions and Closure: Slope Stabilization Using Old Rubber Tires and Geotextiles. *Journal of Performance of Constructed Facilities,* 10**,** 40-41.

BATHURST, R. J. & ROTHENBURG, L. 1990. Observations on stress-force-fabric relationships in idealized granular materials. *Mechanics of materials,* 9**,** 65-80.

BELYTSCHKO, T., LU, Y. Y. & GU, L. 1994. Element‑free Galerkin methods. *International journal for numerical methods in engineering,* 37, 229-256.

BOSSCHER, P. J., EDIL, T. B. & KURAOKA, S. 1997. Design of highway embankments using tire chips. *Journal of Geotechnical and Geoenvironmental Engineering,* 123, 295-304.

BUTLANSKA, J., ARROYO, M., GENS, A. & O'SULLIVAN, C. 2013. Multi-scale analysis of cone penetration test (CPT) in a virtual calibration chamber. *Canadian Geotechnical Journal,* 51, 51-66.

CALVETTI, F., DI PRISCO, C. & NOVA, R. 2004. Experimental and numerical analysis of soil–pipe interaction. *Journal of geotechnical and geoenvironmental engineering,* 130, 1292-1299.

CUNDALL, P. A. 1971. *The measurement and analysis of accelerations in rock slopes.* Imperial College London (University of London).

CUNDALL, P. A. & STRACK, O. D. 1979. A discrete numerical model for granular assemblies. *geotechnique,* 29, 47-65.

DANG, H. K. & MEGUID, M. A. 2013. An efficient finite–discrete element method for quasi‑static nonlinear soil–structure interaction problems. *International journal for numerical and analytical methods in geomechanics,* 37, 130-149.

DE BONO, J. P., MCDOWELL, G. R. & WANATOWSKI, D. 2012. Discrete element modelling of a flexible membrane for triaxial testing of granular material at high pressures. *Géotechnique Letters,* 2, 199-203.

EDIL, T. B. & BOSSCHER, P. J. 1994. Engineering properties of tire chips and soil mixtures. *Geotechnical testing journal,* 17, 453-464.

EL SHAMY, U. & AYDIN, F. 2008. Multiscale modeling of flood-induced piping in river levees. *Journal of Geotechnical and Geoenvironmental Engineering,* 134**,** 1385-1398.

ELDIN, N. N. & SENOUCI, A. B. 1993. Rubber-tire particles as concrete aggregate. *Journal of materials in civil engineering,* 5**,** 478-496.

ELMEKATI, A. & EL SHAMY, U. 2010. A practical co-simulation approach for multiscale analysis of geotechnical systems. *Computers and Geotechnics,* 37**,** 494-503.

EVANS, T. M. & VALDES, J. R. 2011. The microstructure of particulate mixtures in one-dimensional compression: numerical studies. *Granular Matter,* 13**,** 657-669.

FENG, Z.-Y. & SUTTER, K. G. 2000. Dynamic properties of granulated rubber/sand mixtures.

FOOSE, G. J., BENSON, C. H. & BOSSCHER, P. J. 1996. Sand reinforced with shredded waste tires. *Journal of Geotechnical Engineering,* 122**,** 760-767.

GAO, Y. & WANG, Y.-H. 2014. Experimental and DEM examinations of K 0 in sand under different loading conditions. *Journal of Geotechnical and Geoenvironmental Engineering,* 140**,** 04014012.

GARGA, V. K. & O'SHAUGHNESSY, V. 2000. Tire-reinforced earthfill. Part 1: Construction of a test fill, performance, and retaining wall design. *Canadian Geotechnical Journal,* 37**,** 75-96.

GEBHARDT, M. A. 1997. Shear strength of shredded tires as applied to the design and construction of a shredded tire stream crossing.

GHAZAVI, M. 2004a. Shear strength characteristics of sand-mixed with granular rubber. *Geotechnical & Geological Engineering,* 22**,** 401-416.

GHAZAVI, M. 2004b. Shear strength characteristics of sand-mixed with granular rubber. *Geotechnical and Geological Engineering,* 22**,** 401-416.

GHAZAVI, M. & SAKHI, M. A. 2005. Influence of optimized tire shreds on shear strength parameters of sand. *International Journal of Geomechanics,* 5**,** 58-65.

GOODMAN, R. E., TAYLOR, R. L. & BREKKE, T. L. 1968. A model for the mechanics of jointed rock. *Journal of Soil Mechanics & Foundations Div*.

HEIMDAHL, T. C. & DRESCHER, A. 1999. Elastic anisotropy of tire shreds. *Journal of geotechnical and geoenvironmental engineering,* 125**,** 383-389.

HUMPHREY, D. N. & MANION, W. P. Properties of tire chips for lightweight fill. Grouting, soil improvement and geosynthetics, 1992. ASCE, 1344-1355.

HUMPHREY, D. N., SANDFORD, T. C., CRIBBS, M. M. & MANION, W. P. 1993. Shear strength and compressibility of tire chips for use as retaining wall backfill. *Transportation Research Record*.

ITASCA 2008. *PFC3D 4.0 User Manual*, Minneapolis, MN USA.

ITASCA 2014. *PFC3D 5.0 User Manual,* Minneapolis, MN USA.

IWASHITA, K. & ODA, M. 1998. Rolling resistance at contacts in simulation of shear band development by DEM. *Journal of engineering mechanics,* 124**,** 285-292.

IWASHITA, K. & ODA, M. 2000. Micro-deformation mechanism of shear banding process based on modified distinct element method. *Powder Technology,* 109**,** 192-205.

KHANAL, M., ELMOUTTIE, M., POULSEN, B., OLSSON, A. & ADHIKARY, D. 2017. Effect of loading rate on sand pile failure: 2D DEM simulation. *Geotechnical and Geological Engineering,* 35**,** 889-896.

KIM, H.-K. & SANTAMARINA, J. 2008. Sand–rubber mixtures (large rubber chips). *Canadian Geotechnical Journal,* 45**,** 1457-1466.

KUHN, M. R., RENKEN, H. E., MIXSELL, A. D. & KRAMER, S. L. 2014. Investigation of cyclic liquefaction with discrete element simulations. *Journal of Geotechnical and Geoenvironmental Engineering,* 140**,** 04014075.

LANGSTON, P., T Z N, U. & HEYES, D. 1994. Continuous potential discrete particle simulations of stress and velocity fields in hoppers: transition from fluid to granular flow. *Chemical Engineering Science,* 49**,** 1259-1275.

LEE, C., SHIN, H. & LEE, J. S. 2014. Behavior of sand–rubber particle mixtures: experimental observations and numerical simulations. *International Journal for Numerical and Analytical Methods in Geomechanics,* 38**,** 1651-1663.

LEE, C., TRUONG, Q. H. & LEE, J.-S. 2010. Cementation and bond degradation of rubber–sand mixtures. *Canadian Geotechnical Journal,* 47**,** 763-774.

LEE, J., SALGADO, R., BERNAL, A. & LOVELL, C. 1999. Shredded tires and rubber-sand as lightweight backfill. *Journal of geotechnical and geoenvironmental engineering,* 125**,** 132-141.

LEI, Z. & ZANG, M. 2010. An approach to combining 3D discrete and finite element methods based on penalty function method. *Computational Mechanics,* 46**,** 609-619.

LI, X., WU, Y. & SU, L. 2017. Initiation and Displacement Analysis of Cohesive Soil Slopes by Discrete Element Modelling. *Geotechnical and Geological Engineering,* 35**,** 693-705.

LISZKA, T., DUARTE, C. & TWORZYDLO, W. 1996. hp-Meshless cloud method. *Computer Methods in Applied Mechanics and Engineering,* 139**,** 263-288.

LIU, G.-R. 2002. *Mesh free methods: moving beyond the finite element method*, CRC press.

LIU, G.-R. & GU, Y.-T. 2005. *An introduction to meshfree methods and their programming*, Springer Science & Business Media.

LIU, G. & GU, Y. 2001. A local radial point interpolation method (LRPIM) for free vibration analyses of 2-D solids. *Journal of Sound and vibration,* 246**,** 29-46.

LU, M. & MCDOWELL, G. R. 2008. Discrete element modelling of railway ballast under triaxial conditions. *Geomechanics and Geoengineering: An International Journal,* 3**,** 257-270.

LUCY, L. B. 1977. A numerical approach to the testing of the fission hypothesis. *The astronomical journal,* 82**,** 1013-1024.

MASAD, E., TAHA, R., HO, C. & PAPAGIANNAKIS, T. 1996a. Engineering properties of tire/soil mixtures as a lightweight fill material.

MASAD, E., TAHA, R., HO, C. & PAPAGIANNAKIS, T. 1996b. Engineering properties of tire/soil mixtures as a lightweight fill material. *Geotechnical Testing Journal*.

MAYNAR, M. J. & RODR GUEZ, L. E. 2005. Discrete numerical model for analysis of earth pressure balance tunnel excavation. *Journal of Geotechnical and Geoenvironmental Engineering,* 131**,** 1234-1242.

MUNJIZA, A., OWEN, D. & BICANIC, N. 1995. A combined finite-discrete element method in transient dynamics of fracturing solids. *Engineering computations,* 12**,** 145-174.

NAGASAKA, Y., HORIUCHI, S. & HIGAKI, K. 1996. Status on utilization and disposal of industrial waste in Japan. *Environmental geotechnics. Edited by M. Kamon. AA Balkema, Rotterdam***,** 839-844.

NAKHAEI, A., MARANDI, S., KERMANI, S. S. & BAGHERIPOUR, M. 2012. Dynamic properties of granular soils mixed with granulated rubber. *Soil dynamics and earthquake engineering,* 43**,** 124-132.

NGUYEN, T. T. & INDRARATNA, B. 2016. Experimental and numerical investigations into hydraulic behaviour of coir fibre drain. *Canadian Geotechnical Journal,* 54**,** 75-87.

NGUYEN, V. P., RABCZUK, T., BORDAS, S. & DUFLOT, M. 2008. Meshless methods: a review and computer implementation aspects. *Mathematics and computers in simulation,* 79**,** 763-813.

NIGHTINGALE, D. E. & GREEN, W. P. 1997. An unresolved riddle: Tire chips, two roadbeds, and spontaneous reactions. *Testing Soil Mixed with Waste or Recycled Materials.* ASTM International.

O'SHAUGHNESSY, V. & GARGA, V. K. 2000. Tire-reinforced earthfill. Part 2: Pull-out behaviour and reinforced slope design. *Canadian Geotechnical Journal,* 37**,** 97-116.

PAMUKCU, S. & AKBULUT, S. 2006. Thermoelastic enhancement of damping of sand using synthetic ground rubber. *Journal of Geotechnical and Geoenvironmental Engineering,* 132**,** 501-510.

PATIL, U., VALDES, J. R. & EVANS, T. M. 2010. Swell mitigation with granulated tire rubber. *Journal of materials in civil engineering,* 23**,** 721-727.

POH, P. S. & BROMS, B. B. 1995. Slope stabilization using old rubber tires and geotextiles. *Journal of performance of constructed facilities,* 9**,** 76-79.

ROJEK, J. & O ATE, E. 2007. Multiscale analysis using a coupled discrete/finite element model. *Interaction and Multiscale Mechanics,* 1**,** 1-31.

SENETAKIS, K., ANASTASIADIS, A. & PITILAKIS, K. 2012. Dynamic properties of dry sand/rubber (SRM) and gravel/rubber (GRM) mixtures in a wide range of shearing strain amplitudes. *Soil Dynamics and Earthquake Engineering,* 33**,** 38-53.

TING, J. M., CORKUM, B. T., KAUFFMAN, C. R. & GRECO, C. 1989. Discrete numerical model for soil mechanics. *Journal of Geotechnical Engineering,* 115**,** 379-398.

TSANG, H. H., LO, S., XU, X. & NEAZ SHEIKH, M. 2012. Seismic isolation for low‐to‐medium‐rise buildings using granulated rubber–soil mixtures: numerical study. *Earthquake engineering & structural dynamics,* 41**,** 2009-2024.

VALDES, J. R. & EVANS, T. M. 2008. Sand–rubber mixtures: Experiments and numerical simulations. *Canadian Geotechnical Journal,* 45**,** 588-595.

VILLARD, P. & CHAREYRE, B. 2004. Design methods for geosynthetic anchor trenches on the basis of true scale experiments and discrete element modelling. *Canadian Geotechnical Journal,* 41**,** 1193-1205.

VILLARD, P., CHEVALIER, B., LE HELLO, B. & COMBE, G. 2009. Coupling between finite and discrete element methods for the modelling of earth structures reinforced by geosynthetic. *Computers and Geotechnics,* 36**,** 709-717.

WALTON, O. R. 1993. Numerical simulation of inclined chute flows of monodisperse, inelastic, frictional spheres. *Mechanics of materials,* 16**,** 239-247.

WALTON, O. R. & BRAUN, R. L. 1986. Viscosity, granular‐temperature, and stress calculations for shearing assemblies of inelastic, frictional disks. *Journal of rheology,* 30**,** 949-980.

WANG, J. & ZHAO, B. 2014. Discrete-continuum analysis of monotonic pile penetration in crushable sands. *Canadian Geotechnical Journal,* 51**,** 1095-1110.

WANG, Y.-H., XU, D. & TSUI, K. Y. 2008. Discrete element modeling of contact creep and aging in sand. *Journal of geotechnical and geoenvironmental engineering,* 134**,** 1407-1411.

WANG, Y. & LEUNG, S. 2008. Characterization of cemented sand by experimental and numerical investigations. *Journal of geotechnical and geoenvironmental engineering,* 134**,** 992-1004.

WU, W. Y., BENDA, C. C. & CAULEY, R. F. 1997. Triaxial determination of shear strength of tire chips. *Journal of Geotechnical and Geoenvironmental Engineering,* 123**,** 479-482.

YANAGIDA, T., MATCHETT, A. & COULTHARD, J. 2002. Damping and elastic properties of binary powder mixtures. *Powder technology,* 127**,** 107-115.

ZHOU, Y., WRIGHT, B., YANG, R., XU, B. H. & YU, A.-B. 1999. Rolling friction in the dynamic simulation of sandpile formation. *Physica A: Statistical Mechanics and its Applications,* 269**,** 536-553.

ZHU, H., ZHOU, Z., YANG, R. & YU, A. 2007. Discrete particle simulation of particulate systems: theoretical developments. *Chemical Engineering Science,* 62**,** 3378-3396.

ZORNBERG, J. G., CABRAL, A. R. & VIRATJANDR, C. 2004. Behaviour of tire shred sand mixtures. *Canadian Geotechnical Journal,* 41**,** 227-241.

# Chapter 3

# Three-dimensional discrete element modeling of direct shear test for granular rubber–sand (Paper 1)

Can Wang, An Deng[*], Abbas Taheri

School of Civil, Environmental and Mining Engineering, The University of Adelaide, SA 5005, Australia.

[*] Corresponding author.

E-mail addresses: c.wang@adelaide.edu.au (Can Wang). an.deng@adelaide.edu.au (An Deng). abbas.taheri@adelaide.edu.au (Abbas Taheri).

# Statement of Authorship

| Title of Paper | *Three-dimensional discrete element modeling of direct shear test for granular rubber-sand* |
|---|---|
| Publication Status | ☑ Published       ☐ Accepted for Publication<br><br>☐ Submitted for Publication       ☐ Unpublished and Unsubmitted work written in manuscript style |
| Publication Details | Wang, C., Deng, A. and Taheri, A., 2018. Three-dimensional discrete element modeling of direct shear test for granular rubber–sand. *Computers and Geotechnics*, *97*, pp.204-216. |

## Principal Author

| Name of Principal Author (Candidate) | Can Wang | | |
|---|---|---|---|
| Contribution to the Paper | Undertook Literature review, performed parametric study and numerical model analysis. | | |
| Overall percentage (%) | 75% | | |
| Certification: | This paper reports on original research I conducted during the period of my Higher Degree by Research candidature and is not subject to any obligations or contractual agreements with a third party that would constrain its inclusion in this thesis. I am the primary author of this paper. | | |
| Signature | | Date | 05/08/2018 |

## Co-Author Contributions

By signing the Statement of Authorship, each author certifies that:

    i.    the candidate's stated contribution to the publication is accurate (as detailed above);

    ii.    permission is granted for the candidate in include the publication in the thesis; and

    iii.    the sum of all co-author contributions is equal to 100% less the candidate's stated contribution.

| Name of Co-Author | An Deng | | |
|---|---|---|---|
| Contribution to the Paper | Acted as corresponding author, supervised project development and helped with paper editing. | | |
| Signature | | Date | 05/08/2018 |

| Name of Co-Author | Abbas Taheri | | |
|---|---|---|---|
| Contribution to the Paper | Supervised work development and helped with paper editing. | | |
| Signature | | Date | 07/08/2018 |

# ABSTRACT

Three-dimensional discrete element modeling of direct shear test conducted on granular rubber–sand is presented. Excellent agreement was attained between the simulation and test results, verifying the model's capacity of examining mixtures shear behavior. Important particulate-scale observations were attained, including the inter-particle contacts force, particles displacement and rotation, porosity and their variation with rubber particle contents. The observations demonstrate that the rubber particles inclusion amends the mixture stiffness, grading and packing at the particulate level, leading to a corresponding variation in the material shear behavior. Some interesting particulate-level simulations were examined to gain further insight into micro-mechanic characteristics of the mixtures.

**Keywords**: direct shear test; rubber; sand; discrete element; contact force; shear band.

*Chapter 3*

## 3.1    Introduction

There are approximately 48 million tons of waste tires per year generated in Australia; a low percentage is recycled or managed properly (Hannam, 2014). An important solution to increase the recycling rate is to process the wheels tire into a range of smaller pieces of rubber (e.g., shreds, chips, particles or fine powers) and incorporate the sliced rubber elements as reinforcements into soils (Bosscher et al., 1997, Lee et al., 1999, Tsang, 2008). The formed mixtures outperform the soils in respect to resilience, strength, ductility and damping (Zornberg et al., 2004, Anastasiadis et al., 2012, Tsoi and Lee, 2010). The demonstrated advantages arises from the rubber material's capacity of increasing inter-particle interactions which were confirmed in triaxial (Valdes and Evans, 2008, Masad et al., 1996, Lee et al., 1999, Zornberg et al., 2004), direct shear (Ghazavi and Sakhi, 2005, Ghazavi, 2004, Lee et al., 2014, Foose et al., 1996) and uniaxial pull-out tests (Balunaini et al., 2014).

Rubber particles can be mixed with sand into rubber–sand fill (Ghazavi, 2004). The fill exhibits better workability than the shred- or chip-based mixtures (Edil and Bosscher, 1994). For the same reason the granular rubber–sand mixtures avoid segregation problems and aim at applications in locations that are otherwise difficult to access. Additional value lies in the rubber–sand being lighter in weight by 20–40% than the sand backfill depending on the dosage used (Yoon et al., 2006). The use of the lightweight material reduces loads acting on the surrounding infrastructures or utilities (e.g., retaining walls or pipelines). Rubber–sand is also graded to facilitate water percolation and drainage and thus avoid environment or climate related concerns such as frost heave. Direct shear tests conducted on

rubber–sand samples suggested that the material shear strength remains similar in magnitude to that of sand, demonstrating a substitute for the sand in backfilling applications (Lee et al., 1999, Yoon et al., 2006, Youwai and Bergado, 2004). To understand the shear behavior, discrete element modeling was conducted on rubber–sand mixtures subjected to direct shear tests (Lee et al., 1999, Lee et al., 2014, Patil et al., 2010, Evans and Valdes, 2011, Valdes and Evans, 2008). These studies gained insight into the inter-particle interactions and demonstrated the role of the rubber particles in changing the material fabrics and the material stiffness. Most of the discrete element simulations were implemented in a two-dimensional plane which under-represents the three-dimensional shape of the particles and neglects the boundaries associated with the samples (Zhang and Thornton, 2007, Liu et al., 2005, Liu, 2006). The purpose of this study is to conduct three-dimensional numerical simulations on the rubber–sand subjected to direct shear tests. The discrete element method is used to conduct the simulations. The simulations are validated against laboratory test results and then deployed to examine how the rubber particles inclusion influences the material shear behavior.

## 3.2    Materials and method

The materials include sand and rubber particles. Define specific volume fraction $\chi$ = the rubber particle specific volume over the total specific volume of the mixture. Design a series of samples with $\chi$=0, 0.19, 0.34, 0.47, 0.58 and 1, respectively, where $\chi$=0 and $\chi$=1 define the pure sand and the pure rubber particle samples, respectively. A mixture with $\chi$>0.6 was not viable due to particles segregation (Edil and Bosscher, 1994, Kim and Santamarina, 2008). The corresponding dosage

by weight is 0, 0.1, 0.2, 0.3, 0.4 and 1, respectively. A mixer was used, following the steps shown in (Ghazavi, 2004), to gain a uniformly distributed mixture.
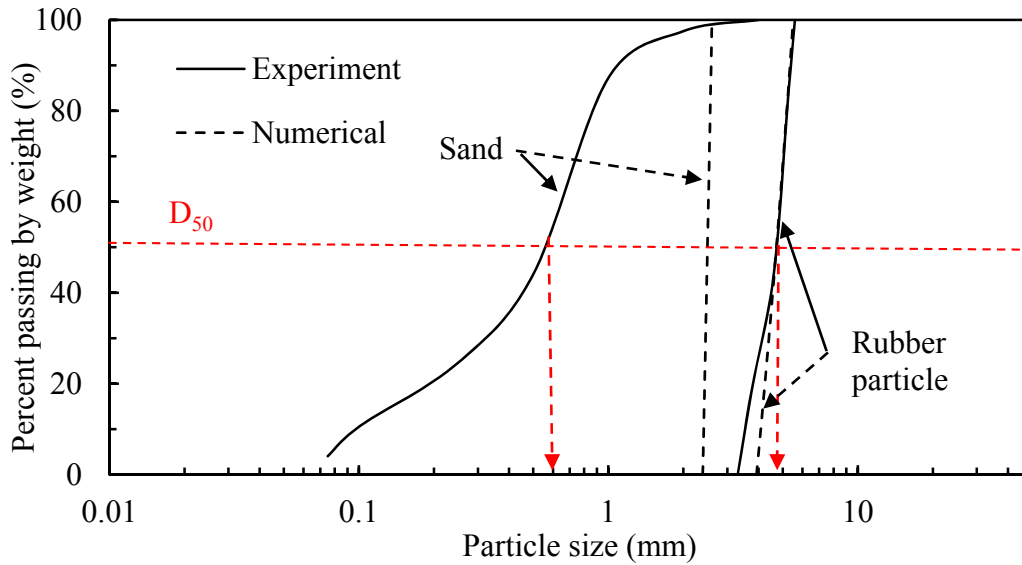


**Figure 3-1.** Particle size distribution of sand and rubber particles.

Standard direct shear tests were performed. The sample size measures $60W \times 60L \times 40D$ mm, which was chosen to satisfy the sample size vs. particle size criterion. Pour the sample into the shear boxes, and even and level the materials, enabling a uniform distribution. Prepare four identical samples for one dosage $\chi$ and subject the four samples to vertical load $\sigma_v$ of 100 kPa, 200 kPa, 300 kPa and 400 kPa, respectively, where dosage indicates the quantity used for rubble material. Shear the samples at a rate of 1 mm/minute until the occurrence of the greatest shear stress or 5 mm displacement, whichever occurs earlier.

Discrete element simulation was conducted using a commercially accessible software package Particle Flow Code (PFC) 3D. Assemble together ten

pieces of wall (a PFC simulation object) to form a compartment, with respective dimensions representing the shear boxes, as shown in Figure 3-2. Inside the box compartment is the spherical particles assembly, with the particle sizes designed in agreement with main portions of rubber particles and sands, respectively. The respective gradation curves for both experiments and simulation are shown in Figure 3-1. The sand ($D_{50}$=0.58 mm) is well graded to fit into the pore space of the rubber particles ($D_{50}$=5 mm). Due to a wide range of sand particle sizes, different scaling methodologies may be applied (Evans and Valdes, 2011). In this context, mass scaling (Belheine et al., 2009, Jacobson et al., 2007, Evans and Frost, 2007) was adopted to increase the particle sizes while remain the same material density The size optimization has proven successful in computation acceleration and simulation accuracy (Feng et al., 2017, Valdes and Evans, 2008). Depending on the dosage examined, there are about 6,000 sand particles and 1,000 rubber particles created to fill up the boxes space. The mixture in the shear box is shown in Figure 3-2. After placing the particles inside the shear boxes, apply the servo-control method (Itasca, 2008) to release excess sphere contact forces where there were.
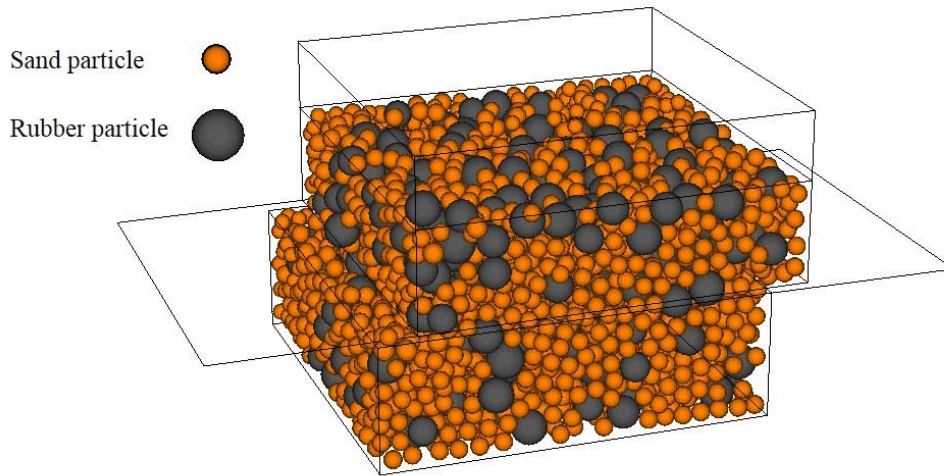
**Figure 3-2.** Material assembly in direct shear boxes.

The linear elastic model of PFC3D was used to replicate the shear stress−displacement relations. The linear model outperforms the nonlinear Hertz model in respect to the use of she servo-control, which is a model in-built developed to maintain a load acting on the materials (Itasca, 2008) The linear model is illustrated in Figure 3-3. Two entities (or particles), 1 and 2, interact. The interaction is modeled through a set of physical units: springs, dashpots and a slider. The springs are used to create a linear elastic relation between relative displacement and contact force. The dashpots are applied to provide viscosity at shear and normal directions, respectively. The material properties for the simulation are summarized in Table 1. In the table, the inter-particle properties were determined by PFC3D using the following equations:

$$\frac{1}{k_n} = \frac{1}{k_{n,1}} + \frac{1}{k_{n,2}} \qquad (3.1)$$

$$\frac{1}{k_s} = \frac{1}{k_{s,1}} + \frac{1}{k_{s,2}} \qquad (3.2)$$

$$\mu = \min(\mu_1, \mu_2) \qquad (3.3)$$

where $k_n$ and $k_s$ are normal and shear stiffness at contact; $k_{n,1}$ and $k_{n,2}$ are normal stiffness of entity 1 and 2, respectively; $k_{s,1}$ and $k_{s,2}$ are respective shear stiffness; $\mu$ is inter-particle friction coefficient; $\mu_1$ and $\mu_2$ are respective entity surface friction.
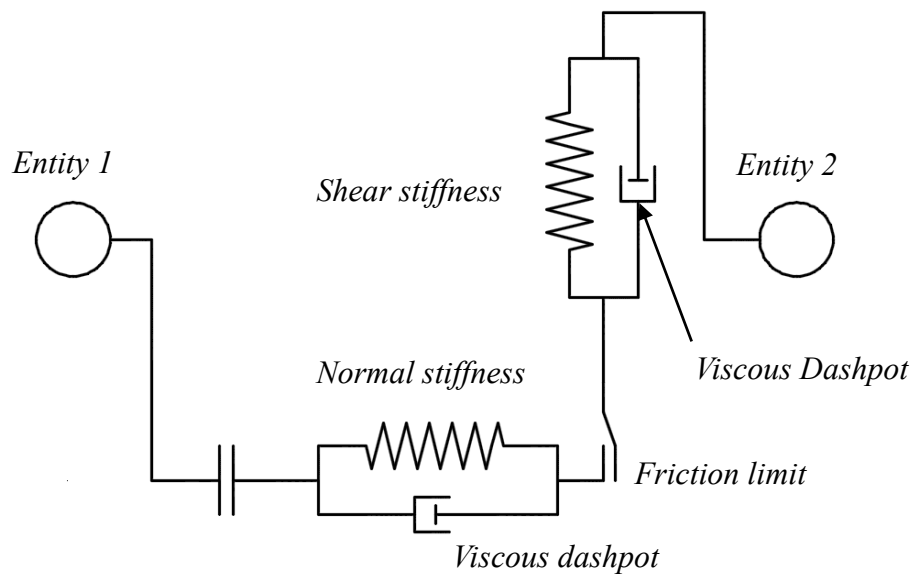


**Figure 3-3.** Linear contact model used in direct shear test

**Table 3-1.** Material properties for discrete element simulation.

| Property | Value | | |
|---|---|---|---|
| | Sand particle | Rubber particle | Wall |
| Contact normal stiffness, $k_n$ (N/m) | $5.9 \times 10^7$ | $8 \times 10^5$ | $1 \times 10^8$ |
| Contact shear stiffness, $k_s$ (N/m) | $5.9 \times 10^7$ | $8 \times 10^5$ | $1 \times 10^8$ |
| Particle diameter, $d$ (mm) | 2.4–2.6 | 4–5.5 | N/A |
| Specific density | 2.65 | 1.2 | N/A |
| Damping coefficient | 0.7 | 0.7 | N/A |
| Inter-particle friction coefficient | 0.55 | 0.60 | 0.20 |

As suggested in previous studies (Nakata et al., 1999, Potyondy and Cundall, 2004, Wang and Leung, 2008), the quartz sand stiffness falls into the order of magnitude of $\times 10^7$ N/m. A lower order of magnitude of $\times 10^5$ N/m was suggested for rubber material (De Bono et al., 2012). These values were taken as the points to depart and, as suggested in Coetzee and Els (2009), plugged into numerical iterations of harmonizing the shear test results, aiming at obtaining the final stiffness and other micro-properties. The simulations are shown in Figure 3-4. Excellent agreement is obtained between the test and simulation results for all series of tests. That means the material properties in Table 1 are verified as input values for the discrete element model to replicate the particles motion. All of the samples exhibit a strain-hardening relation where there is no clear occurrence of failure. The relationship agrees with the results provided in similar rubber–sand studies (e.g., Ghazavi and Sakhi (2005)). The strain-hardening relationships become pronounced when the applied vertical load $\sigma_v$ or rubber content $\chi$ increases.

The strain-hardening curves suggest two aspects: *i*) the sand samples are loosely packed when sheared and there is no clear shear dilation; and *ii*) the rubber particles inclusion improves the material packing. The improved packing promotes the material strain-hardening characteristics as well as ductility, which is in favor of stability of backfilling works.
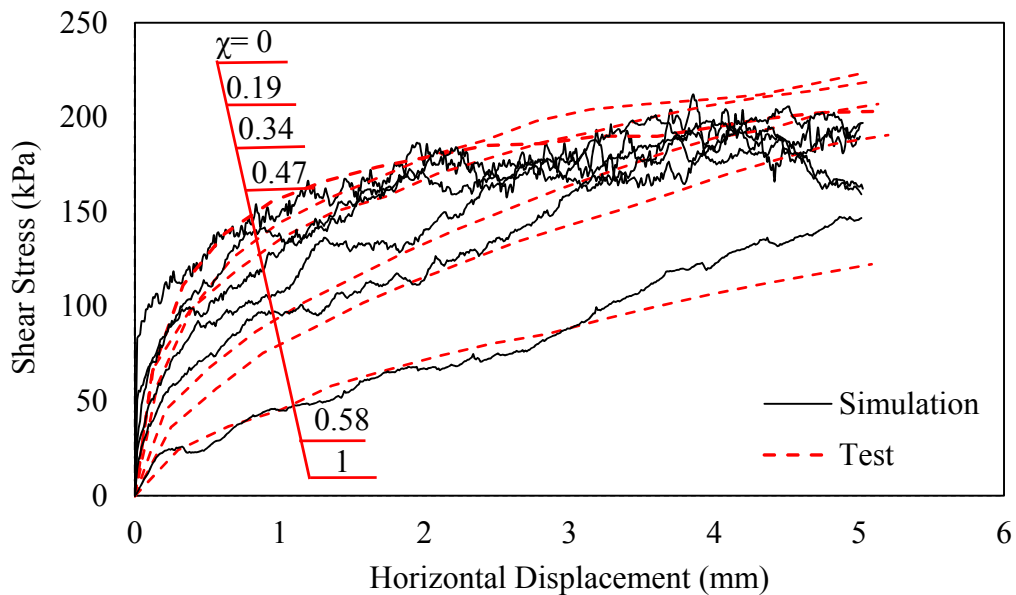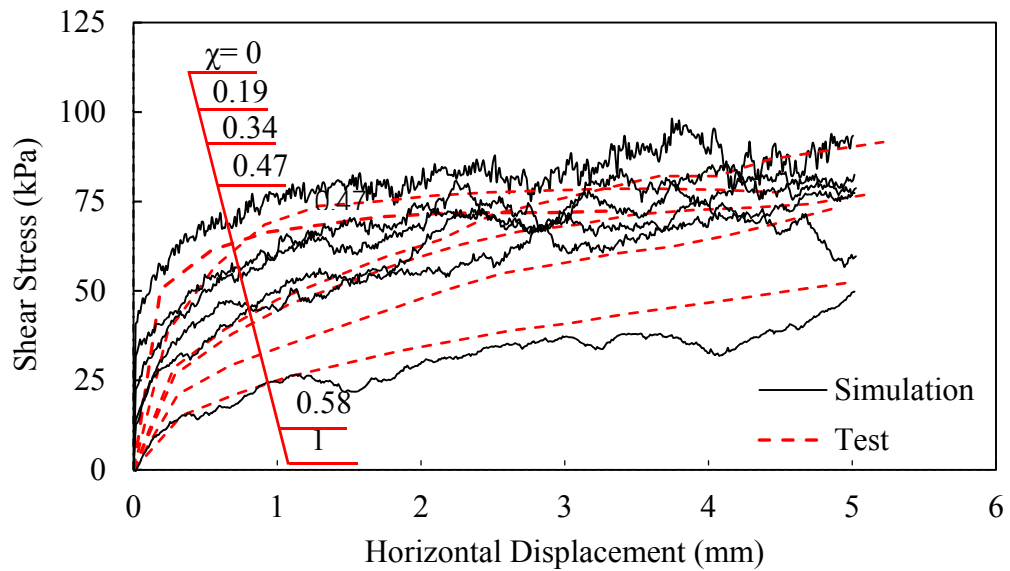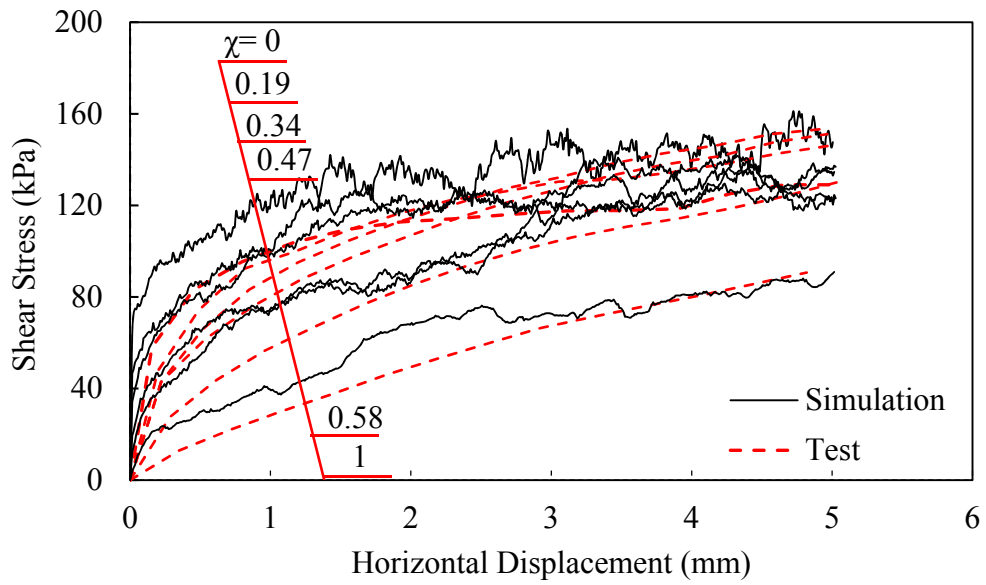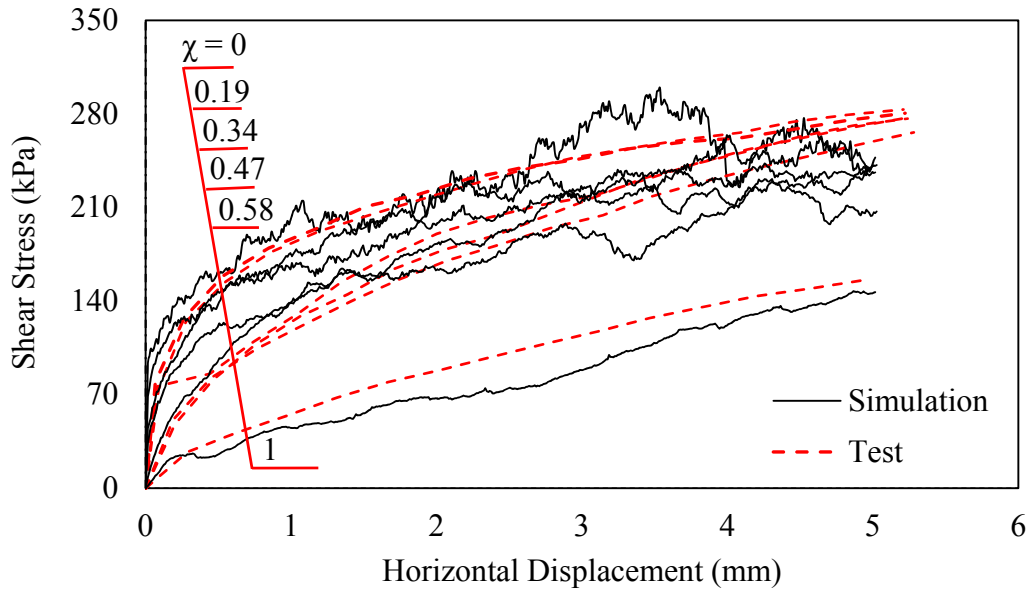
**Figure 3-4.** Shear stress–displacement curves for samples subjected to direct shear test with varying vertical loads.

## 3.3 Particulate-scale simulation results

### 3.3.1 Packing

The material packing is illustrated in Figure 3-5. Four assemblies are presented: rubber particles, poorly-packed rubber–sand, well-packed rubber–sand, and sand. The assemblies vary in mix design, leading to material porosity variation. The rubber particles assembly (i.e., the leftmost diagram) exhibits the greatest porosity. The porosity decreases with the sands inclusion, as the sand particles are finer enough to sit in the pore space formed by the rubber particles skeleton i.e., the two middle diagrams. The trend, however, seems not to continue into the sand assembly; the sand assembly does not yield the least porosity. Plot one single presumed rubber particle in red in the sand assembly as shown in the rightmost diagram. The presumed rubber particle works better to reduce the pore space than the lot of the equivalent sand particles does. That is, there is a rubber fraction enabling packing optimization. To work out the optimal fraction, a set of eleven assemblies of different mix fractions is packed through simulations, aiming at developing the porosity vs. mix fraction relationship. The relationship is shown in Figure 3-6 (i.e., the primary axis vs. the horizontal axis). It is shown that the porosity vs. rubber fraction relationship is not monotonic but concave. The transition sits on sample $\chi$=0.6, less than which the porosity decreases with $\chi$; otherwise the opposite occurs. Therefore $\chi$=0.6 is identified as the optimal packing mix. Similar packing characteristics occur to other binary mixtures. Kim and Santamarina (2008) examined packing of sand and rubber chips ($D_{50}$=3.5 mm) mixtures and recommended an optimal packing fraction of $\chi$=0.67. Mota et al.

(2001) assessed spherical glass beads (0.3 mm to 3.4 mm sizes) with 2 to 10 size

ratios and confirmed a similar optimal fraction $\chi$=0.6 to 0.7 for all series mixtures.

All of these results suggest that packing is sensitive to particles size difference.
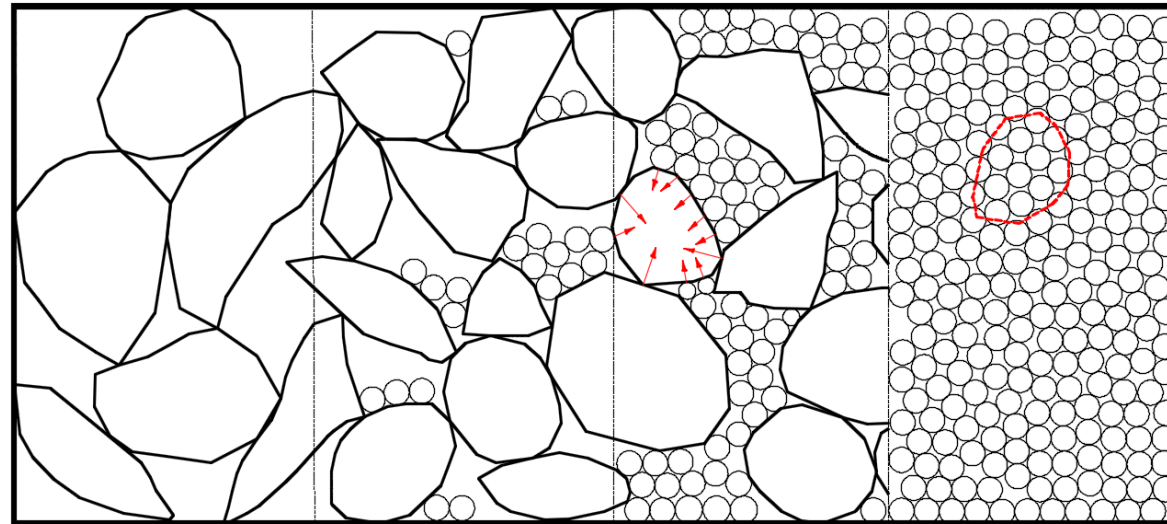
Rubber particles       Rubber-sand       Rubber-sand    Sand particles

(loosely packed)    (densely packed)

**Figure 3-5.** Schematic of mixtures packing.
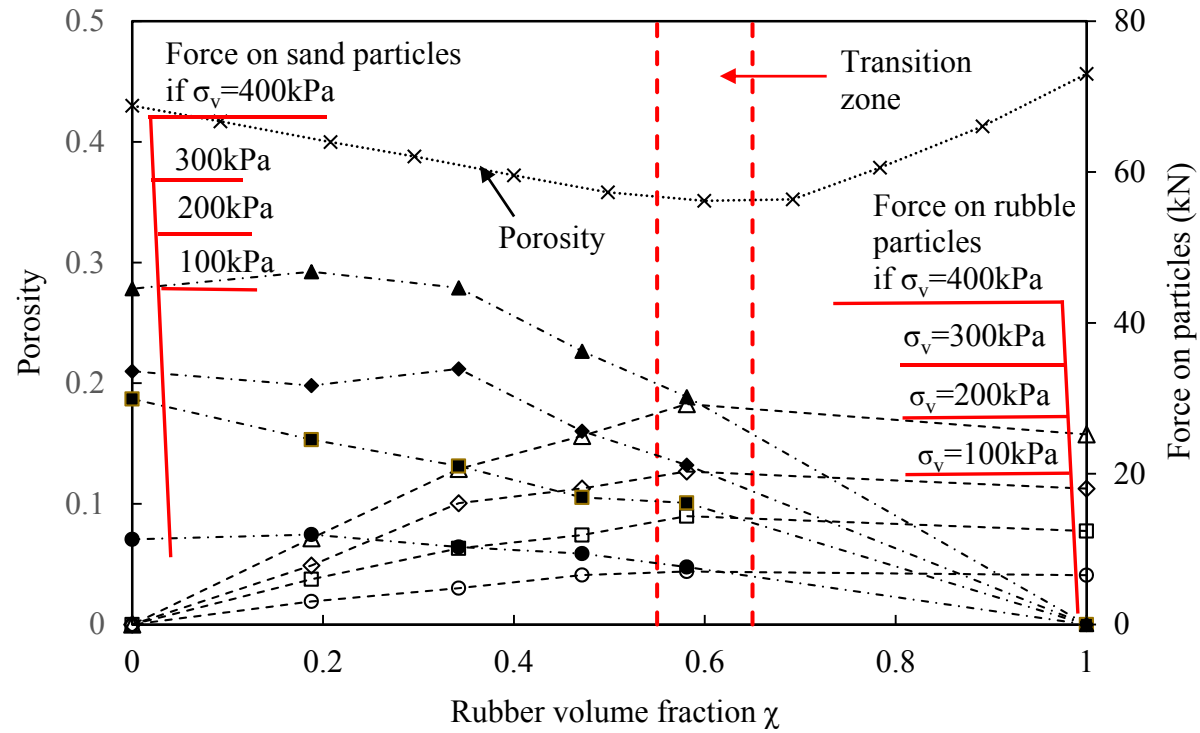
**Figure 3-6.** Porosity and force density for samples in direct shear simulations of varying vertical loads.

Additional mixtures of varying grading characteristics were examined. The simulation results are shown in Figure 3-7. Five mixtures are simulated, with a ratio of larger particle size, *D*, to smaller particle size, *d*, ranging from 10 to 2. An additional variant is the large particle fraction, $\chi_D$, from 0 to 1, aiming at broadening the grading characteristics. The results suggest that the grading does influence the packing (i.e. porosity). The mixture becomes dense with *D/d* increase, meaning small particles infilling the pores of large particles. The infilling effect is optimal at $\chi_D \cong 0.6$, consistently across all of the five series of mixtures. This optimal value agrees with those test results provided in Mota et al. (2001).
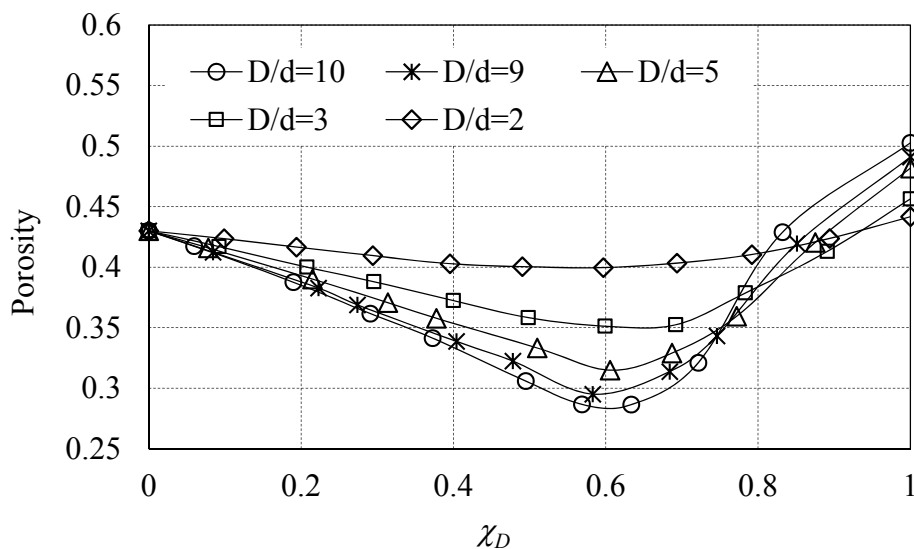


**Figure 3-7**. Porosity changes due to varying mixture fraction and particle size.

The secondary vertical axis of Figure 3-6 reads the force density for the samples examined. The force density is defined as the sum-of-force at contact, *F*, normalized to the sample volume, *V*, and mixture median diameter, $D_{50}$, i.e., $F/(V \times D_{50})$. For demonstration purpose, the forces at the contacts of a single particle are illustrated in the third diagram in Figure 3-5. The value of *F* is the sum

75

of the forces at the contacts of interest, e.g., the rubber particle contacts. Where a particular portion of particles is examined, the force density measures the particles capacity of sharing the inter-particle force. Figure 6 shows the force density at rubber (and sand) contact vs. rubber fraction curves, each corresponding to one of the four vertical loads (i.e., 100, 200, 300 and 400 kPa). For each of the curves, the rubble content is the only variant, with the rest conditions remain the same. The purpose is to examine the rubber (or sand) contact force with respect to rubber content where the load is constant. All of the four curves are convex; and the transitions occur consistently at $\chi = 0.58$, at least for the rubber fractions examined. The transition points also agree with the optimal value $\chi = 0.6$ for packing. Define a transition zone $\chi=0.55$ to 0.65 where the assembly works best in packing and load sharing: the rubber fraction develops into a skeleton where the sands largely infill the skeleton pore spaces and enable optimal packing; in the meantime the rubber particles share the most significant portion of the loads and guarantee material strength capacity.

### 3.3.2    Inter-particle forces

The inter-particle forces are examined on sample $\chi=0.34$ being sheared under the vertical load $\sigma_v=200$ kPa as an example. To gauge the forces evolution, select five points of *A* to *E* on the corresponding shear stress–displacement curve (Figure 3-8). The five points read displacement values of $\delta=0$, 1, 4, 5 and 6 mm, respectively, aiming to span the complete shear process. In addition a separate shear is simulated which conducts an unloading-reloading process in the middle of shear, examining the damping behavior of the model. In the process, the boxes reverse from $\delta=2$

mm to $\delta$=1 mm, then are re-sheared to $\delta$=6 mm. The unloading-reloading process creates a hysteresis loop, demonstrating the elastic-plastic behavior of the shear process. The unloading clearly and quickly releases the shear stress acting on the sample, and meanwhile an opposite shear force occurs and grows. Upon re-loading, the curve moves back to the point where unloaded, recovering the original shear stress released, and interestingly continues in a new pathway. The new pathway rises above that without the load loop, meaning the material stiffens. That is, the load loop helps compact the mixture and the damping properties assigned to the model reflects the physical behavior of the sample.



**Figure 3-8.** Shear stress vs. displacement curve.

The inter-particle forces are plotted as solid lines with its thickness proportional to the force magnitude (Itasca, 2008). The lines connect up into a chain between particles, forming a force chain. The corresponding normal contact force chains that are captured from the front view, together with the illustrated shear boxes, are shown in Figure 3-9. The normal contact force, in relation to the shear force, gives a better picture of the particles overlap and motion. The force

chains for the sand sample ($\chi$ =0) sheared to $\delta$=6 mm is also provided for comparison. It is clear that the contact forces progressively redistribute with the shear advance. The forces distribute evenly where there is no shear but the vertical load $\sigma_v$ applied (Figure 3-9(a)). When the lower box advances to the left, a force concentration band evolves diagonally and becomes pronounced as shown in Figure 3-9(b–e), meaning greater normal contact forces oriented diagonally. When the shear advances, the force band becomes more diagonally oriented. Define a shear advance convention: it is a clockwise shear if the lower box displaces to the left, otherwise an anti-clockwise shear. The clockwise shear which is the case of Figure 9 leads to a force band oriented from the top–left corners to the bottom–right. It is plausible to infer that a top–right to bottom–left force band evolves if the shear acts anti-clockwise. Where sheared to the same displacement $\delta$=6 mm, the sand sample (Figure 3-9(f)) exhibits similar force band orientation, but finer force chains than the corresponding rubber–sand sample does (Figure 3-9(e)). This suggests the capacity of rubber materials in concentrating the contact forces. The rubber particles inclusion brings forth to the soil matrix two changes: particles stiffness reduction and particle size increase. Both contribute to the contact forces concentration in view of contact mechanics. The contributions can be illustrated in Figure 3-10. An assembly of discs is enclosed in a box. The line between two contacting discs represents a contact force where the line thickness is proportional to the force magnitude. In Figure 3-10(a), the presumed larger disc is equivalent in area to the six smaller discs. The substitute shown in Figure 3-10(b) eliminates the inter-particle contacts bounded by the larger disc, reducing the total number of contacts in the assembly and therefore the number of force chains. In addition the material stiffness also alters the force chain. Where the assemblies are

compressed as shown in Figure 3-10 (c–d), a larger overlap at contact is captured

by the software as a greater contact force. In the meantime, the void around large

particle surface provides room for the neighboring small discs to rearrange. The

rearrangement helps release a portion of the force developed between the small

discs.



(a)

(b)

(c)

(d)

(e)

(f)
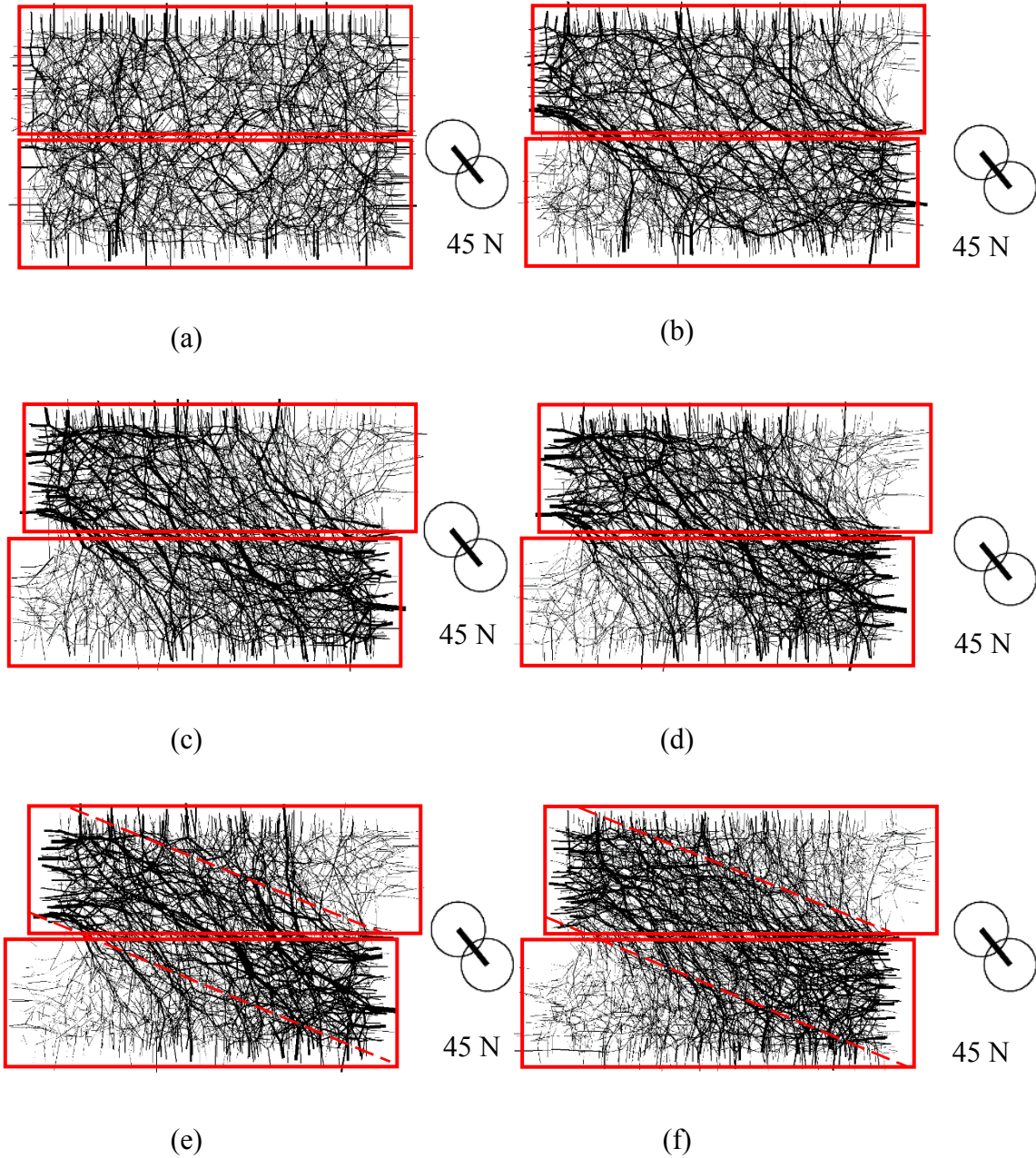
**Figure 3-9.** Contact force chains drawn at the same scale for samples sheared

under $\sigma_v$=200 kPa to different distances.
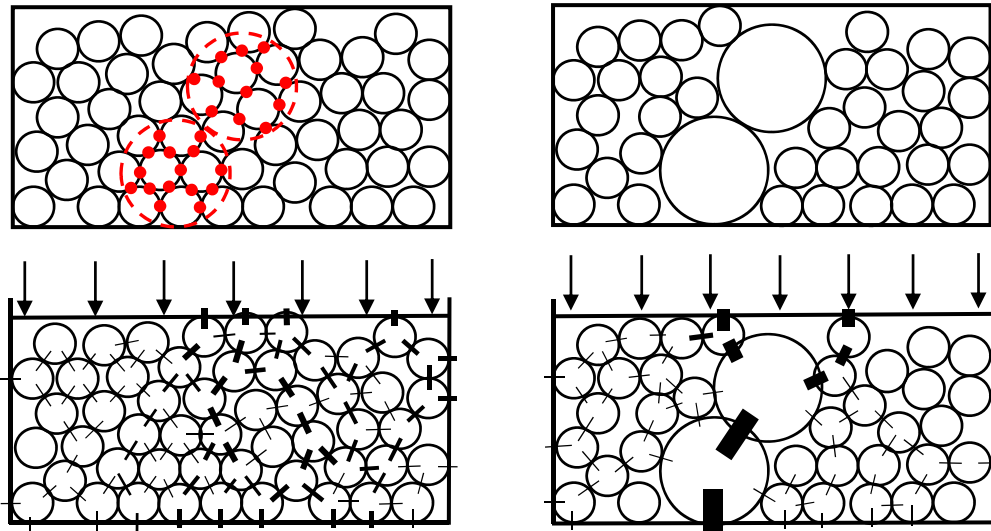
**Figure 3-10.** Schematic of disc contacts under different conditions

The contact force is represented by plotting stress contour lines, aiming at mapping the stress and refining the force band orientation. The measurement sphere approach (Itasca, 2008) is used to plot the stress contours. The sphere is designed to capture the equivalent stress field bounded by the sphere. Figure 3-11(a) illustrates the enlarged view of one measurement sphere as well as the influenced particles. Figure 3-11(b) shows the design of the measurement spheres to the shear boxes. A grid of 4×6 measurement spheres is created in the shear boxes. All of the spheres are equal in size with a diameter of 10 mm, occupying the inner space of the box. Each of the spheres is at least two times larger in size than the particles examined in the direct shear test and can accommodate up to twenty particles depending on the particles size.
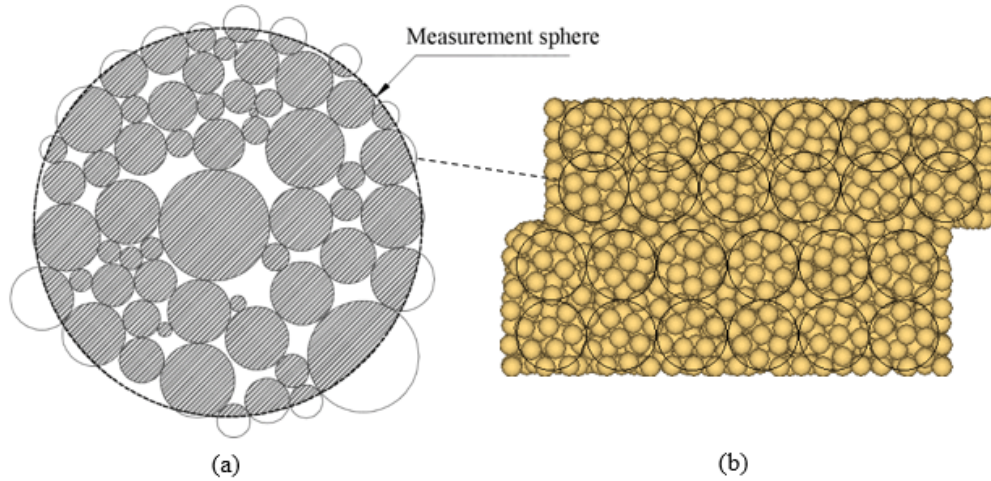
**Figure 3-11.** Diagram of measurement sphere approach: (a) one measurement sphere and bounded particles, and (b) a grid of measurement spheres designed in the shear box.

The stress contour maps plotted for the sand sample before and after the shear test are shown in Figure 3-12. The shear as an example is conducted under the vertical load $\sigma_v$=200 kPa until the displacement $\delta$=6 mm. Plot the contours at three separate vertical planes: the front, middle and back, enabling a 3D view of the stress distribution. The set of contour lines is plotted by using the software package MATLAB to process the stress values captured by the measurement spheres. In a measurement sphere, the stress value is defined as the mean stress at contact, $\sigma_m$, which is expressed as $\sigma_m=(\sigma_{xx}+\sigma_{yy}+\sigma_{zz})/3$ where the dimensional stress $\sigma_{xx}$, $\sigma_{yy}$ and $\sigma_{zz}$ are provided by PFC 3D. It is noteworthy that the contour lines draw on the centers of measurement spheres; therefore the margins are not mapped. The stress contours in Figure 3-12(a, c and e) show that the samples remain broadly even in contact stress before the shearing. At a few spots (e.g. the bottoms and corners) the stress values are relatively lower due to the arching created as illustrated in the broken curves. The overall stress values on the map agree with the vertical load $\sigma_v$ =200 kPa. Where sheared, the sample develops new contour

maps as shown in Figure 3-12(b, d and f). The changes include the contours orientation to the diagonal, stress concentrations in the upper–left and lower–right corners, and uneven stress distribution on the shear plane. These changes confirm the past research outcomes (Wang et al., 2007, Zhou et al., 2009) that displacement (and shear stress) is not constant on the shear plane and the active and passive pressure zones evolve in the lower and upper boxes, respectively.
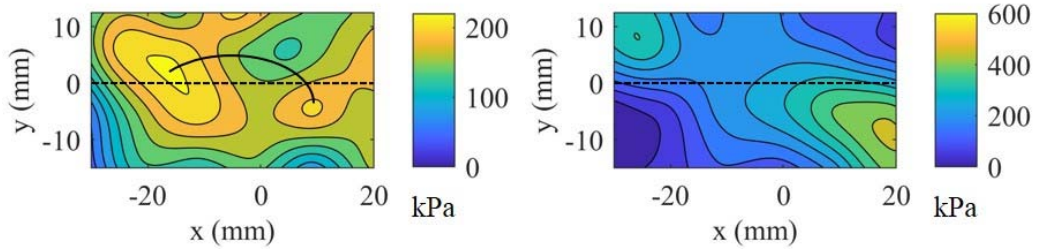


(a) Stress contours before shearing at front elevation



(b)Stress contours after shearing at front elevation
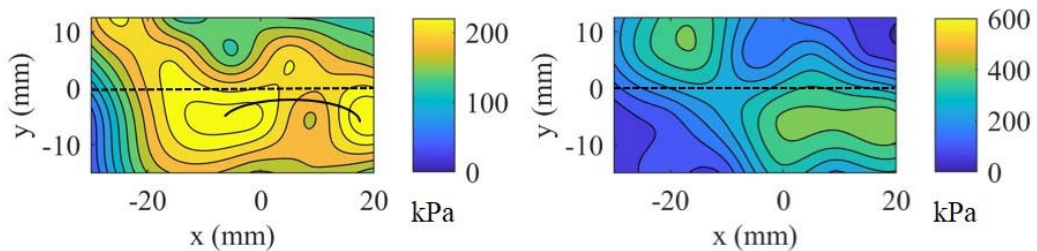


(c) Stress contours before shearing at middle elevation



(d) Stress contours after shearing at middle elevation
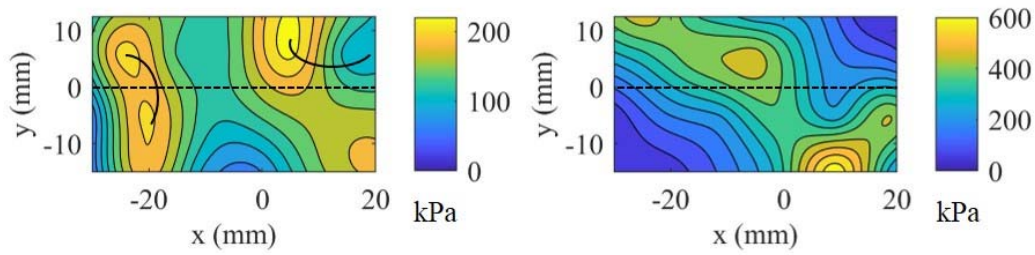
(e) Stress contours before shearing at
back elevation

(f) Stress contours after shearing at
back elevation

**Figure 3-12.** Stress contours of sand sample drawn at different elevations: (a) the front before shear, (b) the front after shear, (c) the middle before shear, (d) the middle after shear, (e) the back before shear, and (f) the back after shear.

The contour maps shown in Figure 3-12 can be illustrated by plotting particles contacts. A collection of discs of different sizes is gathered in the closed box as shown in Figure 3-13. The discs sitting on the diagonal band clearly overlap with respective neighboring discs. Based on the contact model defined in (Cundall and Strack, 1979), the pronounced overlapping demonstrates a greater level of stressing developed at the contacts and thus adds up the load shared by these discs. The discs in the remaining areas show less magnitude of overlapping and thus are less effective in counteracting the shear.
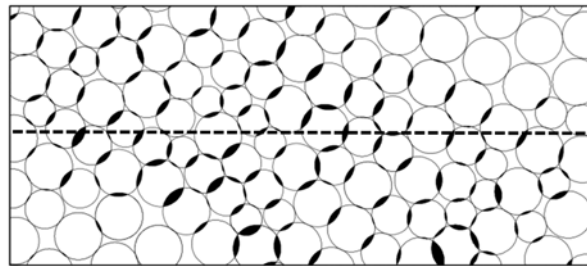


**Figure 3-13.** Schematic of discs overlapping when sheared.

### 3.3.3 Particles Displacement Vector

Particle displacement vectors are provided in Figure 3-14. A vector, as illustrated by the legend, has two independent properties: magnitude and direction. Each of the vectors represents the displacement of a particle, with vector's start (and end) corresponding to the initial (and final) position of the particle and the length for the travel distance. Vectors are drawn for two samples $\chi$ =0.34 and 0, respectively, which are sheared to $\delta$=6 mm under $\sigma_v$=200 kPa. The two samples show similar particles displacement: significant leftward motions of particles in the lower box, and minor convex thrusts of the upper. The difference in displacement magnitude between the upper and lower boxes arises from the lower box advancing to the left which is picked up by the simulations. The convex thrusts shown in the upper box are caused due to the shear dilation (Masson and Martinez, 2001, Liu et al., 2005, Liu, 2006). The convex thrusts are more pronounced in the rubber–sand sample (i.e. $\chi$=0.34) than in the sand sample (i.e. $\chi$=0) as illustrated by the arrows. Similar thrust difference was reported in (Zhou et al., 2009) which concluded that large-size particles tend to generate a larger strain localization zone and result in stronger dilation. To the right of the convex thrust is a small-scale vortex zone as marked out. This is formed due to the shear strain evolution. As the shear advances, the particles in this zone undergo shear compression (Indraratna et al., 2012). The particles in the vortex also fall into the less-overlapping areas (Figure 3-13), and the loose inter-particle contacts are in favor of the particles rotations but interlocking or dilating.
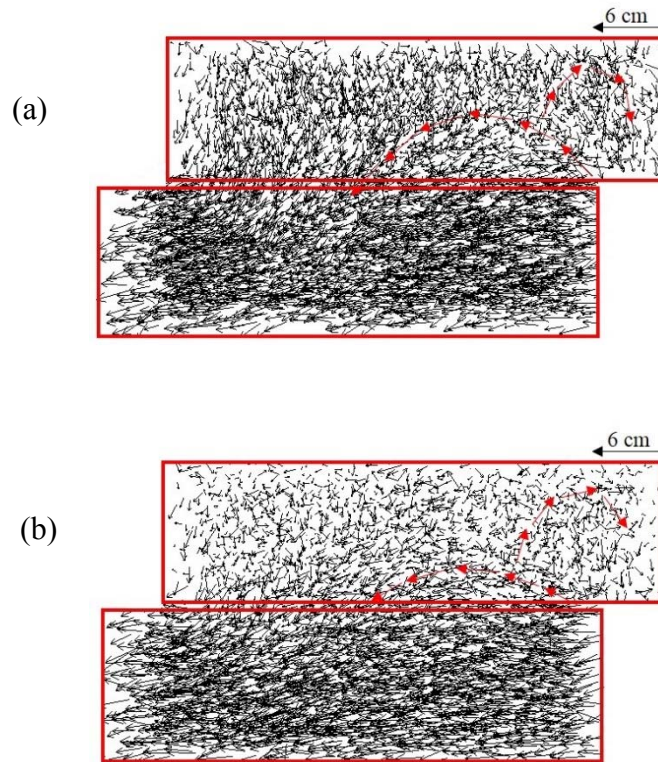
**Figure 3-14.** Particle displacement vectors drawn at the same scale for samples (a) $\chi=0.34$ and (b) $\chi=0$ when sheared to $\delta=6$ mm under $\sigma_v=200$ kPa.

### 3.3.4    Rubber Fraction Dependence

The above test and simulation results exhibit the rubber fraction dependence of the shear behavior. It is thus of importance to examine the dependence and develop a rubber fraction suitable for applications. The approach is to plot the shear stress vs. rubber fraction relationship for samples subjected to a set of high- to low vertical pressure $\sigma_v$. The pressure $\sigma_v$ is accounted for as it influences the shear stress curves. In addition to the aforementioned low- to medium pressures, two high pressures are examined: $\sigma_v=1$ and 2 MPa. The pressure values are suitable for deep (e.g., 50 to 100 m) backfilling works, e.g., mining pit renovations. The shear stress–displacement curves obtained from the developed discrete element

model are presented in Figure 3-15. Four rubber fractions are examined, i.e. $\chi=0$,

0.34, 0.58 and 1. It is shown that samples $\chi=0$ and 0.34 show nearly tied curves

under both pressures and the curves sit noticeably above those of samples $\chi=0.58$

and 1. The curves difference suggests that the fraction $\chi=0.34$ is a dosage in favor

of the mixture gaining (or maintaining) shear stress; a further higher fraction may

likely lead to strength decrease. This trend agrees with the strength development

examined under the low- to medium pressure shear tests (Figure 3-4).
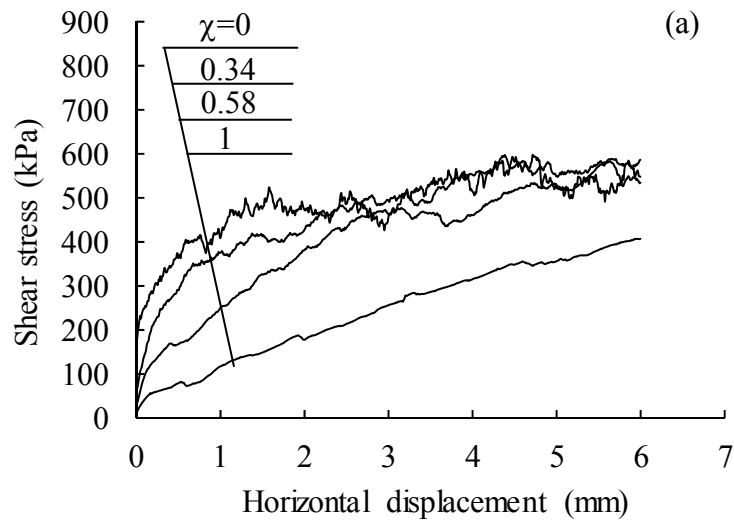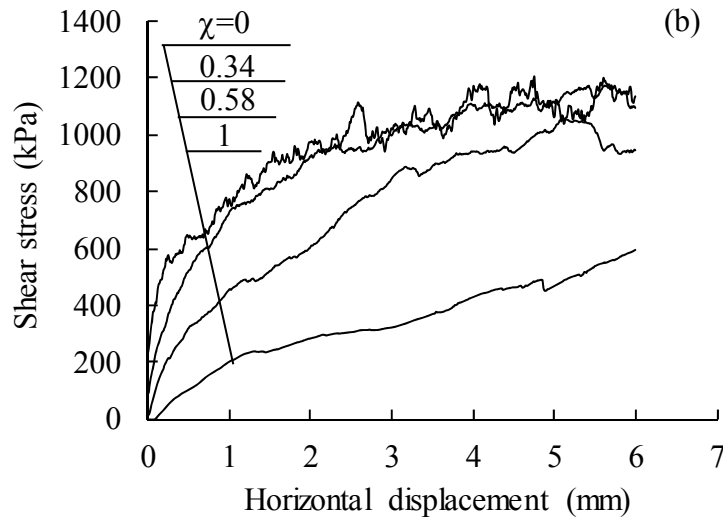
**Figure 3-15.** Shear stress−displacement curves for different samples sheared under high pressures: (a) $\sigma_v$=1 MPa, (b) $\sigma_v$=2 MPa.

Define two stress points, $\sigma_1$ at shear displacement $\delta$=1 mm and $\sigma_6$ at $\delta$=6 mm, as the measures assessing the material early- and late-stage shear strength, respectively. The shear strength vs. rubber fraction relationship obtained under a set of vertical pressures is provided in Figure 3-16. The pressures examined include 2 MPa, 1 MPa, 0.4 MPa and 0.1 MPa. Under the high pressures (i.e., $\sigma_v$=2 and 1 MPa), rubber fraction $\chi$=0.34 is confirmed in favor of the shear strength development and deemed an optimal dosage. Where the vertical load reduces to 0.4 MPa or lower, the rubber inclusions exhibit marginal effect on the shear strength. That is, the rubber particles gain strength in a way similar to the sand particles where the mixtures are subjected to medium- to low loads, such as medium- to shallow-depth backfilling applications. When placed in a deep application, the mixture becomes sensitive in shear strength to the rubber content and a fraction $\chi$=0.34 is a preferred choice to gaining shear strength.
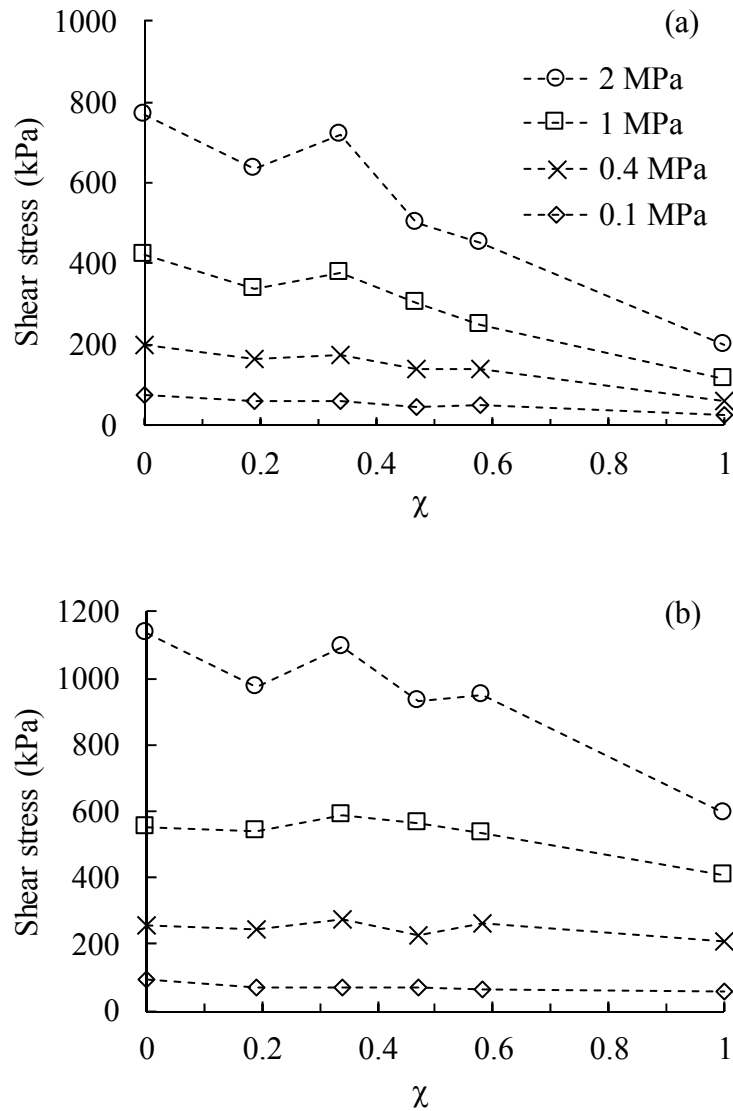
**Figure 3-16.** Shear stress obtained at two shear distances: (a) $\delta$=1 mm, (b) $\delta$=6 mm.

Similar rubber content dependency occurs to other rubber chips or shreds based mixtures. Zornberg et al. (2004) reported the optimal fraction $\chi$=0.55 where the rubber shreds (i.e., 20–30 mm by size) were mixed with sands. Rao and Dutta (2006) found that a rubber chips fraction of $\chi$<0.35 shows strength improvement. The optimal content becomes $\chi$=0.2–0.3 for rubber particles based mixtures (Ghazavi, 2004), which agrees with the outcomes of this current study. These past and current studies suggest that the optimal rubber content is dependent on the

rubber particle size, or increases with the size. When the rubber inclusions become larger, they work more like continuous media or geomemberane materials in the mixtures, enabling better particle–surface frictions. The frictions increase with the rubber contents and help mixtures gain strength. Where the rubber contents exceed respective optimal values, there are insufficient volumes of sands infilling the skeleton formed by the rubber inclusions and the packing becomes loose. In this context, the shear strength reduces.

### 3.3.5    Composite micro–structure

It is worth cross-checking the shear strength development Figure 3-16 against the mixture packing results (Figure 3-6). Greater packing is obtained at $\chi$=0.58 where the pressure acted is 0.4 MPa or less. This $\chi$ value does not agree with the optimal fraction $\chi$=0.34 obtained for the shear strength. That is, the packing and the shear strength correspond to different optimal fractions. This finding disagrees with Ghazavi (2004) associating the shear strength changes exclusively to the mixture packing. In Ghazavi (2004), the maximum shear strength occurs at rubber volume fraction $\chi$=0.2–0.3. The explanation was the occurrence of greatest packing at the same fraction, although the packing was not tested or simulated. The current study suggests that the greatest packing and maximum shear strength may not coincide at the same fraction. The packing is at $\chi$=0.58 and the strength at $\chi$=0.34. That means, the single strength–porosity association seems not conclusive. There are underlying factors influencing the shear strength development, one of which is the particles arrangement, in particular the large size particles (rubber) orientation.

Figure 3-17 illustrates three mixtures of different $\chi$ values and thus varying particles arrangement. From the left to the right, the mixtures decrease in $\chi$ values and thus bring forth varying rubber particles arrangement. An important difference among the diagrams lies in the chance of rubber particles crossing the shear plane and, if there is, the particles number. The chance and number are high where $\chi$ is high, as shown in the leftmost diagram. The particles cross the shear plane, forming a flocculated structure. Given the limited number of particle contacts on the shear plane, the force counteracting the shear is not significant. The force instead builds up where the rubber particles and the sands together sit on the shear plane, as shown in the middle diagram. The number of contacts increases, enabling better frictions and interlocking. Given the rubber particles crossing the plane, an additional component of shear resistance is gained. Where subjected to high pressures, the rubber particles help gain further resistance through the contact flattening mechanism (Valdes and Evans, 2008). These strength-gaining effects fade off and the shear resistance decreases if few rubber particles rest across the plane (i.e., the rightmost diagram), whereupon the sands but the rubber particles counteract the shear. Albeit the sand-contact number is significant, a portion of the on-the-plane sand finds room to relocate as illustrated (due to the rubber particles deforming) and fails to gain major shear strength from interlocking or dilating (Ghazavi, 2004, Ghazavi and Sakhi, 2005). Given these understandings, the mixture particles arrangement is identified as an important factor influencing the shear strength development.
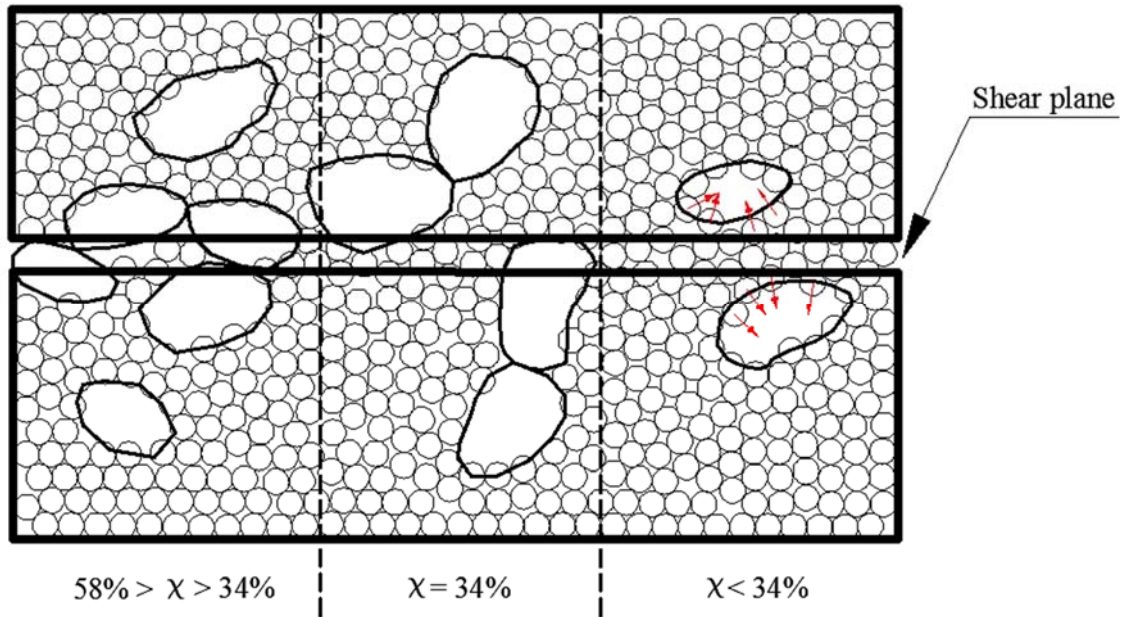
**Figure 3-17.** Schematic of mixing arrangement as a function of rubber content

The above three particle arrangement models can be proven based on the rubber particles sitting on the shear plane. Count the number of rubber–rubber contacts, $N_c$, and rubber particles, $N_r$. The $N_c/N_r$ value suggests how the rubber particles orient and to what extent. Plot the $N_c/N_r$ vs. the rubber fraction $\chi$, as shown in Figure 18. Three representative vertical loads are examined: $\sigma_v = 100$, 1000 and 2000 kPa. Despite the varying loads, $N_c/N_r \cong 1$ where $\chi \cong 0.34$. Otherwise, $N_c/N_r$ moves away from the unity. Where $N_c/N_r=1$, the particles tend to close up. This is illustrated in Figure 3-19. Five diagrams (*a–e*) are plotted, each with different particle numbers or orientations. Diagrams *b–c* align linearly, and Diagrams *d–e* close up. The orientation patterns influence the contacts number. For example, Diagram *c* has 2 contacts; Diagram *d* has 3, although the particle numbers remain the same which is 3. Determine $N_c/N_r$ values for the five scenarios. It is suggested that the $N_c/N_r$ value is less than 1 if particles align linearly, e.g., Diagrams *a–c*; and equal to or near 1 if closed up, e.g., Diagrams *d–e*.
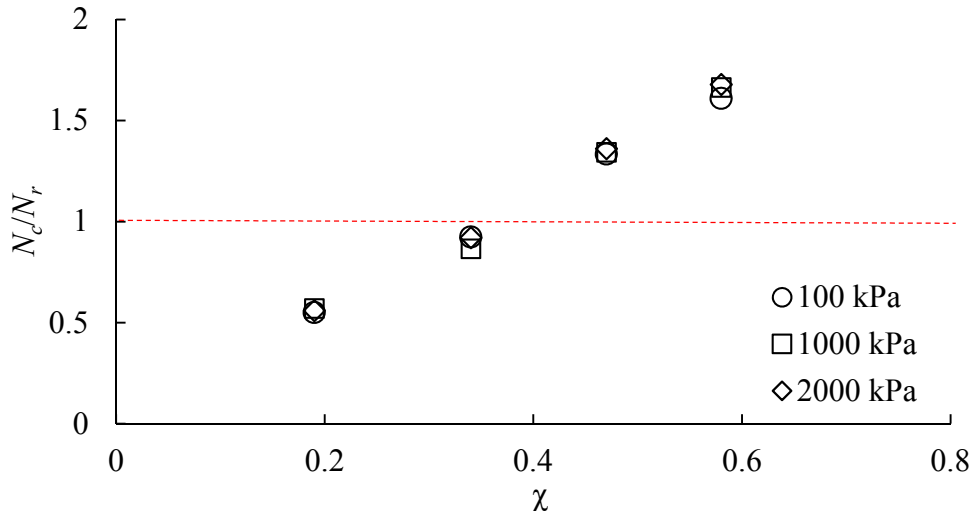
**Figure 3-18.** Rubber–rubber contacts to rubber particles vs. rubber content

obtained under varying vertical loads.



(a)          (b)          (c)          (d)          (e)
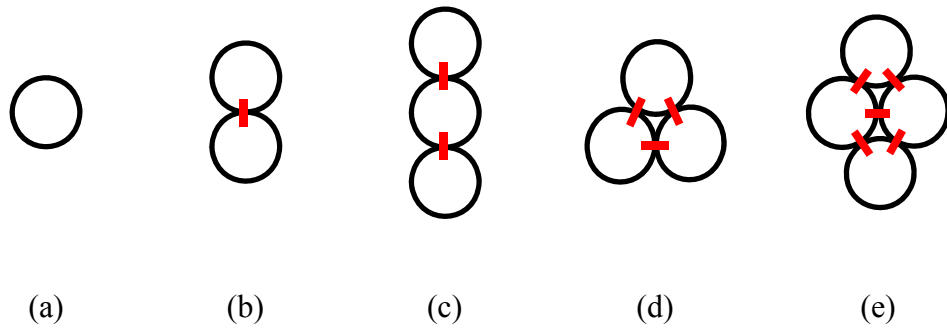
**Figure 3-19.** Particles orientation diagrams

Figure 3-19's results can be applied to the direct shear simulation results. Examine the rubber particle sitting on the shear plane. The rubber particles are illustrated in Figure 20. Where $\chi$ is small, e.g. Figure 3-20(a) and (b), the rubber particles align linearly or are chained. Where $\chi$ increases, as of Figure 20(c) and (d), the rubber particles close up, forming a mesh. The $\chi$-dependent rubber particles arrangement is in support of the conceptual drawings shown in Figure 3-17. Specifically, where $\chi$=0.34, the rubber particles evolve a closed-up arrangement, providing room to accommodate sands. As sands and rubber

particles are in balanced and well-contacted arrangements, sand–sand, sand–rubber and rubber–rubber interlocks grow; the shear strength builds up accordingly.



(a) $\chi$ =0.19 (b) $\chi$ =0.34



(c) $\chi$ =0.47 (d) $\chi$ =0.58
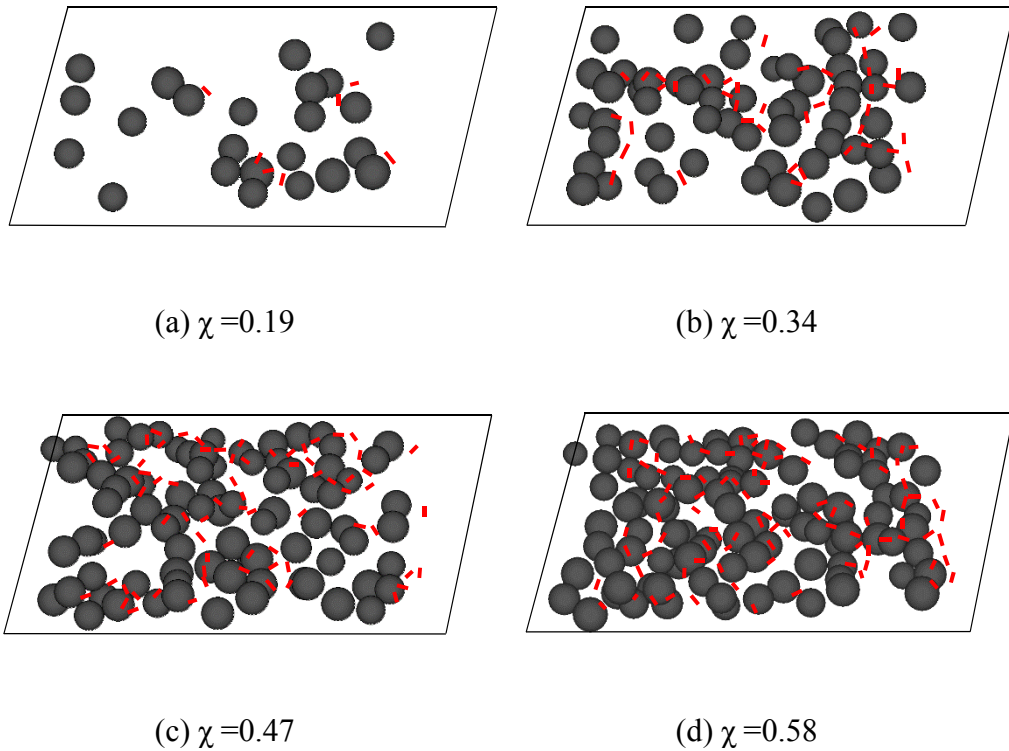
**Figure 3-20.** On-shear-plane rubble particles in samples at varying rubber contents.

### 3.3.6    Particles rotation

Particles rotate when sheared, and the rotations are crucial to material shear behavior (Cui and O'sullivan, 2006) The rotation is assessed by examining the angular velocity of the particles of interest. As the assembly of particles exhibit varying angular velocity values, it helps the assessment if there is a solution to normalizing the values and mapping out the values for the particles of interest.

Figure 3-21 shows the normalized values and mapping results for two samples $\chi$=0.34 and 0, both of which are sheared under $\sigma_v$=200 kPa to $\delta$=6 mm. Both samples exhibit a normal distribution of angular velocity, suggesting equal portions of clockwise and anti-clockwise rotations. The distributions also suggest that particles rotate at varying speed. The majority is at rest or rotates at a slow speed; a small portion (i.e., the tails) rotates faster. The particles falling into the 10% percentile as shaded are mapped out in Figure 3-21(a) for sample $\chi$=0.34 and Figure 21(b) for sample $\chi$=0, respectively. As reported in Zhang and Thornton (2007), these fast-rotation particles largely sit on the diagonal band of top−right to bottom−left, conjugated with the force chains bands (Figure 3-20). The study (Zhang and Thornton, 2007) however does not provide details explaining the conjugation. The conjugation occurs partially due to the mechanism of inter-particle shear (i.e. the Coulomb's law of shear strength) which is illustrated in Figure 3-22. Two discs contact each other and, at the contact, are subjected to the normal pressure $\sigma$. The discs opt for relative displacement due to the shear force $\tau$ acting at the contact, which is expressed as:

$$\tau = \sigma \tan \phi + c \qquad (3.4)$$

where $\phi$ and $c$ are the inter-particle constants. On the top−right to bottom−left diagonal band (Figure 3-9), the particles are subjected to less normal pressures and, based on Eq. (3.4), less shear forces to rotate. That means the threshold to rotating is low, whereby the particles tend to spin faster if subjected to a driving force. The opposite occurs to the particles sitting on the top−left to bottom−right diagonal band where high-pressure contacts occur.
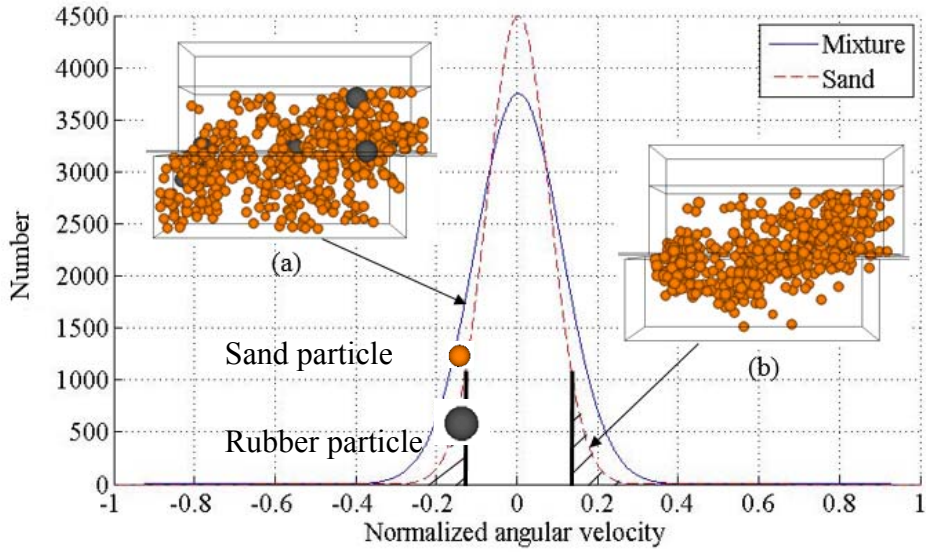
**Figure 3-21.** Mapping of particles angular velocity for samples: (a) χ=0.34; (b)

χ=0.
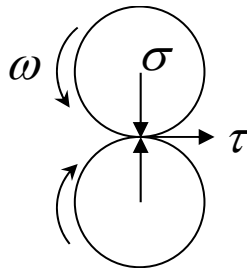


**Figure 3-22.** Inter-particle shear and rotation.

### 3.3.7    Particles relocation

The particles relocation is examined by tracking particles motion occurred at five

points: *A* to *E*, as shown in Figure 3-23. All of the five points originate from sample

χ=0.34 being sheared under $\sigma_v$=200 kPa. The five points sit on critical places:

points *A* to *C* on the shear plane separately, and points *D* and *E* in the upper and

lower boxes, respectively. An accurate positioning is attained by defining the

points in a 3D coordinate system (*x, y, z*) as illustrated. Develop the coordinate system inside the shear boxes and set the origin over the inside center. The points *A* to *E* are positioned, through a target particle, to coordinate (*x, y, z*) = (−20, 0, 0), (0, 0, 0), (20, 0, 0), (−20, 0, 10) and (20, 0, −10) mm, respectively. Then, around the target particle, search all neighboring particles. That is, each of the five points encompasses one target particle and its neighboring particles. The neighboring particles count from 2 to 9 depending on the point of interest. The target particles are marked in the simulation as Nos. 2901, 3481, 3239, 3162 and 10195, respectively. Similar identity marking is provided on the neighboring particles, enabling a complete track of particles. For each point, the pair of particles group illustrate particles arrangement at shear displacement δ=1 and 6 mm, respectively. It is shown that the particles on the shear plane (i.e., points *A*, *B* and *C*) relocate more clearly than the particles inside the boxes (i.e., points *D* and *E*) do. For instance, at point *A*, particle 10249 clearly moves to the left when the shear travels from 1 mm to 6 mm; in the meantime, particle 2823 joins up the target particle and particle 3097 detaches from it. Similar changes occur to points *B* and *C*. At point *D* (and *E*), however, the particles assembly remain similar in number and arrangement when the shear advances. Although the particles on the shear plane relocate noticeably, it is not clear to confirm a relocation law—either the front relocates more than the rear, or vice versa. However, the particles relocation pattern on the shear plane helps shed light on the process of shear dilation. At point *A*, particle 2823 pushes up particle 2507 and gradually takes over the new position. Similar replacement occurs at point *C* where particle 1186 moves leftward and squeezes into the position of particle 2061; particle 2061 relocates upward.

**Figure 3-23.** Particles relocations on shear plane and inside shear boxes.

## 3.4 Conclusions

Three-dimensional discrete element simulations on the direct shear of the rubber–sand mixtures are presented. The discrete element method enables assessing

mixtures shear behavior at a particulate scale. The simulations account for the mixtures dosage, particle stiffness, grading characteristics and normal pressure changes. The simulation results include the mixture packing characteristics, shear stress–displacement relationship, particles contact force chain and contour maps, particles displacement vector and rotations. The following conclusions are drawn.

A rubber specific volume fraction of 0.55 to 0.65 gives rise to greater packing for the mixtures examined in this study. The greater packing enables the rubber particles sharing greater contact force. The improved packing promotes the material strain-hardening characteristics and shear ductility. A rubber specific volume fraction of 0.34 gives rise to greater shear strength when sheared under 1 to 2 MPa pressures. Where sheared under lower pressures, the rubber-fraction dependence of shear strength is not significant. Contact forces orient in parallel with the shear box diagonal. The force orientation becomes pronounced with the shear advance. Rubber particles inclusion is able to harmonize in magnitude the force band by reducing particle contacts and stiffness. The particles rotate in varying speed and the speed values follow a normal distribution. The fast-rotation particles line up diagonally and in conjugation with the force chains. The particles on the shear plane relocate more noticeably than the particles away from the plane. On the plane, the particle relocations are largely consistent.

## 3.5    Acknowledgement

## 3.6 Notations

$d$      particle diameter

$D_{50}$      50% pass particle size

$F$      sum of normal force at contact

$G_s$      specific density of solid

$k_n$      normal stiffness at contact

$k_{n,1}$      normal stiffness of entity 1

$k_{n,2}$      normal stiffness of entity 2

$k_s$      shear stiffness at contact

$k_{s,1}$      shear stiffness of entity 1

$k_{s,2}$      shear stiffness of entity 2

$N_c$      number of rubber–rubber contacts on shear plane

$N_r$      number of rubber particles on shear plane

$V$      sample volume

$\chi$      specific volume fraction

$\delta$      shear displacement

$\mu$      inter-particle friction coefficient

$\mu_1$      surface friction of entity 1

$\mu_2$      surface friction of entity 2

$\sigma_m$      mean stress at contact

$\sigma_v$      vertical or normal load

$\zeta$      damping coefficient

## 3.7 References

ANASTASIADIS, A., SENETAKIS, K., PITILAKIS, K., GARGALA, C. & KARAKASI, I. 2012. Dynamic behavior of sand/rubber mixtures. Part I: Effect of rubber content and duration of confinement on small-strain shear modulus and damping ratio. *Journal of ASTM International,* 9**,** 1-19.

BALUNAINI, U., YOON, S., PREZZI, M. & SALGADO, R. 2014. Pullout response of uniaxial geogrid in tire shred–sand mixtures. *Geotechnical and Geological Engineering,* 32**,** 505-523.

BELHEINE, N., PLASSIARD, J.-P., DONZ , F.-V., DARVE, F. & SERIDI, A. 2009. Numerical simulation of drained triaxial test using 3D discrete element modeling. *Computers and Geotechnics,* 36**,** 320-331.

BOSSCHER, P. J., EDIL, T. B. & KURAOKA, S. 1997. Design of highway embankments using tire chips. *Journal of Geotechnical and Geoenvironmental Engineering,* 123**,** 295-304.

COETZEE, C. & ELS, D. 2009. Calibration of granular material parameters for DEM modelling and numerical verification by blade–granular material interaction. *Journal of Terramechanics,* 46**,** 15-26.

CUI, L. & O'SULLIVAN, C. 2006. Exploring the macro-and micro-scale response of an idealised granular material in the direct shear apparatus. *Geotechnique,* 56**,** 455-468.

CUNDALL, P. A. & STRACK, O. D. 1979. A discrete numerical model for granular assemblies. *geotechnique,* 29**,** 47-65.

DE BONO, J. P., MCDOWELL, G. R. & WANATOWSKI, D. 2012. Discrete element modelling of a flexible membrane for triaxial testing of granular material at high pressures. *Géotechnique Letters,* 2**,** 199-203.

EDIL, T. & BOSSCHER, P. 1994. Engineering properties of tire chips and soil mixtures. *Geotechnical Testing Journal,* 17**,** 453-464.

EVANS, T. M. & FROST, J. D. 2007. Shear banding and microstructure evolution in 2D numerical experiments. *Advances in Measurement and Modeling of Soil Behavior.*

EVANS, T. M. & VALDES, J. R. 2011. The microstructure of particulate mixtures in one-dimensional compression: numerical studies. *Granular Matter,* 13**,** 657-669.

FENG, K., MONTOYA, B. & EVANS, T. 2017. Discrete element method simulations of bio-cemented sands. *Computers and Geotechnics,* 85**,** 139-150.

FOOSE, G. J., BENSON, C. H. & BOSSCHER, P. J. 1996. Sand reinforced with shredded waste tires. *Journal of Geotechnical Engineering,* 122**,** 760-767.

GHAZAVI, M. 2004. Shear strength characteristics of sand-mixed with granular rubber. *Geotechnical & Geological Engineering,* 22**,** 401-416.

GHAZAVI, M. & SAKHI, M. A. 2005. Influence of optimized tire shreds on shear strength parameters of sand. *International Journal of Geomechanics,* 5**,** 58-65.

HANNAM, P. 2014. Tyre industry divided over how to handle toxic waste. *The Sydney Morning Herald*, 20 January.

INDRARATNA, B., NGO, N. T., RUJIKIATKAMJORN, C. & VINOD, J. 2012. Behavior of fresh and fouled railway ballast subjected to direct shear testing: Discrete element simulation. *International Journal of Geomechanics,* 14**,** 34-44.

ITASCA 2008. PFC3D 4.0 User Manual. Minneapolis, MN USA

JACOBSON, D. E., VALDES, J. R. & EVANS, T. M. 2007. A numerical view into direct shear specimen size effects.

KIM, H.-K. & SANTAMARINA, J. 2008. Sand–rubber mixtures (large rubber chips). *Canadian Geotechnical Journal,* 45**,** 1457-1466.

LEE, C., SHIN, H. & LEE, J. S. 2014. Behavior of sand–rubber particle mixtures: experimental observations and numerical simulations. *International Journal for Numerical and Analytical Methods in Geomechanics,* 38**,** 1651-1663.

LEE, J., SALGADO, R., BERNAL, A. & LOVELL, C. 1999. Shredded tires and rubber-sand as lightweight backfill. *Journal of Geotechnical and Geoenvironmental Engineering,* 125**,** 132-141.

LIU, S. 2006. Simulating a direct shear box test by DEM. *Canadian Geotechnical Journal,* 43**,** 155-168.

LIU, S., SUN, D. & MATSUOKA, H. 2005. On the interface friction in direct shear test. *Computers and Geotechnics,* 32**,** 317-325.

MASAD, E., TAHA, R., HO, C. & PAPAGIANNAKIS, T. 1996. Engineering properties of tire/soil mixtures as a lightweight fill material. *Geotechnical Testing Journal,* 19**,** 297-304.

MASSON, S. & MARTINEZ, J. 2001. Micromechanical analysis of the shear behavior of a granular material. *Journal of Engineering Mechanics,* 127**,** 1007-1016.

MOTA, M., TEIXEIRA, J., BOWEN, W. R. & YELSHIN, A. 2001. Binary spherical particle mixed beds: porosity and permeability relationship measurement. *Transactions of the Filtration Society,* 1**,** 101-106.

NAKATA, A., HYDE, M., HYODO, H. & MURATA 1999. A probabilistic approach to sand particle crushing in the triaxial test. *Geotechnique,* 49**,** 567-583.

PATIL, U., VALDES, J. R. & EVANS, T. M. 2010. Swell mitigation with granulated tire rubber. *Journal of materials in civil engineering,* 23**,** 721-727.

POTYONDY, D. & CUNDALL, P. 2004. A bonded-particle model for rock. *International journal of rock mechanics and mining sciences,* 41**,** 1329-1364.

RAO, G. V. & DUTTA, R. 2006. Compressibility and strength behaviour of sand–tyre chip mixtures. *Geotechnical and Geological Engineering,* 24**,** 711-724.

TSANG, H.-H. 2008. Seismic isolation by rubber-soil mixtures for developing countries. *Earthquake Engineering & Structural Dynamics,* 37**,** 283-303.

TSOI, W. & LEE, K. 2010. Mechanical properties of cemented scrap rubber tyre chips. *Géotechnique,* 61**,** 133-141.

VALDES, J. R. & EVANS, T. M. 2008. Sand-rubber mixtures: experiments and numerical simulations. *Canadian Geotechnical Journal,* 45**,** 588-595.

WANG, J., DOVE, J. & GUTIERREZ, M. 2007. Discrete-continuum analysis of shear banding in the direct shear test. *Géotechnique,* 57**,** 513-526.

WANG, Y.-H. & LEUNG, S.-C. 2008. A particulate-scale investigation of cemented sand behavior. *Canadian Geotechnical Journal,* 45**,** 29-44.

YOON, S., PREZZI, M., SIDDIKI, N. Z. & KIM, B. 2006. Construction of a test embankment using a sand–tire shred mixture as fill material. *Waste Management,* 26**,** 1033-1044.

YOUWAI, S. & BERGADO, D. T. 2004. Numerical analysis of reinforced wall using rubber tire chips–sand mixtures as backfill material. *Computers and Geotechnics,* 31**,** 103-114.

ZHANG, L. & THORNTON, C. 2007. A numerical examination of the direct shear test. *Géotechnique,* 57**,** 343-354.

ZHOU, Q., SHEN, H. H., HELENBROOK, B. T. & ZHANG, H. 2009. Scale dependence of direct shear tests. *Chinese Science Bulletin,* 54**,** 4337-4348.

ZORNBERG, J. G., CABRAL, A. R. & VIRATJANDR, C. 2004. Behaviour of tire shred sand mixtures. *Canadian Geotechnical Journal,* 41**,** 227-241.

# Chapter 4

# Digital image processing on segregation of rubber sand mixture (Paper 2)

Can Wang[1], An Deng[2], Abbas Taheri[3]

1. Graduate Student, School of Civil, Environmental and Mining Engineering, Univ. of Adelaide, Adelaide, SA 5005, Australia. E-mail: c.wang@adelaide.edu.au

2. Senior Lecturer, School of Civil, Environmental and Mining Engineering, Univ. of Adelaide, Adelaide, SA 5005, Australia (corresponding author). E-mail: an.deng@adelaide.edu.au

3. Senior Lecturer, School of Civil, Environmental and Mining Engineering, Univ. of Adelaide, Adelaide, SA 5005, Australia. E-mail: abbas.taheri@adelaide.edu.au

# Statement of Authorship

| Title of Paper | Digital image processing on segregation of rubber sand mixture. |
|---|---|
| Publication Status | ☐ Published ☑ Accepted for Publication<br>☐ Submitted for Publication ☐ Unpublished and Unsubmitted work written in manuscript style |
| Publication Details | Wang C, Deng A, Taheri A (2018) Digital image processing on segregation of rubber sand mixture. *ASCE's International Journal of Geomechanics* (In Press). |

## Principal Author

| Name of Principal Author (Candidate) | Can Wang | | |
|---|---|---|---|
| Contribution to the Paper | Undertook Literature review, performed parametric study and numerical model analysis. | | |
| Overall percentage (%) | 75% | | |
| Certification: | This paper reports on original research I conducted during the period of my Higher Degree by Research candidature and is not subject to any obligations or contractual agreements with a third party that would constrain its inclusion in this thesis. I am the primary author of this paper. | | |
| Signature | | Date | 05/08/2018 |

## Co-Author Contributions

By signing the Statement of Authorship, each author certifies that:

  i. the candidate's stated contribution to the publication is accurate (as detailed above);

  ii. permission is granted for the candidate in include the publication in the thesis; and

  iii. the sum of all co-author contributions is equal to 100% less the candidate's stated contribution.

| Name of Co-Author | An Deng | | |
|---|---|---|---|
| Contribution to the Paper | Acted as corresponding author, supervised project development and helped with paper editing. | | |
| Signature | | Date | 05/08/2018 |

| Name of Co-Author | Abbas Taheri | | |
|---|---|---|---|
| Contribution to the Paper | Supervised work development and helped with paper editing. | | |
| Signature | | Date | 07/08/2018 |

# **ABSTRACT**

The segregation of rubber sand mixtures, when they form heaps as observed by the method of digital image processing (DIP), is presented. Through segmenting the digital images into a binary picture, the DIP method enables material ingredients identification and three-dimensional mapping of mixture segregation. This helps reach a better understanding of mixture heterogeneity when incorporating artificial material into conventional geotechnical materials. To gain an insight into the mixture heterogeneity, the DIP results were used to validate a discrete element model and the model was then used to examine the influence of particle properties on the segregation. The discrete element simulations showed that the particle density is critical in material segregation, and the segregation becomes more noticeable when the materials density ratio increases. This trend is restricted by increasing the inter-particle surface roughness.

**Keywords**: segregation; digital image processing; discrete element; density; roughness

## 4.1    Introduction

Waste tires create problems such as landfilling, health, and environmental challenges. The tires can go into recycling facilities for a new life. One of the new-life solutions is to reuse the tires as geomaterial alternatives (Foose et al. 1996; Zornberg et al. 2004). Rubber sand mixture is an attractive alternative and has been widely used in geotechnical applications, including roadway construction (Bosscher et al. 1997; Nightingale and Green 1997), lightweight fill (Ahmed and Lovell 1993; Masad et al. 1996), backfill for retaining walls (Humphrey and Manion 1992; Garga and O'shaughnessy 2000), slope stabilization (Poh and Broms 1995) and seismic isolation system (Tsang et al. 2012). Where the mixtures are prepared, placed or compacted, the ingredients likely segregate. Whichever induces the material segregation, a segregated profile causes heterogeneity and sometimes severe instability problems such as liquefaction (Yoshimine and Koike 2005). The sand and rubber ingredients differ at least in density and surface roughness and, when placed as a mixture, lead to flow-induced segregation as defined by Ottino and Khakhar (2000). In general, the factors causing segregation can be classified into particle sizes, densities, shapes and particle resilience (Williams 1976). Of all the segregation mechanisms, trajectory segregation, percolation of fine particles and the rise of coarse particles on vibration are commonly recognized (Kudrolli 2004). Other mechanisms such as rolling, sieving, water flow, soil crushing etc. were also reported in early works (Kuerbis and Vaid 1988; Ottino and Khakhar 2000; Lőrincz et al. 2005; Watabe et al. 2014).

The first reported work on segregation mechanism came from Donald and Roseman (1962), who investigated the experiment of mixing particles of different

sizes and densities in a rotating horizontal drum. The recent work to study segregation by using the discrete element method (DEM) has become popular as the DEM is regarded as a valuable tool for studying granular flow and mixing mechanisms, e.g., free surface (Shi et al. 2007) and hopper discharge (Anand et al. 2010). These tests have shown unanimously that the particle size and density are the major factors leading to segregation. Other factors, such as shape, chute angle, liquid content, rolling friction and magnetic fields also contribute to material segregation (Anand et al. 2010).

While extensive studies have been performed to test material segregation, there is limited research regarding segregation phenomenon when the rubber sand mixture falls to form a heap. There is also a limited quantitative connection in terms of segregation measurements between numerical simulations and experimental observation. Studies of the sand pile by DEM simulation are limited when it comes to the angle of repose or force of percolation (Zhou et al. 1999; Yang et al. 2000; Zhou et al. 2001). And although significant achievements have been made since Zhou et al. (1999) first introduced the concept 'rolling friction' in studying heap formation, there is a lack of study regarding the phenomenon of segregation.

This paper presents the segregation phenomenon observed when the rubber sand forms a heap. It investigates the influence of particle properties using DEM. Since many studies have been conducted on evaluating particle sizes, this paper focused on studying segregation without size difference, e.g., a mixture with similar ingredient sizes. The results of the study are presented as a comparison between experiments and numerical simulations so that a parametric study can be

performed. Also, it contains the calibration process for restitution coefficient measurements and the angle of repose tests so that important micro-properties could be obtained. These examinations help quantify mixture segregation when the mixture is processed. The parametric study will examine and identify the critical material properties causing the segregation and whereby solutions can be recommended to reduce the segregation.

## 4.2    Methodology

In this section, prior to investigating material segregation, a number of tests are performed to study granular behavior. DEM is adopted as a numerical method to calibrate micromechanical properties. This could be achieved through heap-forming test and repose angle studies. Serious segregation was identified in the mixture pile after the heap-forming process in both numerical simulation and tests. To accurately measure the material segregation, digital image processing is used. Detailed discussion will be provided in the following sections.

### 4.2.1    Discrete Element Method

To simulate the granular interaction, the use of DEM can provide an insight into the micromechanical properties reflecting the macroscopic phenomenon. This method simulates the material as a collection of frictional and rigid spheres so that complex problems can be addressed through observing particles contact (Cundall and Strack 1979). The contact model, as depicted in Itasca (2009), is shown in Figure 4-1. The contact model can be treated as either a linear model or as a non-

linear model (e.g., Hertz–Mindlin contact). Both models produce normal and shear forces based on normal contact and shear stiffness respectively. A Coulomb limit is imposed on the shear force considering a friction coefficient, $u$. The dashpot component is assumed to dissipate extra energy in both normal and shear directions.

Entity 1

Shear stiffness

Entity 2

Viscous dashpot

Normal stiffness

Friction slider

Viscous dashpot
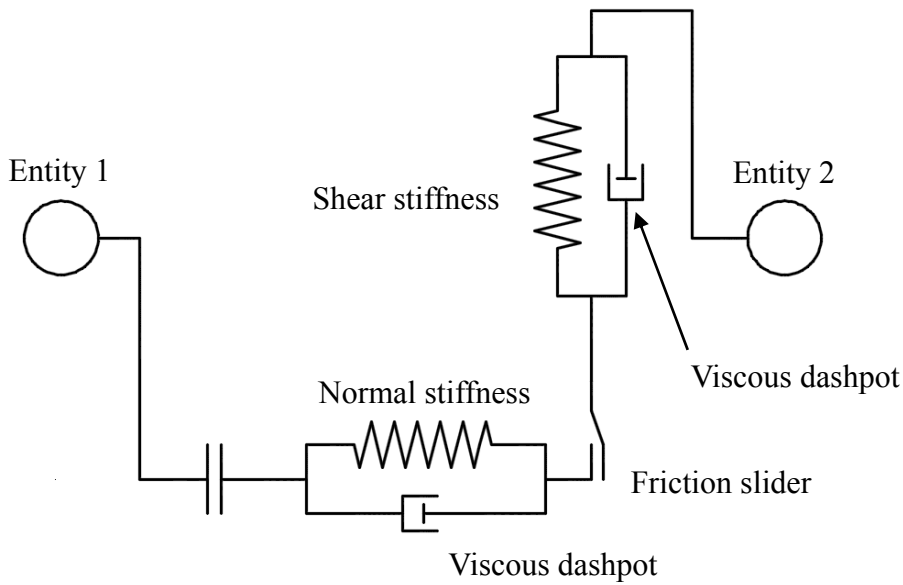
**Figure 4-1.** Schematic of DEM model.

### 4.2.2 Damping Ratio

As a part of an examination of the microscopic properties, it is necessary to evaluate the effect of material damping which could have an impact on mixture segregation. The damping ratio is a dimensionless parameter that quantifies system decay during oscillations, which is an important property input in DEM. Also, for a numerical analysis on rubber sand mixture, the individual damping ratio at granular contact is not clear and lacks a calibration process (Patil et al.

2010; Evans and Valdes 2011; Lee et al. 2014). In the repose angle test, when different particles are dropped from a height, due to the difference in granular rebound height, it may generate a different heap when they are stabilized, which may greatly influence the mixture segregation at its surface. Therefore, calibrating the material damping ratio as a DEM input parameter is necessary. According to Kawaguchi et al. (1992), the restitution height is directly linked to the material properties of energy dissipation, and the relationship can be obtained by solving the motion equation for free vibration with viscous damping, as follows:

$$\alpha = \exp(-\frac{\zeta\pi}{\sqrt{1-\zeta^2}})$$

(4.1)

where $\alpha$ is restitution coefficient which is determined from the restitution height, $h$; $\zeta$ is the ratio of the damping constant to the critical damping constant. For simplification, $\zeta$ is referred to as the 'damping ratio'. It is clear that a granule's damping ratio can be calculated through its re-bound height. Therefore, an experiment was designed to calibrate this parameter input.

The materials used for the experiment were spherical silica beads and rubber beads with a radius of 5 mm, as shown in Figure 4-2. The two materials are identical in composition respectively to the sand and rubber beads used for the mixture. The restitution process used a glass board as a base. Silica and rubber beads were released at a height of $H$=340 mm, against a vertical scale board, and a high resolution camera of 60 fps was placed one meter in front of the scale board. The material size and the release height were determined as being proportional to the sizes of samples used for the tests that followed.

**Figure 4-2.** Rubber and silica beads used in the damping ratio calibration.

Four silica and four rubber beads were chosen at random for the test, as shown in Figure 4-2. Each silica and rubber bead was tested three times independently. Once the beads were released the maximum re-bound height was captured by using the camera to record the whole process, as shown in Figure 4-3. The images were analyzed at each frame so that the maximum restitution height could be determined. The material beads at the maximum re-bouncing height are illustrated in Figure 4-3. The final results of the repeated tests are given in Figure 4-4. Generally, the silica beads had a much higher height of bounce, with an average of 170 mm. Rubber beads rebound to 31.9 mm on average.

(a) Silica bead              (b) Rubber bead
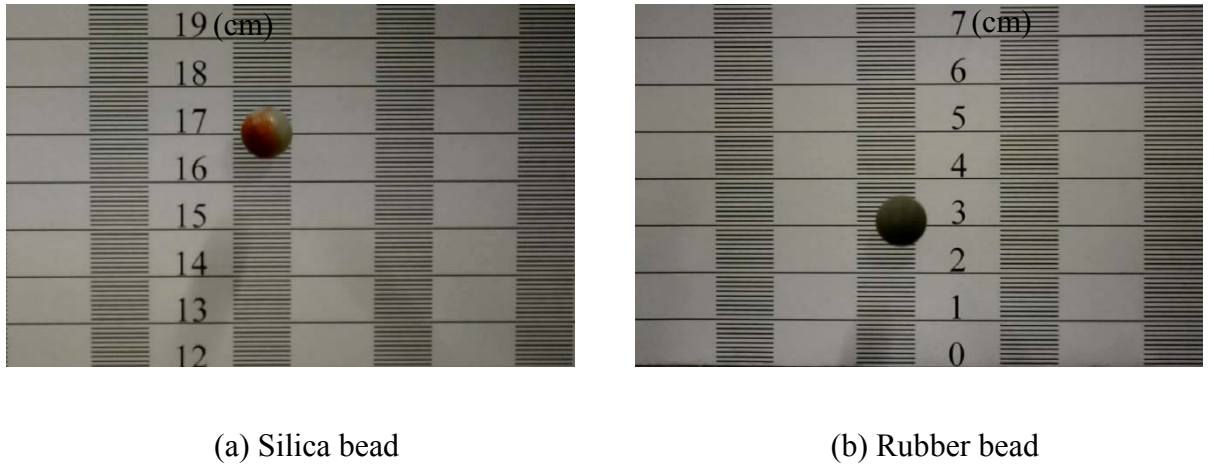
**Figure 4-3.** Maximum restitutive height captured by high resolution camera for silica bead and rubber bead.
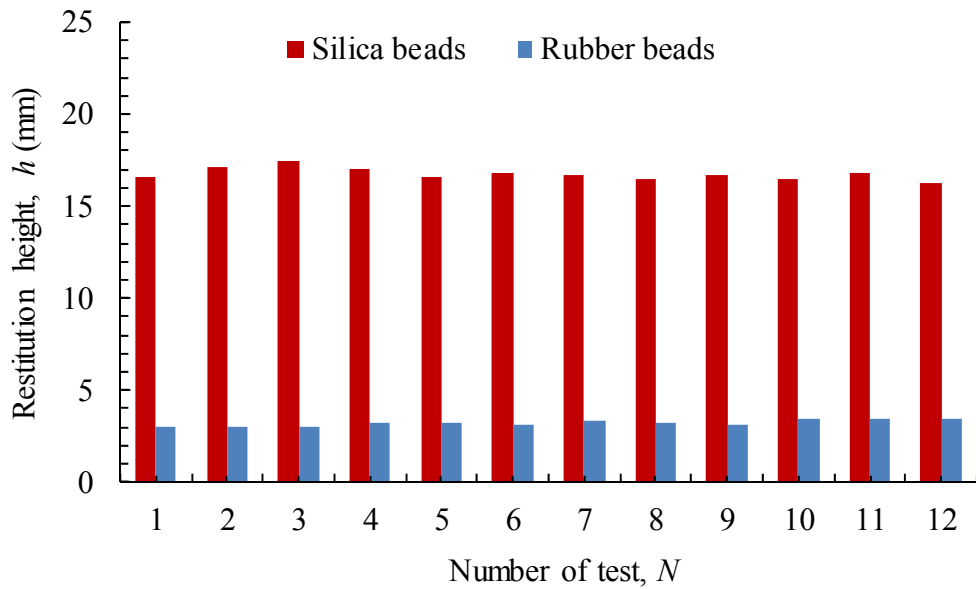


**Figure 4-4.** Restitution height for silica and rubber beads.

For both the silica and rubber beads, the radius of the bead, $r=5$ mm, must be deducted when comparing its height of rebound. Therefore the restitution coefficient $\alpha$ is expressed as:

$$\alpha = \frac{h-r}{H-r} \qquad (4.2)$$

The corresponding restitution coefficients $\alpha$ were 0.49 for sand and 0.078 for rubber. Substituting the results to Eq. (4.1) to obtain the damping ratio, the results were 0.22 and 0.63 for sand and rubber, respectively. The standard deviation for silica beads and rubber beads was found to be 0.3 and 0.16, respectively, suggesting excellent agreement of the tests.

A three-dimensional simulation of the restitution test was also performed by using numerical software Particle Flow Code (PFC) 3D. The purpose of the simulation was to evaluate the materials' restitution heights under the influence of granular micro-properties such as the damping ratio, material density or stiffness. For each sphere, different damping ratios ranging from 0 to 1 were considered. Actual material densities, such as $\rho$=1,300 kg/m³ and 2,600 kg/m³, respectively, were selected as input values. For each density value, various contact types and contact stiffness values were compared, including the linear contact model with effective modulus $E$=1×10$^7$ Pa and 1×10$^9$ Pa, respectively, and the Hertz contact model with shear modulus $G$=3×10$^7$ Pa, Poisson's ratio $v$=0.5, and $G$=3×10$^{10}$ Pa, $v$=0.3, respectively. The same particles size and releasing height were used in the numerical simulation. The restitution coefficient $\alpha$, as defined in Eq. (4.2), is plotted about the damping coefficient $\zeta$ and other parameters. This is shown in Figure 4-5.
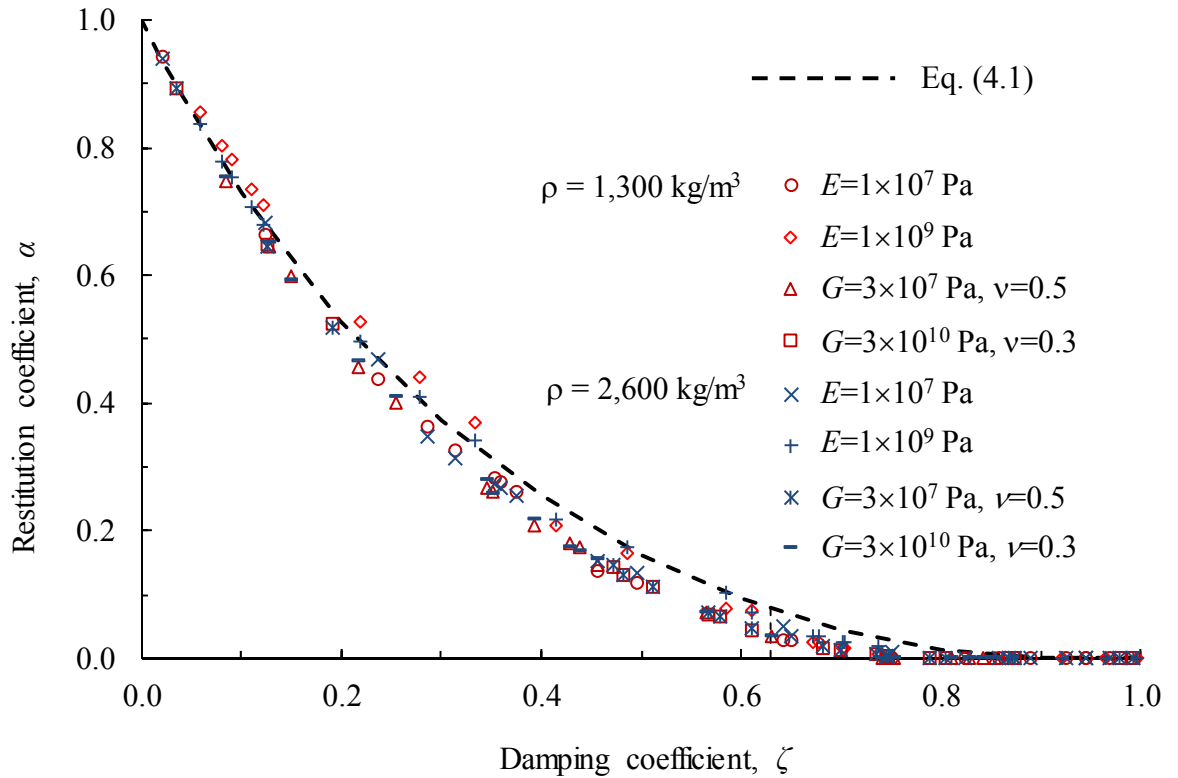
**Figure 4-5.** The relationship between the damping coefficient and the restitution coefficient with various material properties.

In Figure 4-5, the numerical result fits well with the analytical prediction from Eq. (4-1). It is thus evident that the damping ratio $\zeta$ is independent from factors such as contact type, stiffness values or densities, and that the only influence on the damping ratio is its restitution height. The numerical–analytical comparison provides evidence that contact damping between particles and the base surface can be directly obtained from the above calibration. The relevant results are discussed in the DEM model results.

One could argue that material shape or size may create different results. However, it is noted that the rebound height of silica beads is around five times of that of rubber beads, as observed in the test that the irregular and smaller sized rubber and sand beads are used. This can be visually observed but is difficult to

capture using the camera. It is much easier to capture the restitution height of spheres because the irregular ones may bounce in different directions. Also, the spheres were simulated numerically, in order to provide consistency for this experiment.

### 4.2.3 Angle of Repose

The repose angle test was performed in this study to investigate material frictional behavior, as there is a strong correlation between surface characteristics and the repose angle (Liu et al. 2012). For a specific material, its frictional behavior contains two parts: sliding friction and rolling friction, which have been well established through numerical studies (Zhou et al. 1999; Yang et al. 2000; Zhou et al. 2001). In the present study, sliding friction indicates Mohr–Coulomb friction, resisting relative translational movement, while rolling friction indicates the ability of particles to rotate, which reflects particle irregularities. However, one test cannot determine two unknowns (i.e., sliding and rolling friction coefficients) so this study adopted previously reported sliding frictions for sand and rubber materials (Patil et al. 2010). The rolling friction coefficient was determined from the repose angle accordingly.

The experiments used granular sand and rubber materials. Both of the materials were sieved between 1.18 mm to 2.36 mm to obtain the same-sized material, because it might have induced significant differences in both the repose angle and the segregation. The mixture was firstly mixed homogeneously and placed in a funnel with a bottom diameter of 15 mm. A bottom plate was removed to allow the particles to drop by force of gravity. The experiment was performed

over a glass base, and the distance from the bottom cone to the base was 60 mm. The schematic drawing is shown in Figure 4-6(a). Tests were performed for different materials: sand, rubber, and sand–rubber mixture where the two ingredients were equal in volume. The mixture test was conducted to confirm the individual ingredient test results. Each measurement was repeated three times, recording the height and diameter at two directions so that the angle of repose could be determined.



(a)　　　　　　　　　　　　　　　　　　(b)
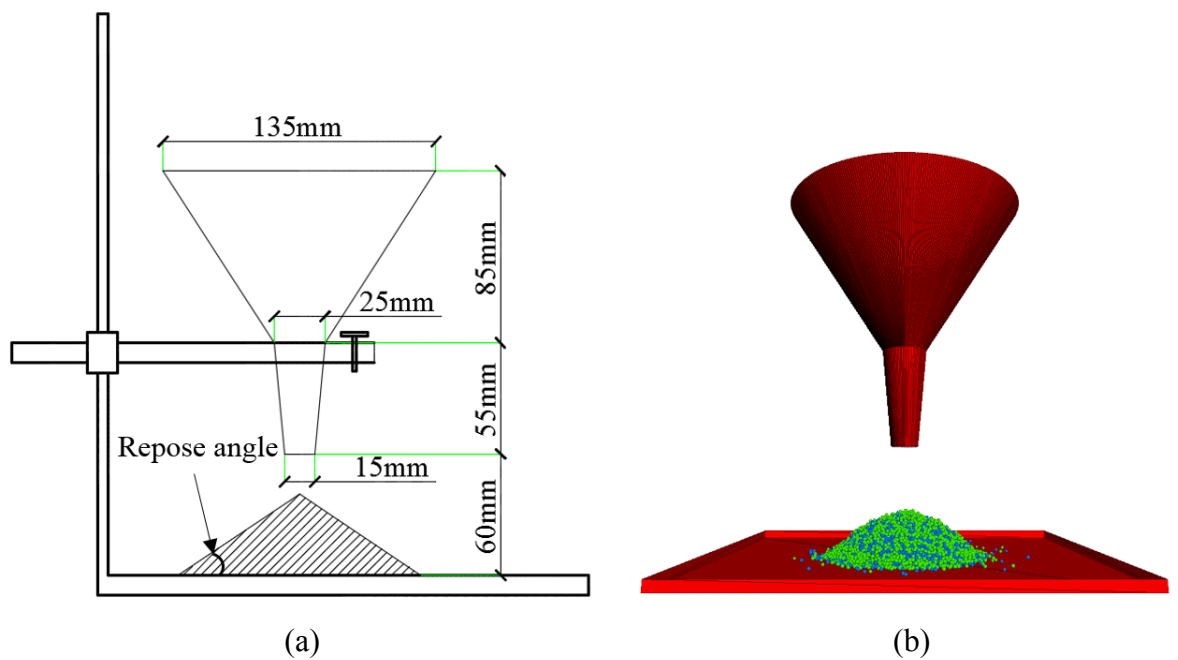
**Figure 4-6.** Repose angle test setup: (a) experimental schematic drawing, and (b) numerical simulation.

The granular frictional properties are calibrated by using the DEM simulation. The small-scale material pile (Figure 4-6 (b)) is meaning in respect to the simulations. Firstly, a small number of particles requires less time to attain computation stabilization. Also, owing to the granules to be displaced from the funnel, a large pile may induce broader spreads which also require a longer period of processing time. In addition, the pile is significantly larger in scale than the

greatest particle size. The pile formation is not subject to a major size effect and the pile dimension satisfies the segregation purpose.

To simulate the shape parameter of the material granules, despite making clumps of the basic shapes of 2D disks or 3D spheres (Indraratna et al. 2012; Chen et al. 2014; Falagush et al. 2015), a rolling resistance behavior at contact could be introduced as suggested by Ai (2010). It has shown great advantages in simulating a stable pile with a finite angle (Zhou et al. 1999; Yang et al. 2000; Zhou et al. 2001). The same technique is used in this simulation. Similar to the Mohr−Coulomb friction theory, the rolling resistance model imposes a granular torque by introducing a rolling friction coefficient $f_r$. A study of rolling resistance model can be found in Ai (2010).

A calibration process is required to determine the rolling friction coefficient, because very limited research has been focused on the rolling behavior of rubber and sand. The funnel was made by assembling wall plates as two cones, as shown in Figure 4-6 (b). More than 12,000 spheres particles were used and were first stabilized in the funnel by use of gravity. This was achieved in the simulation by allowing a long simulation time so that the particles' velocity was reduced almost to zero. The bottom plate was removed before particles settled on the base. The input micromechanical parameters are listed in Table 4-1.

**Table 4-1.** Input parameters used in simulation.

| Parameter | Value |
|---|---|
| Diameter of sand particle, $d_s$, mm | 1.54 – 2 |
| Diameter of rubber particle, $d_r$, mm | 1.54 – 2 |
| Density of sand particle, $\rho_s$, kg/m³ | 2,600 |
| Density of rubber particle, $\rho_r$, kg/m³ | 1,300 |
| Sliding friction of sand particle, $f_{s,s}$ [*] | 0.31 |
| Sliding friction of rubber particle, $f_{s,r}$ [*] | 0.6 |
| Rolling friction of sand particle, $f_{r,s}$ [#] | 0.7 |
| Rolling friction of rubber particle, $f_{r,r}$ [#] | 0.6 |
| Effective modulus of sand particle, $E_s$, Pa | $1 \times 10^7$ |
| Effective modulus of rubber particle, $E_r$, Pa | $1 \times 10^5$ |
| Particle – wall friction, $f_w$ | 0.405 |
| Particle – wall stiffness, $k_w$ | $1 \times 10^6$ |
| Damping ratio of sand particle, $\zeta_s$ [#] | 0.63 |
| Damping ratio of rubber particle, $\zeta_r$ [#] | 0.22 |

[*] data from Patil et al. (2010); [#] data from calibration.

The repose angle cannot be directly measured from the numerical results because there might be systematic errors. For example, the topmost particle may not rest at the center, which induces an inaccurate pile height. Also, as seen in Figure 4-7 the top of the material pile becomes flat, which underestimates the repose angle. Directly measuring the base radiuses in two directions is also problematic because many particles are scattered. Therefore, an indirect measurement method was developed. As shown in Figure 4-7 (d), slice the pile horizontally at two elevations: one at the pile's bottom, and the other one at 80%

of its apex. The 80% plane was selected to avoid the cone altitude inaccuracy. The angle was determined by measuring the radius of the two slices, and the vertical distance between the slices.

Specifically, the centroid of the funnel is assumed to be the centre of the pile bottom rather than the projection of the highest particle at the top. At the chosen height, the upper plane in Figure 4-7 (d) was used to slice the pile. A number of circles were plot, in equally increasing radius, on the plane, as shown in Figure 4-7 (b), and were then referred to, in sequence, from ID 1 to $N$ as the radius increased. The circles were used to determine count, $C_1$, of the particles sitting on the circular plane, as illustrated in Figure 4-7 (a), as well as count, $C_2$, of the particles intersecting the circular periphery, as illustrated in Figure 4-7 (b). Define sphere-intersecting frequency=$C_1/C_2$. The frequency vs. the sequential circles is illustrated in Figure 4-7 (c). The upper plane was regarded as the $14^{th}$ circle because it intersects the maximum number of particles. Similarly the bottom plane sat on the 43th circle. Note that some particles fell outside the circle of preference, e.g., the red sphere in Figure 4-7 (a) and (b), but intersected at the top with the cut plane. In this circumstance, the elevation and plan views were combined to examine the preferred circle.
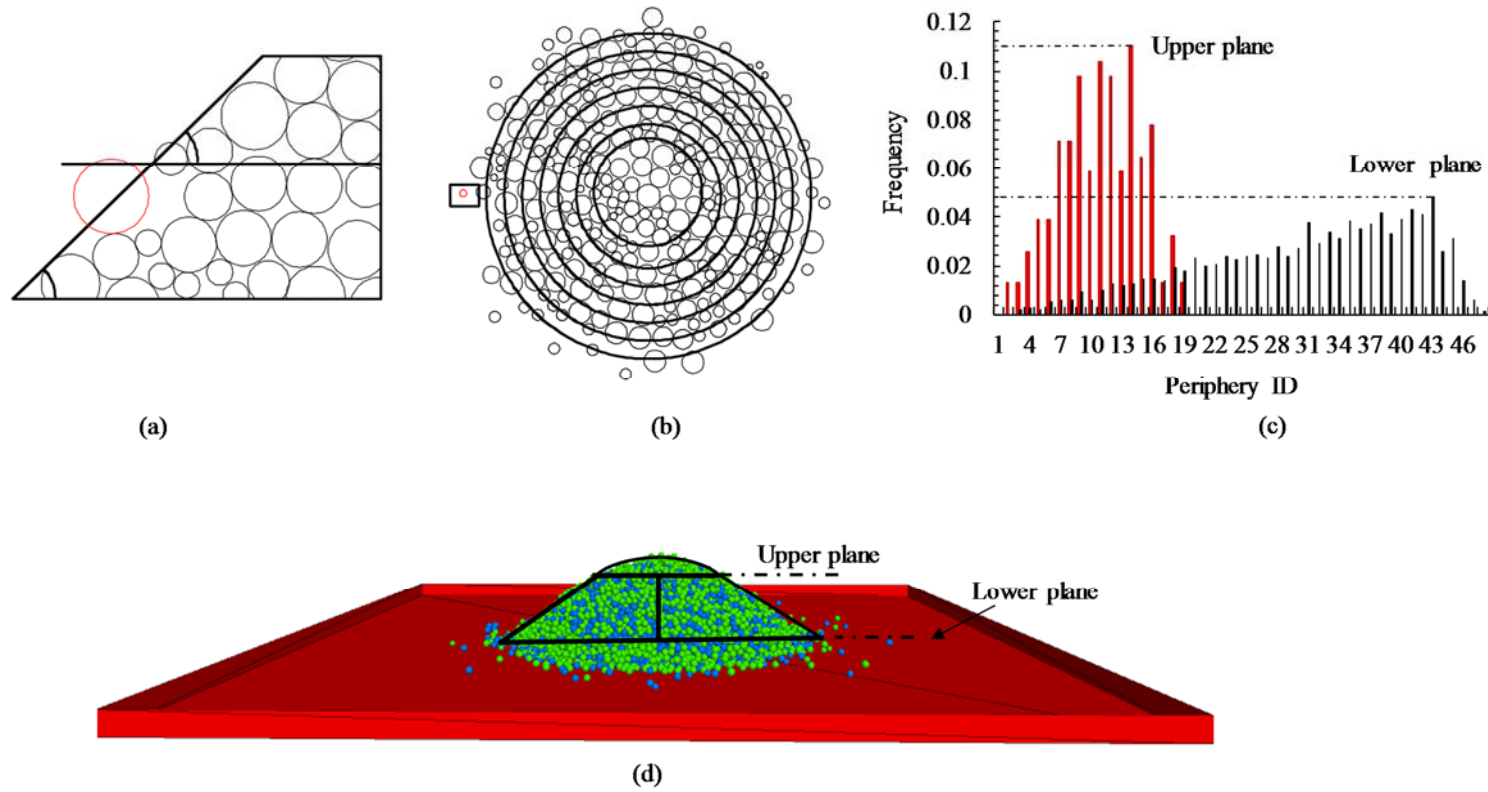
**Figure 4-7.** The numerical measurement of the repose angle: (a) elevation view (not to scale), (b) plan view (not to scale), (c) frequency of particles intersecting the periphery, and (d) sample pile.

Based on calculations and parameters described above, the final results of repose angle were obtained experimentally and numerically. The results are shown in Table 4-2. Through iteration, the rolling friction coefficients were determined. Different coefficients were determined for the sand and rubber, respectively, as shown in Table 4-1. Then, when they were mixed at equal volume, the repose angles were examined again, enabling verification of the coefficients through numerical and experimental tests. The results in Table 4-2 suggest excellent agreement between the numerical and experimental tests. Specifically, for the sand heap, the repose angle is 31.1 ° in the experiment and 31.4 ° in the simulation. Similarly excellent agreement is obtained for the rubber heap and rubber sand mixture heap, verifying the validity of the particle frictions of forming the heaps. At this stage, each single micro parameter has been determined so that digital image processing could be performed.

**Table 4-2.** Measurement of repose angle.

| Sample | Test | Height (mm) | Diameter (mm) | | | Angle (°) | Average angle (°) | Simulation Angle (°) |
|--------|------|-------------|---|---|---------|-----------|-------------------|---------------------|
| | | | X | Y | Average | | | |
| Sand bead | 1 | 28 | 88 | 92 | 90 | 31.9 | | |
| | 2 | 34.5 | 118 | 117 | 117.5 | 30.4 | 31.1 | 31.4 |
| | 3 | 35 | 112 | 120 | 116 | 31.1 | | |
| Rubber bead | 1 | 39 | 103 | 105 | 104 | 36.9 | | |
| | 2 | 40 | 108 | 108 | 108 | 36.5 | 36.3 | 36.5 |
| | 3 | 34 | 95 | 96 | 95.5 | 35.5 | | |
| Mixture | 1 | 39 | 108 | 106 | 107 | 36.1 | | |
| | 2 | 34 | 100 | 102 | 101 | 34.0 | 35.0 | 34.8 |
| | 3 | 35 | 101 | 100 | 100.5 | 34.9 | | |

As a simulation result, it is noted that different groups of material stiffness were used in the simulation but it has negligible impact on the repose angle. Owing to the fact that gravity is the only force considered, the load transmission is negligible at particle contact, so that the impact on the material behavior is minor. The change of material stiffness may have negligible influence to granular behavior for some particular cases. For example, Chung (2006) studied rod penetration and identified that scaling inter-particle contact stiffness did not show any significant variations on the simulation results, but provided considerable simulation efficiency. It was concluded that the main reason was that reducing stiffness has only minor effects on load transmission onto the boundary surfaces.

Ai (2010) illustrated the same finding for stiffness scaling, but argued that if the stiffness is scaled too low, it may result in unstable behavior for a granular

pile. This specified methodology was also adopted by Shi et al. (2007) because it has no essential effect on flow mechanics.

**4.2.4        Segregation Observation**

Segregation was observed in both the numerical simulation and the experimental test. Figure 4-8 (a) and (b) show material piles in elevation view from the experimental and numerical studies, respectively. The rubber and sand beads are represented as green and blue spheres respectively in the numerical simulations. In addition to the similarity in the repose angle, it is also clear that the pile surfaces are mostly covered by rubber material. A similar surface covering can be seen in the plan view as well (Figure 4-8 (c)) and (d)), demonstrating verification of the numerical results. Further quantitative comparison is provided in the subsequent sections.



(a) Elevation of test sample                     (b) Elevation of simulation
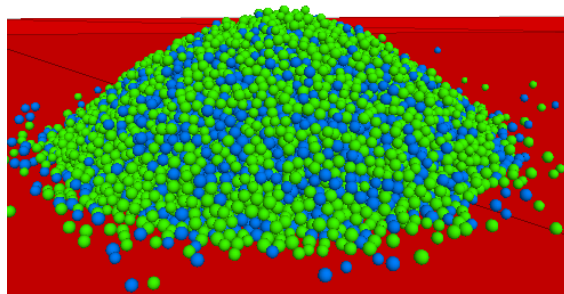
(a) Plan of test sample
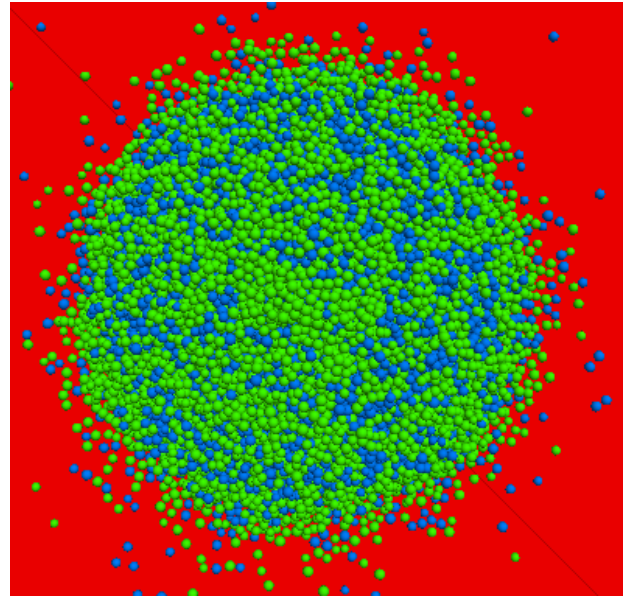
(d) Plan of simulation



(e) Mid cross section of test sample
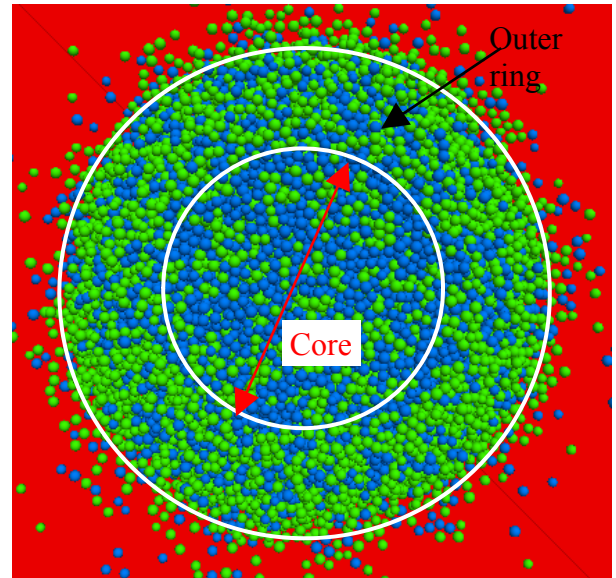
(f) Mid cross section of simulation

**Figure 4-8.** Segregation of mixture pile.

To gain insight into the inner material distribution, the material piles were sliced horizontally at its mid-height, removing the respective top cone and exposing the heap core. The mid-height core was assumed of representing the particle distribution inside the heaps. The particles on the core were examined. For both the test heap and the simulation heap, the majority of sands stayed in the

central area (Figure 4-8 (e) and (f)). Close agreement exists between the experimental and numerical results in respect to particles distribution on both the heap surface and inner core. Again, this agreement is subject to further quantitative comparison which is accomplished through the digital image processing as follows.

### 4.2.5    Digital Image Processing

One of the main objectives of this research was to present a measurement method that could be used to quantify the segregation obtained from the experiment and numerical simulation. Despite other method that has been proposed to quantify the segregation, there is a size difference in the mixture. A more general method was developed based on visual comparison between numerical and experimental results (Shi et al. 2007). As an improvement of visual comparison, this can be quantitatively measured by using the digital image processing (DIP) method, which has been applied in many fields, such as identifying soil features (Aydemir et al. 2004; Manahiloh et al. 2016), diagnosing soil–rock mesostructure (Kemeny et al. 1993; Villeneuve et al. 2011), analyzing coarse aggregate shape and size (Yue and Morin 1996; Altuhafi et al. 2013), and measuring saturation degree (Yoshimoto et al. 2011). In this paper, as size effect is not the primary consideration, the DIP method was adopted to quantify and compare material segregation between the numerical simulation and experimental results. Based on the literature review conducted in this study, it is the first time of such comparison has been conducted in rubber–sand segregation testing.

DIP method refers to the process of converting a picture into a digital form, and then analyzing the digital image to acquire the useful, underlying information.

In the analysis, a picture is represented by a number of pixels. Each pixel is a combination of primary colors. A standard digital picture often uses the red (R), green (G) and blue (B) channels which can be perceived by human eyes and used in simple computer displays. The information extracted from a digital picture can be expressed as a discrete function on a ($N{\times}M$) grid, known as an intensity matrix in the Cartesian coordinate system (Yue and Morin 1996):

$$I_k = \begin{bmatrix} I_k(1,1) & I_k(1,2) & \cdots & I_k(1,M) \\ I_k(2,1) & I_k(2,2) & \cdots & I_k(2,M) \\ \vdots & \vdots & & \vdots \\ I_k(N,1) & I_k(N,2) & \cdots & I_k(N,M) \end{bmatrix} \qquad (4.3)$$

where $I$ is a value often refers to the intensity level of a digital image ranging from 1 to 255; $k$ =1 to 3, representing red, green and blue channels, respectively; therefore there are three separate matrixes for an image. The $I$ value extraction process is accomplished by MATLAB which is equipped to read color channel information. The present paper briefly illustrates the method for a colored image analysis in the next section. As the sample heap was formed on a glass plane, and the glass background color was similar to the color of the sample, it was not easy to find the color difference between sand and the background, and rubber and the background. Some pre-treatment was required to change the background color. It was chosen to substitute a blue background for the glass background so that it is easier to select the threshold value for further analysis. Figure 4-9 (a) was converted from Figure 4-8 (c) by changing the background color. For convenience, some particles scattered on the glass base were excluded because the amount of these particles are negligible compared to the total granular number.

(b)

(a)
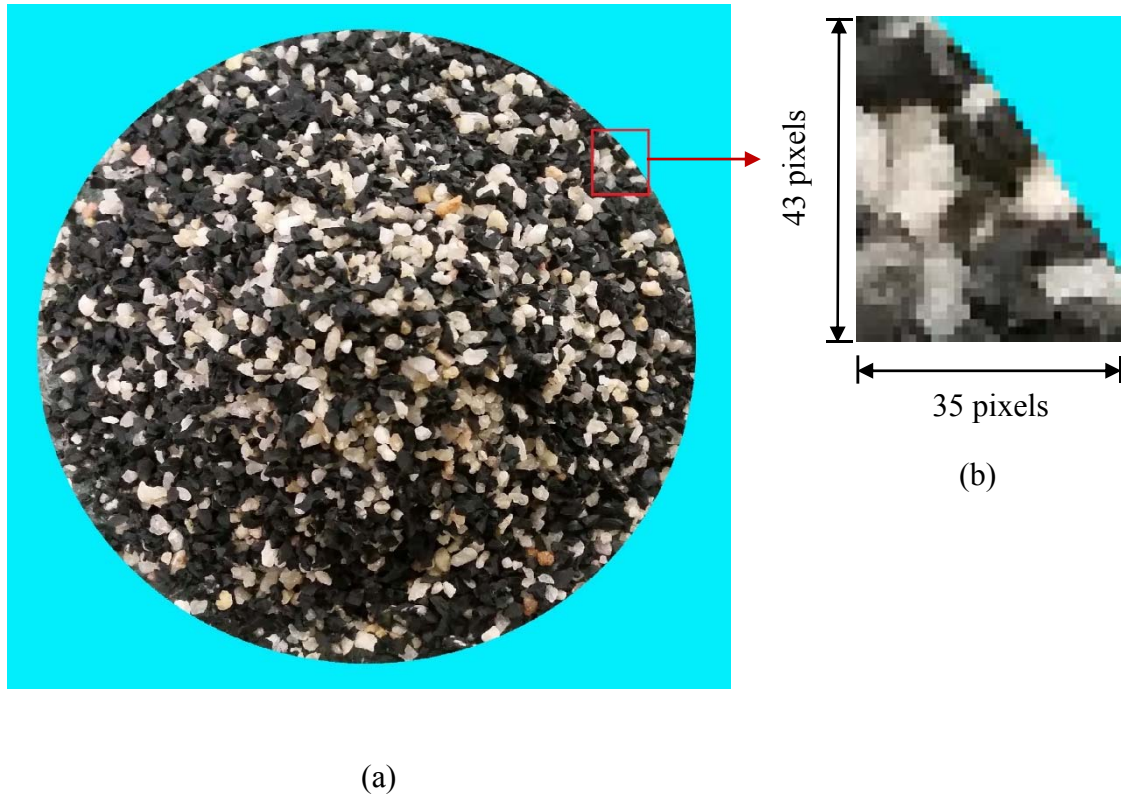
**Figure 4-9.** Calibration of the digital image: (a) sample pile, and (b) an example image.

The threshold value was obtained by processing the pixels of an image. However high quality image files consist of a large number of pixels (> 15 million). Distinguishing color differences directly from the original picture requires long processing time as a result. For simplification in the detailed analysis, a small-sized picture was extracted as an example so that image processing could be performed. Figure 4-9 (b) picked up a small region of $35 \times 43$ pixels, which contains all important elements of the image.

After selecting the small example image as shown in Figure 4-9 (b), a detailed analysis was conducted to find threshold values between color regions. MATLAB was used to read individual pixels into $I_1$ for red, $I_2$ for green, and $I_3$ for blue. However, the three values cannot be directly used to map the regions. A solution is to use an HSI system to identify the materials more easily (Chen et al.

2004). The HSI stands for *hue*, *saturation* and *intensity*. According to Chen et al. (2004), this solution combines the above three intensity values based on appropriate weighting, yielding a weighted intensity value, $I_w$. According to NTSC standard for luminance (IBM 1990), $I_w$ is calculated using the following algorithm:

$$I_w = \frac{0.2989 \times I_1 + 0.5870 \times I_2 + 0.1140 \times I_3}{255}$$

(4.4)

where $I_w$ has an interval of [0, 1]. This $I_w$ is also known as grey level intensity in MATLAB, enabling a bi-color image. Based on the $I_w$ values, contours are drawn for the small example image, as shown in Figure 4-10 (a). Figure 4-10 (a) clearly identifies the color boundaries of different materials, particularly when compared to the original image (Figure 4-9 (b)). However, given there may be multiple intensity threshold values, such as between sand and rubber, between sand and the background and between rubber and the background, it was not guaranteed that all color differences have been distinguished. Since the background intensity is a value in between the values of both sand and rubber, the background regions need to be excluded before calculating the image intensity.

(a)                                                    (b)
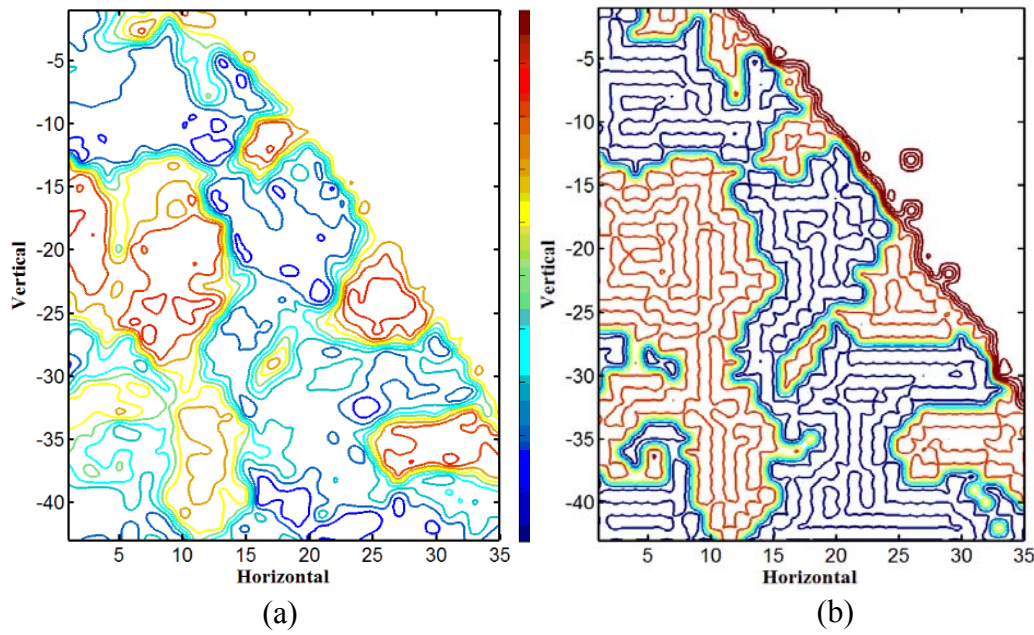
**Figure 4-10.** Intensity contours expressed as: (a) color map, and (b) binary map.

Recall the pre-treatment that the background has been pre-dyed to blue; it is easy to find that these regions because they have very high $I_3$ values (for blue channel). In this study, the background part was identified by searching $I_3 > 245$ and assigning a very high constant, such as 10,000. Using Eq. (4-4), the background intensity has a value $I_w > 1$ while the other parts are not affected. In this way, the background is excluded and the only intensity threshold value will be the one between sand and rubber. Based on a trial-and-error method suggested by Chen et al. (2004), a threshold value $I_w = 0.35$ was taken to be the boundary between the partition sand and rubber after comparing multiple values. To yield a clear definition of regions, the pixels with $I_w < 0.35$ were reassigned as a value of 0 (i.e., rubber particles), otherwise a value of 1 (i.e., sand particles). Figure 4-10 (b) illustrates the intensity contours using the values of 0 and 1. Due to noise influence, such as light intensity, the detection results may not be perfectly correct. However, by comparing Figure 4-10 (a), (b) and Figure 4-9 (b), it is believed that

$I_w = 0.35$ represents the color boundary between sand and rubber particles and can be applied to the rest part of the image in Figure 4-9 (a).

## 4.3    Result discussion

This section presents the results from a comparison of the experimental and numerical results for the present study. The material volume ratio can be expressed as the ratio of an area of color based on the intensity threshold outlined earlier. As segregation varies significantly between the inside area and the pile surface, the comparison was made after removing the pile cap, as shown in Figure 4-8 (e).

### 4.3.1    Segregation Ratio

Digital image processing is further applied here to calculate the area ratio of different colors. Figure 4-8 (e) is separated as a peripheral ring and central circle so as to directly compare segregation outside and inside the pile. The comparison between the experiments and simulations is shown in from Figure 4-11 (a) to Figure 4-12 (a).
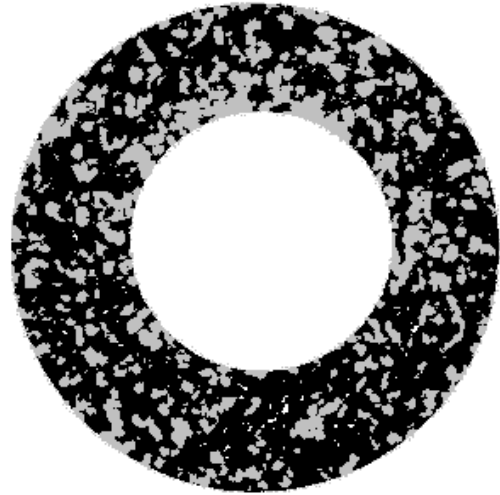
(a) sample
(b) DIP result

**Figure 4-11.** Color segmentation of sand pile at peripheral ring (experiment).
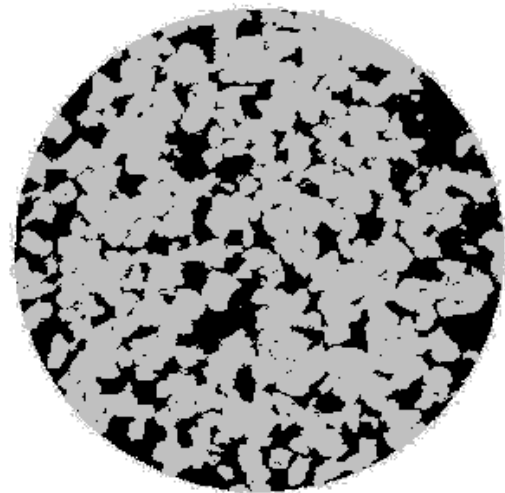


(a) Sample
(b) DIP result

**Figure 4-12.** Color segmentation of sand pile at central circle (experiment).

<div align="center">(a) Sample                             (b) DIP result</div>
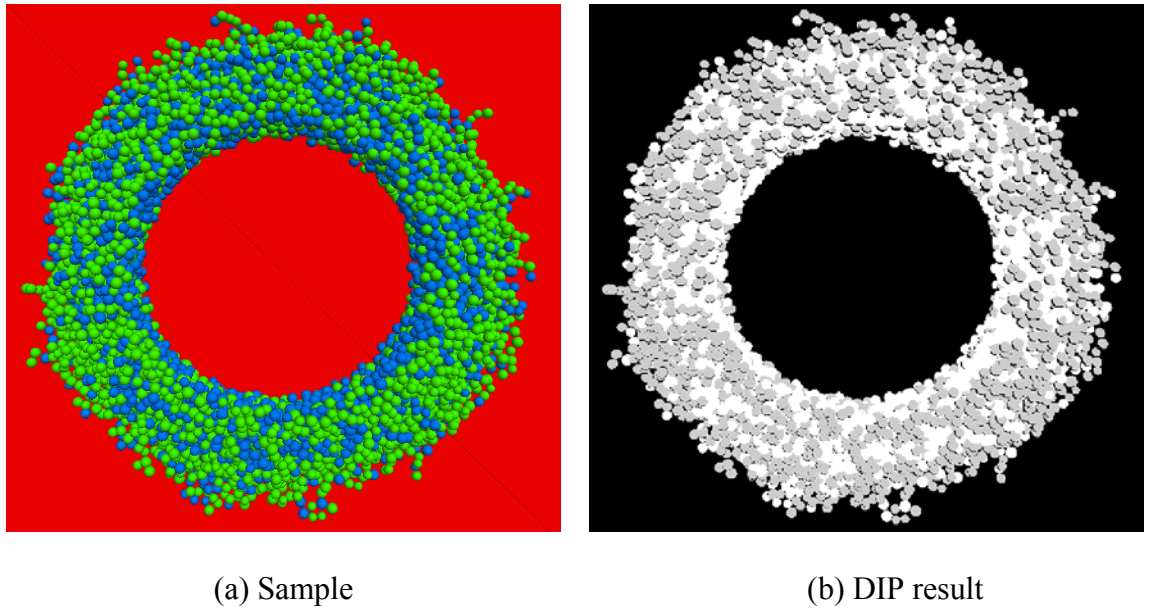
**Figure 4-13.** Color segmentation of sand pile at peripheral ring (numerical).



<div align="center">(a) Sample                             (b) DIP result</div>
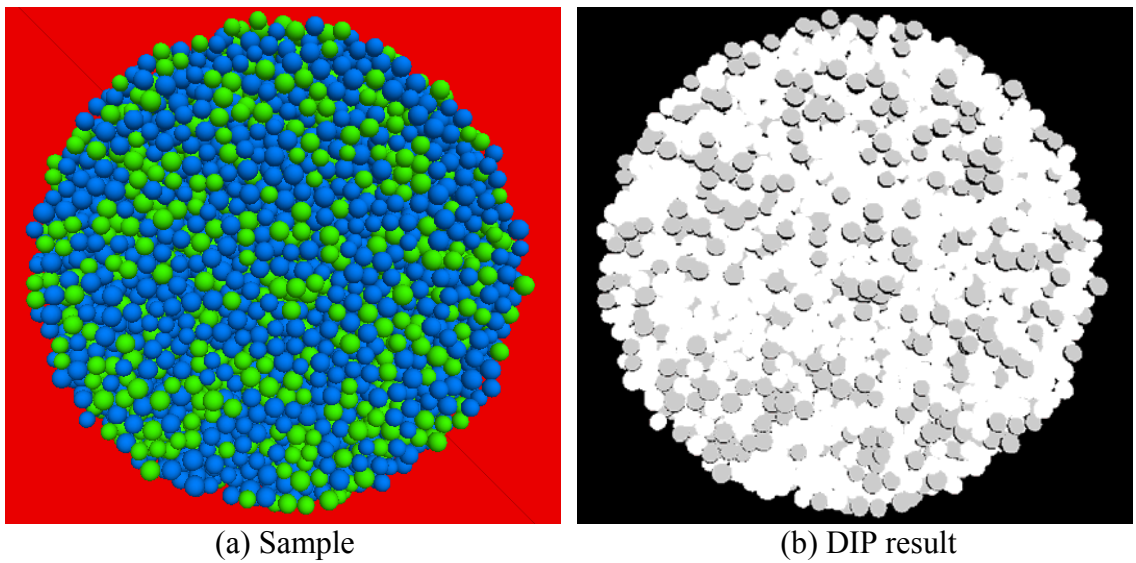
**Figure 4-14.** Color segmentation of sand pile at central circle (numerical).

In the test, the radius of the central circle is half of the bottom of the material heap. It is noted that in the numerical analysis, the image has already been presented as basic RGB colors which saves the intensity threshold value selection. The RGB colors represent the three primary colors of red, green and blue. Each pixel of a digital image can be made by the combinations of these primary colors.

The calculation of the concentration of sand particles was based on color segmentation, shown in Figure 4-11 (b) to 14 (b). These figures present grey images obtained using the aforementioned DIP method. In the experiments, the percentage of sand as calculated from a color area in the peripheral ring and the central circle were 32.09% and 69.86%, respectively. While the numerical result showed that blue particles which represent as sand at peripheral ring and central circle are 39.09% and 66.00%, respectively. Excellent agreement is obtained between the test and numerical results. The agreement is supposed to be valid for the rest parts of the heaps, given the heap surface and the core represent the outer and inner particle distribution profiles. The quantitative comparison based on the DIP results shows a close predication of numerical simulation. This comparison is more convincing than visual comparison used in previous studies. Comparing the segregation in both numerical and experimental results also showed that the chosen material properties (i.e., friction, material rolling friction, and damping coefficient) matched the actual material properties. It is suggested that segregation tests can be used as a useful calibration method.

## 4.3.2    Parametric Study

Due to many input parameters, it is not clear that which parameter had a critical influence on particle segregation. It is necessary to evaluate the impact of each parameter with other parameters unchanged. Table 4-3 lists possible input values for parameters that potentially affect the segregation. Of the parameters, the rolling and sliding friction coefficients determine the particle surface roughness. Five mixtures are defined, each composed of two materials, *A* and *B,* in equal volume.

Again, the mixture ingredients are assumed to be similar in size so that size difference is not considered. In each study, only one parameter was changed while the others remain the same. For example, in case 1, the density for the two ingredients is 2,600 kg/m³ and 1,300 kg/m³ respectively while other parameters such as damping ratio or stiffness etc. remain the same, as listed in Table 4-3. The input values reflect the normal range of materials used as geomaterial ingredients.

**Table 4-3**. Material properties used in the parametric study.

| Case | Ingredient | Density (kg/m³) | Damping ratio | Stiffness (kPa) | Rolling friction coefficient | Sliding friction coefficient |
|------|-----------|-----------------|---------------|-----------------|------------------------------|------------------------------|
| Case 1 | A | 2,600 | 0.2 | $1 \times 10^5$ | 0.6 | 0.3 |
|        | B | 1,300 | 0.2 | $1 \times 10^5$ | 0.6 | 0.3 |
| Case 2 | A | 1,300 | 0.2 | $1 \times 10^5$ | 0.6 | 0.3 |
|        | B | 1,300 | 0.4 | $1 \times 10^5$ | 0.6 | 0.3 |
| Case 3 | A | 1,300 | 0.2 | $1 \times 10^7$ | 0.6 | 0.3 |
|        | B | 1,300 | 0.2 | $1 \times 10^5$ | 0.6 | 0.3 |
| Case 4 | A | 1,300 | 0.2 | $1 \times 10^5$ | 0.3 | 0.3 |
|        | B | 1,300 | 0.2 | $1 \times 10^5$ | 0.6 | 0.3 |
| Case 5 | A | 1,300 | 0.2 | $1 \times 10^5$ | 0.6 | 0.3 |
|        | B | 1,300 | 0.2 | $1 \times 10^5$ | 0.6 | 0.6 |

The five cases were subjected to the segregation test. The test is similar in process to the aforementioned segregation tests, including forming pile through the funnel, slicing the pile at the mid height to compare the inner core and the outer ring. To assess the segregation, define segregation coefficient, $C_s$, as suggested by Williams (1976):

$$C_s = \frac{W_I - W_O}{W_I + W_O} \times 100\% \qquad (4.5)$$

where $W_I$ is the volumetric proportion of material $A$ in the inner core while $W_O$ is the volumetric proportion of material $A$ in the outer ring. Where there is no or negligible segregation, $C_s$ is equal or close to zero, and *vice versa*. The results are provided in Figure 4-15. It is clear that case 1 stands out, with $C_s$=17.97% of suggesting the material density governs the segregation. The friction coefficients (or surface roughness) however do marginal effect on the segregation which agrees with results by Pohlman et al. (2006).



**Figure 4-15.** Segregation coefficient for varying mixtures.

Even though the friction coefficients alone do not cause segregation of the material, it has a certain effect on the mixture once there is already a density difference in the mixture. To examine this density–friction combined effect, a new comparison was made between the mixture density ratios which increase from 1 to 5, according to different sliding friction values $f_s$ = 0.3, 0.4 and 0.5, respectively. The results are provided in Figure 4-16. For each case, the segregation coefficient

$C_s$ increases with the density ratio. This relationship changes if the material surface roughness increases. The rougher the material surface is, the less likely segregation will happen. Similar findings was observed by Lai et al. (1997) that frictional properties sometimes dominate material segregation such as in the event of long range transport. For the funnel discharge in the current study, the density−friction correlation might be explained as follows: when the surface roughness increases, the mobility of the mixture is affected so that flowing from the funnel requires more kinetic energy and material granules tend to move as a whole. Consequently the mixtures are more difficult to be separated during flow.
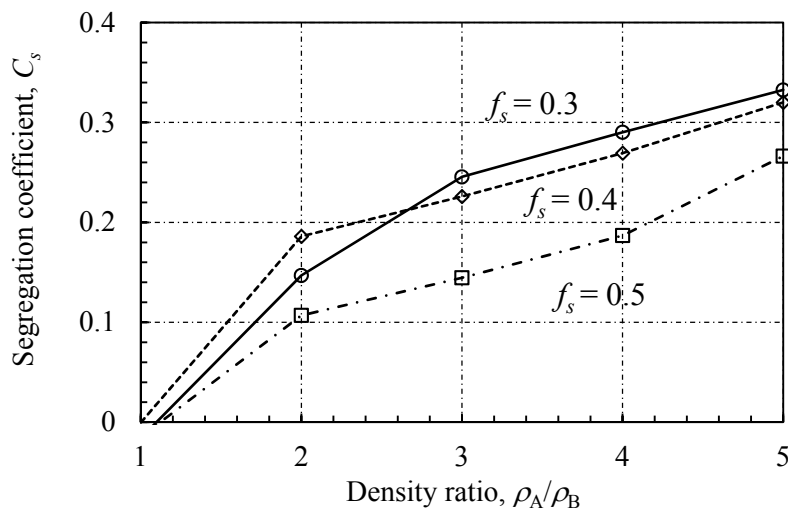


**Figure 4-16.** Segregation coefficient vs. mixture density ratio under different frictions.

## 4.4    Conclusions

This study presented a DIP method used to examine material segregation based on material color difference. The comparison between the DEM simulation and

experiments suggests that DIP could be used as a useful method enabling verification between the DEM and test results.

Material rolling friction and damping ratio for sand and rubber were calibrated by the repose angle and re-bouncing tests, respectively. The parameter values were incorporated into the DEM model for the parametric study. For a uniform mixture, from a microscopic perspective, the density difference had most significant impact to the segregation during the funnel discharge. Other contact properties such as material stiffness, surface roughness or damping ratio had minor to negligible impact. The higher the density difference is, the noticeable the segregation will be. When the segregation needs to be controlled, the material density difference should be considered. However, the density-induced segregation can be offset by the inter-particle friction. The higher the frictional properties are assigned, the less likely the segregation will occur.

## 4.5    Acknowledgement

## 4.6    Notations

$C_1$      count of the particles sitting on a cutting plane

$C_2$      count of the particles intersecting a circular periphery

$C_s$      segregation coefficient

$d_r$      diameter of rubber particle

$d_s$      diameter of sand particle

$E$       effective modulus

$E_r$      effective modulus of rubber particle

$E_s$      effective modulus of sand particle

$f_r$      rolling friction

$f_s$      sliding friction

$f_{r,r}$    rolling friction of rubber particle

$f_{r,s}$    rolling friction of sand particle

$f_{s,r}$    sliding friction of rubber particle

$f_{s,s}$    sliding friction of sand particle

$f_w$      particle−wall friction

$G$       shear modulus

$h$       bead rebound height

$H$       bead drop height

$I$       colour channel intensity

$I_1$      red channel intensity

$I_2$      green channel intensity

$I_3$      blue channel intensity

$I_w$      grey level intensity

$k_w$      particle−wall stiffness

$r$       bead radius

$W_I$      volumetric proportion of material in the inner circle

$W_O$     volumetric proportion of material in the peripheral ring

$\alpha$       restitution coefficient

$\zeta$       damping ratio

$\zeta_r$      damping ratio of rubber particle

$\zeta_s$      damping ratio of sand particle

$\nu$       Poisson's ratio

$\rho$       density

$\rho_r$      density of rubber particle

$\rho_s$      density of sand particle

## 4.7     References

Ahmed, I., and Lovell, C. (1993). "Rubber soils as lightweight geomaterials." *Transportation Research Record*, (1422), 61-70.

Ai, J. (2010). "Particle scale and bulk scale investigation of granular piles and silos."PhD thesis, The University of Edinburgh, Edinburgh, UK.

Altuhafi, F., O'Sullivan, C., and Cavarretta, I. (2013). "Analysis of an image-based method to quantify the size and shape of sand particles." *Journal of Geotechnical and Geoenvironmental Engineering*, 139(8), 1290-1307.

Anand, A., Curtis, J. S., Wassgren, C. R., Hancock, B. C., and Ketterhagen, W. R. (2010). "Segregation of cohesive granular materials during discharge from a rectangular hopper." *Granular Matter*, 12(2), 193-200.

Aydemir, S., Keskin, S., and Drees, L. (2004). "Quantification of soil features using digital image processing (DIP) techniques." *Geoderma*, 119(1), 1-8.

Bosscher, P. J., Edil, T. B., and Kuraoka, S. (1997). "Design of highway embankments using tire chips." *Journal of Geotechnical and Geoenvironmental Engineering*, 123(4), 295-304.

Chen, C., McDowell, G. R., and Thom, N. H. (2014). "Investigating geogrid-reinforced ballast: Experimental pull-out tests and discrete element modelling." *Soils Found*, 54(1), 1-11.

Chen, S., Yue, Z., and Tham, L. (2004). "Digital image-based numerical modeling method for prediction of inhomogeneous rock failure." *International Journal of Rock Mechanics and Mining Sciences*, 41(6), 939-957.

Chung, Y.-C. (2006). "Discrete element modelling and experimental validation of a granular solid subject to different loading conditions."PhD thesis, The University of Edinburgh, Edinburgh, UK.

Cundall, P. A., and Strack, O. D. (1979). "A discrete numerical model for granular assemblies." *Geotechnique*, 29(1), 47-65.

Donald, M., and Roseman, B. (1962). "Mixing and demixing of solid particles. Part I: Mechanisms in a horizontal drum mixer." *Br Chem Eng*, 7(10), 749-752.

Evans, T., and Valdes, J. R. (2011). "The microstructure of particulate mixtures in one-dimensional compression: Numerical studies." *Granular Matter*, 13(5), 657-669.

Falagush, O., McDowell, G. R., and Yu, H. S. (2015). "Discrete element modeling of cone penetration tests incorporating particle shape and crushing." *International Journal of Geomechanics*, 15(6), 04015003.

Foose, G. J., Benson, C. H., and Bosscher, P. J. (1996). "Sand reinforced with shredded waste tires." *Journal of Geotechnical Engineering*, 122(9), 760-767.

Garga, V. K., and O'shaughnessy, V. (2000). "Tire-reinforced earthfill. Part 1: Construction of a test fill, performance, and retaining wall design." *Canadian Geotechnical Journal*, 37(1), 75-96.

Humphrey, D. N., and Manion, W. P. "Properties of tire chips for lightweight fill." *Proc., Grouting, Soil Improvement and Geosynthetics*, ASCE, 1344-1355.

IBM (1990). "NTSC luminance/chrominance equation definition for digital systems." *IBM Tech Disclosure Bull*, 32(10A), 208-209.

Indraratna, B., Ngo, N. T., Rujikiatkamjorn, C., and Vinod, J. (2012). "Behavior of fresh and fouled railway ballast subjected to direct shear testing: Discrete element simulation." *International Journal of Geomechanics*, 14(1), 34-44.

Itasca (2009). "PFC3D 4.0 User's Manual. ." Itasca Consulting Group, Inc., Minnesota, USA.

Kawaguchi, T., Tanaka, T., and Tsuji, Y. (1992). "Numerical simulation of fluidized bed using the discrete element method: The case of spouting bed." *Trans Jpn Soc Mech Eng Ser B*, 58(551), 79-85.

Kemeny, J. M., Devgan, A., Hagaman, R. M., and Wu, X. (1993). "Analysis of rock fragmentation using digital image processing." *Journal of Geotechnical Engineering*, 119(7), 1144-1160.

Kudrolli, A. (2004). "Size separation in vibrated granular matter." *Reports on Progress in Physics*, 67(3), 209-248.

Kuerbis, R., and Vaid, Y. (1988). "Sand sample preparation-the slurry deposition method." *Soils Found*, 28(4), 107-118.

Lai, P.-Y., Jia, L.-C., and Chan, C. (1997). "Friction induced segregation of a granular binary mixture in a rotating drum." *Physical Review Letters*, 79(25), 4994-4997.

Lee, C., Shin, H., and Lee, J. S. (2014). "Behavior of sand–rubber particle mixtures: Experimental observations and numerical simulations." *International Journal for Numerical and Analytical Methods in Geomechanics*, 38(16), 1651-1663.

Liu, J., Yun, B., and Zhao, C. B. (2012). "Identification and validation of rolling friction models by dynamic simulation of sandpile formation." *International Journal of Geomechanics*, 12(4), 484-493.

Lőrincz, J., Imre, E., Gálos, M., Trang, Q., Rajkai, K., Fityus, S., and Telekes, G. (2005). "Grading entropy variation due to soil crushing." *International Journal of Geomechanics*, 5(4), 311-319.

Manahiloh, K. N., Muhunthan, B., and Likos, W. J. (2016). "Microstructure-based effective stress formulation for unsaturated granular soils." *International Journal of Geomechanics*, 16(6), D4016006.

Masad, E., Taha, R., Ho, C., and Papagiannakis, T. (1996). "Engineering properties of tire/soil mixtures as a lightweight fill material." *Geotech Test J*, 19(3), 297-304.

Nightingale, D. E., and Green, W. P. (1997). "An unresolved riddle: Tire chips, two roadbeds, and spontaneous reactions." *Testing Soil Mixed with Waste or Recycled Materials*, ASTM International, STP1275, 265-285.

Ottino, J., and Khakhar, D. (2000). "Mixing and segregation of granular materials." *Annual Review of Fluid Mechanics*, 32(1), 55-91.

Patil, U., Valdes, J. R., and Evans, T. M. (2010). "Swell mitigation with granulated tire rubber." *Journal of Materials in Civil Engineering*, 23(5), 721-727.

Poh, P. S., and Broms, B. B. (1995). "Slope stabilization using old rubber tires and geotextiles." *Journal of performance of constructed facilities*, 9(1), 76-79.

Pohlman, N. A., Severson, B. L., Ottino, J. M., and Lueptow, R. M. (2006). "Surface roughness effects in granular matter: Influence on angle of repose and the absence of segregation." *Physical Review E*, 73(3), 031304.

Shi, D., Abatan, A. A., Vargas, W. L., and McCarthy, J. (2007). "Eliminating segregation in free-surface flows of particles." *Physical Review Letters*, 99(14), 148001.

Tsang, H. H., Lo, S., Xu, X., and Neaz Sheikh, M. (2012). "Seismic isolation for low‐to‐medium‐rise buildings using granulated rubber–soil mixtures: numerical study." *Earthquake engineering & structural dynamics*, 41(14), 2009-2024.

Villeneuve, M. C., Diederichs, M. S., and Kaiser, P. K. (2011). "Effects of grain scale heterogeneity on rock strength and the chipping process." *International Journal of Geomechanics*, 12(6), 632-647.

Watabe, Y., Shinsha, H., Yoneya, H., and Ko, C. J. (2014). "Description of partial sandy layers of dredged clay deposit using penetration resistance in installation of prefabricated vertical drains." *Soils Found*, 54(5), 1006-1017.

Williams, J. C. (1976). "The segregation of particulate materials. A review." *Powder Technology*, 15(2), 245-251.

Yang, R., Zou, R., and Yu, A. (2000). "Computer simulation of the packing of fine particles." *Physical Review E*, 62(3), 3900-3908.

Yoshimine, M., and Koike, R. (2005). "Liquefaction of clean sand with stratified structure due to segregation of particle size." *Soils Found*, 45(4), 89-98.

Yoshimoto, N., Orense, R. P., Tanabe, F., Kikkawa, N., Hyodo, M., and Nakata, Y. (2011). "Measurement of degree of saturation on model ground by digital image processing." *Soils Found*, 51(1), 167-177.

Yue, Z. Q., and Morin, I. (1996). "Digital image processing for aggregate orientation in asphalt concrete mixtures." *Can J Civil Eng*, 23(2), 480-489.

Zhou, Y., Wright, B., Yang, R., Xu, B., and Yu, A. (1999). "Rolling friction in the dynamic simulation of sandpile formation." *Physica A: Statistical Mechanics and its Applications*, 269(2), 536-553.

Zhou, Y., Xu, B., Yu, A., and Zulli, P. (2001). "Numerical investigation of the angle of repose of monosized spheres." *Physical Review E*, 64(2), 021301.

Zornberg, J. G., Cabral, A. R., and Viratjandr, C. (2004). "Behaviour of tire shred sand mixtures." *Canadian Geotechnical Journal*, 41(2), 227-241.

# Chapter 5

# Modelling particle kinetic behaviour considering asperity contact

Can Wang, An Deng[*], Abbas Taheri

School of Civil, Environmental and Mining Engineering, The University of Adelaide, SA 5005, Australia.

[*] Corresponding author.

E-mail addresses: c.wang@adelaide.edu.au (Can Wang). an.deng@adelaide.edu.au (An Deng). abbas.taheri@adelaide.edu.au (Abbas Taheri).

# Statement of Authorship

| Title of Paper | Modelling particle kinetic behaviour considering asperity contact |
|---|---|
| Publication Status | ☐ Published      ☐ Accepted for Publication <br> ☑ Submitted for Publication      ☐ Unpublished and Unsubmitted work written in manuscript style |
| Publication Details | Wang C, Deng A, Taheri A (2018). Modelling particle kinetic behaviour considering asperity contact. *Granular Matters*. |

## Principal Author

| Name of Principal Author (Candidate) | Can Wang | | |
|---|---|---|---|
| Contribution to the Paper | Undertook Literature review, performed parametric study and numerical model analysis. | | |
| Overall percentage (%) | 75% | | |
| Certification: | This paper reports on original research I conducted during the period of my Higher Degree by Research candidature and is not subject to any obligations or contractual agreements with a third party that would constrain its inclusion in this thesis. I am the primary author of this paper. | | |
| Signature | | Date | 05/08/2018 |

## Co-Author Contributions

By signing the Statement of Authorship, each author certifies that:

     i.      the candidate's stated contribution to the publication is accurate (as detailed above);

     ii.      permission is granted for the candidate in include the publication in the thesis; and

     iii.      the sum of all co-author contributions is equal to 100% less the candidate's stated contribution.

| Name of Co-Author | An Deng | | |
|---|---|---|---|
| Contribution to the Paper | Acted as corresponding author, supervised project development and helped with paper editing. | | |
| Signature | | Date | 05/08/2018 |

| Name of Co-Author | Abbas Taheri | | |
|---|---|---|---|
| Contribution to the Paper | Supervised work development and helped with paper editing. | | |
| Signature | | Date | 07/08/2018 |

# **Abstract**

A model of formulating particle kinetic behaviour considering contact asperity is presented. The contact asperity is created by lining up a set of particles in varying distances. A moving particle is assigned a velocity to travel on the rugged surface where the particle trajectory and mechanical energy are gauged. The results are used to validate a discrete element framework which is developed and applied to examine the effect of particulate-scale properties on the kinetic behaviour. Some interesting case studies are designed and simulated. The simulations suggest that the surface roughness influences the energy dissipation caused by multiple collisions. The research outcomes define the inter-particle reaction from a micro-scale perspective and help predict asperity-induced wear.

**Keywords**: collision, surface asperity, DEM, energy dissipation

## 5.1    Introduction

Upon contacting, particles behaviour is closely dependent on its physical characteristics, such as the density, shape, size and surface at contact (Yang and Wei, 2012, Jensen et al., 2001, Dai et al., 2015). On the contact surface, the asperity, or roughness, governs the particle response, mainly in the form of energy loss, in a dynamic process (e.g., the wheel rolling on the rail) (Senetakis et al., 2013, Consoli et al., 2007, Anastasiadis et al., 2012, Doménech-Carbó, 2016). Although the energy loss, at least a major portion of it, is recognised arising from the surface adhesion and frictional properties, e.g. Persson et al. (2004) which suggested the energy loss in itself is caused primarily by the surface deformation at contact. According to Buckley (1981), the deformation includes the elastic and plastic components. The two components are nested inside the contacting conditions occurred between the particles of concern and, depending on the contacting conditions, are subject to variation in magnitude. As a result, the relationship between the surface asperity, deformation components, and energy loss is still poorly understood (Tayebi and Polycarpou, 2004; Svahn et al., 2003). Albeit there are experimental solutions (Dai, 2015; Buckley, 1981) developed to deal with the lack of understanding, the test conditions are less than ideal, and the corresponding results are not accurate enough. The reasons, as per Zappone et al. (2007), are the challenge to validate the solutions through a well-defined rough surface and the difficulty to avoid environmental noises (e.g., the surface chemistry characteristics) surrounding the particles in the test. These difficulties can be resolved through mathematical tools which enable a system without environment intervention.

In this study, a discrete element model (DEM) is developed to reproduce the particle kinetic behaviour in response to the surface asperity the particle is subjected to. The surface asperity characteristics are defined specifically to subject the particle to a unique, exclusive rugged surface. On the rugged surface, the particle is assigned with a velocity and allowed to travel. The model is used to gauge the particle trajectory and velocity in travel so that the energy loss is recorded. The model is validated against the analytical solution established in the same asperity conditions as for the DEM model. DEM simulations are performed on some interesting case studies in order to gain a further insight into the particle kinetic behaviour at micro-scale.

## 5.2    Model Development

### 5.2.1    Geometry

The geometry used to develop the model is provided in Figure 5-1. An array of semicircular discs, 1 to $N$, are lined up at fixed positions in $(x, y)$ plane, forming the asperity based on the substrate of $x$-axis. The discs are equal in radius, $r_j$, where $j=1, 2,…, N$, and placed edge to edge with individual centroids sitting on the $x$-axis. At time $t$, disc $M$ moves at a velocity, $v$, in the $x$-direction. Disc $M$ measures $r$ in radius and $m$ in mass. The position of the moving disc in relation to disc $j$ is determined by the contact angle, $\gamma$, which measures the angle from the $x$-axis to the centre-to-centre line drawn between discs $M$ and $j$. Disc $M$ contacts disc $j$ at point $A$. As suggested in past studies (Jensen et al., 1999; Dippel et al., 1996), this geometry defines a clear, continuous and manageable asperity surface. This geometry facilitates: *i*) the expression of the asperity

surface (i.e. circular function), *ii*) the assessment of discs contacting condition, and *iii*) the adaption of the geometry to the analytical model (Greenwood and Williamson, 1996). Similar geometry was adopted in past discrete element studies (Dippel et al., 1996; Batrouni et al., 1996; Henrique, 1998; Valance and Bideau, 1886). Given the model geometry provided in Figure 5-1, there is no sub-asperity at the particle surface; the inter-particle friction is assumed to be zero as its contribution to energy loss is assumed in the part of collisional energy dissipation rate (Gollin et al., 2017); and the energy loss of disc *M* is based on the asperities of the surface plane. The energy loss is determined using two approaches: the discrete element simulation method and the analytical solution. The analytical results are used to verify the simulation results. The two approaches and the method verification are presented in the following sections.
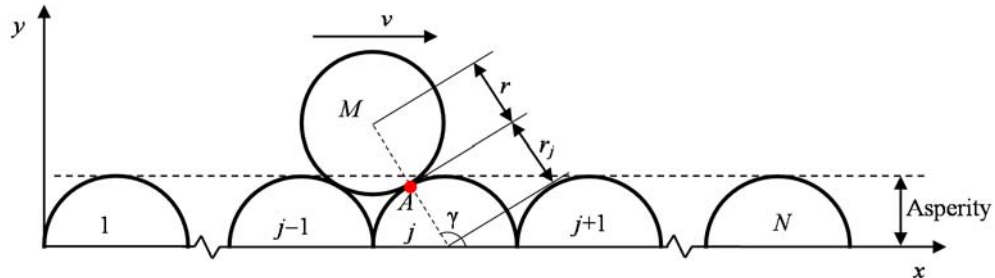


**Figure 5-1.** The model geometry of disc moving on asperity surface.

### 5.2.2   DEM model

The DEM model is developed to reproduce the mechanical responses of two or more discs at contact, e.g., point *A* in Figure 5-1. As per Cundall (1988), the mechanical responses at contact can be represented by using a combination of simple mechanical elements, such as the spring, slider and dashpot. The

combination is dependent on the materials to be examined and, as suggested in the past similar studies (Batrouni et al., 1996; Henrique et al., 1998; Valance and Bideau, 1998), is often governed by using the Hertz Contact model (Mindlin, 1953). The Hertz Contact model uses the least number of physical units, as illustrated in Figure 5-2, but enables mimicking a wide range of distinct element based problems. The model is simple and preferably applicable to represent the contacting occurred between smooth, elastic particles.
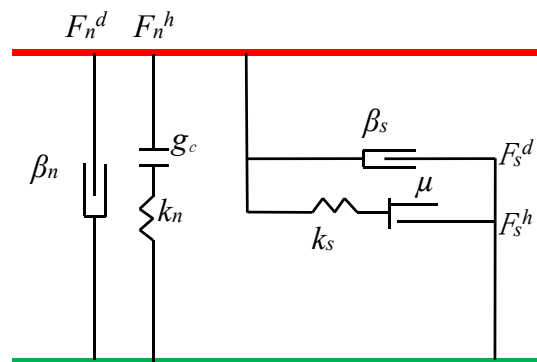


**Figure 5-2.** Diagram of the Hertz Contact model (adapted from ITASCA (2007)), where $F_n^h$, $F_s^h$: are respectively non-linear contact force at normal, and shear direction; $F_n^d$, $F_s^d$ are dashpot (viscous) forces at normal and shear direction, respectively.

In the Hertz Contact model, the individual mechanical elements govern energy transformation occurred at contact. The energy transformation arises from three components: the elastic strain energy, $E_s$, stored in the spring elements, the slip energy, $E_\mu$, dissipated by frictional sliding, and the dashpot energy, $E_\beta$, being lost due to damping (Cundall and Strack, 1979). The energy is lost to other forms of energy, e.g., heat and sound. It is assumed that there is no friction at contact as defined in Figure 5-1. Therefore, the dashpot energy dissipation $E_\beta$ is the only source of energy loss at contact. Considering the

absence of surface friction, the moving disc changes merely the normal velocity

component (Beacker et al., 2008). The energy loss $E_\beta$ is expressed as:

$$E_\beta = -\sum F_n^d \left( \dot{\delta}_n \Delta t \right) \qquad (5.1)$$

where $\delta_n$ is the relative normal displacement; $\Delta t$ is the time step increment;

$F_n^d$ is the normal dashpot force at contact and, as per Itasca (2017), is calculated

as:

$$F_n^d = 2\dot{\delta}_n^2 \beta_n \sqrt{m_c k_n} \qquad (5.2)$$

where $\beta_n$ is the normal critical damping ratio, $k_n$ is the normal stiffness, and $m_c$

is the mass of the system of interest and defined by:

$$m_c = \frac{m_1 m_2}{m_1 + m_2} \qquad (5.3)$$

where $m_1$ and $m_2$ are the mass of discs 1 and 2 respectively.

In a DEM model, the particles are assumed to be non-deformable. An

overlap is allowed to develop at the point of contact in order to account for disc-

to-disc interactions (Cundall and Strack, 1979). This overlap likely influences

the trajectory of the moving disc, as illustrated in Figure 5-3. Figure 5-3 shows

the potential overlap at the contact between moving disc $P$ and stationary disc

$Q$. The two discs collide at an eccentricity of $L$. DEM algorithm allows disc $P$

to penetrate into disc $Q$, creating a contact overlap as shaded between the two

discs. As a result, the centroid of disc $P$ passes the trajectory of points $A$, $B$ and

$C$ in DEM simulation, but in reality point $B$ may not be a point to pass through.

The influence to the trajectory of disc $P$ may be negligible in one collision.

However, where a continuously bumpy surface as in Figure 5-3 is of the choice

and multiple collisions occur, the overlap influences accumulate, likely leading

to noticeable trajectory deviation. The change in trajectory is supposed to affect

the prediction of the contact angle $\gamma$ which in turn brings possible inaccuracy to estimate the energy loss of the moving disc. The overlap influence can be examined by developing the analytical solution.
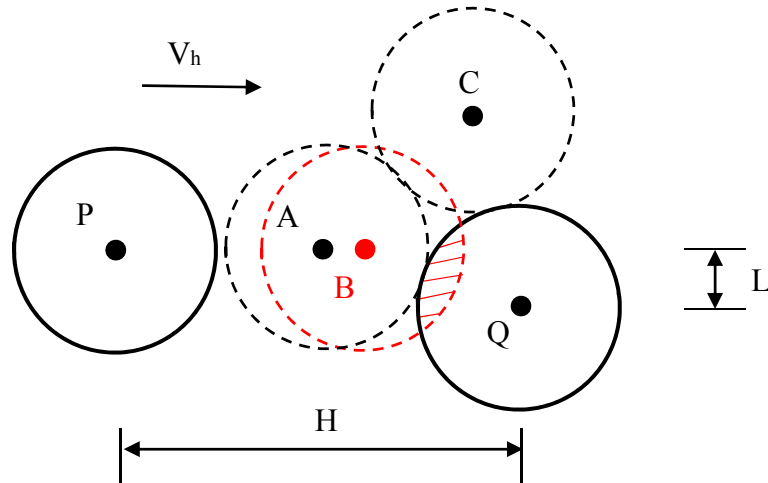


**Figure 5-3.** The trajectory of particle *P* during an oblique collision with particle *Q*.

### 5.2.3     Analytical solution

This section presents the analytical solution to the same problem of the disc travelling on asperity surface as simulated by the DEM approach. The DEM adopts the Newton's laws of motion, and the analytical solution considers the restitution of material. According to Becker et al.(2008), both the Newton's laws of motion and the restitution can be used to describe the dissipative interaction of particles. The restitution coefficient, as per (Doménech-Carbó, 2016; Chang and Ling, 1992), quantifies the elastic energy restored at contact, which is recovered back to kinetic energy, and the energy dissipation that results from plastic deformation. Upon surface colliding, no body penetration

between the discs of interest is allowed. Therefore, the analytical method offers an accurate prediction of the disc trajectory and can be used to examine the overlap influences in the DEM simulation.

### 5.2.3.1  Model description

The geometry in Figure 5-1 is refined into the geometry in Figure 5-4. The new element added is the centroid profile where the centroid of disc *M* lies on. The profile is set based on the radii of the discs so that the overlap issue is avoided. On the centroid profile, a sub-profile, curve *BC*, is plotted to illustrate one disc bounce. Multiple bounces may occur depending on the kinetic energy of the moving disc and the disc material properties assigned. The rest conditions such as the surface asperity, velocity and radii remain the same as in Figure 5-1. When disc *M* moves on the bumpy surface, the following conditions are assumed: *i*) Only point of contact is used during the collision; and *ii*) Disc collision completes instantaneously, so that the collision time is negligible. These conditions are used to simplify the model.
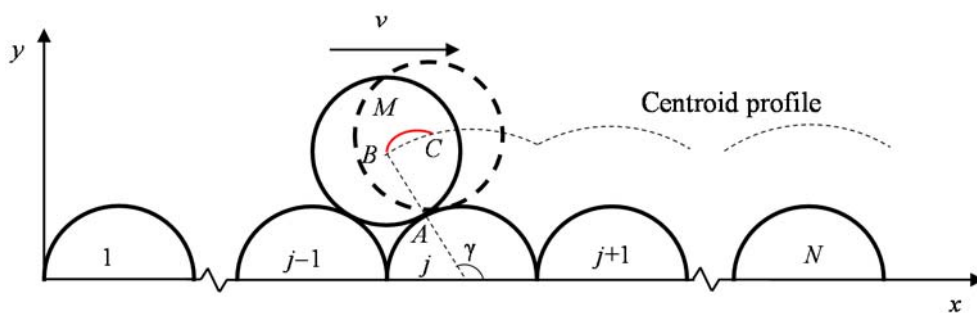


**Figure 5-4**. Model geometry of disc moving on asperity surface considering bounce.

At a moment when disc *M* travels on the asperity surface, the disc takes one of three moves: rotating, sliding and bouncing. As there is no surface

friction, the disc does not spin. Therefore the disc either slides or bounces on the surface, depending on the condition of contact between the moving disc and one of the base discs. The contact condition can be judged based on the distance $D_j^t$ measured at time $t$ between disc $M$ and the base disc $j$:

$$D_j^t = \sqrt{\left(x^t - x_j\right)^2 + \left(y^t - y_j\right)^2} \tag{5.4}$$

where $(x_j,\ y_j)$ and $(x^t,\ y^t)$ are the coordinates of the centres of discs $j$ and $M$, respectively. Disc $M$ is bouncing if $D_j^t > r + r_j$ or sliding if $D_j^t = r + r_j$. The condition $D_j^t < r + r_j$ is not allowed to avoid the surface overlap. For the base disc $j$, the centre coordinate is expressed as:

$$x_j = r_j + 2\sum_{i=1}^{j-1} r_i \tag{5.5}$$

$$y_j = 0 \tag{5.6}$$

### 5.2.3.2 Trajectory of bouncing

Upon a collision with disc $j$, disc $M$ loses a portion of the normal velocity. The residual normal velocity drives the disc to bounce up which then falls under gravity, as of the profile *BC* shown in Figure 5-4. This bouncing process continues several times until the normal velocity vanishes. Assume disc $M$ is in collision with disc $j$ at time $t$. Meanwhile, the disc bounces up at velocity components $(v_x^t, v_y^t)$. If, at time step $t+\Delta t$, disc $M$ is in the move of the first bounce, the corresponding velocity components become:

$$v_x^{t+\Delta t} = v_x^t \tag{5.7}$$

$$v_y^{t+\Delta t} = v_y^t + g \times \Delta t \tag{5.8}$$

The centre relocates to ($x^{t+\Delta t}, y^{t+\Delta t}$) which are respectively expressed

as:

$$x^{t+\Delta t} = x^t + v_x^t \times \Delta t \tag{5.9}$$

$$y^{t+\Delta t} = y^t + \frac{\left(v_y^{t+\Delta t} + v_y^t\right) \times \Delta t}{2} \tag{5.10}$$

The centre coordinate ($x^{t+\Delta t}, y^{t+\Delta t}$) are plugged in Eq. (5.4) to update

$D_j^{t+\Delta t}$. The updated $D_j^{t+\Delta t}$ is then used to confirm the presumed first bounce of

disc *M*. If $D_j^{t+\Delta t} > r + r_j$ the presumption is confirmed; if $D_j^{t+\Delta t} = r + r_j$, the

disc is sliding; and if $D_j^{t+\Delta t} < r + r_j$, disc *M* has performed two or more bounces

in the time step increment $\Delta t$.

Where two or more bounces occur in the time step increment $\Delta t$, the

time $t+\Delta t_0$ when the first bounce completes needs to be determined. As $\Delta t$ is

sufficiently small, the horizontal and vertical velocities are assumed to be

constant during the collision period $\Delta t_0$. Also assuming a linear trajectory

during (*t*, *t*+$\Delta t_0$). The centre of disc *M* ($x^{t+\Delta t_0}, y^{t+\Delta t_0}$) becomes:

$$y^{t+\Delta t_0} = y^t + \frac{v_y^{t+\Delta t_0}}{v_x^{t+\Delta t_0}} x^{t+\Delta t_0} - \frac{v_y^{t+\Delta t_0}}{v_x^{t+\Delta t_0}} x^t \tag{5.11}$$

At time $t+\Delta t_0$, discs *M* and *j* are in contact, leading to

$$\left(y^{t+\Delta t_0}\right)^2 + \left(x^{t+\Delta t_0} - x_j\right)^2 = \left(r + r_j\right)^2 \tag{5.12}$$

Solving Eqs. (5.11) and Eqs. (5.11) yields roots $x^{t+\Delta t_0} = x_1$ and $x_2$ respectively as follow:

$$x^{t+\Delta t_0} = \begin{cases} x_1, \text{if} |x_1 - x^t| < |x_2 - x^t| \\ x_2, \text{if} |x_1 - x^t| > |x_2 - x^t| \end{cases} \qquad (5.13)$$

The time increment $\Delta t_0$ is calculated as:

$$\Delta t_0 = \left| \frac{x^{t+\Delta t_0} - x^t}{v_x^t} \right| \qquad (5.14)$$

During the time increment $\Delta t_0$, the $x$-velocity component of disc $M$ remains unchanged:

$$v_x^{t+\Delta t_0} = v_x^t \qquad (5.15)$$

Disc $M$ changes in elevation, the $y$-velocity component is updated as:

$$v_y^{t+\Delta t_0} = \lim_{\Delta t_0 \to 0} \frac{v_y^t}{|v_y^t|} \sqrt{\left(v_y^t\right)^2 - 2g\left(y^t - y^{t+\Delta t_0}\right)} \qquad (5.16)$$

The contact angle $\gamma$ at $t+\Delta t_0$ becomes:

$$\gamma^{t+\Delta t_0} = \arctan \frac{y^{t+\Delta t_0} - y_j}{x^{t+\Delta t_0} - x_j} \qquad (5.17)$$

The tangential and normal velocity components are calculated respectively as:

$$v_s^{t+\Delta t_0} = v_x^{t+\Delta t_0} \cos\gamma^{t+\Delta t_0} + v_y^{t+\Delta t_0} \sin\gamma^{t+\Delta t_0} \qquad (5.18)$$

$$v_n^{t+\Delta t_0} = v_x^{t+\Delta t_0} \sin\gamma^{t+\Delta t_0} + v_y^{t+\Delta t_0} \cos\gamma^{t+\Delta t_0} \qquad (5.19)$$

If the disc rebounds, the normal velocity is subjected to damping and reduces to:

$$v_{n,r}^{t+\Delta t_0} = -\alpha_n v_n^{t+\Delta t_0} \tag{5.20}$$

where $\alpha_n$ is the material restitution coefficient. Kawaguchi et al (1992) expressed $\alpha_n$ as a function of damping ratio $\beta_n$:

$$\alpha_n = e^{\frac{\beta_n \pi}{\sqrt{1-\beta_n^2}}} \tag{5.21}$$

Substituting Eq.(5.21) into Eq.(5.20) yields:

$$v_{n,r}^{t+\Delta t_0} = -e^{\frac{\beta_n \pi}{\sqrt{1-\beta_n^2}}} v_n^{t+\Delta t_0} \tag{5.22}$$

Convert the tangential and normal velocity components in the $(x, y)$ plane:

$$v_x^{t+\Delta t_0} = v_s^{t+\Delta t_0} \cos\gamma - v_{n,d}^{t+\Delta t_0} \sin\gamma \tag{5.23}$$

$$v_y^{t+\Delta t_0} = v_s^{t+\Delta t_0} \sin\gamma - v_{n,d}^{t+\Delta t_0} \cos\gamma \tag{5.24}$$

The new velocity components drive the disc to bounce up. At time step $t+\Delta t$, the velocity of disc $M$ and the coordinate of the centre are determined respectively as:

$$v_x^{t+\Delta t} = v_x^{t+\Delta t_0} \tag{5.25}$$

$$v_y^{t+\Delta t} = v_y^{t+\Delta t_0} + g\left(\Delta t - \Delta t_0\right) \tag{5.26}$$

$$x^{t+\Delta t} = x^{t+\Delta t_0} + v_x^{t+\Delta t_0}\left(\Delta t - \Delta t_0\right) \tag{5.27}$$

$$y^{t+\Delta t} = y^{t+\Delta t_0} + v_y^{t+\Delta t_0}\left(\Delta t - \Delta t_0\right) \tag{5.28}$$

The coordinate of the centre is subject to the contact criterion (i.e. $D_j^{t+\Delta t}$ vs. $r + r_j$). If $D_j^{t+\Delta t} > r + r_j$, disc $M$ is in the move of the second bounce. The algorithm proceeds to the next time step. Otherwise, Eqs. (11-28) are saved. This is because the normal velocity at $t+\Delta t_0$ is sufficiently small and there are

only micro bounces between $(t+\Delta t_0, t+\Delta t)$. It is assumed that the normal velocity is fully dissipated so that the moving disc continues with sliding. This assumption would lead to a small amount of kinetic energy loss as some micro bounces are eliminated. However, the assumption would not influence the simulation results because a small time step $\Delta t$ is selected. Changing different time step increment, e.g., $\Delta t = 10^{-4}$ s and $10^{-6}$ s does not affect the trajectories of the moving disc.

### 5.2.3.3   Trajectory of sliding

Where the normal velocity of disc *M* dissipates completely at time $t+\Delta t_0$, the disc does not bounce but starts to slide on the surface. Upon departure, the angular velocity is determined as:

$$\omega^{t+\Delta t_0} = \frac{v_s^{t+\Delta t_0}}{r+r_j} \tag{5.29}$$

where the tangential velocity $v_s^{t+\Delta t_0}$ is determined based on Eq. (5.18). Meanwhile, the angular acceleration $\dot{\omega}^{t+\Delta t_0}$ is equal to:

$$\dot{\omega}^{t+\Delta t_0} = \frac{g \times \cos \gamma^{t+\Delta t_0}}{r+r_j} \tag{5.30}$$

The angle of rotation $\theta$ completed during the time increment $(\Delta t - \Delta t_0)$ is calculated as:

$$\theta^{t+\Delta t_0, t+\Delta t} = \omega^{t+\Delta t_0} \times (\Delta t - \Delta t_0) + 0.5 \times \dot{\omega}^{t+\Delta t_0} \times (\Delta t - \Delta t_0)^2 \tag{5.31}$$

Define angles $\theta$ and $\gamma$ to be positive if they rotate in clockwise and anti-clockwise directions respectively, as shown in Figure 5-5.
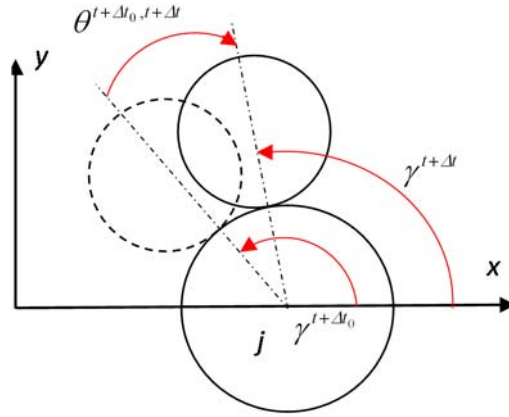
**Figure 5-5**. Increment of contact angle and rotation angle.

At time step $t+\Delta t$, the contact angle is expressed as:

$$\gamma^{t+\Delta t} = \gamma^{t+\Delta t_0} - \theta^{t+\Delta t_0, t+\Delta t} \tag{5.32}$$

The centre of disc $M$ relocates to:

$$x^{t+\Delta t} = x^{t+\Delta t_0} + (r + r_j) \times \left( \cos\left(\gamma^{t+\Delta t_0} - \theta^{t+\Delta t_0, t+\Delta t}\right) - \cos\gamma^{t+\Delta t_0} \right) \tag{5.33}$$

$$y^{t+\Delta t} = y^{t+\Delta t_0} + (r + r_j) \times \left( \sin\left(\gamma^{t+\Delta t_0} - \theta^{t+\Delta t_0, t+\Delta t}\right) - \sin\gamma^{t+\Delta t_0} \right) \tag{5.34}$$

The angular velocity $\omega$, tangential velocity $v_s$, $x$-velocity component $v_x$, and $y$-velocity component $v_y$, respectively, are updated as:

$$\omega^{t+\Delta t} = \frac{\omega^t}{|\omega^t|} \times \sqrt{\left(\omega^t\right)^2 - 2 \times g \times \frac{y^{t+\Delta t} - y^t}{(r + r_j)^2}} \tag{5.35}$$

$$v_s^{t+\Delta t} = \omega^{t+\Delta t} \times (r + r_j) \tag{5.36}$$

$$v_x^{t+\Delta t} = v_s^{t+\Delta t} \times \cos\left(\gamma^{t+\Delta t}\right) \tag{5.37}$$

$$v_y^{t+\Delta t} = v_s^{t+\Delta t} \times \sin\left(\gamma^{t+\Delta t}\right) \tag{5.38}$$

Eqs. (5.29) to (5.38) are used to calculate the trajectory of disc *M* performed during time step $(t+\Delta t_0, \ t+\Delta t)$. Continue the same algorithm at the next $(t+\Delta t, \ t+2\Delta t)$ if disc *M* is in the move of sliding based on the contact criterion of $D_j^{t+2\Delta t}$ *vs.* $r + r_j$. Otherwise, the algorithm developed for bouncing, i.e. Eqs. (5.11) to (5.28), is used. An additional position check is performed on the contact between disc *M* and *j*+1. If, at time *t*, $x^t > x_j + r_j$, disc *M* is in contact with disc *j*+1 which becomes the disc of interest in the algorithm.

**5.2.3.4   Model flow chart**

A flowchart of the model is shown in Figure 5-6. The initial input values include the velocity components and the position of the centre of disc *M*. The position values are plugged in the contact criterion of $D_j^t$ *vs.* $r + r_j$ to determine the motion of the disc. Where in the move of bouncing, disc *M* is updated, using the corresponding algorithm, in respect to its centre coordinate and velocity components. The new values are subject to the contact criterion again. Where disc *M* is in the move of sliding, the new values are plugged into the algorithm for sliding in order to update the centre position and disc velocity, and the new values flow to the contact criterion again. Whether in the move sliding or bouncing, disc *M* is subject to the check of contact with a new base disc. If there is, the base disc of concern becomes disc *j*+1, and a new loop runs. Before the flowchart ends, the *x*-velocity component is checked. If the velocity component remains, the loop keeps running. Otherwise, the program ends.
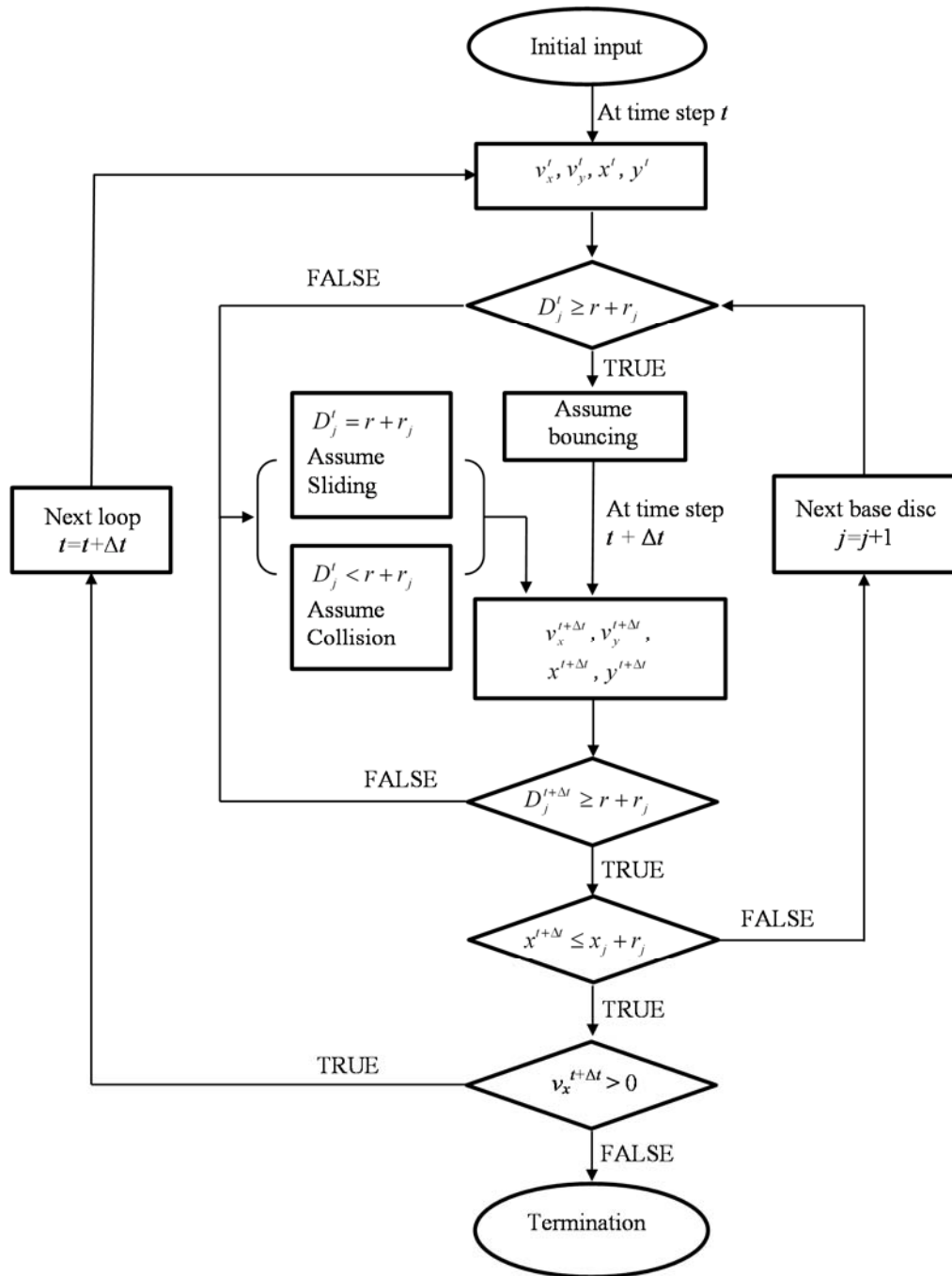
**Figure 5-6**. Flowchart of a single disc moving on a bumpy surface.

## 5.3   DEM Validation

The DEM model is validated against the analytical solution. Both approaches are applied to the model shown in Figure 5-1. The models are established using the following properties. The radii are 0.3 m for the moving disc and 0.05 m for the base disc. All discs have a density of 2,000 kg/m³. In the DEM, the Hertz

contact is used which adopts a Poisson's ratio of 0.3 and a shear modulus of 100 GPa. The relatively large shear modulus is assumed to reduce the influence of the contact overlap, enabling a simulation environment similar to that for the analytical solution. For both methods, a damping ratio $\beta_n = 0.5$ is used to dissipate energy at each collision. The moving disc is assigned to three initial velocities $= 0.3$, 0.5 and 1.0 m/s respectively. The results of the horizontal velocity versus the distance for the disc assigned with the three initial velocities are provided in Figure 5-7.
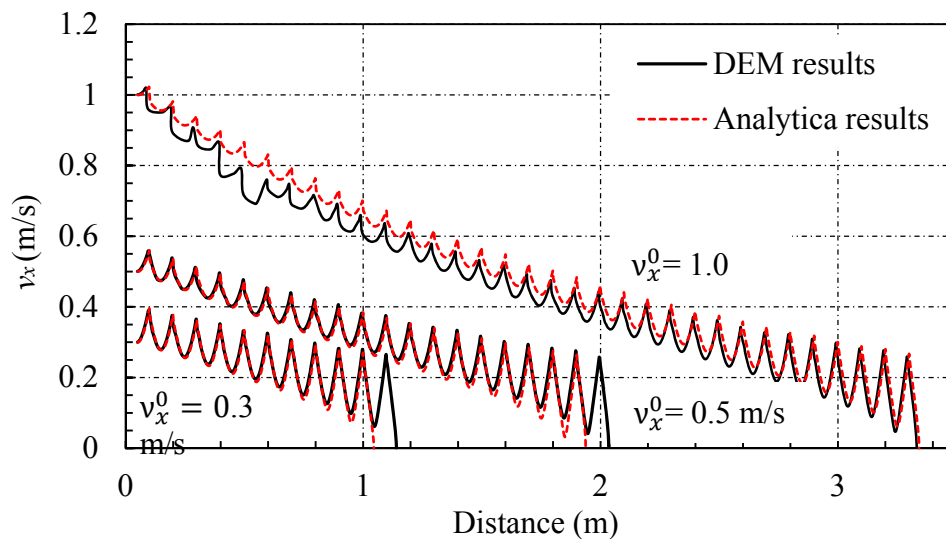


**Figure 5-7.** The results of the horizontal velocity versus the distance for the disc assigned an initial velocity to travel on a bumpy surface.

In Figure 5-7, all three curves exhibit a 'saw-tooth' mode, which is caused by the rugged surface: accelerating on down-slopes and decelerating on up-slopes. The horizontal velocity, however, goes down at the end of the travel, as a result of energy loss at collisions. Excellent agreement is attained between the DEM results and the analytical solutions across all of the three velocities. Both curves exhibit agreed amplitudes, frequencies, gradient and the end distances. This suggests that the DEM simulation can satisfactorily capture the

trajectory of the object moving under various velocities, validating the capability of the DEM model to predict the loss of kinetic energy. In both of the numerical and analytical scenarios, the dissipation of energy is attributed to the asperity collision along the base surface. At each collision, the velocity reduces at a gradient of 0.013 m/s per disc or 0.25 m/s per meter. It is noted that the numerical predictions deviate from the exact results at the early stage of travel if increase from 0.5 to 1.0 m/s. The possible cause arises from the velocity change occurred at each of the collisions where the disc travels at relatively high velocity. In addition, as the velocity increases, the moving disc takes a longer time to complete the move of bouncing, leading to a larger change in the next collision position and collision angle.

## 5.4    Simulation Results

The validated DEM model is used to implement a parametric study. The study is focused on the travel mode of the disc of interest where important material properties and surface asperity characteristics change. The properties examined include the material damping, collision angle and irregular asperity surface. In addition, the energy transformation associated with the disc travel in each of the simulation cases is examined.

**5.4.1    Damping ratio**

Damping influences the energy loss at collision. To gain an insight into the influence, the DEM model is applied to the discs assigned with two different damping ratios, $\beta_n = 0.1$ and 0.9, respectively. The moving disc is assigned with an initial velocity of 0.5 m/s. The rest conditions remain the same as the model used in the validation section. The simulation results are provided in Figure 5-8. As shown in Figure 5-8 (a) and (c), the velocity vs. distance curves agree between the two cases $\beta_n = 0.1$ and 0.9. In either case, the moving disc travels through 19 discs and stops between the 19th and 20th base discs. This agreement suggests that the damping ratio less likely influences the overall energy dissipation of the moving disc, where the other conditions remain the same. However, the energy dissipation at each collision can be different, as shown in Figure 5-8 (b) and (d). These two figures present the velocity vs. distance relationship for the disc travelling through the first three base discs. Where the damping ratio is relatively small (Figure 5-8(b), two collisions as represented by the corresponding vertical short lines and one bounce as of the short horizontal short line occur. Where the damping ratio increases as in Figure 5-8(d), one collision (and no bounce) as of the short vertical line occurs. The moving disc is in the move of sliding for the rest part of the travel on the same base disc. For both trajectories with different damping coefficients, the moving object eventually loses the normal velocity when it contacts the base asperity. For example, in Figure 5-7, the moving object finally slides at the surface of base disc $j+1$, no matter how many collisions it has, and the only change to it is its normal velocity. This explains that the damping coefficient does not affect

the actual trajectory of movement on the surface, but energy dissipation is greatly influenced in a single collision (Figure 5-8 (b) and (d)).
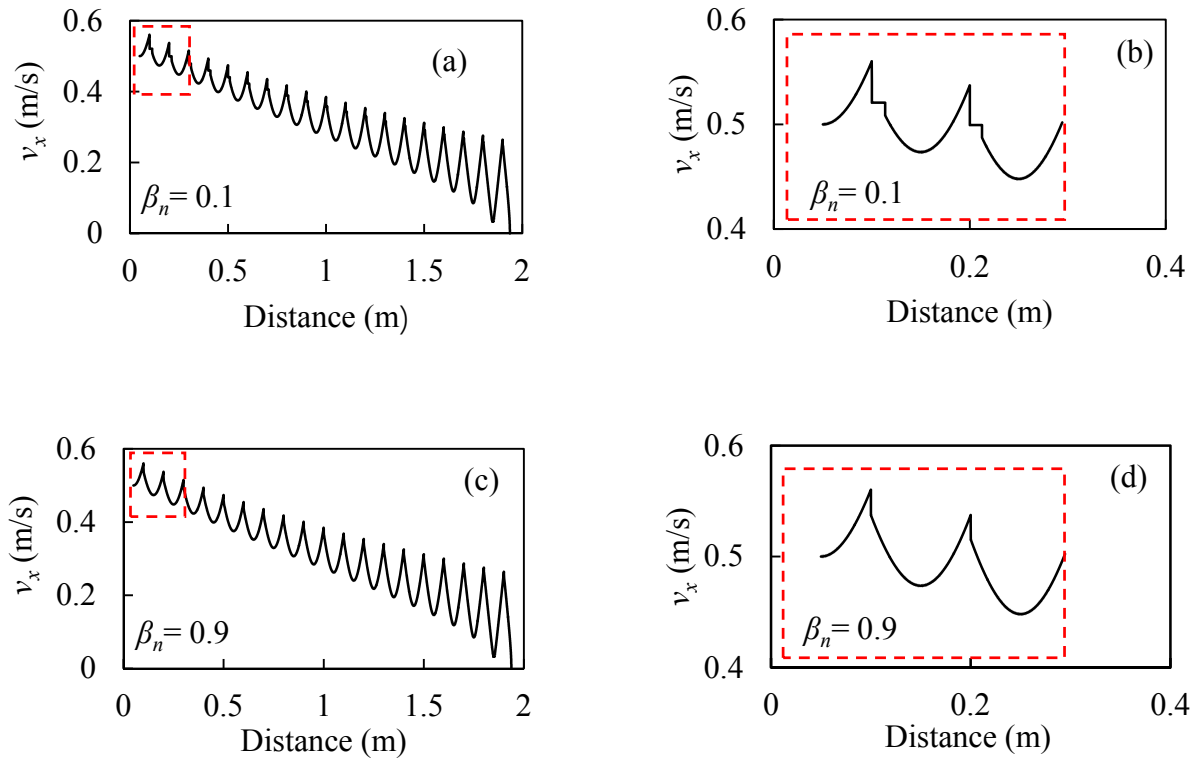


**Figure 5-8.** Horizontal velocity vs. distance for the disc traveling on asperity surface under different damping conditions: (a) complete travel for damping $\beta_n$= 0.1; (b) travel through the first 3 discs for $\beta_n$= 0.1;(c) complete travel for $\beta_n$= 0.9; (d) travel through the first 3 discs for $\beta_n$= 0.9.

### 5.4.2    Loss of energy at different damping conditions

To gain a further insight into the effect of damping on the travel mode of the disc, energy dissipation developed in different damping conditions is examined. The DEM model is applied to asperity surface assigned with a total of six different damping ratios $\beta_n$ = 0.1, 0.2, 0.3, 0.4, 0.5, and 0.9. The initial velocity

of the disc is 0.5 m/s, whereas the rest conditions remain the same as in the validation study. In order to quantify the loss of energy at each asperity contact, define the following equation:

$$\Delta E_{\beta,j} = -(E_{m,j} - E_{m,j-1}) \tag{5.39}$$

where $\Delta E_{\beta,j}$ is the energy dissipated at the base disc $j$; $E_{m,j}$ and $E_{m,j-1}$ are the system mechanical energy measured when the moving disc is in contact with base disc $j$ and $j-1$, respectively. The mechanical energy of the system can be calculated as:

$$E_m = E_k + E_s + U \tag{5.40}$$

where $E_k$, $E_s$ and $U$ are the kinetic energy, strain energy at contact, and gravity potential, respectively, and are calculated by the program. The gravity potential takes the initial elevation as the reference. Energy dissipation at the first collision between the moving disc and a new substrate asperity is of particular interest, because it denotes the primary collision while the remaining bounces are categorized as secondary collisions.

The relationships of energy loss at each primary collision versus the distance for the discs assigned with different damping ratios are provided in Figure 5-9. In all cases, the energy dissipation rate (i.e., the curve gradient) decreases with the distance. This is because the slower the particle is moving, the less the kinetic energy is dissipated. However, the proportion of energy dissipation is quite different between $\beta_n = 0.1$ and 0.9 in each collision. With a lower damping coefficient ($\beta_n = 0.1$), multiple collisions are identified at each base substrate, and the energy loss in the primary collision is only a proportion of the total energy (the solid line in Figure 5-9). In comparison, when $\beta_n$ increases to 0.9, the loss of primary energy is nearly equal to the loss of total

energy. Despite the variation in energy dissipation in primary collisions with different damping coefficients, the total energy loss is similar in all cases. As explained in the model development section, the total energy loss at each base substrate is dependent on the normal velocity when the moving disc first contacts a new substrate. Figure 5-9 also suggests that asperity-induced energy loss is velocity-dependent, which results in viscous behaviour.
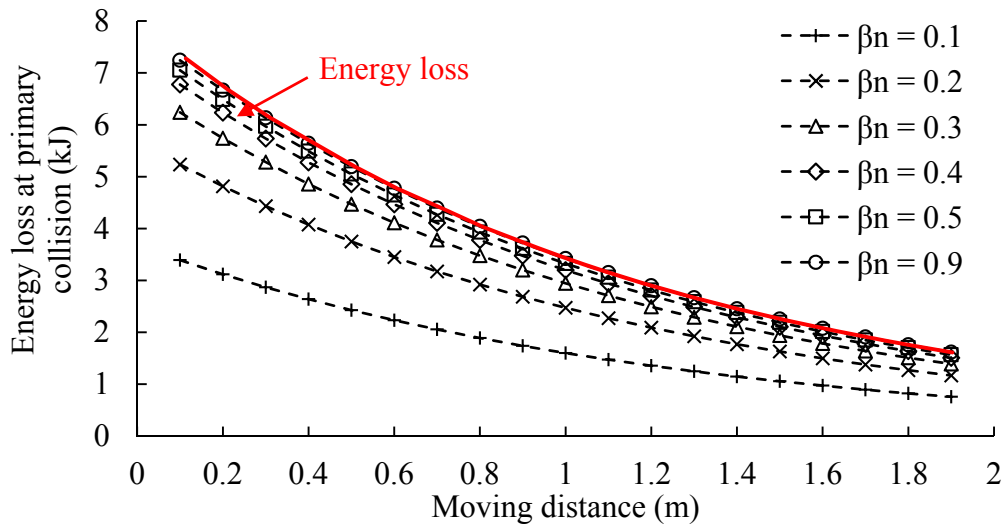


**Figure 5-9.** Energy Loss versus distance for discs assigned with different damping ratios.

### 5.4.3    Energy transformation

This section further examines the energy transformation occurred when the disc moves on the asperity surface. The total energy of the system $E_t$ contains two parts: the mechanical energy $E_m$ and dashpot energy $E_\beta$. The relationship is expressed as:

$$E_t = E_m + E_\beta \tag{5.41}$$

Apply the above relationship to the case of $\beta_n = 0.9$ and $=1.0$ m/s. The total energy and the energy components versus the distance are plotted in Figure 5-10. At the initial position, the dashpot energy and strain energy are zero. Since the moving disc is placed at the top of the base asperity, the sum of the gravity potential and kinetic energy is in the peak value. With an increase in the moving distance, a portion of the kinetic energy and gravity potential transforms to the strain energy, while the other part dissipate at collisions, in the form of heat and sound. It is clear that the loss of kinetic energy is equal to the increase of dashpot energy, because the total energy is constant through the whole process. Where the horizontal velocity decreases to a small value to slide over the last disc, the moving disc bounces, back and forth, in the space of the last two base discs until the kinetic energy dissipates to zero. Figure 5-10 also shows the contribution of contact overlap to the energy transformation, as captured by strain energy $E_s$. When the velocity reduces at the later stage of travel, the influence of contact overlap becomes less significant. The strain energy is nearly zero after the moving disc travels to 0.5 m.
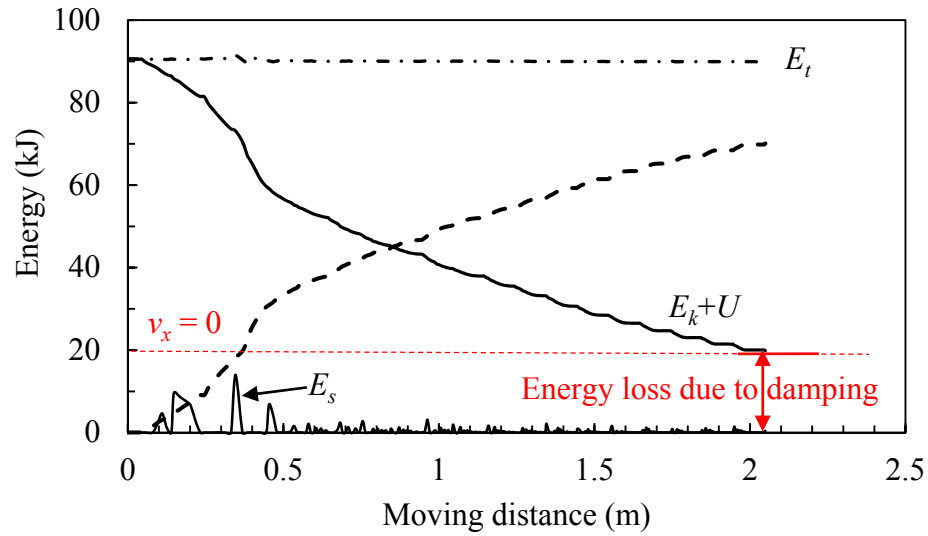
**Figure 5-10**. Energy transformation and dissipation versus travel distance for the disc travelling on the asperity surface.

### 5.4.4    Surface asperity gap

The previous sections confirm that surface asperity can influence the trajectory of the moving object. According to Greenwood and Williamson (1966), however, the bumpy surface can be described as a collection of different asperities (i.e. varying amplitudes). It is worth gaining an insight into the choices of surface asperity and examining how the different asperity characteristics influence to the travel of the disc. For example, it is still not clear about the relationship between the asperity amplitude parameters and energy dissipation, such as whether it is linearly related to energy loss or not. In this section, the asperity properties, including the average asperity and asperity variance, are evaluated against energy loss.

There are a number of different methods that can be used to constitute the roughness degrees of the substrate. Gadelmawla et al (2002) suggested

using the asperity amplitude parameters. Specifically, one of the basic properties used to describe a rough surface is $R_a$, which is the mathematical average of the absolute values of the profile height deviation from the mean line, recorded with the elevation length. This method is complicated and subject to the determination of the mean line. As a further step to the approach illustrated on Figure 5-1, a simplified approach is developed. The concept is to constitute the surface asperity using a set of discs with the same radius $\bar{r}$ which are spaced per $\eta \times \bar{r}$ where $\eta$ is the gap coefficient. The radius $\bar{r}$ ranges from 0.04 to 0.07 m, and $\eta$ from 0 to 1. The model developed based on the disc gaps is illustrated in Figure 5-11. The average asperity per distance, $\bar{y}$, is expressed as:

$$\bar{y} = \frac{\int_0^{\bar{r} \times (1+0.5\eta)} y \, dy}{\bar{r} \times (1+0.5\eta)}, \quad y \in \left[0, \bar{r} \times (1+0.5\eta)\right] \tag{5.42}$$

The variance of the asperity is expressed as:

$$\text{Var}(y) = \frac{\int_0^{\bar{r} \times (1+0.5\eta)} (y - \bar{y})^2 \, dy}{\bar{r} \times (1+0.5\eta)}, \quad y \in \left[0, \bar{r} \times (1+0.5\eta)\right] \tag{5.43}$$
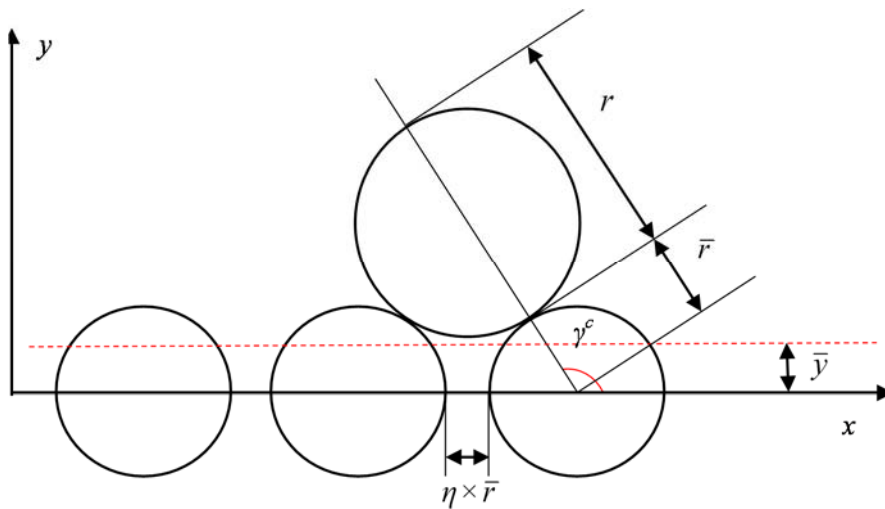


**Figure 5-11**. The asperity model developed based on gap coefficient.

Simulations were performed based on the model shown in Figure 5-11. The simulations focus on the disc travel distance versus the asperity characteristics, including the average asperity elevation and asperity variance. These characteristics are examined by accounting for the base disc radii, disc gaps and asperity average elevation. The rest of simulation conditions remain the same as in the validation section. A total of 44 simulations were performed to collect the disc travel distance information and were plotted against surface average height or height variance. The simulation results are provided in Figure 5-12 and Figure 5-13 respectively.
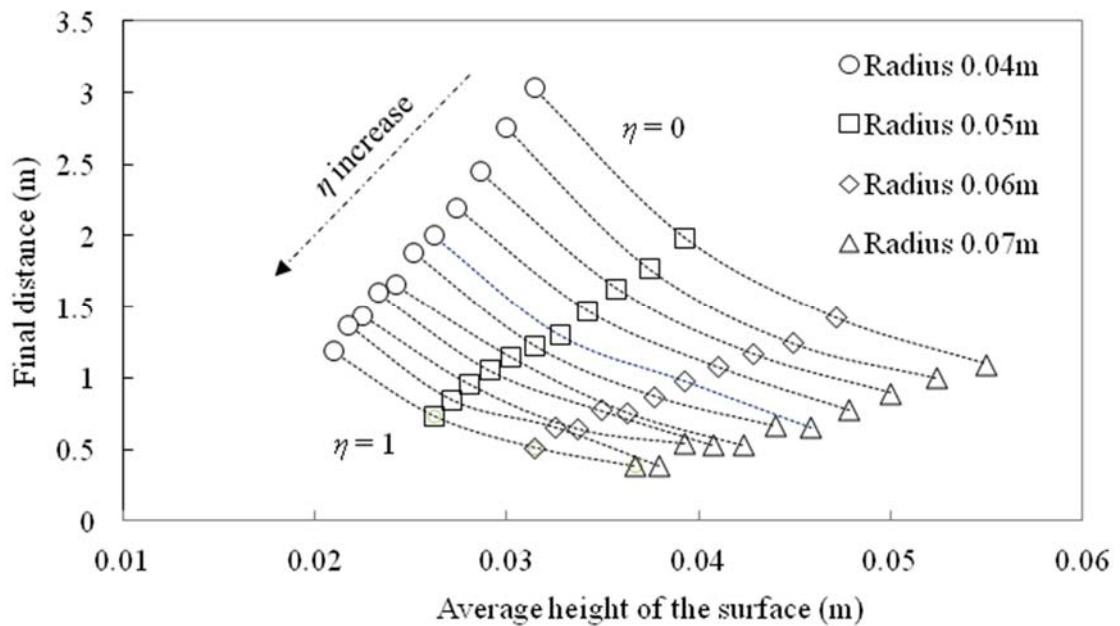


**Figure 5-12**. The relationship between the final distance and surface average height.
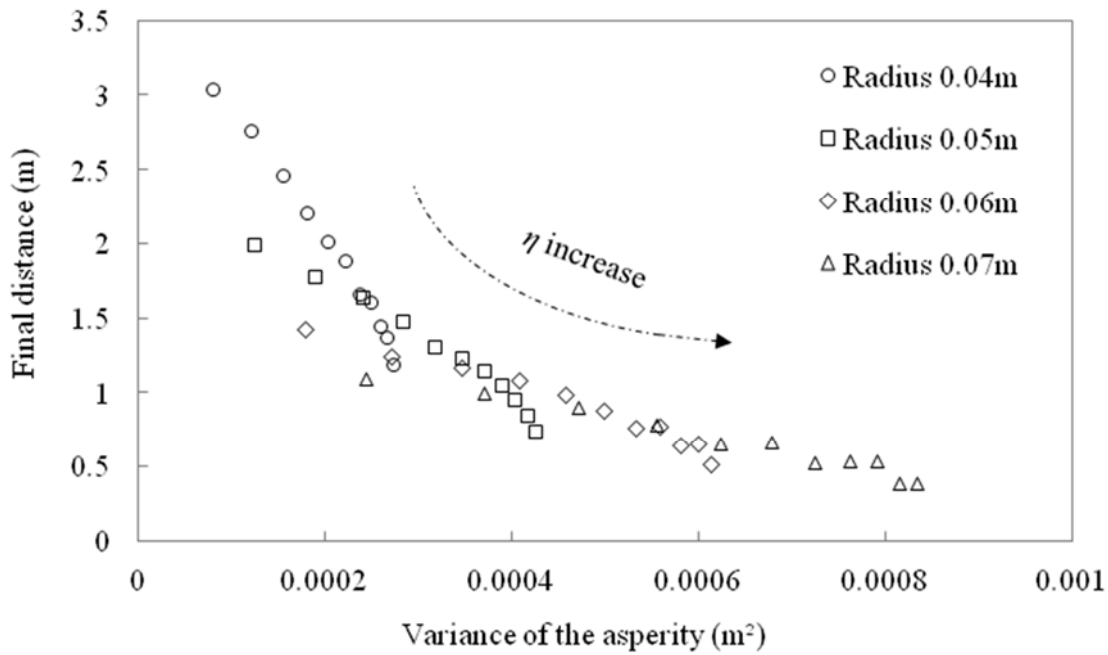
**Figure 5-13**. The relationship between the final distance and variance of asperity.

In Figure 5-12, the final displacement of the moving disc is plotted per the base disc radius $\bar{r}$ and gap coefficient $\eta$. With the same gap coefficient, the asperity average height increases with the disc radius, resulting in a decrease of in the final displacement. When the disc radius remains constant, an increase in the gap ratio decreases the substrate height, which in turn decreases the final displacement. However, the final displacement is independent on the average height of the surface substrate, because the actual maximum displacement occurs at an intermediate surface height (e.g., the case with $\bar{r} = 0.04$ m and $\eta = 0$). This indicates that the average surface height is not linearly related to the trajectory of the disc. In comparison, the surface-height variance provides better quantification of final displacement. It can be identified that the lower the asperity-height variance, the farther the object can travel. Technically, this

176

property describes how rough or bumpy the surface is. However, there are still some slight overlaps between different groups of radii, and these points inside the overlap area produce a reverse trend against the general relationship. Hence, it is necessary to seek additional description of surface roughness which is discussed in the following section.

### 5.4.5    Collision angle

In this section, the collision angle $\gamma^c$ is used to characterise surface roughness. At each collision, the collision angle influences the loss of the normal velocity of the moving disc as shown in Figure 5-14. The collision angle $\gamma^c$ is different from the contact angle $\gamma$ . The collision angle $\gamma^c$ is defined as the contacting angle when the moving disc hits a new base disc and, as shown in Figure 5-11, is calculated as:

$$\gamma^c = \arccos\frac{\bar{r}\times\left(1+0.5\eta\right)}{r+\bar{r}}, \ \gamma^c \in \left[\frac{\pi}{2},\pi\right] \qquad (5.44)$$

It should be noted that there may be other collisions occurred between the moving disc and the base disc of interest. However, due to a relatively low horizontal velocity, the collision must happen in the middle of the two base discs where most of the kinetic energy is dissipated, as shown in Figure 5-11.

The final displacements were plotted against the collision angle $\gamma^c$ as shown in Figure 5-14. A monotonic relationship is observed: the smaller the collision angle is, the shorter the distance the disc can move on the surface. The final displacement is entirely dependent on the collision angle. From this perspective, the collision angle is a parameter governing the surface roughness.
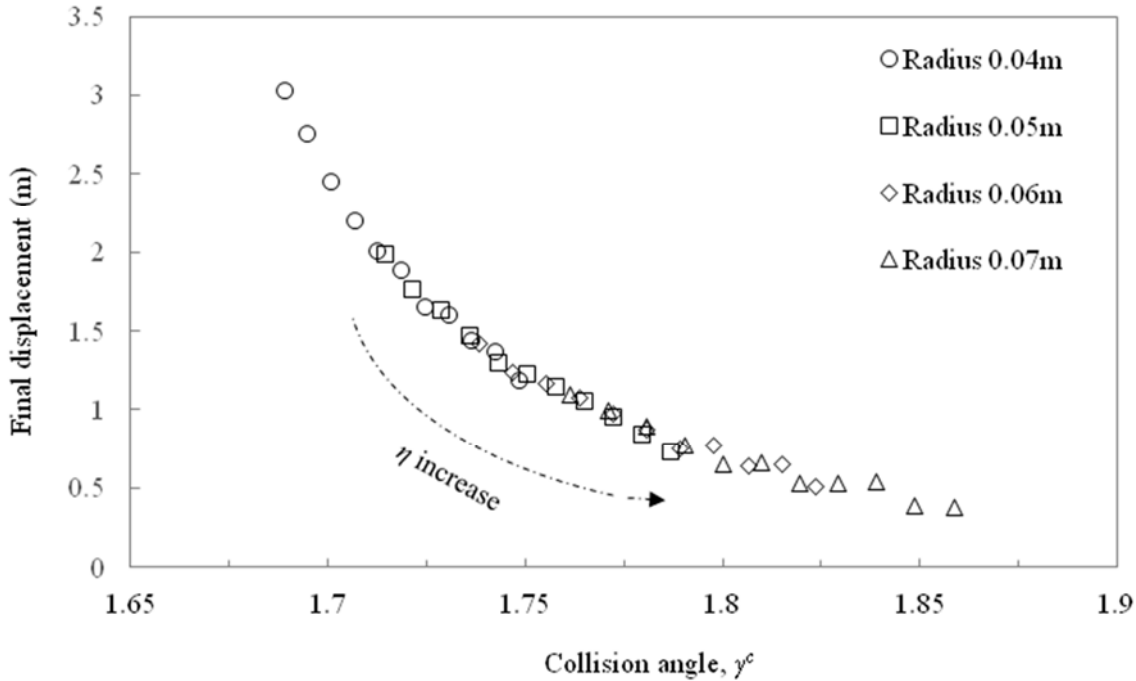
**Figure 5-14.** The relationship between final displacement and collision angle.

### 5.4.6    Mixed asperities

An even surface asperity facilitates model development and simulation. However, as per Persson et al. (2004), the height of the surface asperities usually follows a normal distribution. To account for the mixed asperities, the substrate is constituted with a group of discs of different radius $r_j$ and gap coefficients $\eta$. The schematic is shown in Figure 5-15. The two governing parameters $r_j$ and $\eta$ are assumed to be independent, and respectively follow a normal distribution.
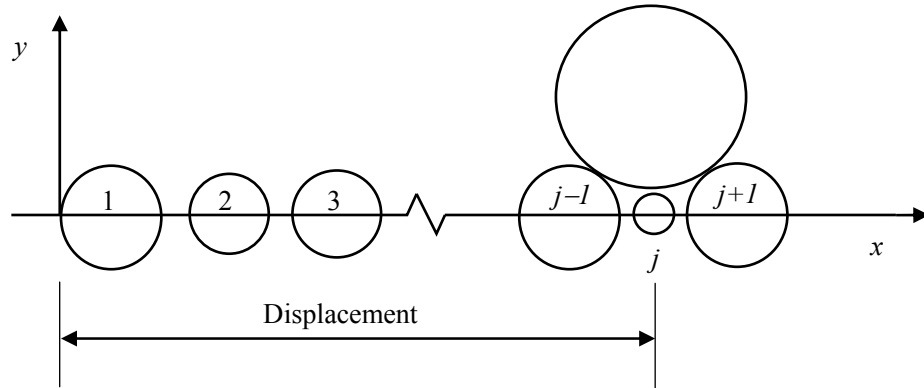
**Figure 5-15**. The model developed based on mixed asperities.

Similar to the previous simulations, the moving disc is first placed at the top of base disc $i$, assigned a velocity of 0.5 m/s. After a number of collisions, the kinetic energy is sufficiently damped and the disc rests at a distance. Due to the mixed asperity of the substrate, the final distance varies significantly, but, due to the existence of varying collision angles, the distance is relatively less than that obtained in even asperity case. In order to measure the actual collision angle, the disc radii and gaps are controlled to allow the moving object to travel over about 20 base discs. The normal distribution used for the base disc radii and the base gap is shown in Figure 5-16 and Figure 5-17 respectively.
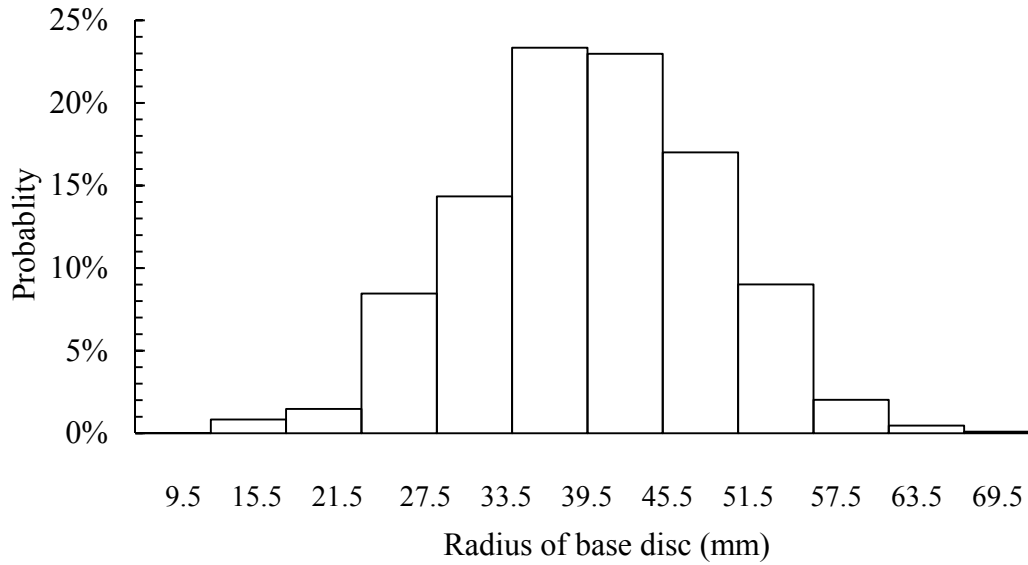
**Figure 5-16.** Normal distribution of base disc radii.
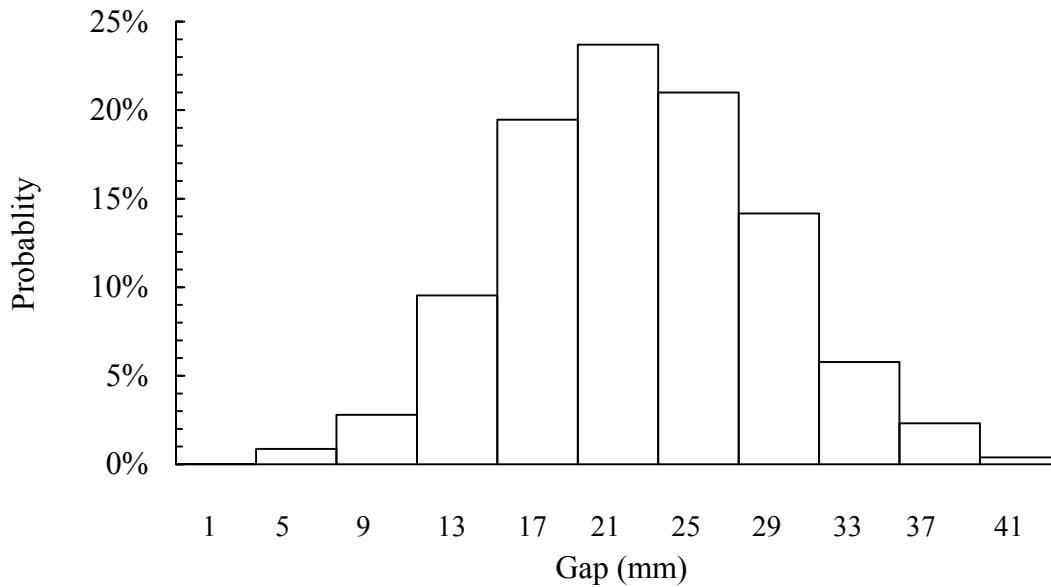


**Figure 5-17.** Normal distribution of base disc gaps

Additional efforts were made to gauge the actual collision angle. In the case of even asperity surface, where the collision angle is estimated, the actual collision angle cannot be determined before the disc rests. For example, Figure 5-15 shows that the moving disc does not contact the base disc *j*. Therefore, the

collision angle between the moving disc and the substrate $j$ does not have physical meaning. Also, due to the complication of the substrate shape, the moving object may exhibit some significant jumps depending on its initial velocity. For these reasons, the actual trajectory of the moving disc is gauged to attain the actual collision angles.

In order to validate the surface properties of energy dissipation for an actual bumpy surface, a sufficient number of different surfaces need to be generated. This surface of randomly distributed asperity can be generated in PFC2D by using a random number, called 'seed', which controls particle generation. Changing this value can generate different assemblies. In this way, a large sample of different rough surfaces can be made. The relationship between the collision angle and dissipated energy is presented in Figure 5-18. The dissipated energy occurred at the $15^{th}$ collision with respect to the average actual collision angle is calculated. The moving disc can slide more than 20 particles, but the number of the effective collisions is less, as some base discs, e.g., the $j$th particle as shown in Figure 5-15, are of low elevation and do not contact the moving object.
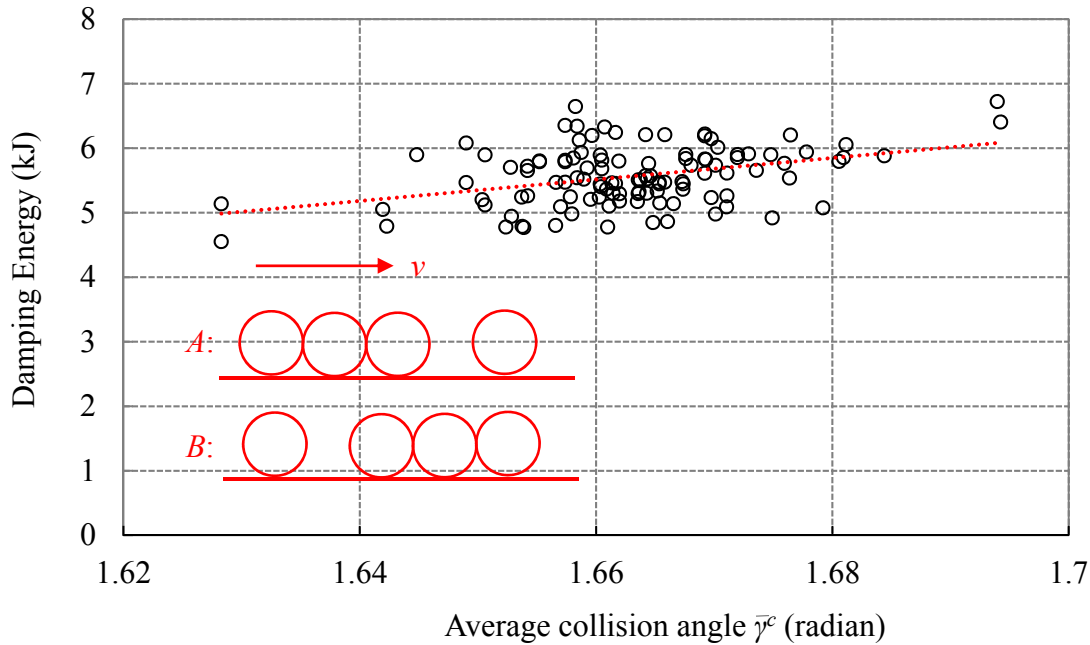
**Figure 5-18**. The relationship between the dissipated energy at the 15<sup>th</sup>
collision and the average actual collision angle.

In Figure 5-18, the average collision angle $\bar{\gamma}^c$ is calculated as the sum of the collision angles divided by the number of collisions. As can be seen, the dissipated energy increases with the decrease in the average collision angle, which generates a linear distribution. However, considering the individual scatter points in the relationship, even when the average collision angle is similar, the results may vary. This is because the surface substrate distribution influences significantly on energy dissipation. For example, surfaces *A* and *B* may exhibit identical substrate properties, such as the same collision angle, average height and height variance, but if the upslopes and downslopes occur in different sequences, the kinetic energy will dissipate in different modes. With respect to the energy dissipation regime, the disc travelling on the mixed asperity surface is in a different regime from the one on an even surface asperity.

On the even asperity surface, the kinetic energy of the moving disc is gradually damped at each collision, while on the mixed asperity surface the disc experiences a sudden stop where the moving disc hits into a relatively large gap on the surface. The influence of the maximum collision angle on the surface is evaluated in the next section.

### 5.4.7 Determination of the maximum collision angle on a rough surface

Theoretically, the moving disc can rest at any trough on a bumpy surface, but the simulations suggest that the moving disc often rests at the trough where the maximum collision angle occurs. This section aims to investigate the relationship between the distance the moving disc is at rest and the maximum collision angle.

Define the relative distance where the maximum collision angle occurs:

$$L_r = \frac{S_{\gamma,\max}}{S_{stop}}, \ L_r \in [0,1] \tag{5.45}$$

where $S_{\gamma,max}$ is the position at the maximum collision angle, $S_{stop}$ is the total moving distance. A total of 250 different asperity surfaces were tested, and the probability of the distance where the moving disc rests is plotted in Figure 5-19.
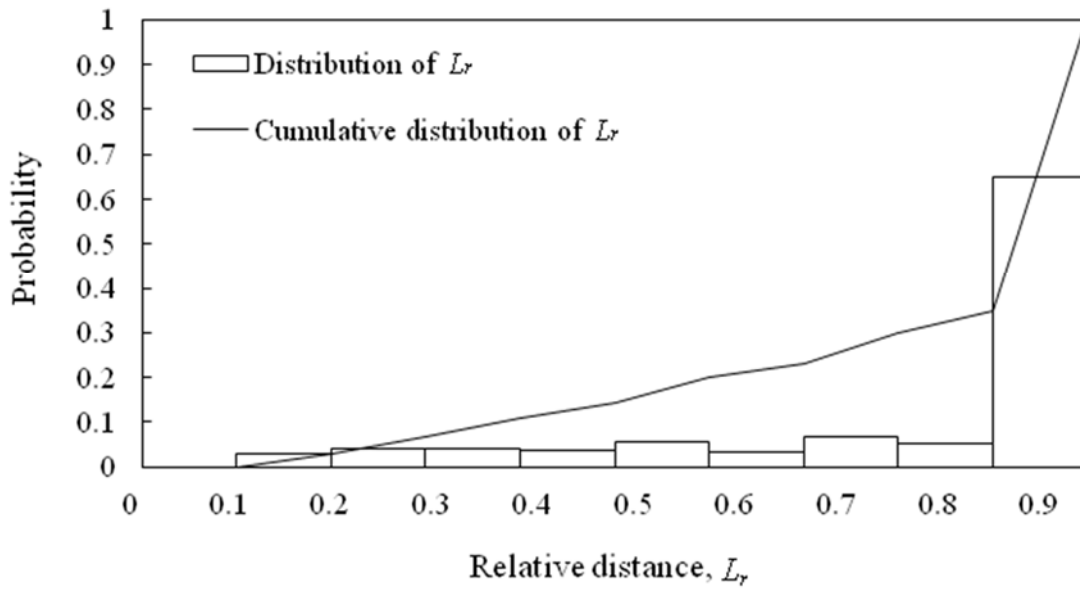
**Figure 5-19**. The relationship between the probability of the disc being trapped and normalised distance $L_r$.

On a mixed asperity surface, the moving disc exhibits the actual collision angle ranging between 100 to 105 degrees. Figure 5-19 shows that the farther distance the maximum collision angle occurs, the more likely the moving disc is at rest as a result. The probability is 60% or greater than the moving disc is at rest at the maximum collision angle, suggesting a sudden stop regime. Generally, when the disc hits into a relatively large gap, a higher kinetic energy is required for the disc to slide over the gap. This energy is the threshold that determines whether the moving disc can slide over the asperity gap or not. If the particle collides at the maximum angle at an earlier stage, a good number of kinetic energy remains which drives the disc to travel farther. If the maximum collision angle occurs at a later stage, the disc is of low energy and less kinetic to slide over the base disc with a relatively greater collision angle.

**5.4.8     Asperity and sub-asperity mixed surface**

In the previous sections, the study is performed on the moving disc travelling on an asperity surface. However, on a real surface, there are sub-asperities affixed over the asperity surface which may influence the trajectory and energy loss of the moving disc. To take into account the influence of the micro-asperities at the surface, the following simulations were performed. To constitute a surface with primary and sub-asperities, a clump of discs is used. The clump models are provided in Figure 5-20. Clump *A* is spherical. Clumps *B* and *C* exhibit different sub-asperities. The sub-asperities are formed by affixing a set of discs together, each disc sharing a section of the circular perimeter. If travelling on such a surface, the moving disc is subjected to more collisions than on the asperity surface and the additional collisions are expected to cause greater energy loss in a shorter distance. Similar asperity and sub-asperity mixed surface can occur to the moving disc, which prompts the importance of simulations.
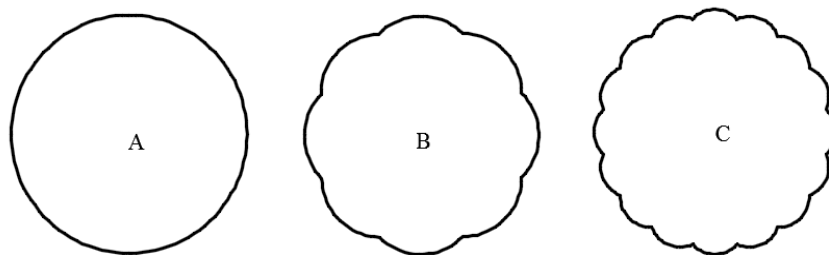


**Figure 5-20**. Clumps used to represent primary and secondary asperities.

Clumps *A*, *B* and *C* are paired to reproduce the moving disc and base discs. Use number '1' to denote the moving disc and number '2' to the base discs. For example, the combination *A*1*A*2 represents the model of the spherical

disc moving on the spherical base discs. In simulations, four combinations were designed: *A*1*A*2, *A*1*B*2, *B*1*B*2 and *C*1*B*2, in the order of increasing number of asperities. The moving disc of the last three models was initially placed in the trough of interest to stand still. The properties of the clump object, such as the damping coefficient, density, volume and contact stiffness, remain the same as in the validation case. An initial horizontal velocity of 0.5 m/s is assigned to the moving disc. Note that, for a clump of discs, the discs collide eccentrically, leading to a residual rolling velocity. In the simulation, to create the same condition, rolling was restricted for all cases. The simulation results are provided in Figure 5-21. The figure shows the relationship between the horizontal velocity and moving distance captured for the four models.
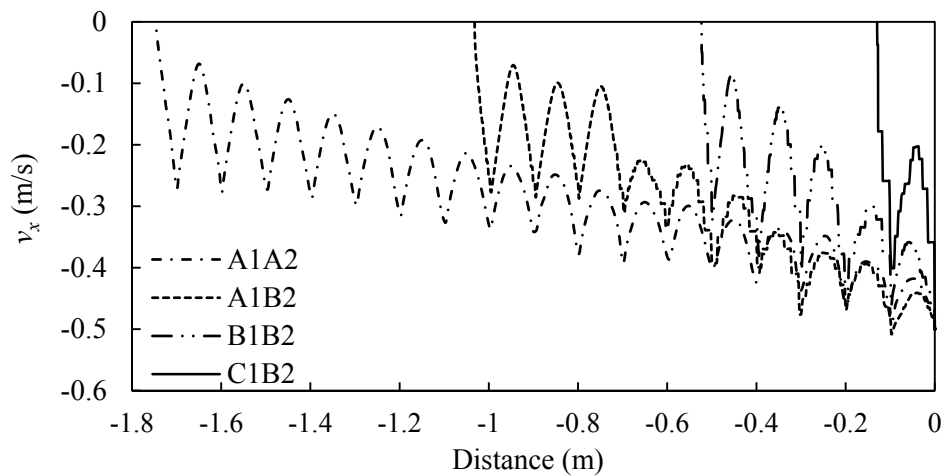


**Figure 5-21**. The relationship between horizontal velocity and distance obtained under different asperity and sub-asperity conditions.

In Figure 5-21, when the surface asperity becomes denser, the moving disc travels a shorter distance. For example, model *C*1*B*2 travels around one-tenth of the distance attained by combination model *A*1*A*2. It suggests that the sub-asperity exhibits a significant effect on the final displacement. In this circumstance, at the surface of a primary asperity, the micro-asperities increase

the number of effective collisions. Greater energy is dissipated by model $C1B2$ at the same distance, compared to the other models with fewer sub-asperities. In addition, the sub-asperities on the base discs cause a lower collision angle and thus dissipate more energy. Note that, for model $A1A2$, initiating the moving object from the asperity trough reproduces the relationship as with initiating the disc from the asperity peak, as shown in Figure 5-22. The simulation results suggest that the denser the contact asperity is, the greater energy is dissipated at the same distance.
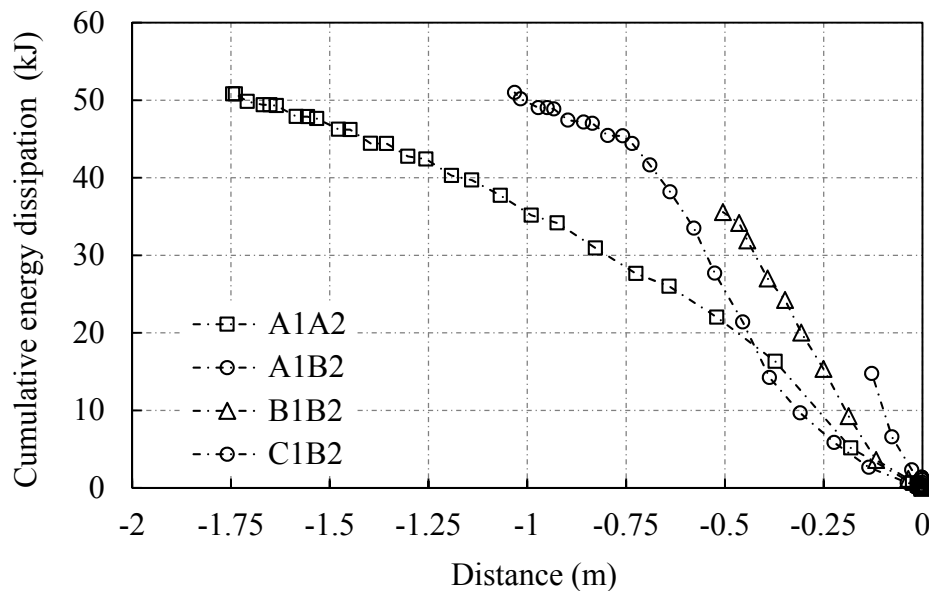


**Figure 5-22**. The relationship between cumulative dissipation and distance under different combinations.

The simulations performed in this study suggest that surface asperity-induced friction can be considered as a larger number of individual collisions, and that these collisions cause the dissipation of kinetic energy. One of the major differences between the two conceptions is that the collision-induced energy loss is velocity-dependent, as shown in Figure 5-7, while the friction conception assumes that the friction force is independent on the velocity of the

moving object. The former conception agrees with recent studies performed at an atomic level (Valance and Bideau, 1998; Gnecco et al, 2000). In these two studies, the friction force experiences velocity-dependent viscous behaviour. Research on atomic friction (Gnecco et al., 2000; Fujisawa et al., 1995) also identifies a sawtooth friction behaviour at the nanoscale, which is in further support of the current simulation results. This means that the surface of interest contains a large number of asperities and sub-asperities, and that the collisions at individual asperities and sub-asperities are the cause of friction attained at the macroscale.

Where the sub-asperity surface occurs, the moving disc rotates due to the eccentric force acting on the disc. In this section, the rotation of the moving disc is examined. Design three models: *A*1*B*2, *B*1*B*2 and *C*1*B*2, where the moving disc is assigned with the clumps *A*, *B* and *C* respectively, and the substrate surface uses clump *B* throughout. The relationship between the rolling velocity and the sliding distance is plotted in Figure 5-23. Define the anti-clockwise rolling to be positive. The moving disc in model *C*1*B*2 travels a longer distance than the distance obtained by model *B*1*B*2, which is different from the condition if rolling was restricted. As shown in Figure 5-21, the moving disc in model *B*1*B*2 travels much farther than the disc in model *C*1*B*2 does. This can be explained from the perspective of a collision impact. For model *B*1*B*2, the collision sometimes induces a negative angular velocity, and rotation at this direction prohibits its movement at the surface. The translational velocity at the contact point is consequently reduced, and the moving object is finally at rest.
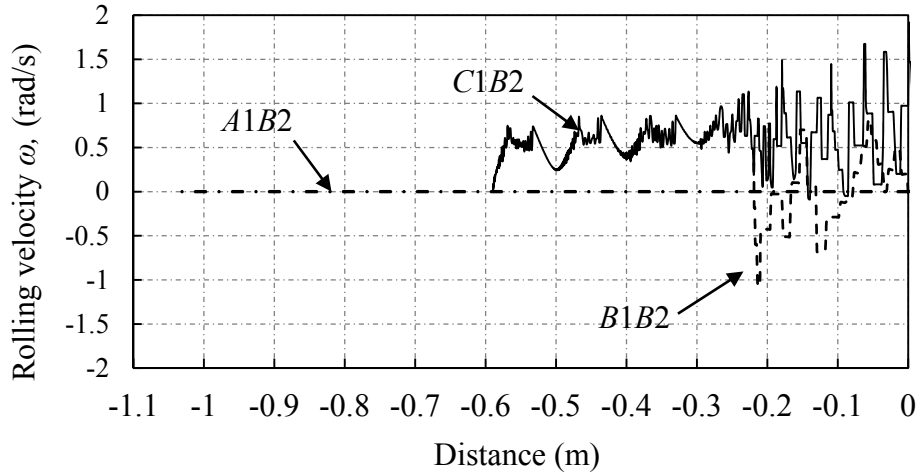
**Figure 5-23**. The influence of rolling behaviour on the relationship between angular velocity and distance.

## 5.5 Conclusions

This paper presents a study on collision-induced energy dissipation of an object moving on a bumpy surface. An analytical model based on a single-contact collision model is developed. The model is able to reproduce the trajectory of the moving disc. The analytical model is established and applied to validate a DEM model. The DEM model is applied to examine the effects of important surface asperity properties on the kinetic behaviour of the moving object. The properties include the material damping, average asperity height, height variance, gaps, collision angle and sub-asperities. The energy loss associated with the property changes is also examined. The simulations draw the following conclusions.

The moving object contacts the new asperity at several bounces. Afterwards, the disc is in the move of sliding on the same asperity. The first collision between the moving disc and the base disc consumes most of the

189

kinetic energy, while energy dissipated at other bounces is negligible. The actual collision angle reflects a monotonic relationship with maximum travelling distance; and the collision angle is an important parameter used to describe surface roughness when compared to other geometric properties, such as the average asperity height and surface-height variance.

The surface sub-asperities accelerate the loss of kinetic energy. If the sub-asperities are dense enough, it is likely to dissipate a high level of kinetic energy. Rolling induced by the asperity collision can restrict the motion of the object because less translational velocity remains. The energy dissipation of the moving disc is positively proportional to the velocity of the moving disc. The asperity-induced loss of kinetic energy reflects the effects of collisions and gains an insight into the development of surface friction.

## 5.6    Acknowledgements

## 5.7    Notations

$D_j^t$    relative distance between the moving disc and base disc at time step $t$

$E_m$        system mechanical energy

| | |
|---|---|
| $E_t$ | total energy |
| $E_k$ | kinetic energy |
| $E_\beta$ | dashpot energy loss |
| $F_n^d$, $F_s^d$ | normal and dashpot force |
| $F_n^h$, $F_s^h$ | nonlinear normal and shear contact force |
| $g$ | gravity acceleration |
| $k_n$ | normal stiffness |
| $L_r$ | relative distance of the collision angle |
| $m_c$ | mass of the system |
| $m_1$, $m_2$ | mass of the bodies 1 and 2 |
| $r$ | radius of the moving disc |
| $r_j$ | radius of base disc $j$ |
| $\bar{r}$ | average radius of the base disc |
| $S_{\gamma,\max}$ | distance where the maximum collision angle occurs |
| $S_{\text{stop}}$ | total moving distance |
| $t$ | time step |
| $\Delta t,$ | time step increment |
| $\Delta t_0$ | time step increment at bounce |
| $v$ | velocity |
| $v_n$ | normal velocity before collision |
| $v_s$ | tangential velocity before collision |

| | |
|---|---|
| $v_{n,r}$ | normal velocity after collision |
| $x^t, y^t$ | centre position of the moving disc at time step $t$ |
| $U$ | gravity potential |
| $\alpha_n$ | restitution coefficient |
| $\beta_n$ | damping ratio |
| $\gamma$ | contact angle |
| $\gamma^c$ | collision angle |
| $\bar{\gamma}^c$ | average collision angle |
| $\dot{\delta}_n$ | relative normal translational velocity |
| $\omega$ | angular velocity |
| $\theta$ | rotation angle |
| $\eta$ | gap ratio |

## 5.8    References:

ANASTASIADIS, A., SENETAKIS, K., PITILAKIS, K., GARGALA, C. & KARAKASI, I. 2012. Dynamic behavior of sand/rubber mixtures. Part I: Effect of rubber content and duration of confinement on small-strain shear modulus and damping ratio. *Journal of ASTM International,* 9**,** 1-19.

BATROUNI, G., DIPPEL, S. & SAMSON, L. 1996. Stochastic model for the motion of a particle on an inclined rough plane and the onset of viscous friction. *Physical Review E,* 53**,** 6496.

BECKER, V., SCHWAGER, T. & P SCHEL, T. 2008. Coefficient of tangential restitution for the linear dashpot model. *Physical Review E,* 77**,** 011304.

BUCKLEY, D. H. 1981. *Surface effects in adhesion, friction, wear, and lubrication*, Elsevier.

CONSOLI, N. C., HEINECK, K. S., COOP, M. R., FONSECA, A. V. D. & FERREIRA, C. 2007. Coal bottom ash as a geomaterial: Influence of particle morphology on the behavior of granular materials. *Soils and foundations,* 47**,** 361-373.

CUNDALL, P. 1988. Computer simulations of dense sphere assemblies. *Micromechanics of granular materials*.

CUNDALL, P. A. & STRACK, O. D. 1979. A discrete numerical model for granular assemblies. *geotechnique,* 29**,** 47-65.

DAI, B. B., YANG, J. & ZHOU, C. Y. 2015. Observed effects of interparticle friction and particle size on shear behavior of granular materials. *International Journal of Geomechanics,* 16**,** 04015011.

DIPPEL, S., BATROUNI, G. & WOLF, D. 1996. Collision-induced friction in the motion of a single particle on a bumpy inclined line. *Physical Review E,* 54**,** 6845.

DOMÉNECH-CARBÓ, A., 2016. On the independence of friction and restitution: an operational approach. *Granular Matter*, *18*(1), p.9.

FUJISAWA, S., KISHI, E., SUGAWARA, Y. & MORITA, S. 1995. Atomic-scale friction observed with a two-dimensional frictional-force microscope. *Physical Review B,* 51**,** 7849.

CHANG, W.R. AND LING, F.F., 1992. Normal impact model of rough surfaces. *Journal of tribology*, *114*(3), pp.439-447

GADELMAWLA, E., KOURA, M., MAKSOUD, T., ELEWA, I. & SOLIMAN, H. 2002. Roughness parameters. *Journal of materials processing technology,* 123**,** 133-145.

GNECCO, E., BENNEWITZ, R., GYALOG, T., LOPPACHER, C., BAMMERLIN, M., MEYER, E. & G NTHERODT, H.-J. 2000. Velocity dependence of atomic friction. *Physical Review Letters,* 84**,** 1172.

GOLLIN, D., BERZI, D. AND BOWMAN, E.T., 2017. Extended kinetic theory applied to inclined granular flows: role of boundaries. *Granular Matter*, *19*(3), p.56.

GREENWOOD, J. & WILLIAMSON, J. Contact of nominally flat surfaces. Proceedings of the Royal Society of London A: Mathematical, Physical and Engineering Sciences, 1966. The Royal Society, 300-319.

HENRIQUE, C., AGUIRRE, M., CALVO, A., IPPOLITO, I., DIPPEL, S., BATROUNI, G. & BIDEAU, D. 1998. Energy dissipation and trapping of particles moving on a rough surface. *Physical Review E,* 57**,** 4743.

ITASCA. PFC2D 5.0 User Manual. Minneapolis, MN USA2017.

JENSEN, R. P., BOSSCHER, P. J., PLESHA, M. E. & EDIL, T. B. 1999. DEM simulation of granular media—structure interface: effects of surface roughness and particle shape. *International Journal for Numerical and Analytical Methods in Geomechanics,* 23**,** 531-547.

JENSEN, R. P., EDIL, T. B., BOSSCHER, P. J., PLESHA, M. E. & KAHLA, N. B. 2001. Effect of particle shape on interface behavior of DEM-simulated granular materials. *International Journal of Geomechanics,* 1**,** 1-19.

KAWAGUCHI, T., TANAKA, T. & TSUJI, Y. 1992. Numerical simulation of fluidized bed using the discrete element method (the case of spouting bed). *JSME (B),* 58**,** 79-85.

PERSSON, B., ALBOHR, O., TARTAGLINO, U., VOLOKITIN, A. & TOSATTI, E. 2004. On the nature of surface roughness with application to contact mechanics, sealing, rubber friction and adhesion. *Journal of Physics: Condensed Matter,* 17**,** R1.

SENETAKIS, K., ANASTASIADIS, A., PITILAKIS, K. & COOP, M. R. 2013. The dynamics of a pumice granular soil in dry state under isotropic resonant column testing. *Soil Dynamics and Earthquake Engineering,* 45**,** 70-79.

SVAHN, F., KASSMAN-RUDOLPHI, Å. & WALLEN, E. 2003. The influence of surface roughness on friction and wear of machine element coatings. *Wear,* 254**,** 1092-1098.

TAYEBI, N. & POLYCARPOU, A. A. 2004. Modeling the effect of skewness and kurtosis on the static friction coefficient of rough surfaces. *Tribology international,* 37**,** 491-505.

VALANCE, A. & BIDEAU, D. 1998. Dynamics of a ball bouncing on a rough inclined line. *Physical Review E,* 57**,** 1886.

YANG, J. & WEI, L. 2012. Collapse of loose sand with the addition of fines: the role of particle shape. *Géotechnique,* 62**,** 1111-1125.

ZAPPONE, B., ROSENBERG, K. J. & ISRAELACHVILI, J. 2007. Role of nanometer roughness on the adhesion and friction of a rough polymer surface and a molecularly smooth mica surface. *Tribology Letters,* 26**,** 191.

# Chapter 6
# A coupled EFG–DE method for continuum and discontinuum modelling

Can Wang[1], An Deng[2], Abbas Taheri[3]

1.  Graduate Student, School of Civil, Environmental and Mining Engineering, Univ. of Adelaide, Adelaide, SA 5005, Australia. E-mail: c.wang@adelaide.edu.au

2.  Senior Lecturer, School of Civil, Environmental and Mining Engineering, Univ. of Adelaide, Adelaide, SA 5005, Australia (corresponding author). E-mail: an.deng@adelaide.edu.au

3.  Senior Lecturer, School of Civil, Environmental and Mining Engineering, Univ. of Adelaide, Adelaide, SA 5005, Australia. E-mail: abbas.taheri@adelaide.edu.au

# Statement of Authorship

| Title of Paper | A coupled EFG-DE method for continuum and discontinuum modelling |
|---|---|
| Publication Status | ☐ Published      ☐ Accepted for Publication<br>☑ Submitted for Publication      ☐ Unpublished and Unsubmitted work written in manuscript style |
| Publication Details | Wang C, Deng A, Taheri A (2018). A coupled EFG-DE method for continuum and discontinuum modelling. *International Journal for Numerical Methods in Engineering*. |

## Principal Author

| Name of Principal Author (Candidate) | Can Wang | | |
|---|---|---|---|
| Contribution to the Paper | Undertook Literature review, performed parametric study, analytical study and numerical model analysis. | | |
| Overall percentage (%) | 75% | | |
| Certification: | This paper reports on original research I conducted during the period of my Higher Degree by Research candidature and is not subject to any obligations or contractual agreements with a third party that would constrain its inclusion in this thesis. I am the primary author of this paper. | | |
| Signature | | Date | 05/08/2018 |

## Co-Author Contributions

By signing the Statement of Authorship, each author certifies that:

    i.     the candidate's stated contribution to the publication is accurate (as detailed above);

    ii.     permission is granted for the candidate in include the publication in the thesis; and

    iii.     the sum of all co-author contributions is equal to 100% less the candidate's stated contribution.

| Name of Co-Author | An Deng | | |
|---|---|---|---|
| Contribution to the Paper | Acted as corresponding author, supervised project development and helped with paper editing. | | |
| Signature | | Date | 05/08/2018 |

| Name of Co-Author | Abbas Taheri | | |
|---|---|---|---|
| Contribution to the Paper | Supervised work development | | |
| Signature | | Date | 07/082018 |

# **Abstract**

This paper presents an algorithm to couple element free Galerkin (EFG) and discrete element (DE) methods to approximate dynamic interaction occurred between continuum and discontinuum media. The exchange of the contact force between the two domains is attained in the form of point loads acting on the domain interface using the Dirac delta function. To prevent the ill-conditioned problems, a weighted orthogonal base function is used to compute the shape functions. A penalty method is applied to meet with the essential boundary conditions. In both the EFG and DE domains, an implicit Newmark-$\beta$ time integration scheme is developed. The coupled EFG–DE method was applied to two example problems. It is shown that the EFG and DE methods work in a compatible mode as implemented by the self-developed MATLAB codes. Excellent agreement between the modelling and analytical results is attained, demonstrating the capability of the coupling method to approximate multibody, multiscale dynamic problems.

**Key words**: meshless, EFG, discrete element, coupling, dynamic

## 6.1    Introduction

Nowadays multi-domain coupling has become a tool widely employed to analyse

interactions occurred between multiple bodies where a single platform based

computation is insufficient or inaccurate to attain the goal. In engineering, one of the

most important tools is to couple continuum and discontinuum computing methods

(Potyondy and Cundall, 2004; Munjiza, 2004; Xiao and Belytschko, 2004). The

coupled methods enable material response examination at multiscale, i.e. the continuum

at macroscale and the discontinuum or granular medium at microscale. Continuum and

discontinuum modelling methods can be coupled in a number of ways. A popular

method is to combine the finite element method (FEM) and the discrete element method

(DEM) (Munjiza, 2004; Onate and Rojek, 2004; Li et al., 2015). Other numerical

combinations, such as the finite difference method (FDM) coupled with DEM, are also

widely applied in simulations of boundary problems (Potyonde and Cundall, 2004; Cai

et al., 2007; Li et al., 2015). However, there are constraints identified in respect to

combining FEM (or FDM) with DEM. One of the major constraints is the

computational costs associated with the combination where the domain of interest is of

a large scale. The time and efforts are in high demand even if the computer CPU

capacity has been noticeably faster than before (Chen et al, 2015; Zang et al., 2011;

Zheng et al., 2017). Another concern is the cost associated with the mesh-based

interpolation when using FEM or FDM (Liu and Gu, 2005). The two methods count on

predefined meshes, and therefore may require excessive iterations in time and efforts to generate satisfactory meshes when the domain of interest is large in space and complex in geometry. Furthermore, re-meshing is often required in a large deformation problem where the original meshes distort, or when low quality meshes are defined initially. A solution is to use a meshless method that can be used to couple with the discrete method.

Meshless methods were developed in the 1970s with the intention of reducing engineers' dependence on meshes. Not until the 1990s, the element-free Galerkin (EFG) method was developed by Belytschko et al. (1994) to predict fracture and crack growth. EFG method uses a global, weak form that makes it suitable for many mechanical problems, including shell analysis Krysl and Belytschko (1996), beam elastodynamics Zhang et al. (2013), wave propagation and crack development (Lu et al., 1995; Belytschko et al., 1994), electromagnetic fields Cingoski (1998), heat transfers (Singh et al., 2002; Singh et al., 2003), and fluid flow problems (Singh et al., 2004). Unlike the FEM, EFG method defines a grid of nodes which are distributed over the problem domain, and constructs the shape function based on the nodes distribution. This method adopts the moving least square (MLS) approximation to establish algebraic equations for the shape function.

In this study, the EFG method is coupled with the DE method to examine contact mechanics occurred between continuum and discontinuum domains. The discontinuum

domain comprises of an assemblage of discrete particles. The contact force from the discrete particles is simulated as a point load acting over the boundaries of the two domains. The domain shape functions are constructed based on weighted, orthogonal basis functions. This improved MLS method has proven capable of solving the ill-conditioned problem of algebraic equations. In simulating the dynamic interaction occurred between the two domains, the Newmark–β method is adopted in the Galerkin weak form, solving differential equations associated with the dynamic interaction. The penalty method is applied to satisfy the boundary conditions between the two domains. Case studies are performed to demonstrate the capacity of the coupled EFG–DE method. Although plug-ins are often coded to bridge the programing platforms, i.e., Abaqus for FEM and PFC for DEM, as in many of the past studies (Onate and Rojek, 2004; Li et al., 2015; Cai et al., 2015), the coupling in this present study is programmed based on MATLAB. Therefore this single-platform programming adds further computational efficiency.

## 6.2    Governing equation

In this section, the formulations for the EFG and DE domains in a two-dimensional (2D) space are presented. The information obtained from the two domains is exchanged at the boundaries, i.e., the resulted contact forces at each time step. The forces exchange is governed by Newton's law of motion, and the calculation of nodes and particles are

evaluated in corresponding domains. The details of the algorithm developed for the

forces change are discussed.

### 6.2.1 Continuum part

The mesh-free methods use scattered nodes to represent the problem domain and its

boundaries so that the shape functions can be formed in a local support domain.

Although the method of node selection and the choice of the domain shape are arbitrary,

a grid of nodes in a square domain, as shown in Figure 6-1, is usually used for

simplification purpose. The problem domain and the local support domain are

represented by $\Omega$ and $\Omega_I$ respectively. Based on a Gauss quadrature rule, Gauss points

can be distributed in the background cell so that the influenced nodes will be identified

in the local domain.
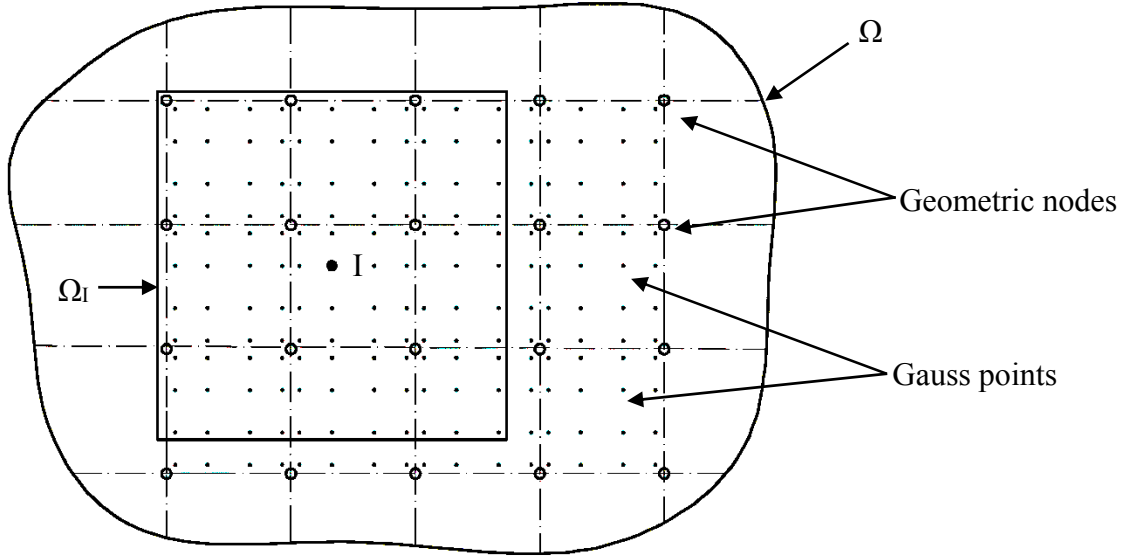
**Figure 6-1.** An illustration of the EF domain

To construct the shape functions for the continuum domain, mesh-free methods usually adopt the MLS approximations. This approach was originally used for data fitting and surface construction (Liu and Gu, 2005). Using EFG, this method implements MLS approximation to construct the shape functions based on the local domain $\Omega_I$, covering a group of pre-determined nodes. As a set of equations should be solved at the point of interest, an ill-conditioned equation system may be generated (Zhang et al., 2013; Lu et al., 1995). To address this issue, an orthogonal basis function with MLS application is used. For the displacement, the improved trial function $u^h(x)$, defined in the problem domain, is written as:

$$u^h(x) = \sum_{j}^{m} q_j(x, \bar{x}) a_j(\bar{x}) \equiv q^T(x, \bar{x}) a(\bar{x}) \tag{6.1}$$

where $u^h(x)$ is an approximation of the actual displacement $u(x)$ at the point of interest, $q_j(x, \bar{x})$ are orthogonal basis functions corresponding to the monomial basis function

$p(x)$, $a_j(\bar{x})$ are the coefficients, and $m$ is the number of elements in the monomial basis function. To simplify the coupling framework with the DEM, a linear basis function in a 2D domain is created as:

$$p^T(x) = [1, x, y], \quad m=3 \tag{6.2}$$

By using the Schmidt method [20], the orthogonal basis function $q_j(x, \bar{x})$ is obtained:

$$q_k(x, \bar{x}) = p_k(x) - \sum_{j}^{k-1} \alpha_{kj}(\bar{x}) q_j(x, \bar{x}) \tag{6.3}$$

where, $k=1$ to 3, and the coefficient $a_{kj}(\bar{x})$ is expressed as:

$$\alpha_{kj}(\bar{x}) = \frac{\sum_I^n w_I(\bar{x}) p_k(x_I) q_j(x_I, \bar{x})}{\sum_I^n w_I(\bar{x}) q_j^2(x_I, \bar{x})} \tag{6.4}$$

where the index $n$ refers to the count of nodes in the local support domain $\Omega_I$, and $w_I(\bar{x})$ is the weight function and usually based on the exponential weight function or the conical weight function Belytschko et al. (1994). In this study, the cubic spine weight function is adopted:

$$w(x - x_I) = w(r) = \begin{cases} 2/3 - 4r^2 + 4r^3, & r \le 0.5 \\ 4/3 - 4r + 4r^2 - 4/3r^4, & 0.5 < r \le 1 \\ 0, & r > 1 \end{cases} \tag{6.5}$$

In a 2D problem the weight function is given by,

$$w(x - x_I) = w(r_x)w(r_y) = w_x w_y \tag{6.6}$$

where $r_x$ and $r_y$ can be determined by Eqs (6.7-6.8) with $r$ replaced by $r_x$ or $r_y$ so that

$$r_x = \frac{|x - x_I|}{d_{mx}} = \frac{|x - x_I|}{d_{max} c_{xI}} \tag{6.7}$$

$$r_y = \frac{|y - y_I|}{d_{my}} = \frac{|x - x_I|}{d_{max} c_{xI}} \tag{6.8}$$

where $d_{mx}$ and $d_{my}$ are sizes of the support domain $\Omega_I$, and $c_{xI}$ and $c_{yI}$ are coefficients calculated at node $I$ by searching for nodes to satisfy the base function in both directions.

In the Hilbert space span $q$, for the selected point $x$ and weight function $w$, the orthogonal function $q_j(x, \bar{x})$ should satisfy:

$$\sum_I^m w(x_I, \bar{x}) q_k(x_I, \bar{x}) q_j(x_I, \bar{x}) = 0 \tag{6.9}$$

where $m=3$, $k \neq j$, and $k, j=I,\ldots,m$. Using the MLS approximation, the difference between the trial function $u^h(x)$ and displacement $u(x)$ should be minimised. Define a function:

$$\begin{aligned} J &= \sum_{I=1}^n w(x - x_I)[u^h(x, x_I) - u(x_I)]^2 \\ &= \sum_{I=1}^n w(x - x_I)[q^T(x_I, \bar{x}) a_i(\bar{x}) - u(x_I)]^2, \end{aligned} \tag{6.10}$$

By minimizing the difference defined by $J$, the coefficients $a_j(\bar{x})$ can be obtained by:

$$a_j(\bar{x}) = \frac{\sum_I^n w_I(\bar{x}) q_j(x_I, \bar{x}) u_I}{\sum_I^n w_I(\bar{x}) q_j^2(x_j, \bar{x})}, j=1 \text{ to } m \tag{6.11}$$

Applying the MLS approximation, we have:

$$u^h(x) = \sum_I^n \phi_I(x) u_I \tag{6.12}$$

Therefore the shape function $\phi_I(x)$ is defined as:

206

$$\phi_I(x) = w_I(x) \sum_j^m \frac{q_j(x,x)q_j(x_I,x)}{\sum_I^n w_I(\overline{x})q_j^{\,2}(x_I,\overline{x})} \tag{6.13}$$

The partial derivative of the shape function $\phi_{I,k}(x)$ is determined using the following equation:

$$\phi_{I,k}(x) = w_{I,k}(x) \sum_j^m \frac{q_j(x,x)q_j(x_I,x)}{\sum_I^n w_I(\overline{x})q_j^{\,2}(x_I,\overline{x})} + w_I(x) \sum_j^m \frac{A1-A2}{[\,\sum_I^n w_I(\overline{x})q_j^{\,2}(x_I,\overline{x})\,]^2} \tag{6.14}$$

where parameters $A1$ and $A2$ are expressed respectively as

$$A1 = w_I(x) \sum_j^m \frac{q_j(x,x)q_j(x_I,x)}{\sum_I^n w_I(\overline{x})q_j^{\,2}(x_I,\overline{x})} \tag{6.15}$$

$$A2 = q_j(x,x)q_j(x_I,x)[\sum_I^n w_{I,k}(x)q_j^{\,2}(x_I,x) + 2\sum_I^n w_I(x)q_j(x_I,x)q_{j,k}(x_I,x)] \tag{6.16}$$

Note that $w_I(x)$, $q_j(x,x)$ and $q_j(x_I,x)$ are derivable with respect to $x$. The subscript symbol $k$ denotes partial derivative to $x$ or $y$ due to the linear basis function.

## 6.2.2    Dynamic problem

According to (Liu and Gu, 2005), the dynamic equation for node $I$ in the local domain is expressed as:

$$\int_{\Omega_I} \widehat{W}_I(\sigma_{ij,j} + b_i - \rho\ddot{u}_i - c\dot{u}_i)d\Omega = 0 \tag{6.17}$$

where $\widehat{W}_I$ is the weight function. In a discretised system, the dynamic equation for node $I$ is written as:

$$\mathbf{M_I \ddot{u}(t) + C_I \dot{u}(t) + K_I u(t) = F_I(t)} \tag{6.18}$$

where $\mathbf{M_I}$, $\mathbf{K_I}$ are mass and stiffness matrix respectively for node *I*, $\mathbf{C_I}$ is the corresponding damping matrix, and $\mathbf{F_I}$ is the force acting on the domain.

On the traction boundary $\Gamma_t$, the boundary conditions are written as:

$$\sigma \cdot \mathbf{n} = \bar{\mathbf{t}} \tag{6.19}$$

where σ is the stress tensor, **n** is the unit normal to the domain Ω, and $\bar{\mathbf{t}}$ are the prescribed tractions. On the displacement boundary $\Gamma_u$, the boundary conditions become

$$\mathbf{u} = \bar{\mathbf{u}} \tag{6.20}$$

where $\bar{\mathbf{u}}$ are the displacements. In order to satisfy the essential boundary conditions, the penalty method is adopted. By introducing the penalty coefficient *α*, the Galerkin weak form for a dynamic problem is written as:

$$\int_\Omega \delta\, \mathbf{u}^{\mathrm{T}} \rho\, \ddot{\mathbf{u}}\, d\Omega + \int_\Omega \delta\, \mathbf{u}^{\mathrm{T}} c\, \dot{\mathbf{u}}\, d\Omega + \int_\Omega \delta\, \varepsilon^{\mathrm{T}} \sigma d\Omega - \int_\Omega \delta\, \mathbf{u}^{\mathrm{T}} \mathbf{b} d\Omega$$

$$\tag{6.21}$$

$$- \int_{\Gamma_t} \delta\, \mathbf{u}^{\mathrm{T}} \bar{\mathbf{t}}\, d\Gamma + \int_{\Gamma_u} \delta\, \mathbf{u}^{\mathrm{T}} \boldsymbol{\alpha} (\mathbf{u} - \bar{\mathbf{u}})\, \Gamma = 0,$$

where **δ** is the test function, and $\boldsymbol{\alpha} = \begin{bmatrix} \alpha_1 & 0 \\ 0 & \alpha_2 \end{bmatrix}$. The penalty factors $\alpha_i$ are usually assigned as constant, large, positive number and this study adoptes $\alpha_i = 10^5 \times E$. Using Eq. (6.21), the discretised function for a dynamic problem can be developed. The detailed process has been discussed in Zhang et al. (2013), and is expressed as:

$$\mathbf{M\ddot{U}} + \mathbf{C\dot{U}} + (\mathbf{K} + \mathbf{K}^{\alpha})\mathbf{U} = \mathbf{F} + \mathbf{F}^{\alpha} \tag{6.22}$$

In Eq. (6. 22), $\mathbf{U}$, $\mathbf{\dot{U}}$ and $\mathbf{\ddot{U}}$ are global vectors of nodal displacement, velocity and acceleration, respectively; $\mathbf{M}$ and $\mathbf{K}$ are respectively the mass matrix and stiffness matrix in the problem domain, $\mathbf{C}$ is the damping matrix, $\mathbf{F}$ is the global external force vector, $\mathbf{K}^{\alpha}$ is the global penalty matrix, and the additional force vector $\mathbf{F}^{\alpha}$ is derived from the essential boundary conditions. And, these parameters are expanded as:

$$\mathbf{M}_{IJ} = \int_{\Omega} \mathbf{\Phi}_I^T \rho \mathbf{\Phi}_J d\Omega \tag{6.23}$$

$$\mathbf{C}_{IJ} = \int_{\Omega} \mathbf{\Phi}_I^T c \mathbf{\Phi}_J d\Omega \tag{6.24}$$

$$\mathbf{K}_{IJ} = \int_{\Omega} \mathbf{B}_I^T \mathbf{D} \mathbf{B}_J d\Omega \tag{6.25}$$

$$\mathbf{K}_{IJ}^{\alpha} = \int_{\Omega} \mathbf{B}_I^T \alpha \mathbf{B}_J d\Omega \tag{6.26}$$

$$\mathbf{F} = \int_{\Omega} \mathbf{\Phi}_I^T \mathbf{b} d\Omega + \int_{\Gamma_t} \mathbf{\Phi}_I^T \mathbf{\bar{t}} d\Gamma \tag{6.27}$$

$$\mathbf{F}^{\alpha} = \int_{\Gamma_u} \mathbf{\Phi}_I^T \alpha \mathbf{\bar{u}} d\Gamma \tag{6.28}$$

where c is the damping coefficient, and the other coefficients are defined as follow

$$\mathbf{\Phi_I} = \begin{bmatrix} \phi_I & 0 \\ 0 & \phi_I \end{bmatrix} \tag{6.29}$$

$$\mathbf{B} = \begin{bmatrix} \phi_{I,1} & 0 \\ 0 & \phi_{I,2} \\ \phi_{I,1} & \phi_{I,2} \end{bmatrix} \tag{6.30}$$

$$\mathbf{D} = \frac{E}{1-v^2} \begin{bmatrix} 1 & v & 0 \\ v & 1 & 0 \\ 0 & 0 & (1-v)/2 \end{bmatrix}.$$
(6.31)

### 6.2.3    Discontinuum part

In the discontinuum domain, the interaction between the particles, or the particles and wall, is determined based on Newton's second law of motion and the force-displacement law. The two laws define the motion of the entities of interest and update the contact force based on the displacement. Similar to the nodal dynamic problem described in Eq. (6.18), in the discontinuum domain, as per Cundall and Strack (1979), the particle motion is expressed as:

$$m_i \ddot{\mathbf{u}}_i(t) + c\,\dot{\mathbf{u}}_i(t) = \mathbf{F}_i(t)$$
(6.32)

$$I_i \ddot{\boldsymbol{\theta}}_i(t) + c^*\,\dot{\boldsymbol{\theta}}_i(t) = \mathbf{M}_i(t)$$
(6.33)

where $m_i$ is the mass of disc $i$, $I_i$ is the moment of inertia of disc $i$, $\dot{\mathbf{u}}_i(t)$ and $\dot{\boldsymbol{\theta}}_i(t)$ are respectively the translational and angular velocities for disc $i$, $c$ and $c^*$ are global and local damping coefficient, respectively, and $\mathbf{F}_i(t)$ and $\mathbf{M}_i(t)$ are resultant force and moment at contact, respectively.

The DEM model uses a set of mechanical elements (i.e., spring and dashpot) to calculate the contact force occurred between two entities (i.e. particles) of interest. One of the widely used models is the linear contact, as presented in Figure 6-2. A finite

overlap is allowed between the rigid particles to simulate particle's deformation. The dashpot element is used to reflect viscous behaviour at contact. The contact force is determined based on the deformation of these mechanical elements, or the relative displacement between the particles. In the model, the normal and shear forces between the entities (or discs) $i$ and $j$, $F_{ij}^n$ and $F_{ij}^s$, respectively, are calculated as:

$$F_{ij}^n = k_n \Delta n + \beta k_n \Delta n \tag{6.34}$$

$$F_{ij}^s = k_s \Delta s + \beta k_s \Delta s \tag{6.35}$$

where $k_n$ and $k_s$ are contact normal and shear stiffness respectively, $\Delta n$ and $\Delta s$ are relative displacement measured at the normal and shear directions, and $\beta$ is a damping coefficient. To model the stick-slip contact occurred between entities, a Coulomb-friction criterion is employed as follows:

$$(F_{ij}^s)_{max} \leq F_{ij}^n \tan\varphi_u + c \tag{6.36}$$

where $(F_{ij}^s)_{max}$ is the maximum magnitude of shear force, $\varphi_u$ is the smaller of the interparticle friction angle of entities $i$ and $j$, and $c$ is the smaller of entity cohesion. The moment acting on entity $i$ is the result of all the shear forces applied at its contacts and expressed as:

$$M_i = \sum_{j=1}^{n} F_{ij}^s r_i \tag{6.37}$$

where $r_i$ is the radius of entity $i$.
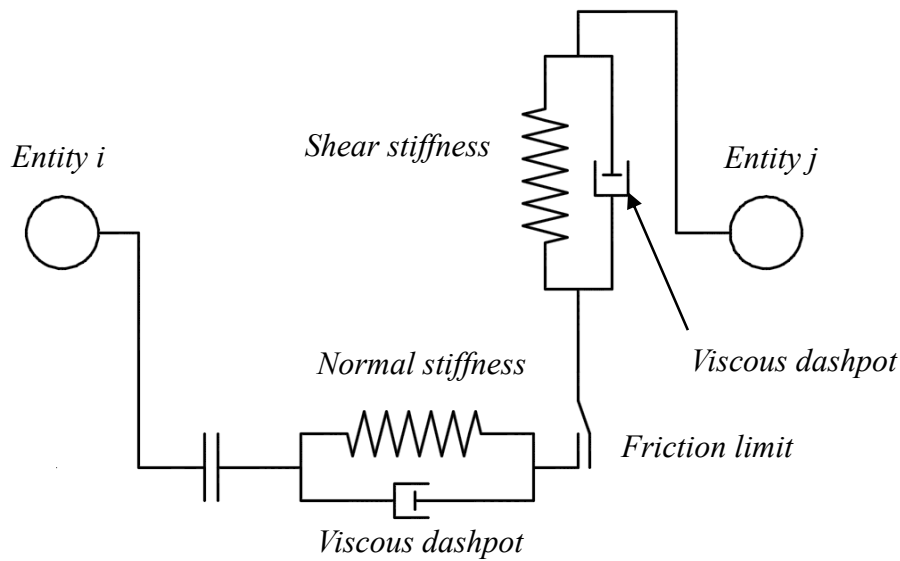
**Figure 6-2.** Linear contact spring model used in DEM

### 6.2.4    Continuum–discontinuum boundary

The continuum–discontinuum interface is examined to communicate the force–displacement relationship between the two domains. The domains interface is modelled as the disc–wall contact, which is commonly used in other coupling methods such as the DE–FE method (Nakashima and Oida, 2004). Where the DE–FE method is applied to a 2D problem, the DE–FE interface becomes disc–segment contacts. At each contact, paired disc–segment contact forces are transmitted to the ball centroid and the nodes of each element at the interface. The FE domain deformation is therefore subjected to the nodal force that arises from the disc–segment contact.

A similar conception for the interface force exchange is used in the EFG–DE method as follows: 1) determine the valid contact between discs and segments, including contact forces and their positions; and 2) compute the external force matrix resulting from the contacts at the interface. It is noted that the EFG–DE method processes the interface force in a way different from that for the FE–DE method. In the current study, the discrete contact force cannot be transmitted directly to the node forces at the interface, because the shape function obtained does not have Kronecker delta function property (Liu and Gu, 2005). A new approach is developed to transmit the forces.

### 6.2.4.1   Contact detection

In a multi-body dynamic system, objects often contact to transfer the load and the detection of the contacting process influences the approximation of objects response. In the current EFG–DE modelling framework, contacts occur in the forms of disc–disc in the DE domain and disc–segment in the EFG–DE interface. In the DE domain, contact detection algorithms are well-established and able to provide satisfactory results as in commercially accessible software package e.g. PFC, or open source code such as Yade. This study, however, develops the coupled model under the MATLAB platform and therefore detects the contact by writing independent code. The code was written based on the algorithm suggested by Muth et al. (2007) which accommodates a small

number of particles in the DE domain. The limitation in particles number may influence the approximation for a DE domain including a large number of particles. Muth's algorithm however supports the development and validation of the EFG–DE method where a modified, simple system is of interest, and therefore is adopted in this study. Regarding the contacts occurred on the domains interface, there are algorithms (Zang et al., 2011; Zheng et al., 2017; Lei and Zang., 2010) developed to detect the contacts on the DE–FE interface. These algorithms, however, are not applicable to the EFG–DE interface and a separate approach is developed.

In the detection of the EFG–DE contact, the first step is to gather position information for the nodes and discs on the interface. Figure 6-3 illustrates disc $O$ and nodes $i$ to $i+N$ which contact and sit on the domains interface. To detect the disc–segment contact, the following subroutines are performed: $a$) Calculate $d_{i,O}$, the distance between centroid $O$ and node $i$ , where $i=i,\ldots,i+N$; $b$) Determine the minimum distance $(d_{i,O})_{min}$ and the corresponding node number $j$; $c$) Calculate distances $d_{j-1,O}$ and $d_{j+1,O}$; $d$) Determine the interface segment. The segment is section $(j-1, j)$ if $d_{j-1,O} > d_{j+1,O}$, or section $(j, j+1)$ if $d_{j-1,O} < d_{j+1,O}$. If $d_{j-1,O} = d_{j+1,O}$, the segment is dependent on the distance between the centroid and the segments of interest which is discussed in the next paragraph; $e$) Calculate $d_{H,O}$, the distance between centroid $O$ and point $H$. Line $OH$ is drawn normal to the segment determined in Step $d$); and $f$) Calculate the velocity at point $H$ based on the shape function of this segment, and the velocity of nodes $j$ and $j-1$ based on the EFG method.
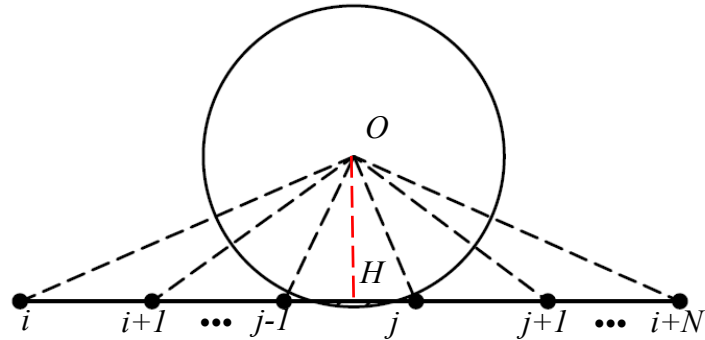
**Figure 6-3.** An illustration of disc position and boundary line segments

The next step is to determine the contact geometric primitives. In DE–FE coupling work, Zang et al. (2011) categorised the contact geometric primitives into particle–facet, particle–edge and particle–vertices problems. These contacts are not applicable to the EFG–DE coupling. In this current study, two types of disc–segment contact are discussed, as shown in Figure 6-4 (a) and (b) respectively. Figure 6-4 (a) shows the particle–segment contact where no nodes sit within the interface segment. Figure 6-4 (b) shows the particle–point contact where disc $O$ contacts node $j$. In the particle–point contact, the segment $(j–1, j+1)$ deforms into two sub-segments $(j–1, j)$ and $(j, j+1)$. In this case, the contact force is doubled. To eliminate this error, distance $d_{H,O}$ is replaced by $d_{j,O}$ in Step $f$) in the subroutine.

j-1     j     j-1     j+1

(a)       (b)
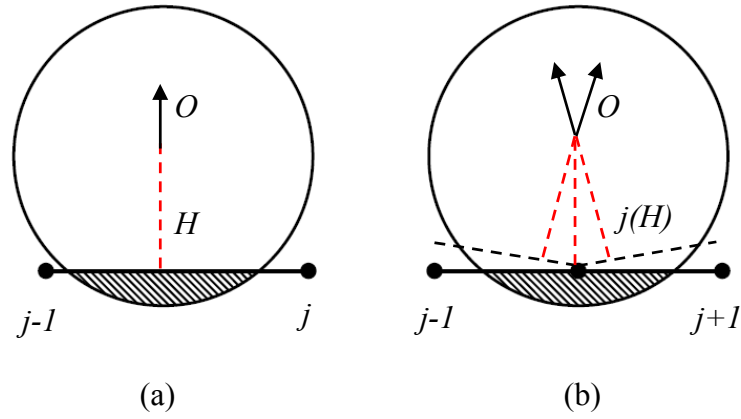
**Figure 6-4.** Illustration of a disc and a wall segment: (a) particle—segment contact

(b) particle—point contact

Using the difference method, the discrete equation used to calculate the increment of disc–segment force is written as:

$$\Delta F_{HO}^{n} = k_n(v_O - v_H)\Delta t + \beta k_n(v_O - v_H)\Delta t \tag{6.38}$$

$$\Delta F_{HO}^{s} = k_s(v_O - v_H)\Delta t + \beta k_s(v_O - v_H)\Delta t \tag{6.39}$$

where $v_o$ and $v_H$ are the average velocities of centroid $O$ and point $H$ at the segment during time step $\Delta t$. The velocity of $v_H$ is expressed as:

$$v_H = v_i + \frac{l_{i,H}}{l_{i,i+1}}(v_{i+1} - v_i) \tag{6.40}$$

or, if $d_{j-1,O} = d_{j+1,O}$, is simplified into

$$v_H = v_i \tag{6.41}$$

### 6.2.4.2 Determination of contact force

The contact forces acting on the interface are determined and adapted to transmit the external load across the domains. A conventional method in FEM is to convert the contact force into a point load at the boundary nodes (Fakhimi, 2009). However, in the EFG domain, the contact forces cannot be directly applied to boundary nodes due to the use of MLS (Belytschko, 1994). To impose the point loads to the EFG boundary, each load is regarded as a distributed traction, and multiple tractions are superposed. According to Zuohui (2006), if a point load $F$ acts at position $(x_0, y_0)$ on interface $\Gamma_t$ as shown in Figure 6-5, the following equation is obtained:

$$\int_{\Gamma_t} \Phi_I^T t_i d\Gamma = \int_{\Gamma_t} \Phi_I^T F_i \delta(\, x - x_i \,) d\Gamma = \Phi_i^T F_i \tag{6.42}$$

where $\delta$ is the Dirac delta function. Assuming a total of $N$ point loads act on the boundary, the superposed traction is expressed as:

$$\bar{t}(x) = \sum_{i=1}^{N} t_i = \sum_{i=1}^{N} F_i \delta(x - x_i) \tag{6.43}$$

Eq. (6.42) then becomes,

$$\int_{\Gamma_t} \Phi_I^T \bar{t} d\Gamma = \sum_{i=1}^{N} \Phi_i^T F_i \tag{6.44}$$

Substituting Eq. (6.44) to Eq. (6.27) and we have,

$$F = \int_{\Omega} \Phi_I^T b \mathrm{d}\Omega + \sum_{i=1}^{N} \int_{\Gamma_t} \Phi_I^T F_i \delta(x - x_i) \mathrm{d}\Gamma = \int_{\Omega} \Phi_I^T b \mathrm{d}\Omega + \sum_{i=1}^{N} \Phi_i^T F_i \qquad (6.45)$$
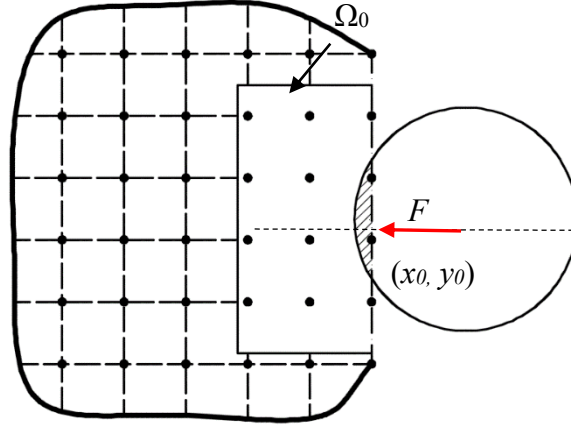


**Figure 6-5**. The interaction between a disc and a EF domain

In Eq. (6.45), the external force $F$ at domain $\Omega$ contains two components: the body force such as gravity, and the point load. The latter part of Eq. (6.45) has the following meaning: when a point load $F_i$ acts at point $(x_0, y_0)$ on a continuous boundary, this load is distributed to the surrounding points in the local supporting domain $\Omega_0$ based on shape function $\phi_0(x)$ which is determined by Eq. (6.13). The supporting domain area may be affected by the chosen domain scaling factor $d_{max}$.

## 6.3    Time integration

In the EFG–DE approximation, the force–displacement relationship is discretised in terms of finite time steps. To enable the approximation to converge, the value of the time step is properly set to ensure the algorithms are stable in both DE and EFG domains.

This section describes the method developed to determine the time step and present the governing equations in the two domains.

### 6.3.1 Stable time step

A time step is determined either explicitly or implicitly. Belytschko et al. (2013) discussed the differences between the explicit and implicit methods and suggested that the choice of method should be determined based on the partial differential equations, smoothness of data, and material response to examine. In a particle-based discrete element analysis, the central difference method is often used (Cundall and Strack, 1979). This method guarantees numerical stability so that each time step does not exceed the critical time step in the explicit time scheme. Also when particle number increases, the implicit time schemes may require solving multiple matrices at each time step, which significantly increases processing time (O'Sullivan and Bray, 2004). Due to the above reasons, one common method in the coupled model is to determine the time step using explicit–explicit schemes (Zheng et al., 2017, Lei and Zang, 2010):

$$\Delta t \leq \min\left\{\Delta t_{fcr}, \Delta t_{dcr}\right\} \tag{6.46}$$

where $\Delta t_{fcr}$ and $\Delta t_{dcr}$ are the minimum time steps in the continuum and discontinuum domains, respectively. Another method was proposed by Elmekati and El Shamy (2010) who uses the predictor–corrector method, a two staged iterative process. As the time step in the discontinuum domain is usually much smaller than the one in the continuum

domain, the algorithms may allow different time steps in each domain. Therefore the time step in the main routine is expressed as:

$$\Delta t = \Delta t_{fcr} = n\Delta t_{dcr} = n\sqrt{\frac{m}{K}} \tag{6.47}$$

where $n$ is an integer, $m$ is the particle mass and $K$ is the contact sprint stiffness.

In this present study, an explicit–implicit time integration scheme was adopted in the coupled analysis. In the continuum domain, the iterations are unconditionally stable due to the advantages of the explicit method. Therefore, time steps need to be determined in the DE domain. Also, the calculation is consistent in the combined model because the results of the DE simulation can be transmitted to the EFG domain at each time step. In this context, important information such as the contact detection on the interface should not be ignored, so that the node and particle statuses are evaluated explicitly while executing major iterations. To discretise the governing equations, Newmark-$\beta$ algorithms and the central difference method are adopted in both the continuum and discontinuum domains.

## 6.3.2    Partial difference solution

Difference method is used to discretise the time domain so that the EFG–DE approximation is implemented properly. Motion governing equations relating to accelerations, velocities and displacements resulted from the force acting on the two

domains are updated at each time step. However, the calculation methods for the equations of the two domains are slightly different. In the EFG domain, the governing equations are solved based on a matrix, because the domain is continuous as shown in Figure 6-6 (a). In the DE domain, stiffness matrix dimensions may vary in different steps because some particles may not in contact as shown in Figure 6-6 (b). Therefore, the contact state needs to be determined at the end of each step. It is computationally expensive to compute a stiffness matrix at each loop. This is why the method in the DE domain usually focuses on individual particles. It avoids excessive iterations of the stiffness matrix. In the EFG domain, the nodes are numbered sequentially and the displacement, velocity and acceleration are obtained in matrices, denoted as $\mathbf{U}$, $\dot{\mathbf{U}}$ and $\ddot{\mathbf{U}}$, respectively. In the DE domain, the displacement, velocity and acceleration are only calculated based on individual discs such as $u_i$, $\dot{u}_i$ and $\ddot{u}_i$ respectively, because discs contact is subject to change at each time step increment.
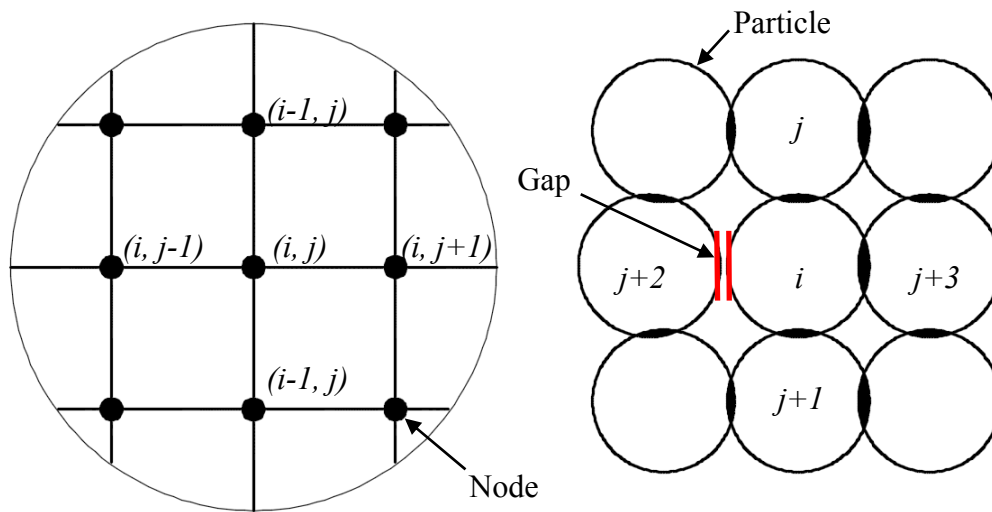
**Figure 6-6**. Schematic illustrating EFG–DE domains: (a) EFG domain with difference nodes, and (b) DE domain with particles at contact.

Table 6-1 presents the sets of governing equations used in the EFG and DE domains respectively. These equations demonstrate the motions occurred in a time step increment from $t$ to $t+\Delta t$. The two sets of equations are tabularised to compare the difference in conception when computing element motions. In the continuum domain, an external force matrix is the major concern; in the discontinuum domain, internal disc–disc contact forces are computed to provide the force–displacement relationship. In the EFG part, the Taylor expansion is used to obtain the recurrence relationship at the end of the time increment. In contrast, as a central difference method in the DE part, it is required to determine velocity at $t+\dfrac{\Delta t}{2}$ which is known as the average speed during a time step. Extra rolling behaviour at disc $i$, such as rolling angle $\theta_i$, rolling velocity $\dot{\theta}_i$, and rolling acceleration $\ddot{\theta}_i$, was added in the DE analysis.

1

**Table 6-1.** Governing equations to depict motion of elements in EFG and DE domains.

| | EFG domain | | DE domain | |
|---|---|---|---|---|
| Displacement | $U_{t+\Delta t} = \dfrac{F_{t+\Delta t} + M(\alpha_1 U_t + \alpha_2 \dot{U}_t + \alpha_3 \ddot{U}_t)}{\alpha_1 M + \overline{K}}$ | (6.48) | $(u_i)_{t+\Delta t} = (u_i)_t + (u_i)_{t+\Delta t/2} \times \Delta t$ <br><br> $(\theta_i)_{t+\Delta t} = (\theta_i)_t + (\theta_i)_{t+\Delta t/2} \times \Delta t$ | (6.49) <br><br> (6.50) |
| Velocity | $\dot{U}_{t+\Delta t} = \dot{U}_t + (1 - \beta_1)\Delta t \ddot{U}_t + \beta_1 \Delta t \ddot{U}_{t+\Delta t}$ | (6.51) | $(\dot{u}_i)_{t+\Delta t/2} = (\dot{u}_i)_{t-\Delta t/2} + (\ddot{u}_i)_t \times \Delta t$ <br><br> $(\dot{\theta}_i)_{t+\Delta t/2} = (\dot{\theta}_i)_{t-\Delta t/2} + (\ddot{\theta}_i)_t \times \Delta t$ | (6.52) <br><br> (6.53) |
| Acceleration | $\ddot{U}_{t+\Delta t} = \alpha_1(U_{t+\Delta t} - U_t) - \alpha_2 \dot{U}_t - \alpha_3 \ddot{U}_t$ | (6.54) | $(\ddot{u}_i)_t = (\sum_{j=1}^{N} F_{ij} / m_i)\Delta t$ <br><br> $(\ddot{\theta}_i)_t = (\sum_{j=1}^{N} M_{ij} / I_i)\Delta t$ | (6.55) <br><br> (6.56) |
| Force | External force Eqs. (6.27-6.28) | | $(F_{ij})_{t+\Delta t} = (F_{ij})_t + k(\dot{u}_i)_{t+\Delta t/2}\Delta t + \beta k(\dot{u}_i)_{t+\Delta t/2}\Delta t$ <br><br> $(M_{ij})_{t+\Delta t} = (M_{ij})_t + k_s\{(\dot{u}_i)_{t+\Delta t/2}s\}r_i\Delta t$ | (6.57) <br><br> (6.58) |

2

Where in Eq. (6.48) the parameters are respectively expressed as:

$$\overline{K} = K + K^{\alpha} \tag{6.59}$$

$$\alpha_1 = \frac{2}{\beta_2 \Delta t^2} \tag{6.60}$$

$$\alpha_2 = \frac{2}{\beta_2 \Delta t} \tag{6.61}$$

$$\alpha_3 = \frac{1}{\beta_2} - 1 \tag{6.62}$$

two constants $\beta_1 = 1.5$ and $\beta_2 = 1.6$ are used as Newmark parameters.

## 6.4    Example problems

Two example problems were examined and solved using the EFG–DE method, aiming to validate the coupling method. The first example problem is to assess a cantilever beam which is subjected to a disc acting at the end of the beam; the second one is developed based on the *Nine Disc Test* (Cundall and Strack, 1979). The two example problems consider multi-body interactions, but involves less number of nodes/discs than in other large-scale problems. This means the computational costs are affordable, and this special settings satisfy the aim of developing and validating the EFG–DE method.

### 6.4.1 Example problem 1

This section presents a study on the dynamic interaction occurred between a disc and a cantilever beam. The EFG–DE method is applied to the example problem and the numerical results are compared with the analytical solutions developed for the same example problem.

#### 6.4.1.1 Problem description

In this example problem, the cantilever beam is fixed to a rigid surface and the disc sits on the other end, as shown in Figure 6-7. The beam measures 1 ($L$) × 0.2 ($H$) × 0.025 ($D$) m. The material density of the beam is $\rho_b$=2,000 kg/m³. The radius of the disc is $r$=0.05 m and its density is $\rho_d$=1,000 kg/m³. It was assumed that the material of the beam exhibits linear elastic behaviour with the Young's modulus $E$=2.1×10$^8$ Pa and Poisson ratio $v$=0.3, and that the disc material is simulated with the linear contact model with $k_n$=$k_s$=10$^6$ N/m.
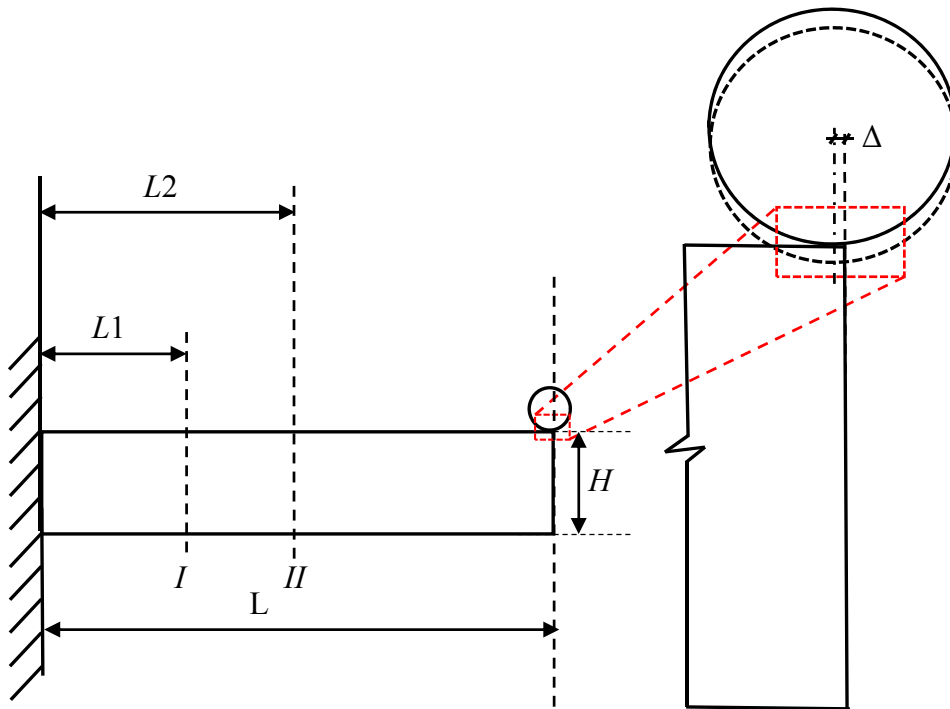
**Figure 6-7**. Configuration of a disc and a cantilever beam

In the approximation, the beam is discretised by a node arrangement of 20×4. The node grid is refined by a 4×4 Gauss quadrature scheme. At time $t$=0, the beam is in equilibrium and its upper-right boundary is in contact with the disc edge (no overlap or deformation). The disc centroid sits at a small distance $\Delta$=$10^{-3}$ mm from the beam end, to ensure that the centroid falls inside the boundary of the beam. When $t$ increases, the disc goes down gradually and penetrates the boundary of the beam until equilibrium is reached.

### 6.4.1.2 Termination condition

The termination condition was determined in terms of the move of the disc centroid. The centroid tends to move opposite to the rigid surface when the beam is bent downward. Where the projection of the centroid falls out of the boundary

of the beam, the interaction between the disc and beam becomes instable and the approximation tends to be less accurate. To determine the moment when the centroid projection moves out of the boundary, the vertical displacement of the end of the beam and the disc centroid is captured and plotted against time as shown in Figure 6-8. Where the two displacement values disagree, the corresponding time signals the disc falling off. It is shown that the time point is $t$=0.1431 s where the falling-off occurs. It is noteworthy that excellent agreement is obtained between the two displacement curves before the time point is reached, demonstrating the stability of the simulation.
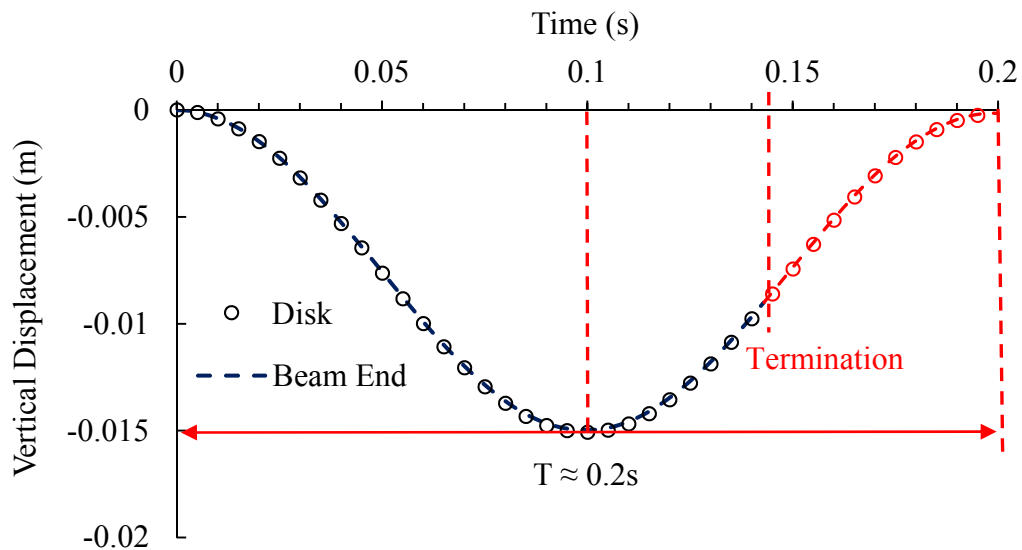


**Figure 6-8**. Displacement profile for the end of the beam and the centroid of the disc.

### 6.4.1.3 Model validation

In this section, the numerical results are compared with the analytical solutions obtained for the same example problem. The problem was solved in a plane stress condition—a point load $P$ acting at the upper right corner of the beam. According

to Euler–Bernoulli beam theory, the axial stress, $\sigma_{11}$, and the deflection of the beam, $w_x$, are respectively expressed as:

$$\sigma_{11} = \frac{P(L-x)y}{I} \tag{6.63}$$

$$w(x) = \frac{Px^2(3L-x)}{6EI} \tag{6.64}$$

where $(x, y)$ is the coordinate of the cross section of interest, and $I_m$ is the moment of inertia of the beam.

The axial stress $\sigma_{11}$ profiles at two cross sections *I* at $L_1$=0.3 m and *II* at $L_2$=0.5 m as shown in Figure 6-7 are obtained. For the simulation results, the axial stress at the same cross sections are captured. But, due to the beam acting without damping, the results where the beam is in its minimal acceleration $t=T/4$, are used. The results are presented in Figure 6-9. The axial stress is plotted as a function of the vertical depth $y$ for both the simulation and analytical results. At either of the cross sections, excellent agreement between the simulation and analytical results is obtained. Similar agreement is obtained for the deflection profile of the beam, as presented in Figure 6-10. The results agreement verifies the capability of the EFG–DE model in simulating the dynamic response of the beam. Furthermore, the orthogonal basis function was used in the iterations and this function avoids the occurrence of the ill-conditioned problem discussed in Section 1. Similar advantage in simulation effectiveness is brought through by the uses of the explicit–implicit algorithm and the penalty method.
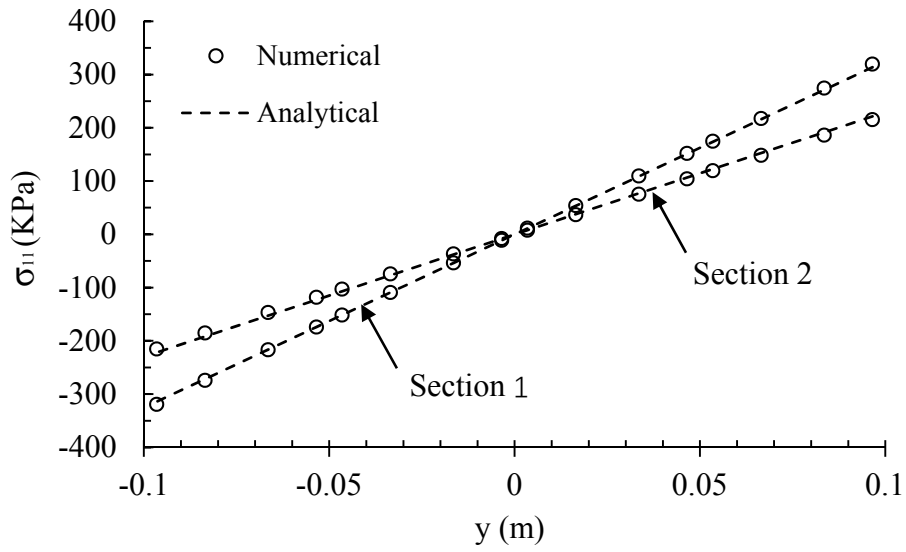
**Figure 6-9**. Comparison of $\sigma_{11}$ in numerical and analyticsal solutions in different sections
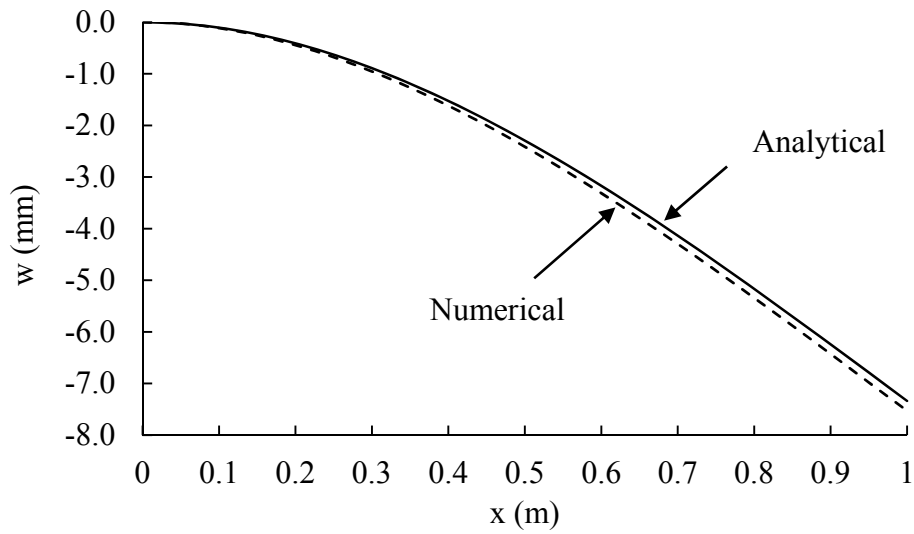


**Figure 6-10**. Comparison of the beam's deflection between numerical and analytical solutions

**6.4.1.4  Stress distribution along the cantilever beam**

When the beam is subjected to a dynamic vibration, the contact forces acting on the boundary change over time. The results of the contact forces are provided in Figure 6-11. In the figure, four critical time steps are marked up: $t$=0.001, 0.05, 0.1, and 0.143 s, which are labelled as points (*a*), (*b*), (*c*), and (*d*) respectively. It is shown that the contact force gradually increases with time at the early stage of the test. At $t$=0.05 s where the contact force equals the gravity force, the acceleration becomes zero, and negative where the contact force exceeds the gravity. In the meantime, the disc velocity gradually decreases, but the contact force grows at a similar gradient. The contact force attains the peak value when $t$=0.1 s, and at this moment, the disc attains the maximum displacement and penetration into the beam. After the peak point, the penetration releases gradually and the contact force does down. At $t$=0.143 s the contact force is less than the gravity and the disc falls off the end of the beam.
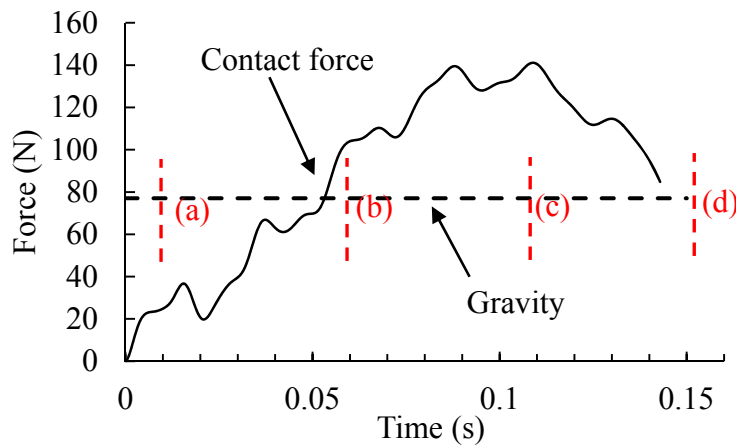


**Figure 6-11**. Development of disc–segment contact force over time

## 6.4.2 Example problem 2

Example problem 2 modifies the *Nine Disc Test* (Cundall and Strack, 1979). In the original test, two pairs of plates were used to compress an assemblage of 9 discs. The plates were assumed ideally rigid. In example problem 2, the plates are allowed to deform to avoid the assumption. In this present study, the *Nine Disc Test* is employed because of the following reasons: *i*) This test is designed to record the single contact force occurred between the discs and walls, enabling a smooth gauging profess. *ii*) The test can capture the effects of the change of plate on the contact force. And, *iii*) the test uses a small number of discs and facilitates contact detection and simulation in a short time period.

### 6.4.2.1 Problem description

An assemblage of nine discs is sandwiched by two pairs of plates, as shown in Figure 6-12. The setup remain the same as in Cundall and Strack (1979), except the left-hand side plate which is replaced with a deformable strip plate. This plate dimensions are 50 (*L1*) × 300 (*H*) × 1 (*D*) units, which enables a plane stress problem. As per Cundall and Strack (1979), no physical unit is provided to the properties of the elements, but a number. Specifically, the radii are 50 units, the density is 1000 units, and the normal and shear stiffness are $k_n=k_s=1.35\times10^9$ units for the linear contact model used for the discs. In the DE domain, the object wall is not assigned with physical properties such as a Young's modulus, Poisson ratio or density. However, in the EFG domain (i.e., the strip plate), the material properties are specified in order to constitute a motion. These properties include Young's Modulus of $2.1\times10^{14}$ units (to create a very rigid plate), Poisson's ratio

of 0.3, density of 2000 units. The plates were assumed to be undamped ($c=0$ in Eqs. (6.24), and fixed at the top and bottom boundaries.
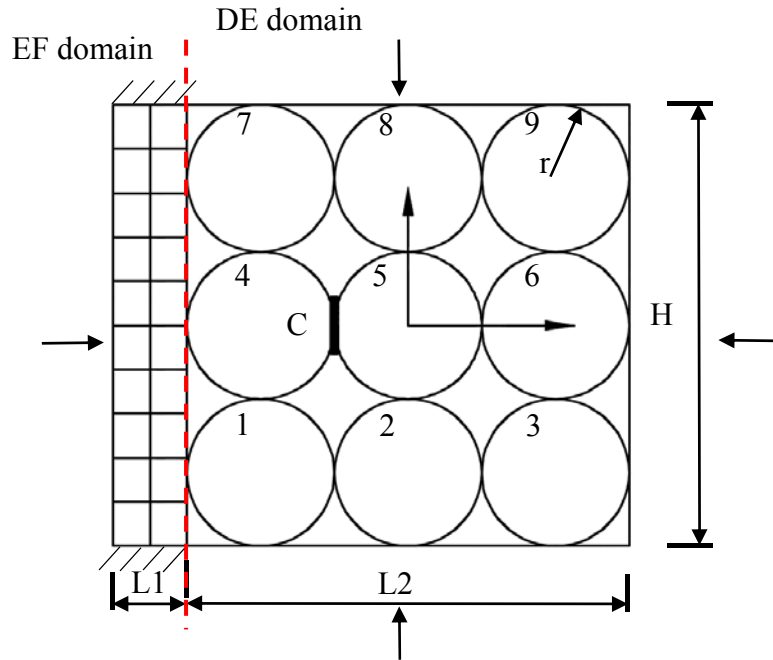


**Figure 6-12**. Nine disc test with a deformable boundary

### 6.4.2.2 Model validation

In the simulation, the assembly of the nine discs is subjected to the bi-axial compression provided by the two pairs of the plates. Two tests were performed. In Test 1, the enclosed facets travel at a velocity of 0.12 units, and stop after 40 cycles. In Test 2, the velocity reduces to 0.04 units, but the facets continue to move until the 120th cycle. As per Cundall and Strack (1979), both simulations continue to the 150th cycle, and use a time step $\Delta t=0.01525$ units and damping coefficient of 0.1. The continuous domain uses the cubic spline function and a 3×11 nodal arrangement. In this arrangement, the discs fall into the choices of disc–segment and disc–point contact, depending on the disc locations as discussed in Figure 6-4.

The normal contact force at point *C* (i.e., the contact of discs 4 and 5) throughout the loading process is examined. The results of the contact force are presented in Figure 6-13. The results include the simulations provided by the EFG–DE method based on MATLAB, DEM based on PFC, and the simulations in Cundall and Strack (1979). The EFG–DE results agree with the results of the other two simulations, verifying the capability of the coupling method in approximating the dynamic response occurred between the continuum and discontinuum domains. A slight discrepancy between the EFG–DE simulation and the other two simulations is observed in Test 1 where the facets stop stressing the discs. This discrepancy is probably attributed to the deformation of the plates.
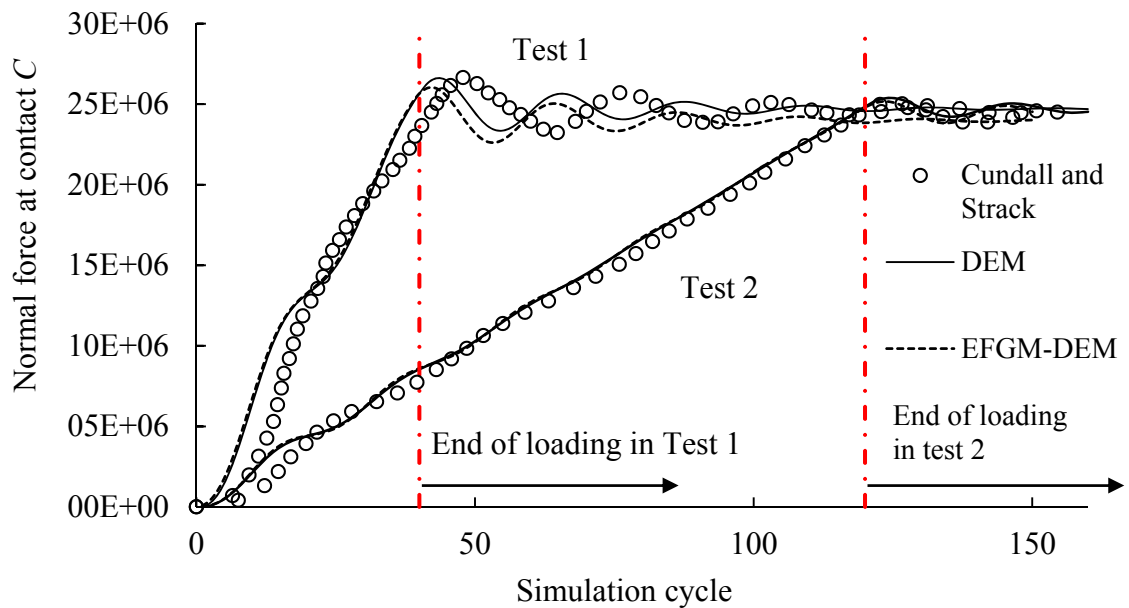


**Figure 6-13**. Normal force at contact *C* versus simulation cycle determined by different simulation methods.test

**6.4.2.3   Error discussion**

The deformability of the plates influences the displacement of the discs. The vertical displacement of disc 4 calculated by the EFG–DE method and DEM method is presented in Figure 6-14. In the figure, the EFG–DE results show that disc 4 oscillates in $y$ direction after the $20^{th}$ cycle. This suggests that the contact forces in $y$ direction are not in equilibrium in the course of the test. The changing contact force is related to the deformation of the plate which is used as the boundaries. Based on the penalty method, Eq. (6-22) gives rise to a small difference in the displacement of the top and bottom boundaries. This is because the boundary condition was only approximately satisfied. Consequently, the deformation of the beam is not perfectly symmetrical. The asymmetric problem nests in the floating numbers used in the matrix. This error accumulates in simulations. For example, the displacement of the discs increases with time as shown in Figure 6-14. In the test performed by Cundall and Strack (1979), the plates were assumed rigid and the simulations ignored the disc displacement and contact force changing. This assumption is tolerable for a short term of simulations (i.e., 20 cycles) but not a longer term. This is mainly because of the algorithm used to calculate the contact force between disc–segment as specified in Eq. (6.40). The orientation of the segment largely affects the force values and directions. In this context, a termination can be applied to the dynamic process when the displacement in $y$-direction of disc 4 is sufficiently large, e.g., $\Delta y > 1e-5$.
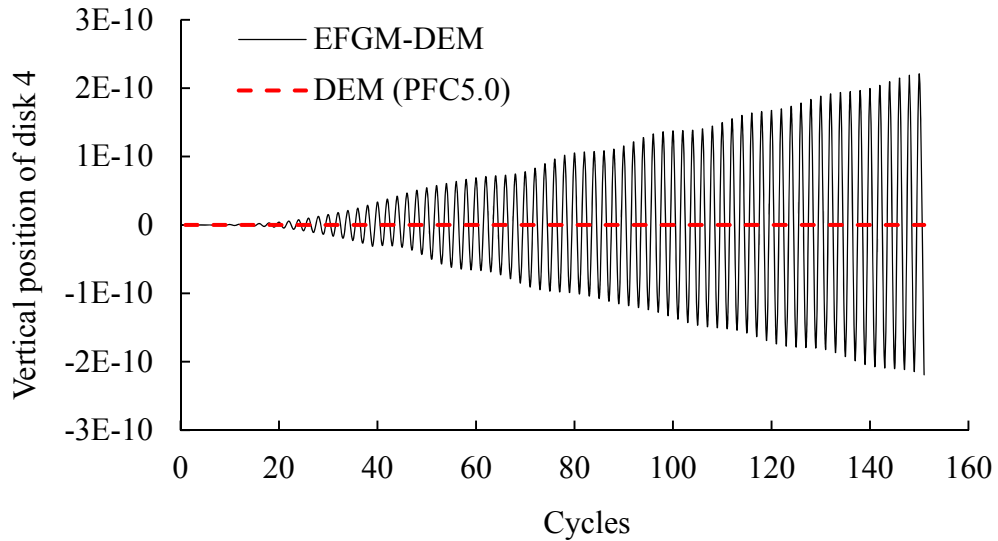
**Figure 6-14**. The vertical displacement of disc 4 obtained using the EFG–DE method and DEM method.

The simulation error can be discussed by examining the deformation of the nodes on the boundary. The nodes arrangement is provided in Figure 6-15. A total of 33 nodes sit along the edge of the plate, and for some representative nodes, the displacement in $x$ direction occurred at the $10^{th}$ and $150^{th}$ cycles is recorded and provided in Table 6-2. The results show that the boundary conditions is well satisfied in the coupling work. Specifically a sufficiently small displacement occurs at nodes 1, 11, 12, 22, 23 and 33. However, as discussed above on the simulation error, the actual displacement is not symmetric, but the difference is marginal.
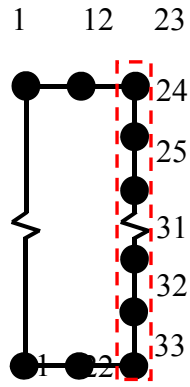
**Figure 6-15**. Boundary nodes of the beam.

**Table 6-2**. Displacement at boundary

| | Displacement (x) | |
| --- | --- | --- |
| Node | 10th cycle | 150th cycle |
| 1 | −5.426E−13 | −3.905E-11 |
| 11 | −5.426E−13 | −3.905E-11 |
| 12 | −2.522E−13 | −1.825E−11 |
| 22 | −2.522E−13 | −1.825E−11 |
| 23 | −5.099E−13 | −3.715E−11 |
| 24 | −6.561E−07 | −4.625E−05 |
| 25 | −1.686E−06 | −1.197E−04 |
| 31 | −1.686E−06 | −1.197E−04 |
| 32 | −6.561E−07 | −4.625E−05 |
| 33 | −5.098E−13 | −3.715E−11 |

**6.4.2.4   Influence of Young's Modulus**

To gain an insight into the effects of plate deformation on the discs contact force, additional EFG–DE simulations were performed on scenarios with varying Young's modulus for the plate of interest. Where the modulus is small, a large contact overlap tends to occur, and the results likely become unstable which is called *contact buckling* (Nakashima and Oida, 2004). In this circumstance, as pointed out by Kanto and Yagawa (1990), numerical oscillation may occur at contact because of the discontinuous velocity and acceleration when enforcing geometric compatibility. To prevent a severe contact overlap, Young's modulus was trialled and assigned with $E=2.1\times10^{14}$, $2.1\times10^{13}$, $2.1\times10^{12}$, and $1\times10^{10}$ units for the plate. Similarly, scenarios Tests 1 and 2 were performed to examine the effects of the simulation cycles on the results. The results of the normal force at contact $C$ obtained in the two tests under the varying plate stiffness conditions are presented in Figure 6-16. In either test, the plate stiffness noticeably influences the development of the contact force. The higher the wall stiffness is, the greater the contact force will be. This relationship is more pronounced in stage two of the tests, i.e., the period when the plates stop compressing the assembly of discs. Where the plate stiffness is relatively high i.e., $E\geq2.1\times10^{13}$ units, the curves coincide and approach an equilibrium at the end of the simulation. This trendline agrees with the results obtained in the DEM simulation (Figure 6-13). This means that the plate stiffness of $E\geq2.1\times10^{13}$ units is high enough to satisfy the rigid assumption made in the DEM simulation. Where the plate is less stiff, the contact force attenuates over time. This is probably caused by the discs moving toward the wall segment when it deforms, decreasing the overlap at contact $C$.
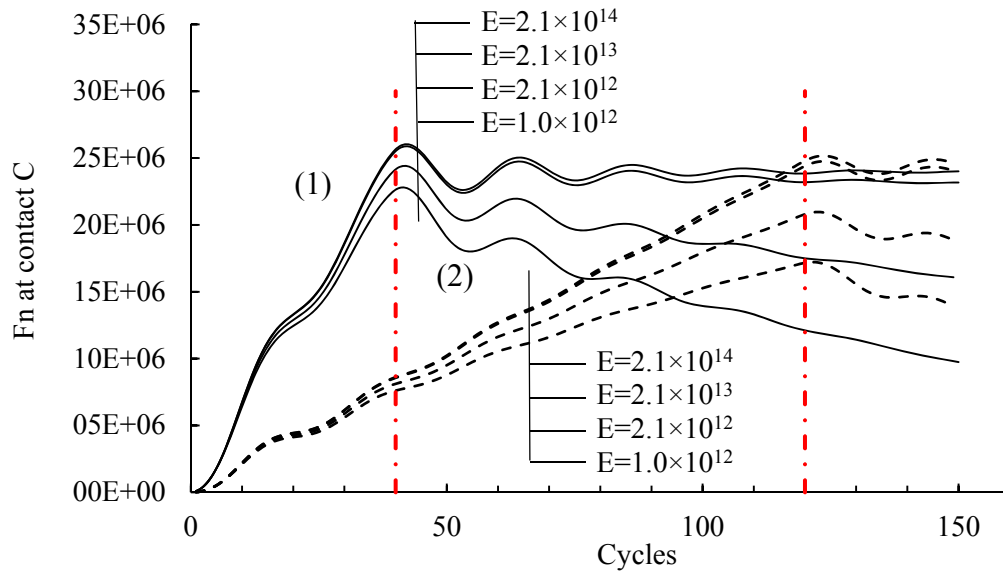
**Figure 6-16**. Relationship between the contact force and the cycles subjected to different Young's moduli

To gain a further insight into the response of a less stiff plate (i.e., $E=1.0\times10^{12}$ units), the deformation occurred to the boundary nodes of the plate as shown in Figure 6-17 is examined. An enlarged view of the nodes displacement captured at the 40th cycle is shown in Figure 6-18. Due to the use of a deformation plate, the actual displacement at the wall boundary is not uniform. The central nodes displace significantly larger than the ones on the upper and bottom. This differential displacement of the deformable plates agrees with the observations occurred in the tri-axial tests (Oda, 1972; Fakhimi, 2009). In these tests, the samples under compression dilated in the central section of the samples tested.
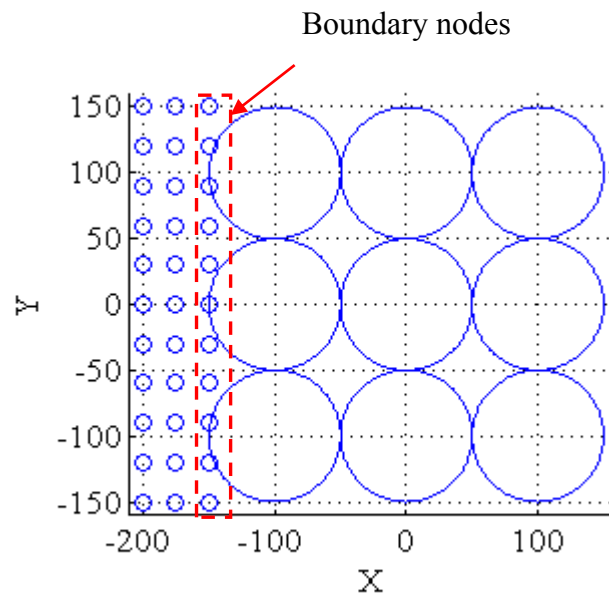
**Figure 6-17**. Boundary nodes on the plate–discs interface examined for the plate deformation.
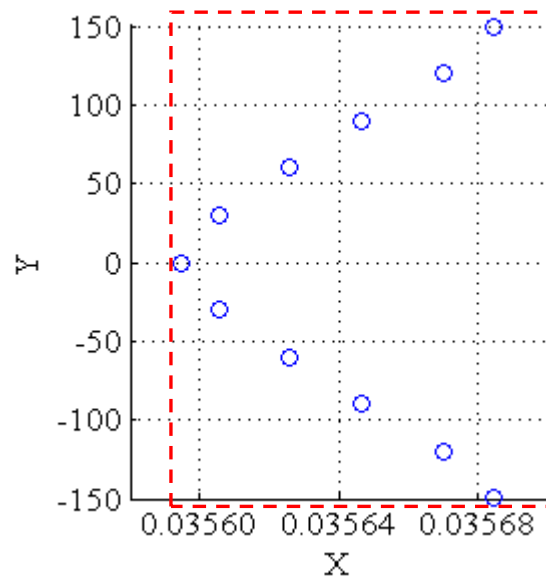


**Figure 6-18**. Displacement of the boundary nodes on the plate–discs interface recorded at the 40th cycle.

## 6.5    Conclusion

This paper presents a 2D elastrodynamic EFG–DE method. This coupling method is capable of simulating multi-body interactions, in particular the continuum–discontinuum contact problems. This method uses a transient disc–segment contact algorithm for the contact problems and is applied to two example problems. This study draws the following conclusions.

(1) The coupling EFG–DE method is free of finite elements and saves computational costs and simulation efficiency. The method is successfully applied to the two example problems and verified against the existing analytical and approximation results. The method is able to approximate dynamic interaction occurred between continuum and discontinuum media.

(2) This coupling method applies the Newmark-$\beta$ method and central difference method to the continuum and discontinuum domains to solve the dynamic problem in a discrete form. Using this implicit–explicit time scheme, the stability condition for the combined work is unconditionally satisfied.

(3) This coupling method develops a transient contact detection algorithm. After detecting the valid contact, the contact force can be treated as point load at the boundary and integrated as distribution. This feature enables simulations to account for deformable boundaries of the continuum and discontinuum media.

(4) Using the penalty method, the essential boundary condition is well satisfied. However, due to an accumulated error during the dynamic process, advanced techniques may be required to achieve higher accuracy.

## 6.6 Acknowledgement

## 6.7 References

BELYTSCHKO, T., GU, L. & LU, Y. 1994a. Fracture and crack growth by element free Galerkin methods. *Modelling and Simulation in Materials Science and Engineering,* 2**,** 519.

BELYTSCHKO, T., LIU, W. K., MORAN, B. & ELKHODARY, K. 2013. *Nonlinear finite elements for continua and structures*, John wiley & sons.

BELYTSCHKO, T., LU, Y. Y. & GU, L. 1994b. Element‑free Galerkin methods. *International journal for numerical methods in engineering,* 37**,** 229-256.

CAI, M., KAISER, P., MORIOKA, H., MINAMI, M., MAEJIMA, T., TASAKA, Y. & KUROSE, H. 2007. FLAC/PFC coupled numerical simulation of AE in large-scale underground excavations. *International Journal of Rock Mechanics and Mining Sciences,* 44**,** 550-564.

CHEN, H., ZHANG, Y., ZANG, M. & HAZELL, P. J. 2015. An accurate and robust contact detection algorithm for particle‑solid interaction in

combined finite ‑ discrete element analysis. *International Journal for Numerical Methods in Engineering,* 103**,** 598-624.

CINGOSKI, V., MIYAMOTO, N. & YAMASHITA, H. 1998. Element-free Galerkin method for electromagnetic field computations. *IEEE Transactions on Magnetics,* 34**,** 3236-3239.

CUNDALL, P. A. & STRACK, O. D. 1979. A discrete numerical model for granular assemblies. *geotechnique,* 29**,** 47-65.

ELMEKATI, A. & EL SHAMY, U. 2010. A practical co-simulation approach for multiscale analysis of geotechnical systems. *Computers and Geotechnics,* 37**,** 494-503.

FAKHIMI, A. 2009. A hybrid discrete–finite element model for numerical simulation of geomaterials. *Computers and Geotechnics,* 36**,** 386-395.

KANTO, Y. & YAGAWA, G. 1990. A dynamic contact buckling analysis by the penalty finite element method. *International Journal for Numerical Methods in Engineering,* 29**,** 755-774.

KRYSL, P. & BELYTSCHKO, T. 1996. Analysis of thin shells by the element-free Galerkin method. *International Journal of Solids and Structures,* 33**,** 3057-3080.

LEI, Z. & ZANG, M. 2010. An approach to combining 3D discrete and finite element methods based on penalty function method. *Computational Mechanics,* 46**,** 609-619.

LI, M., YU, H., WANG, J., XIA, X. & CHEN, J. 2015. A multiscale coupling approach between discrete element method and finite difference method for dynamic analysis. *International Journal for Numerical Methods in Engineering,* 102**,** 1-21.

LIU, G.-R. & GU, Y.-T. 2005. *An introduction to meshfree methods and their programming*, Springer Science & Business Media.

LU, Y., BELYTSCHKO, T. & TABBARA, M. 1995. Element-free Galerkin method for wave propagation and dynamic fracture. *Computer Methods in Applied Mechanics and Engineering,* 126**,** 131-153.

LU, Y.Y., BELYTSCHKO, T. AND GU, L., 1994. A new implementation of the element free Galerkin method. *Computer methods in applied mechanics and engineering*, *113*(3-4), pp.397-414.

MUNJIZA, A. A. 2004. *The combined finite-discrete element method*, John Wiley & Sons.

MUTH, B., M LLER, M.-K., EBERHARD, P. & LUDING, S. 2007. Collision detection and administration methods for many particles with different sizes.

NAKASHIMA, H. & OIDA, A. 2004. Algorithm and implementation of soil–tire contact analysis code based on dynamic FE–DE method. *Journal of Terramechanics,* 41**,** 127-137.

O'SULLIVAN, C. & BRAY, J. D. 2004. Selecting a suitable time step for discrete element simulations that use the central difference time integration scheme. *Engineering Computations,* 21**,** 278-303.

ODA, M. 1972. Deformation mechanism of sand in triaxial compression tests. *Soils and Foundations,* 12**,** 45-63.

ONATE, E. & ROJEK, J. 2004. Combination of discrete element and finite element methods for dynamic analysis of geomechanics problems. *Computer methods in applied mechanics and engineering,* 193**,** 3087-3128.

POTYONDY, D. & CUNDALL, P. 2004. A bonded-particle model for rock. *International journal of rock mechanics and mining sciences,* 41**,** 1329-1364.

SINGH, I. 2004. Application of meshless EFG method in fluid flow problems. *Sadhana,* 29**,** 285-296.

SINGH, I., SANDEEP, K. & PRAKASH, R. 2002. The element free Galerkin method in three dimensional steady state heat conduction. *International Journal of Computational Engineering Science,* 3**,** 291-303.

SINGH, I., SANDEEP, K. & PRAKASH, R. 2003. Heat transfer analysis of two-dimensional fins using meshless element free Galerkin method. *Numerical Heat Transfer: Part A: Applications,* 44**,** 73-84.

XIAO, S. & BELYTSCHKO, T. 2004. A bridging domain method for coupling continua with molecular dynamics. *Computer methods in applied mechanics and engineering,* 193**,** 1645-1669.

ZANG, M., GAO, W. & LEI, Z. 2011. A contact algorithm for 3D discrete and finite element contact problems based on penalty function method. *Computational Mechanics,* 48**,** 541-550.

ZHANG, Z., HAO, S., LIEW, K. & CHENG, Y. 2013. The improved element-free Galerkin method for two-dimensional elastodynamics problems. *Engineering Analysis with Boundary Elements,* 37**,** 1576-1584.

ZHENG, Z., ZANG, M., CHEN, S. & ZHAO, C. 2017. An improved 3D DEM-FEM contact detection algorithm for the interaction simulations between particles and structures. *Powder Technology,* 305**,** 308-322.

ZUOHUI, P. 2000. Treatment of point loads in element free Galerkin method (EFGM). *International Journal for Numerical Methods in Biomedical Engineering,* 16**,** 335-341.

# Chapter 7
# Conclusions

## 7.1    Summary

Despite the fact that the use of rubber reinforced sand material is becoming more popular today, the complexity of soft—rigid material interaction still limits the understanding of the granular mechanism. The use of the numerical tool such as the DEM promotes the knowledge of granular material behaviour and visualises the granular movement such as the material flow and inter–particle contact force development. Gaining the knowledge on the soft—rigid particle interaction enhances the better application of tyre-reinforced geotechnical materials. To achieve this, the research uses a series of different numerical methodologies to study the material behaviour in a wide range of aspects. These include important material properties and using the selective methods, the material behaviour is presented comprehensively. The purpose of the research includes investigating the material shear behaviour, the determination of material segregation based on colour difference, the influence of material surface roughness from a dynamic perspective and combined methodologies with other numerical tools.

## 7.2    Research Contributions

This work contains research contributions in various aspects and they are summarised as follow:

1) A three-dimensional discrete element model was built to investigate the granular behaviour of rubber—sand. Despite the simplicity of linear contact mechanism, this model shows an accurate match with the laboratory results. The micromechanical material behaviour is thus investigated numerically which is impossible to be obtained at laboratory condition. The relocation of particle shows a great influence to the macro material behaviour. The displacement and rotation of granular materials determines the porosity of the material, which leads to the redistribution of contact forces and the change of shear behaviour. The visulalization of the numerical results provides a link between the micro and macro perspectives, promoting a further understanding of the granular material science.

2) A digital image based study is adopted in studying the rubber—sand composite segregation. As a matter of fact, despite the widely application of rubber reinforced material, the material segregation has not been fully discussed which can lead to great heterogeneity due to density difference. The major purpose of the study is to reach a better understanding and identification of the mixture heterogeneity. Comparing the digital image results from numerical and test results, it illustrates the accuracy of the numerical model. The usage of digital image also prevails the previous used visual comparison as it quantifies the segregation degree. Through converting the colour image into a binary picture, the concentration of each material can be easily identified. The using digital image processing (DIP) method quantifies density as the most influential factors to segregation among other material properties such as surface friction, stiffness and damping ratio. With density increases, the

material segregation is more likely to occur but it is restricted by the material surface roughness.

3) A study on the influence of surface roughness is conducted during a dynamic process. A DEM model is developed based on single contact theorem and the numerical model is validated with the theoretical model which connects the restitution coefficient to the loss of energy. In the model, a single disc is allocated with a constant velocity which moves on a roughed surface created by a line of discs. In the dynamic process of DEM, a viscous energy dissipation behaviour is observed during each contact collision, as opposed to the friction induced energy loss. In other words, friction is the material macro behaviour which is considered as a reflection of micro contact collisions. Further studying on the surface roughness identified that the actual collision angle has the most significant influence to the amount of energy loss.

4) A combined numerical method between the DEM and EFG is introduced to simulate the contact relationship between rigid—soft material. Two domains are created which represent the rigid and soft material by using the DEM and EFG, respectively. The advantages of using the EFG includes avoiding the volumetric locking and the numerical mesh. In the EFG method, the material is represented by a number of scatter nodes while the background cell is supported by gauss points. The base function is constructed by using an orthogonal weighted function. A Newmark-β method is adopted to solve the dynamic equation in the element–domain. To bridge the two different domains, the contact force is converted to point loads test and applied at the domain boundary by using Dirac delta function. This coupling method illustrates an

efficient simulation between soft—rigid materials by considering the deformation of the soft domain and it is more advantageous than DEM–FEM coupling with the improvement of computer power.

## 7.3    Limitation and recommendations for future research

1) One of the limitations of the DEM based method is the challenge of numerical efficiency. As the geotechnical material contains a large number of particles, simulating all the material granules is impossible so that a feasible method is to scale the particle sizes or to neglect the particles which are insignificant regarding their sizes. This is not always realistic but with the improvement of the computer efficiency, it is likely to take the real particle number into account in the future.

2) The current research takes the disc or spherical shape for 2D and 3D analysis, respectively. To restrict the particle's rotation, a rolling friction parameter is introduced. However, the actual shape of the particle varies and it is difficult to quantify them in the numerical analysis. Previous researchers used sphere clumps or polyhedron in the analysis but it generates other problems. For example, a sphere clump still has a point contact with other clumps while the polyhedron may induce a larger degrees of freedom which exacerbates the numerical efficiency. The best method to solve the problems is still depend on the power of the computer which may take the realistic particle shapes into consideration.

3) The soft–rigid contact relationship is the biggest challenge of using DEM as this method considers all particles to be non-deformable. This may lead to an unrealistic penetration into soft material due to particle overlap assumption at the contact. With the introduction of combining EFG, it is possible to consider the soft material deformation but it complicates the numerical calculation and more computer power is required. At this stage there is no commercial package to combine these two methods and the difficulty to implement the algorithms limits its application. A recommendation to address this issue includes either to develop a constitutive material relationship between soft and rigid material or to increase the computer power to improve the calculation.

# Appendix:

# Copy of Paper 1 (As published)

Publication: Wang, C., Deng, A. & Taheri, A. 2018. Three-dimensional discrete element modelling of direct shear test for granular rubber-sand. *Computers and geotechnics*, 97, 204-216.

# Copy of Paper 2 (In Press)

Publication: Wang, C., Deng, A. & Taheri, A. 2018. Three-dimensional discrete element modelling of direct shear test for granular rubber-sand. *Computers and geotechnics*, 97, 204-216.
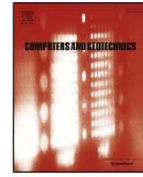
# Copy of Conference Paper 3 (As published)

Wang, C., Deng, A. and Taheri, A., 2018, May. Energy Dissipation Due to Surface Asperity: A Micro-scale Study. In *GeoShanghai International Conference* (pp. 975-983). Springer, Singapore.

Research Paper

# Three-dimensional discrete element modeling of direct shear test for granular rubber–sand

Can Wang, An Deng[*], Abbas Taheri

*School of Civil, Environmental and Mining Engineering, The University of Adelaide, SA 5005, Australia*

A R T I C L E   I N F O

A B S T R A C T

Three-dimensional discrete element modeling of direct shear test conducted on granular rubber–sand is presented. Excellent agreement was attained between the simulation and test results, verifying the model's capacity of examining mixtures shear behavior. Important particulate-scale observations were attained, including the inter-particle contacts force, particles displacement and rotation, porosity and their variation with rubber particle contents. The observations demonstrate that the rubber particles inclusion amends the mixture stiffness, grading and packing at the particulate level, leading to a corresponding variation in the material shear behavior. Some interesting particulate-level simulations were examined to gain further insight into micro-mechanic characteristics of the mixtures.

## 1. Introduction

There are approximately 48 million tons of waste tires per year generated in Australia; a low percentage is recycled or managed properly [1]. An important solution to increasing the recycling rate is to process the wheels tire into a range of smaller pieces of rubber (e.g., shreds, chips, particles or fine powers) and incorporate the sliced rubber elements as reinforcements into soils [2–4]. The formed mixtures outperform the soils in respect to resilience, strength, ductility and damping [5–7]. The demonstrated advantages arises from the rubber material's capacity of increasing inter-particle interactions which were confirmed in triaxial [3,5,8,9], direct shear [10–13] and uniaxial pull-out tests [14].

Rubber particles can be mixed with sand into rubber–sand fill [11]. The fill exhibits better workability than the shred- or chip-based mixtures [15]. For the same reason the granular rubber–sand mixtures avoid segregation problems and aim at applications where otherwise are difficult to access. Additional value lies in the rubber–sand being lighter in weight by 20–40% than the sand backfill depending on the materials per cent used [16]. The use of the lightweight material reduces loads acting on the surrounding infrastructures or utilities (e.g., retaining walls or pipelines). Rubber–sand is also graded to facilitate water percolation and drainage and thus avoid environment or climate related concerns such as frost heave. Direct shear tests conducted on rubber–sand samples suggested that the material shear strength remains similar in magnitude to that of sand, demonstrating a substitute for sand backfills [3,16,17]. To understand the shear behavior, discrete

element modeling was conducted on rubber–sand mixtures subjected to direct shear tests [3,8,12,18,19]. These studies gained insight into the inter-particle interactions and demonstrated the role of rubber particles in changing the material fabrics and the material stiffness. Most of the discrete element simulations were implemented in a two-dimensional plane which under-represents the three-dimensional shape of the particles and neglects the boundaries associated with the samples [20–22]. The purpose of this study is to conduct three-dimensional numerical simulations on the rubber–sand subjected to direct shear tests. The discrete element method is used to conduct the simulations. The simulations are validated against laboratory test results and then deployed to examine how the rubber particles inclusion influences the material shear behavior.

## 2. Materials and method

The materials include sand and rubber particles. The respective gradation curves are shown in Fig. 1. The sand ($D_{50} = 0.58$ mm) is well graded to fit into the pore space of the rubber particles ($D_{50} = 5$ mm). Define specific volume fraction $\chi$ = the rubber particle specific volume over the total specific volume of the mixture. Design a series of samples with $\chi = 0, 0.19, 0.34, 0.47, 0.58$ and 1, respectively, where $\chi = 0$ and $\chi = 1$ define the pure sand and the pure rubber particle samples, respectively. A mixture with $\chi > 0.6$ was not viable due to particles segregation [15,23]. The corresponding weight fraction is 0, 0.1, 0.2, 0.3, 0.4 and 1, respectively. A mixer was used, following the steps shown in Ghazavi [11], to gain a uniformly distributed mixture.

[*] Corresponding author.
*E-mail addresses:* c.wang@adelaide.edu.au (C. Wang), an.deng@adelaide.edu.au (A. Deng), abbas.taheri@adelaide.edu.au (A. Taheri).

| Nomenclature | | $N_c$ | number of rubber–rubber contacts on shear plane |
|---|---|---|---|
| | | $N_r$ | number of rubber particles on shear plane |
| $d$ | particle diameter | $V$ | sample volume |
| $D_{50}$ | 50% pass particle size | $\chi$ | specific volume fraction |
| $F$ | sum of normal force at contact | $\delta$ | shear displacement |
| $G_s$ | specific density of solid | $\mu$ | inter-particle friction coefficient |
| $k_n$ | normal stiffness at contact | $\mu_1$ | surface friction of entity 1 |
| $k_{n,1}$ | normal stiffness of entity 1 | $\mu_2$ | surface friction of entity 2 |
| $k_{n,2}$ | normal stiffness of entity 2 | $\sigma_m$ | mean stress at contact |
| $k_s$ | shear stiffness at contact | $v$ | vertical or normal load |
| $k_{s,1}$ | shear stiffness of entity 1 | $\zeta$ | damping coefficient |
| $k_{s,2}$ | shear stiffness of entity 2 | | |



**Fig. 1.** Particle size distribution of sand and rubber particles.

Standard direct shear tests were performed. The sample size measures $60\,W \times 60\,L \times 40\,D$ mm, which was chosen to satisfy the sample size vs. particle size criterion. Pour the sample into the shear boxes, and even and level the materials, enabling a uniform distribution. Prepare four identical samples for one fraction $\chi$ and subject the four samples to vertical load $\sigma_v = 100$, 200, 300 and 400 kPa, respectively. Shear the samples at a rate of 1 mm/min until the occurrence of the greatest shear stress or 5 mm displacement, whichever occurs earlier.

Discrete element simulation was conducted using a commercially accessible software package Particle Flow Code (PFC) 3D. Assemble together ten pieces of wall (a PFC simulation object) to form a compartment, with respective dimensions representing the shear boxes, as shown in Fig. 2. Inside the box compartment is the spherical particles

assembly, with the particle sizes designed in agreement with main portions of rubber particles and sands, respectively. A mass scaling [19] was applied to the particle sizes, enabling a better computer simulation, as having been attained in other studies [8,24]. The scaling results are provided in Fig. 1. Depending on the mixture examined, there are about 6000 sand particles and 1000 rubber particles created to fill up the boxes space. The mixture in the shear boxes is shown in Fig. 2. After placing the particles inside the shear boxes, apply the servo-control method [25] to release excess sphere contact forces where there were.

The linear elastic model of PFC3D was used to replicate the shear stress–displacement relations. The linear model outperforms the non-linear Hertz model in respect to the use of the servo-control, which is a model in-built developed to maintain a load acting onto the material

**Fig. 2.** Material assembly in direct shear boxes.



Sand particle

Rubber particle
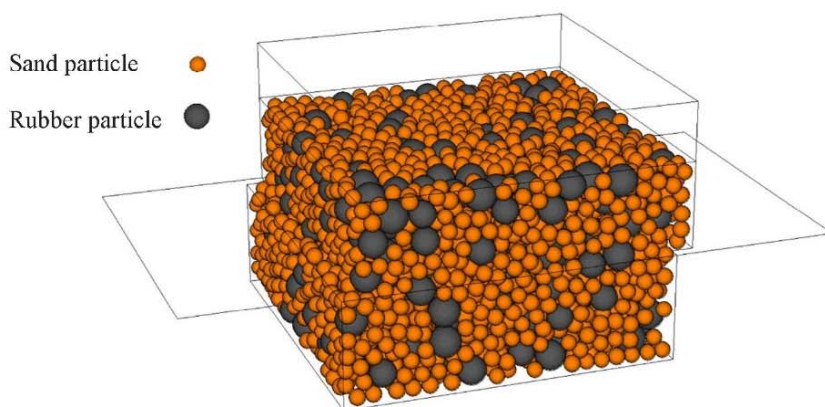
[25]. The linear model is illustrated in Fig. 3. Two entities (or particles), 1 and 2, interact. The interaction is modeled through a set of physical units: springs, dashpots and a slider. The springs are used to create a linear elastic relation between relative displacement and contact force. The dashpots are applied to provide viscosity at shear and normal directions, respectively. The material properties for the simulation are summarized in Table 1. In the table, the inter-particle properties were determined by PFC3D using the following equations:

$$\frac{1}{k_n} = \frac{1}{k_{n,1}} + \frac{1}{k_{n,2}} \tag{1}$$

$$\frac{1}{k_s} = \frac{1}{k_{s,1}} + \frac{1}{k_{s,2}} \tag{2}$$

$$\mu = \min(\mu_1, \mu_2) \tag{3}$$

where $k_n$ and $k_s$ are normal and shear stiffness at contact; $k_{n,1}$ and $k_{n,2}$ are normal stiffness of entity 1 and 2, respectively; $k_{s,1}$ and $k_{s,2}$ are respective shear stiffness; $\mu$ is inter-particle friction coefficient; $\mu_1$ and $\mu_2$ are respective entity surface friction.

As suggested in previous studies [26–28], the quartz sand stiffness falls into the order of magnitude of $\times 10^7$ N/m. A lower order of magnitude of $\times 10^5$ N/m was suggested for rubber material [29]. These values were taken as the points to depart and, as suggested in Coetzee and Els [30], plugged into numerical iterations of harmonizing the shear test results, aiming at obtaining the final stiffness and other micro-properties. The simulations are shown in Fig. 4. Excellent agreement is obtained between the test and simulation results for all series of tests. That means the material properties in Table 1 are verified as input values for the discrete element model to replicate the particles motion. All of the samples exhibit a strain-hardening relation where there is no clear occurrence of failure. The relationship agrees with the results provided in similar rubber–sand studies (e.g., [10]). The strain-hardening relationships become pronounced when the applied vertical load $\sigma_v$ or rubber content $\chi$ increases. The strain-hardening curves suggest two aspects: (i) the sand samples are loosely packed when sheared and there is no clear shear dilation; and (ii) the rubber particles inclusion improves the material packing. The improved packing promotes the material strain-hardening characteristics as well as ductility, which is in favor of stability of backfilling works.

## 3. Particulate-scale simulation results

### 3.1. Packing

The material packing is illustrated in Fig. 5. Four assemblies are presented: rubber particles, loose-packing rubber–sand, dense-packing rubber–sand, and sand. The assemblies vary in mix fraction, leading to material porosity variation. The rubber particles assembly (i.e., the leftmost diagram) exhibits the greatest porosity. The porosity decreases with the sands inclusion, as the sand particles are finer enough to sit in the pore space formed by the rubber particles skeleton, i.e., the two middle diagrams. The trend, however, seems not to continue into the sand assembly; the sand assembly does not yield the least porosity. Plot one single presumed rubber particle in red in the sand assembly as shown in the rightmost diagram. The presumed rubber particle works better to reduce the pore space than the lot of the equivalent sand particles does. That is, there is a rubber fraction enabling packing optimization. To work out the optimal fraction, a set of eleven assemblies of different mix fractions is packed through simulations, aiming at developing the porosity vs. mix fraction relationship. The relationship is shown in Fig. 6 (i.e., the primary axis vs. the horizontal axis). It is shown that the porosity vs. rubber fraction relationship is not monotonic but concave. The transition sits on sample $\chi = 0.6$, less than which the porosity decreases with $\chi$; otherwise the opposite. Therefore $\chi = 0.6$ is identified as the optimal packing mix. Similar packing

characteristics occur to other binary mixtures. Kim and Santamarina [23] examined packing of sand and rubber chips ($D_{50} = 3.5$ mm) mixtures and recommended an optimal packing fraction of $\chi = 0.67$. Mota et al. [31] assessed spherical glass beads (0.3–3.4 mm sizes) with 2–10 size ratios and confirmed a similar optimal fraction $\chi = 0.6$–0.7 for all series mixtures. All of these results suggest that packing is sensitive to particles size.

Additional mixtures of varying grading characteristics were examined. The simulation results are shown in Fig. 7. Five mixtures are simulated, with a ratio of larger particle size, $D$, to smaller particle size, $d$, ranging from 10 to 2. An additional variant is the large particle fraction, $\chi_D$, from 0 to 1, aiming at broadening the grading characteristics. The results suggest that the grading does influence the packing (i.e. porosity). The mixture becomes dense with $D/d$ increase, meaning small particles infilling the pores of large particles. The infilling effect is optimal at $\chi_D \cong 0.6$, consistently across all of the five series of mixtures. This optimal value agrees with those test results provided in Mota et al. [31].

The secondary vertical axis of Fig. 6 reads the force density for the samples examined. The force density is defined as the sum-of-force at contact, $F$, normalized to the sample volume, $V$, and mixture median diameter, $D_{50}$, i.e., $F/(V \times D_{50})$. For demonstration purpose, the forces at the contacts of a single particle are illustrated in the third diagram in Fig. 5. The value of $F$ is the sum of the forces at the contacts of interest, e.g., the rubber particle contacts. Where a particular portion of particles is examined, the force density measures the particles capacity of sharing the inter-particle force. Fig. 6 shows the force density at rubber (and sand) contact vs. rubber fraction curves, each corresponding to one of the four vertical loads (i.e., 100, 200, 300 and 400 kPa). For each of the curves, the rubble content is the only variant, with the rest conditions remain the same. The purpose is to examine the rubber (or sand) contact force with respect to rubber content where the load is constant. All of the four curves are convex; and the transitions occur consistently at $\chi = 0.58$, at least for the rubber fractions examined. The transition points also agree with the optimal value $\chi = 0.6$ for packing. Define a transition zone $\chi = 0.55$–0.65 where the assembly works best in packing and load sharing: the rubber fraction develops into a skeleton where the sands largely infill the skeleton pore spaces and enable optimal packing; in the meantime the rubber particles share the most significant portion of the loads and guarantee material strength capacity.

### 3.2. Inter-particle forces

The inter-particle forces are examined on sample $\chi = 0.34$ being sheared under the vertical load $\sigma_v = 200$ kPa as an example. To gauge the forces evolution, select five points of $A$ to $E$ on the corresponding shear stress–displacement curve (Fig. 8). The five points read displacement values of $\delta = 0$, 1, 4, 5 and 6 mm, respectively, aiming to
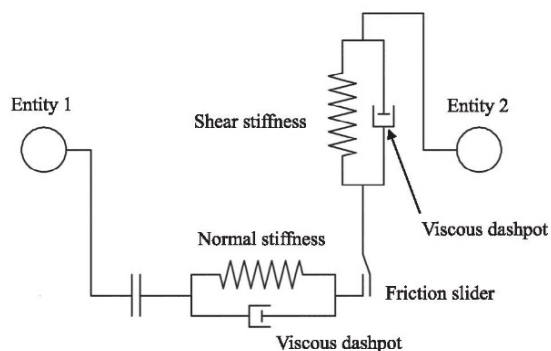


Fig. 3. Inter-particle linear contact model.

**Table 1**
Micro- properties for discrete element simulation.

| Property | Value | | |
|---|---|---|---|
| | Sand particle | Rubber particle | Shear box |
| Contact normal stiffness, $k_n$ (N/m) | $5.9 \times 10^7$ | $8 \times 10^5$ | $1 \times 10^8$ |
| Contact shear stiffness, $k_s$ (N/m) | $5.9 \times 10^7$ | $8 \times 10^5$ | $1 \times 10^8$ |
| Particle diameter, $d$ (mm) | 2.4–2.6 | 4–5.5 | N/A |
| Specific density of solid, $G_s$ | 2.65 | 1.2 | N/A |
| Damping coefficient, $\zeta$ | 0.7 | 0.7 | N/A |
| Inter-particle friction coefficient, $\mu$ | 0.55 | 0.60 | 0.20 |

span the complete shear process. In addition a separate shear is simulated which conducts an unloading-reloading process in the middle of shear, examining the damping behavior of the model. In the process, the boxes reverse from $\delta = 2$ mm to $\delta = 1$ mm, then are re-sheared to $\delta = 6$ mm. The unloading-reloading process creates a hysteresis loop, demonstrating the elastic-plastic behavior of the shear process. The unloading clearly and quickly releases the shear stress acting on the sample, and meanwhile an opposite shear force occurs and grows. Upon re-loading, the curve moves back to the point where unloaded, recovering the original shear stress released, and interestingly continues in a new pathway. The new pathway rises above that without the load loop, meaning the material stiffens. That is, the load loop helps compact the mixture and the damping properties assigned to the model reflects the physical behavior of the sample.

The inter-particle forces are plotted as solid lines with its thickness proportional to the force magnitude [25]. The lines connect up into a chain between particles, forming a force chain. The corresponding normal contact force chains that are captured from the front view, together with the illustrated shear boxes, are shown in Fig. 9. The normal contact force, in relation to the shear force, gives a better picture of the particles overlap and motion. The force chains for the sand sample ($\chi = 0$) sheared to $\delta = 6$ mm is also provided for comparison. It is clear that the contact forces progressively redistribute with the shear advance. The forces distribute evenly where there is no shear but the vertical load $\sigma_v$ applied (Fig. 9(a)). When the lower box advances to the left, a force concentration band evolves diagonally and becomes pronounced as shown in Fig. 9(b–e), meaning greater normal contact forces oriented diagonally. When the shear advances, the force band becomes more diagonally oriented. Define a shear advance convention: it is a clockwise shear if the lower box displaces to the left, otherwise an anti-clockwise shear. The clockwise shear which is the case of Fig. 9 leads to a force band oriented from the top–left corners to the bottom–right. It is plausible to infer that a top–right to bottom–left force band evolves if the shear acts anti-clockwise. Where sheared to the same displacement $\delta = 6$ mm, the sand sample (Fig. 9(f)) exhibits similar force band orientation, but finer force chains than the corresponding rubber–sand sample does (Fig. 9(e)). This suggests the capacity of rubber materials in concentrating the contact forces. The rubber particles inclusion brings forth to the soil matrix two changes: particles stiffness reduction and particle size increase. Both contribute to the contact forces concentration in view of contact mechanics. The contributions can be illustrated in Fig. 10. An assembly of discs is enclosed in a box. The line between two contacting discs represents a contact force where the line thickness is proportional to the force magnitude. In Fig. 10(a), the presumed larger disc is equivalent in area to the six smaller discs. The substitute shown in Fig. 10(b) eliminates the inter-particle contacts bounded by the larger disc, reducing the total number of contacts in the assembly and therefore the number of force chains. In addition the material stiffness also alters the force chain. Where the assemblies are compressed as shown in Fig. 10(c and d), a larger overlap at contact is captured by the software as a greater contact force. In the meantime, the void around large particle surface provides room for the neighboring small discs to rearrange. The rearrangement helps release a
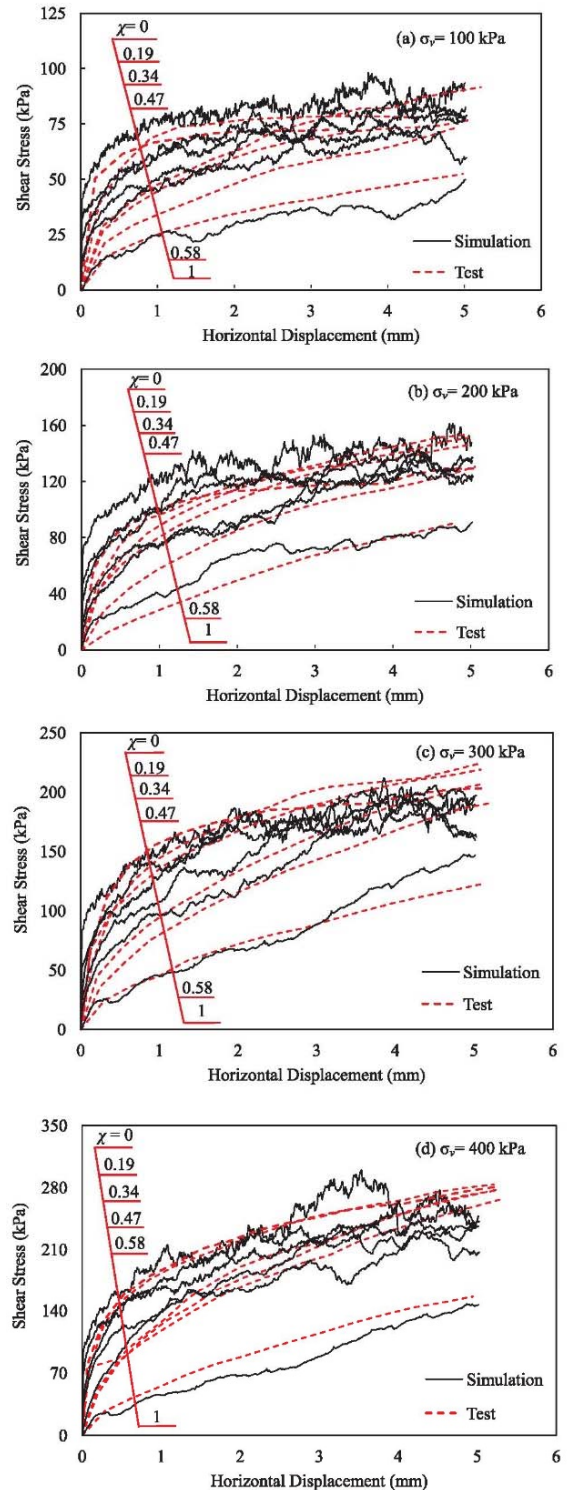


**Fig. 4.** Shear stress–displacement curves for samples subjected to direct shear test with varying vertical loads.

**Fig. 5.** Schematic of mixtures packing.

Rubber particles | Rubber-sand (loose packing) | Rubber-sand (dense packing) | Sand particles
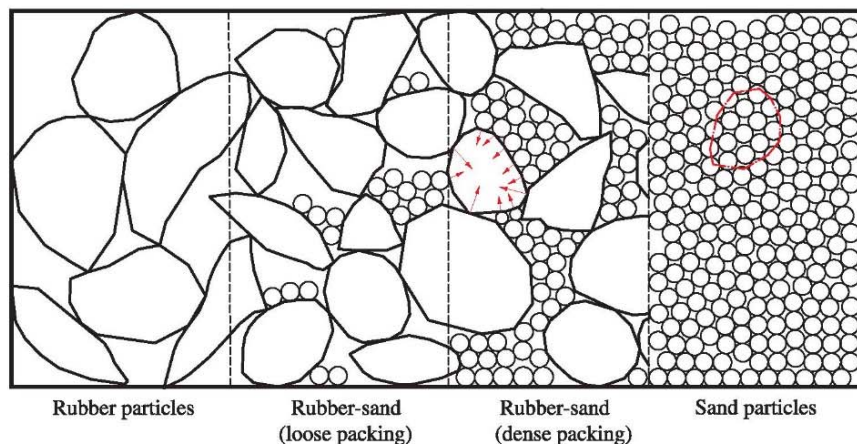
portion of the force developed between the small discs.

The contact force is represented by plotting stress contour lines, aiming at mapping the stress and refining the force band orientation. The measurement sphere approach [25] is used to plot the stress contours. The sphere is designed to capture the equivalent stress field bounded by the sphere. Fig. 11(a) illustrates the enlarged view of one measurement sphere as well as the influenced particles. Fig. 11 (b) shows the measurement spheres designed to the shear boxes. A grid of $4 \times 6$ measurement spheres is created in the shear boxes. All of the spheres are equal in size with a diameter of 10 mm, occupying the inner space of the box. Each of the spheres is at least two times larger in size than the particles examined in the direct shear test and can accommodate up to twenty particles depending on the particles size.

The stress contour maps plotted for the sand sample before and after the shear test are shown in Fig. 12. The shear as an example is conducted under the vertical load $\sigma_v = 200$ kPa until the displacement $\delta = 6$ mm. Plot the contours at three separate vertical planes: the front, middle and back, enabling a 3D view of the stress distribution. The set
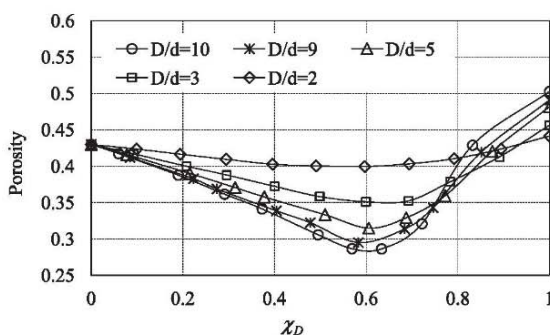


**Fig. 7.** Porosity changes due to varying mixture fraction and particle size.



**Fig. 6.** Porosity and force density for samples in direct shear simulations of varying vertical loads.

**Fig. 8.** Shear stress vs. displacement curve for sample $\chi = 0.34$ sheared under $\sigma_v = 200\,kPa$.

of contour lines is plotted by using the software package MATLAB to process the stress values captured by the measurement spheres. In a measurement sphere, the stress value is defined as the mean stress at contact, $\sigma_m$, which is expressed as $\sigma_m = (\sigma_{xx} + \sigma_{yy} + \sigma_{zz})/3$ w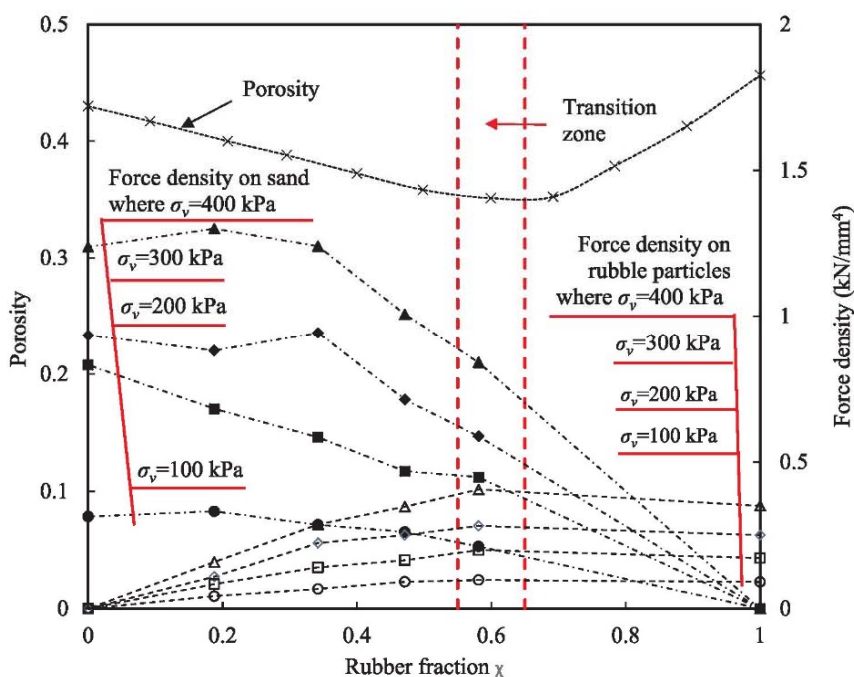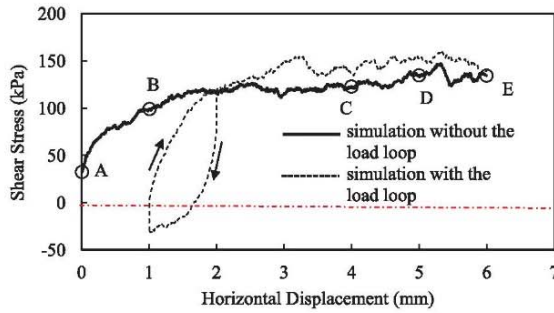here the dimensional stress $\sigma_{xx}$, $\sigma_{yy}$ and $\sigma_{zz}$ are provided by PFC 3D. It is noteworthy that the contour lines draw on the centers of measurement

spheres; therefore the margins are not mapped. The stress contours in Fig. 12(a, c and e) show that the samples remain broadly even in contact stress before the shearing. At a few spots (e.g. the bottoms and corners) the stress values are relatively lower due to the arching created as illustrated in the broken curves. The overall stress values on the map agree with the vertical load $\sigma_v = 200\,kPa$. Where sheared, the sample develops new contour maps as shown in Fig. 12(b, d and f). The changes include the contours orientation to the diagonal, stress concentrations in the upper–left and lower–right corners, and uneven stress distribution on the shear plane. These changes confirm the past research outcomes [32,33] that displacement (and shear stress) is not constant on the shear plane and the active and passive pressure zones evolve in the lower and upper boxes, respectively.

The contour maps shown in Fig. 12 can be illustrated by plotting a diagram of particles contacts. A collection of discs of different sizes is gathered in the closed box as shown in Fig. 13. The discs sitting on the diagonal band clearly overlap with respective neighboring discs. Based on the contact model defined in Cundall and Strack [34], these pronounced overlaps demonstrate greater levels of stressing developed at the contacts and thus add up the load shared by these discs. The discs in the remaining areas show less magnitude of overlap and thus are less



(a) $\delta$=0 mm and $\chi$ =0.34



(b) $\delta$=1 mm and $\chi$ =0.34



(c) $\delta$=4 mm and $\chi$ =0.34



(d) $\delta$=5 mm and $\chi$ =0.34



(e) $\delta$=6 mm and $\chi$ =0.34



(f) $\delta$=0 mm and $\chi$ =0

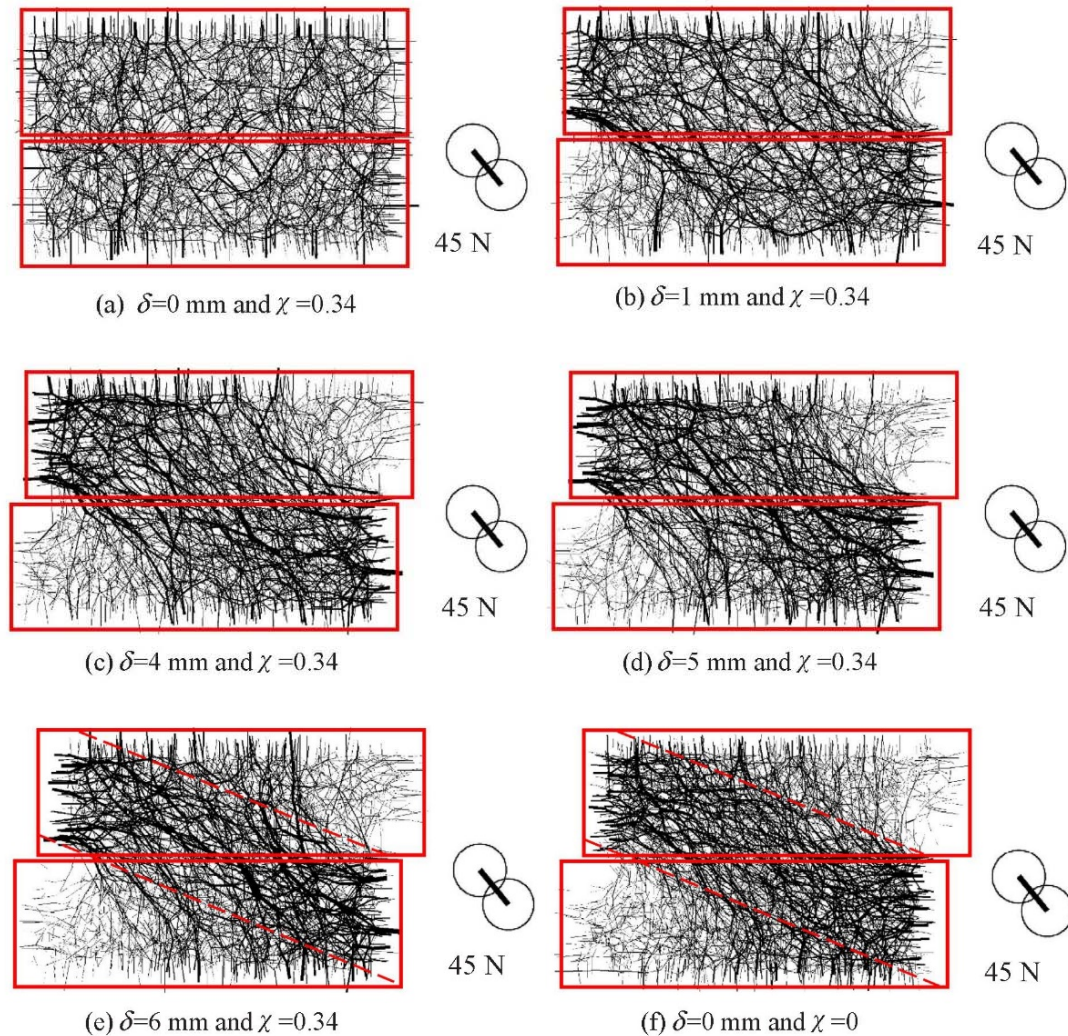**Fig. 9.** Contact force chains drawn at the same scale for samples sheared under $\sigma_v = 200\,kPa$ to different distances.

(a) Free-loading small discs assembly      (b) Free-loading mixed discs assembly

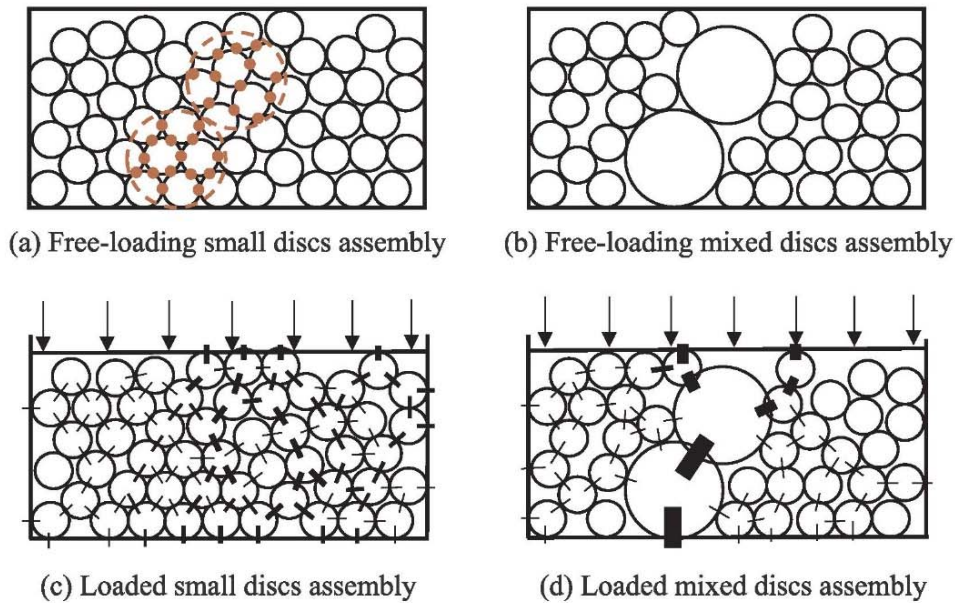(c) Loaded small discs assembly      (d) Loaded mixed discs assembly

**Fig. 10.** Schematic of disc contacts under different load conditions.

effective in counteracting the shear.

### 3.3. Particles displacement vector

Particle displacement vectors are provided in Fig. 14. A vector, as illustrated by the legend, has two independent properties: the magnitude and acting direction. Each of the vectors represents the displacement of a particle, with vector's start (and end) corresponding to the initial (and final) position of the particle, and the length for the travel distance. Vectors are drawn for two samples $\chi = 0.34$ and 0, respectively, both of which are sheared under $\sigma_v = 200$ kPa to $\delta = 6$ mm. The two samples show similar particles displacement: significant leftward motions of particles in the lower box, and minor convex thrusts in the upper. The difference in displacement magnitude between the upper and lower boxes arises from the lower box advancing to the left which is picked up by the simulations. The convex thrusts shown in the upper

box are caused due to the shear dilation [21,22,35]. The convex thrusts are more pronounced in the rubber–sand sample (i.e. $\chi = 0.34$) than in the sand sample (i.e. $\chi = 0$) as illustrated by the vectors. Similar thrust difference was reported in Zhou et al. Zhou et al. [33] which concluded that large-size particles tend to generate a larger strain localization zone and result in stronger dilation. To the right of the convex thrust is a small-scale vortex zone as marked out. This is formed due to the shear strain evolution. As the shear advances, the particles in this zone undergo shear compression [36]. The particles in the vortex also fall into the less-overlap areas (Fig. 13), and the loose inter-particle contacts are in favor of the particles rotations but interlocking or dilating.

### 3.4. Rubber fraction dependence

The above test and simulation results exhibit the rubber fraction dependence of the shear behavior. It is thus of importance to examine
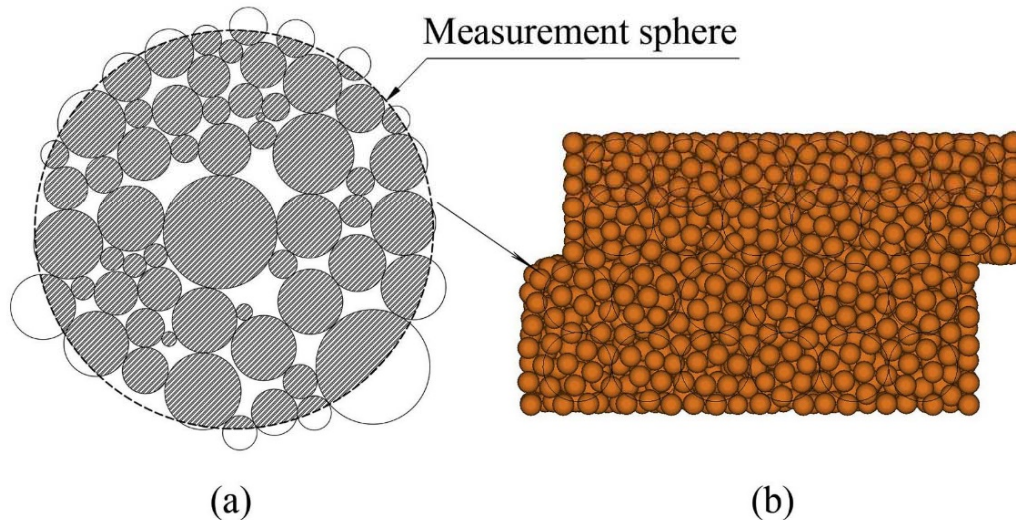


(a)          (b)

**Fig. 11.** Diagram of measurement sphere approach: (a) one measurement sphere and bounded particles, and (b) a grid of measurement spheres designed in the shear box.
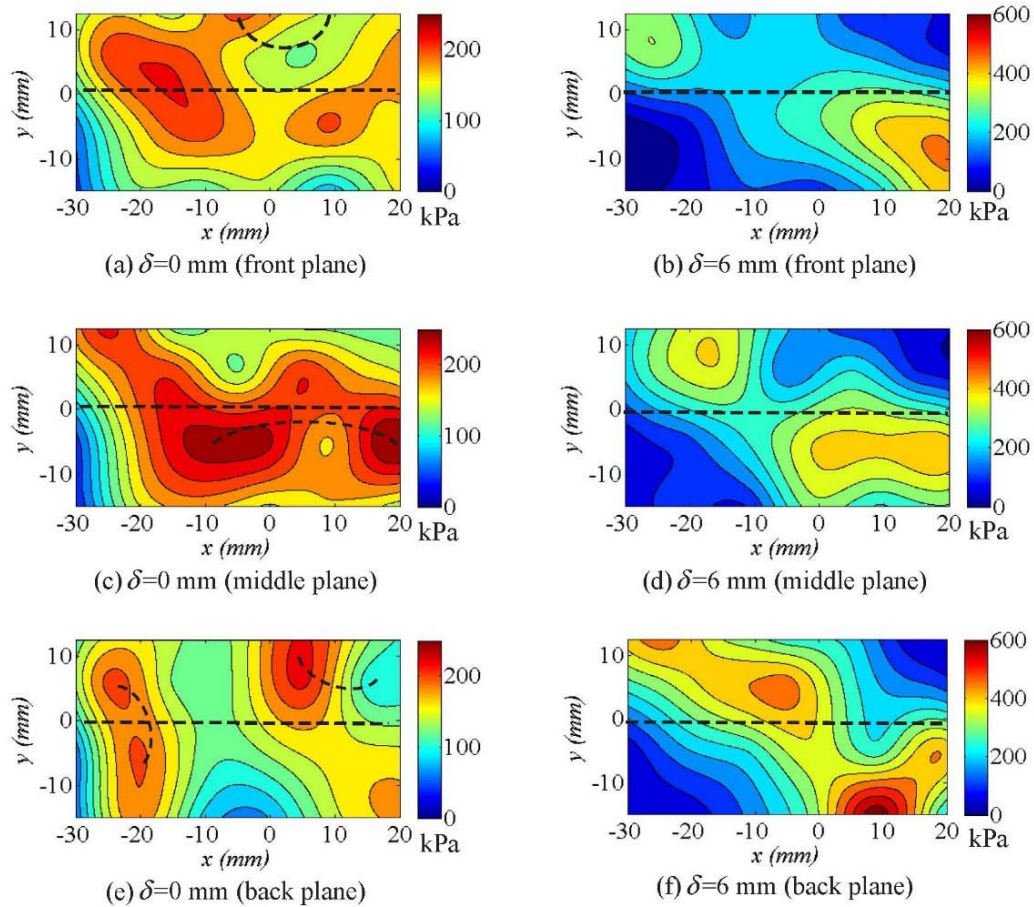
(a) $\delta$=0 mm (front plane)

(b) $\delta$=6 mm (front plane)

(c) $\delta$=0 mm (middle plane)

(d) $\delta$=6 mm (middle plane)

(e) $\delta$=0 mm (back plane)

(f) $\delta$=6 mm (back plane)

**Fig. 12.** Stress contours drawn on vertical planes for sand sample before and after shear.
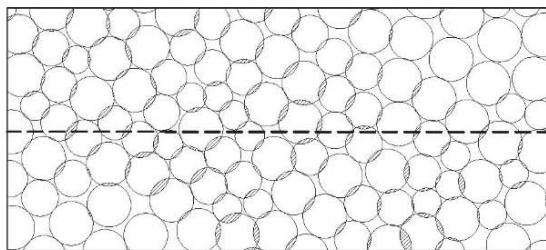


**Fig. 13.** Schematic of discs overlapping when sheared.

the dependence and develop a rubber fraction suitable for applications. The approach is to plot the shear stress vs. rubber fraction relationship for samples subjected to a set of high- to low vertical pressure $\sigma_v$. The pressure $\sigma_v$ is assessed as it influences the shear stress curves. In addition to the aforementioned low- to medium pressures, two high pressures are examined: $\sigma_v = 1$ and 2 MPa. The pressure values are suitable for deep (e.g., 50–100 m) backfilling works, e.g., mining pit renovations. The shear stress–displacement curves obtained from the developed discrete element model are presented in Fig. 15. Four rubber fractions are examined, i.e. $\chi = 0$, 0.34, 0.58 and 1. It is shown that samples $\chi = 0$ and 0.34 show nearly tied curves under both pressures and the curves sit noticeably above those of samples $\chi = 0.58$ and 1. The curves difference suggests that the fraction $\chi = 0.34$ is in favor of the mixture gaining (or maintaining) shear stress; a further higher

fraction may likely lead to strength decrease. This trend agrees with the strength development examined under the low- to medium pressure shear tests (Fig. 4).

Define two stress points, $\sigma_1$, corresponding to the shear displacement $\delta = 1$ mm, and $\sigma_6$, to $\delta = 6$ mm, as the measures assessing the material early- and late-stage shear strength, respectively. The shear strength vs. rubber fraction relationship obtained under a set of vertical pressures is provided in Fig. 16. The pressures examined include 2, 1, 0.4 and 0.1 MPa. Under the high pressures (i.e., $\sigma_v = 2$ and 1 MPa), rubber fraction $\chi = 0.34$ is confirmed in favor of the shear strength development and deemed an optimal mixture. Where the vertical load reduces to 0.4 MPa or lower, the rubber inclusions exhibit marginal effect on the shear strength. That is, the rubber particles gain strength in a way similar to the sand particles where the mixtures are subjected to medium- to low loads, such as medium- to shallow-depth backfilling applications. When placed in a deep application, the mixture becomes sensitive in shear strength to the rubber content and a fraction $\chi = 0.34$ is a preferred choice to gaining shear strength.

Similar rubber content dependency occurs to other rubber chips or shreds based mixtures. Zornberg et al. [5] reported the optimal fraction $\chi = 0.55$ where the rubber shreds (i.e., 20–30 mm by size) were mixed with sands. Rao and Dutta [37] found that a rubber chips fraction of $\chi < 0.35$ shows strength improvement. The optimal content becomes $\chi = 0.2$–0.3 for rubber particles based mixtures [11], which agrees with the outcomes of this current study. These past and current studies suggest that the optimal rubber content is dependent on the rubber particle size, or increases with the size. When the rubber inclusions
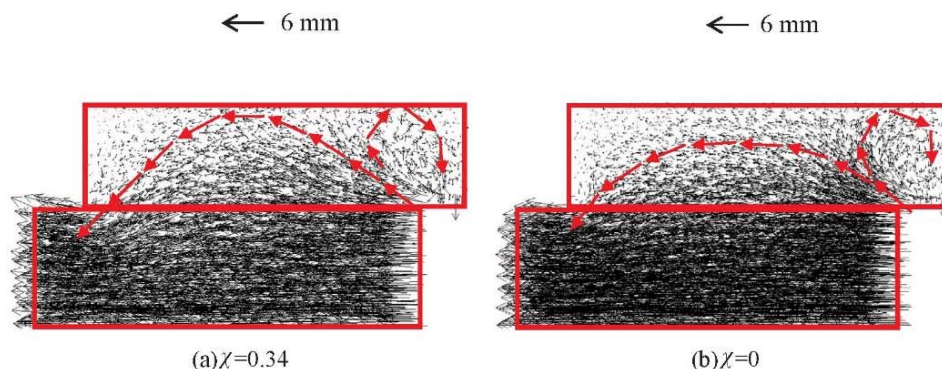
211

Fig. 14. Particle displacement vectors drawn at the same scale for two samples sheared under $\sigma_v = 200$ kPa to $\delta = 6$ mm.



Fig. 15. Shear stress–displacement curves for samples sheared under high pressures.
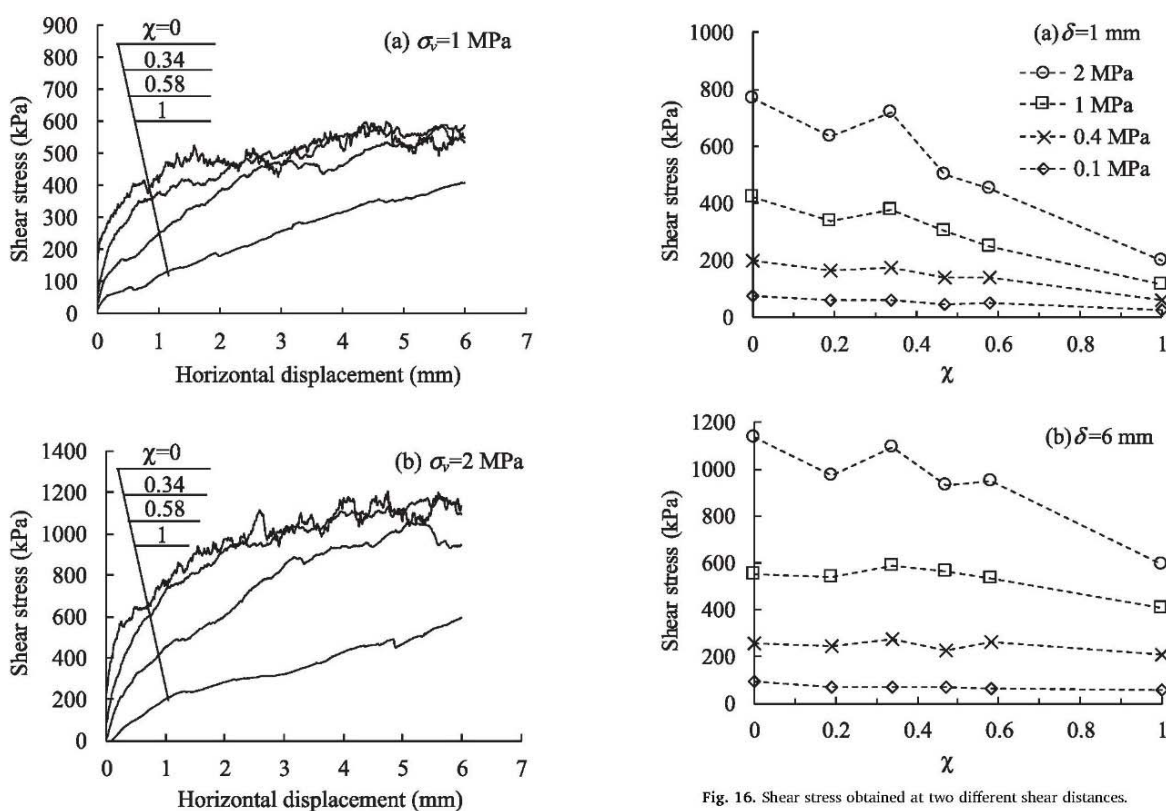


Fig. 16. Shear stress obtained at two different shear distances.

become larger, they work more like continuous media or geo-memberane materials in the mixtures, enabling better particle–surface frictions. The frictions increase with the rubber contents and help mixtures gain strength. Where the rubber contents exceed respective optimal values, there are insufficient volumes of sands infilling the skeleton formed by the rubber inclusions and the packing becomes loose. In this context, the shear strength reduces.

### 3.5. Composite micro-structure

It is worth cross-checking the shear strength development (Fig. 16) against the mixture packing results (Fig. 6). Greater packing is obtained at $\chi = 0.58$ where the pressure acted is 0.4 MPa or less. This $\chi$ value does not agree with the optimal fraction $\chi = 0.34$ obtained for the shear strength. That is, the packing and the shear strength correspond to different optimal fractions. This finding disagrees with Ghazavi [11] associating the shear strength changes exclusively to the mixture packing. In Ghazavi [11], the maximum shear strength occurs at rubber volume fraction $\chi = 0.2$–0.3. The explanation was the occurrence of greatest packing at the same fraction, although the packing was not tested or simulated. The current study suggests that the greatest packing and maximum shear strength may not coincide at the same fraction. The packing is at $\chi = 0.58$ and the strength at $\chi = 0.34$. That means, the single strength–porosity association seems not conclusive. There are underlying factors influencing the shear strength development, one of which is the particles arrangement, in particular the large size particles (rubber) orientation.

Fig. 17 illustrates three mixtures of different $\chi$ values and thus

**Fig. 17.** Schematic of mixtures arrangement as a function of rubber content.

Shear plane

$58\% > \chi > 34\%$     $\chi = 34\%$     $\chi < 34\%$

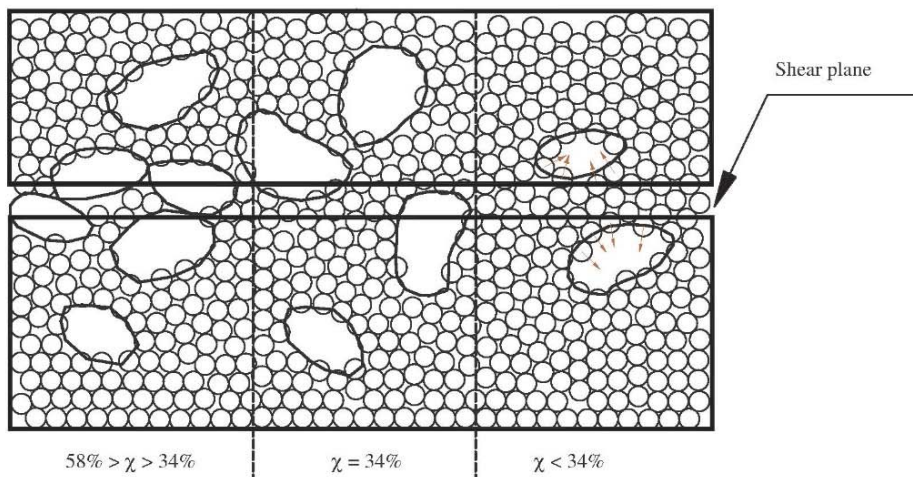varying particles arrangement. From the left to the right, the mixtures decrease in $\chi$ values and thus bring forth varying rubber particles arrangement. An important difference among the diagrams lies in the chance of rubber particles crossing the shear plane and, if there is, the particles number. The chance and number are high where $\chi$ is high, as shown in the leftmost diagram. The particles cross the shear plane, forming a flocculated structure. Given the limited number of particle contacts on the shear plane, the force counteracting the shear is not significant. The force instead builds up where the rubber particles and the sands together sit on the shear plane, as shown in the middle diagram. The number of contacts increases, enabling better frictions and interlocking. Given the rubber particles crossing the plane, an additional component of shear resistance is gained. Where subjected to high pressures, the rubber particles help gain further resistance through the contact flattening mechanism [8]. These strength-gaining effects fade off and the shear resistance decreases if few rubber particles rest across the plane (i.e., the rightmost diagram), whereupon the sands but the rubber particles counteract the shear. Albeit the sand-contact number is significant, a portion of the on-the-plane sand finds room to relocate as illustrated (due to the rubber particles deforming) and fails to gain major shear strength from interlocking or dilating [10,11]. Given these understandings, the mixture particles arrangement is identified as an important factor influencing the shear strength development.

The above three particle arrangement models can be proven based on the rubber particles sitting on the shear plane. Count the number of rubber–rubber contacts, $N_c$, and rubber particles, $N_r$. The $N_c/N_r$ value suggests how the rubber particles orient and to what extent. Plot the $N_c/N_r$ vs. the rubber fraction $\chi$, as shown in Fig. 18. Three representative vertical loads are examined: $\sigma_v = 100$, 1000 and 2000 kPa. Despite the varying loads, $N_c/N_r \cong 1$ where $\chi \cong 0.34$. Otherwise, $N_c/N_r$ moves away from the unity. Where $N_c/N_r = 1$, the particles tend to close up. This is illustrated in Fig. 19. Five diagrams (a–e) are plotted, each with different particle numbers or orientations. Diagrams b–c align linearly, and Diagrams d–e close up. The orientation patterns influence the contacts number. For example, Diagram c has 2 contacts; Diagram d has 3, although the particle numbers remain the same which is 3. Determine $N_c/N_r$ values for the five scenarios. It is suggested that the $N_c/N_r$ value is less than 1 if particles align linearly, e.g., Diagrams a–c; and equal to or near 1 if closed up, e.g., Diagrams d–e.

Fig. 19's results can be applied to the direct shear simulation results. Examine the rubber particle sitting on the shear plane. The rubber particles are illustrated in Fig. 20. Where $\chi$ is small, e.g. Fig. 20(a) and (b), the rubber particles align linearly or are chained. Where $\chi$ increases, as of Fig. 20(c) and (d), the rubber particles close up, forming a mesh. The $\chi$-dependent rubber particles arrangement is in support of

the conceptual drawings shown in Fig. 17. Specifically, where $\chi = 0.34$, the rubber particles evolve a closed-up arrangement, providing room to accommodate sands. As sands and rubber particles are in balanced and well-contacted arrangements, sand–sand, sand–rubber and rubber–rubber interlocks grow; the shear strength builds up accordingly.

### 3.6. Particles rotation

Particles rotate when sheared, and the rotations are crucial to material shear behavior [38]. The rotation is assessed by examining the angular velocity of the particles of interest. As the assembly of particles exhibit varying angular velocity values, it helps the assessment if there is a solution to normalizing the values and mapping out the values for the particles of interest. Fig. 21 shows the normalized values and mapping results for two samples $\chi = 0.34$ and 0, both of which are sheared under $\sigma_v = 200$ kPa to $\delta = 6$ mm. Both samples exhibit a normal distribution of angular velocity, suggesting equal portions of clockwise and anti-clockwise rotations. The distributions also suggest that particles rotate at varying speed. The majority is at rest or rotates at a slow speed; a small portion (i.e., the tails) rotates faster. The particles falling into the 10% percentile as shaded are mapped out in Fig. 21(a) for sample $\chi = 0.34$ and Fig. 21(b) for sample $\chi = 0$, respectively. As reported in Zhang and Thornton [20], these fast-rotation particles largely sit on the diagonal band of top–right to bottom–left, conjugated with the force chains bands (Fig. 9). The study [20] however does not provide details explaining the conjugation. The conjugation occurs partially due to the mechanism of inter-particle shear (i.e. the Coulomb's law of shear strength) which is illustrated in Fig. 22. Two discs contact each other and, at the contact, are subjected to the normal pressure $\sigma$. The discs opt for relative displacement due to the
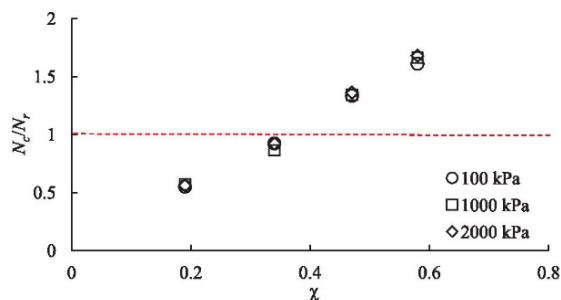


**Fig. 18.** Rubber–rubber contacts to rubber particles vs. rubber content obtained under varying vertical loads.
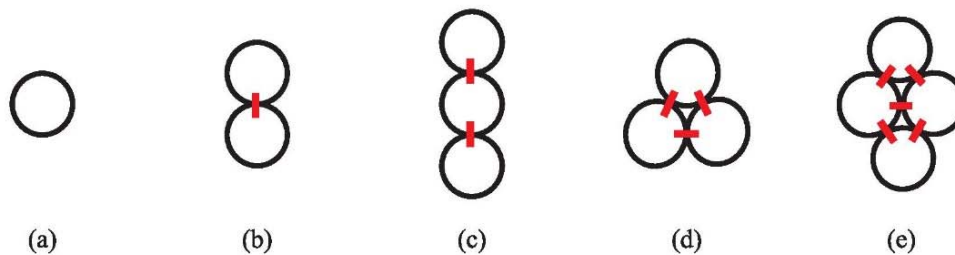
**Fig. 19.** Particles orientation diagrams.

shear force $\tau$ acting at the contact, which is expressed as:

$$\tau = \sigma \tan\phi + c \tag{4}$$

where $\phi$ and $c$ are the inter-particle constants. On the top–right to bottom–left diagonal band (Fig. 9), the particles are subjected to less normal pressures and, based on Eq. (4), less shear forces to rotate. That means the threshold to rotating is low, whereby the particles tend to spin faster if subjected to a driving force. The opposite occurs to the particles sitting on the top–left to bottom–right diagonal band where high-pressure contacts occur.

### 3.7. Particles relocation

The particles relocation is examined by tracking particles motion occurred at five points: *A* to *E*, as shown in Fig. 23. All of the five points originate from sample $\chi = 0.34$ being sheared under $\sigma_v = 200$ kPa. The five points sit on critical places: points *A* to *C* on the shear plane separately, and points *D* and *E* in the upper and lower boxes, respectively. An accurate positioning is attained by defining the points in a 3D coordinate system ($x, y, z$) as illustrated. Develop the coordinate system inside the shear boxes and set the origin over the inside center. The points *A* to *E* are positioned, through a target particle, to coordinate ($x, y, z$) = ($-20, 0, 0$), ($0, 0, 0$), ($20, 0, 0$), ($-20, 0, 10$) and ($20, 0, -10$) mm, respectively. Then, around the target particle, search all neighboring particles. That is, each of the five points encompasses one target particle and its neighboring particles. The neighboring particles count from 2 to 9 depending on the point of interest. The target particles are marked out in the simulation as Nos. 2901, 3481, 3239, 3162 and 10,195, respectively. Similar identity marking is provided on the neighboring particles, enabling a complete track of particles. Each of
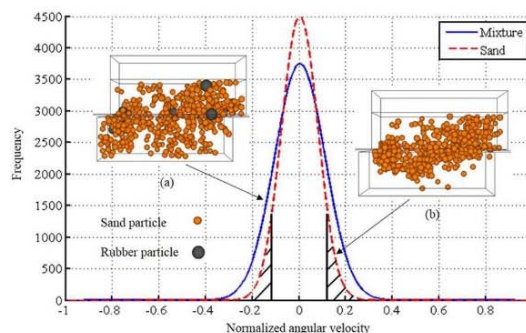


**Fig. 21.** Particles angular velocity distribution and fast-spin particles mapping.
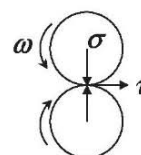


**Fig. 22.** Inter-particle shear and rotation.

the five points comes with a pair of diagrams illustrating the particles arrangement at shear displacement $\delta = 1$ and 6 mm, respectively. It is shown that the particles on the shear plane (i.e., points *A*, *B* and *C*) relocate more clearly than the particles inside the boxes (i.e., points *D* and *E*) do. For instance, at point *A*, particle 10,249 clearly moves to the
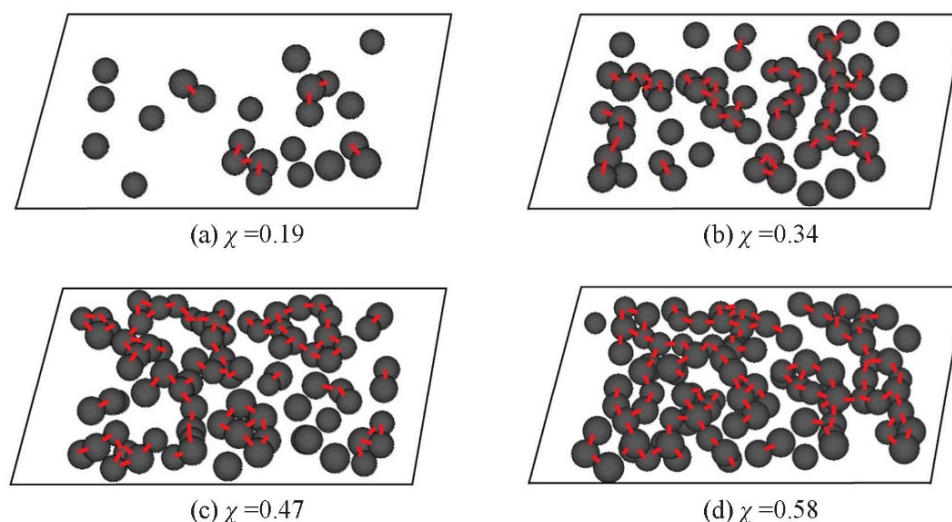


**Fig. 20.** On-shear-plane rubble particles in samples at varying rubber contents.
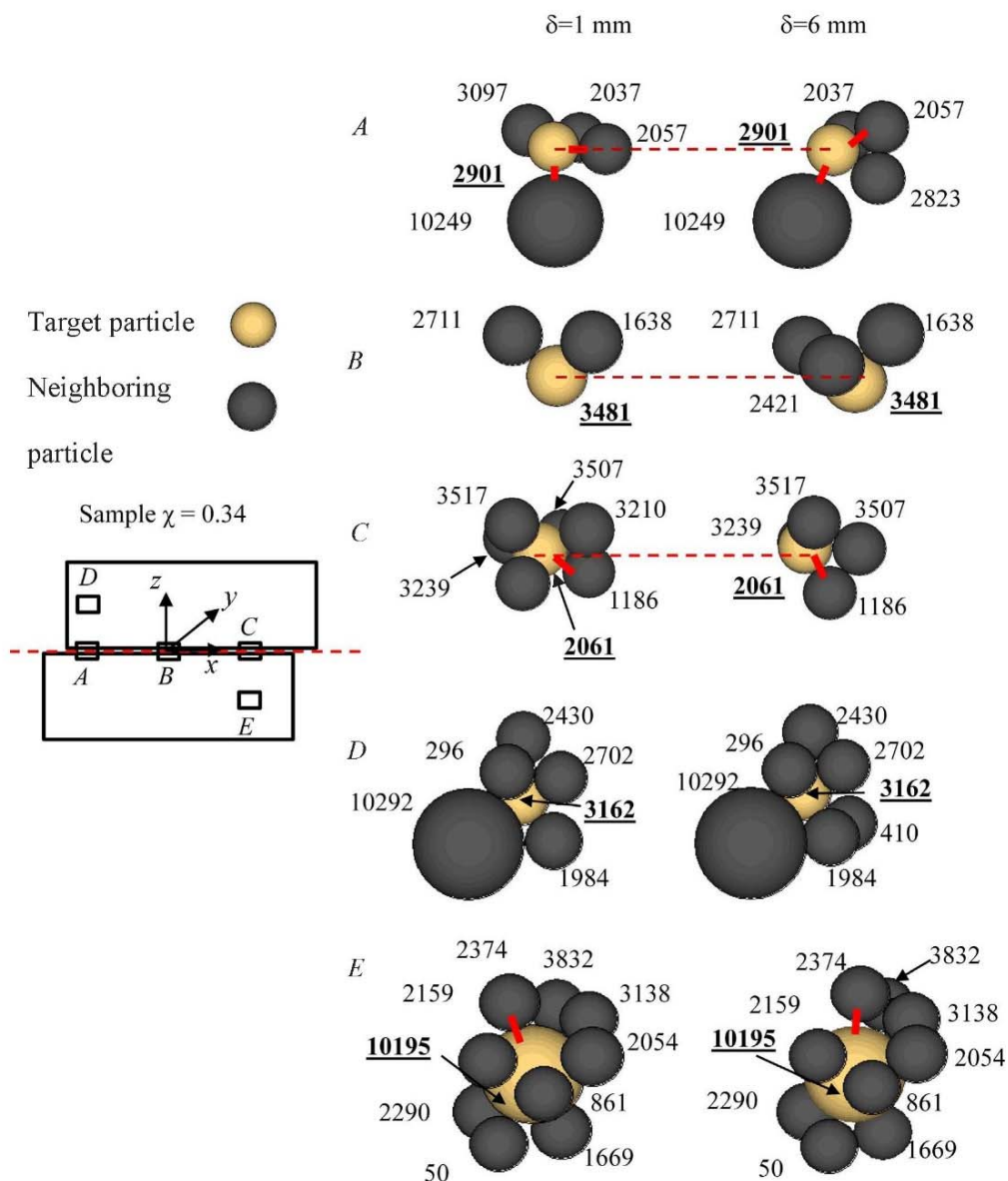
**Fig. 23.** Particles relocations on shear plane and inside shear boxes.

left when the shear travels from 1 mm to 6 mm; in the meantime, particle 2823 joins up the target particle and particle 3097 detaches from it. Similar changes occur to points *B* and *C*. At point *D* (and *E*), however, the particles assembly remain similar in number and arrangement when the shear advances. Although the particles on the shear plane relocate noticeably, it is not clear to confirm a relocation law—either the front relocates more than the rear, or vice versa. However, the particles relocation pattern on the shear plane helps shed light on the process of shear dilation. At point *A*, particle 2823 pushes up particle 2507 and gradually takes over the new position. Similar replacement occurs at point *C* where particle 1186 moves leftward and squeezes into the position of particle 2061; particle 2061 relocates upward.

## 4. Conclusions

Three-dimensional discrete element simulations on the direct shear of the rubber–sand mixtures are presented. The discrete element method enables assessing mixtures shear behavior at a particulate scale. The simulations account for the mixtures fraction, particle stiffness, grading characteristics and normal pressure changes. The simulation results include the mixture packing characteristics, shear stress–displacement relationship, particles contact force chain and force contour maps, particles displacement vector and rotations. The following conclusions are drawn.

A rubber volume fraction of $\chi = 0.55$–$0.65$ offers greater packing for the mixtures examined in this study. The greater packing enables the rubber particles sharing greater contact force. The improved packing promotes the material strain-hardening characteristics and shear ductility. A rubber volume fraction of $\chi = 0.34$ yields greater

shear strength when sheared under 1–2 MPa pressures. Where sheared under lower pressures, the rubber-fraction dependence of shear strength is not significant. The contact forces orient diagonally. The force orientation becomes pronounced with the shear advance. Rubber particles inclusion is able to harmonize in magnitude the force band by reducing particle contacts and stiffness. The particles rotate in varying speed and the speed values follow a normal distribution. The fast-spin particles line up diagonally and in conjugation with the force chains. The particles on the shear plane relocate more noticeably than the particles away from the plane. On the plane, the particle relocations are largely consistent.

### Acknowledgement

### References

[1] Hannam P. Tyre industry divided over how to handle toxic waste. The Sydney Morning Herald. Sydney: Fairfax Media; 2014.

[2] Bosscher PJ, Edil TB, Kuraoka S. Design of highway embankments using tire chips. J Geotech Geoenviron Eng 1997;123(4):295–304.

[3] Lee J, Salgado R, Bernal A, Lovell C. Shredded tires and rubber-sand as lightweight backfill. J Geotech Geoenviron Eng 1999;125(2):132–41.

[4] Tsang H-H. Seismic isolation by rubber-soil mixtures for developing countries. Earthq Eng Struct Dyn 2008;37(2):283–303.

[5] Zornberg JG, Cabral AR, Viratjandr C. Behaviour of tire shred sand mixtures. Can Geotech J 2004;41(2):227–41.

[6] Anastasiadis A, Senetakis K, Pitilakis K, Gargala C, Karakasi I. Dynamic behavior of sand/rubber mixtures. Part I: effect of rubber content and duration of confinement on small-strain shear modulus and damping ratio. J ASTM Int 2012;9(2):1–19.

[7] Tsoi W, Lee K. Mechanical properties of cemented scrap rubber tyre chips. Géotechnique 2010;61(2):133–41.

[8] Valdes JR, Evans TM. Sand-rubber mixtures: experiments and numerical simulations. Can Geotech J 2008;45(4):588–95.

[9] Masad E, Taha R, Ho C, Papagiannakis T. Engineering properties of tire/soil mixtures as a lightweight fill material. Geotech Test J 1996;19(3):297–304.

[10] Ghazavi M, Sakhi MA. Influence of optimized tire shreds on shear strength parameters of sand. Int J Geomech 2005;5(1):58–65.

[11] Ghazavi M. Shear strength characteristics of sand-mixed with granular rubber. Geotech Geol Eng 2004;22(3):401–16.

[12] Lee C, Shin H, Lee JS. Behavior of sand–rubber particle mixtures: experimental observations and numerical simulations. Int J Numer Anal Meth Geomech 2014;38(16):1651–63.

[13] Foose GJ, Benson CH, Bosscher PJ. Sand reinforced with shredded waste tires. J Geotech Eng 1996;122(9):760–7.

[14] Balunaini U, Yoon S, Prezzi M, Salgado R. Pullout response of uniaxial geogrid in tire shred–sand mixtures. Geotech Geol Eng 2014;32(2):505–23.

[15] Edil T, Bosscher P. Engineering properties of tire chips and soil mixtures. Geotech Test J 1994;17(4):453–64.

[16] Yoon S, Prezzi M, Siddiki NZ, Kim B. Construction of a test embankment using a sand–tire shred mixture as fill material. Waste Manage (Oxford) 2006;26(9):1033–44.

[17] Youwai S, Bergado DT. Numerical analysis of reinforced wall using rubber tire chips–sand mixtures as backfill material. Comput Geotech 2004;31(2):103–14.

[18] Patil U, Valdes JR, Evans TM. Swell mitigation with granulated tire rubber. J Mater Civ Eng 2010;23(5):721–7.

[19] Evans TM, Valdes JR. The microstructure of particulate mixtures in one-dimensional compression: numerical studies. Granular Matter 2011;13(5):657–69.

[20] Zhang L, Thornton C. A numerical examination of the direct shear test. Géotechnique 2007;57(4):343–54.

[21] Liu S, Sun D, Matsuoka H. On the interface friction in direct shear test. Comput Geotech 2005;32(5):317–25.

[22] Liu S. Simulating a direct shear box test by DEM. Can Geotech J 2006;43(2):155–68.

[23] Kim H-K, Santamarina J. Sand–rubber mixtures (large rubber chips). Can Geotech J 2008;45(10):1457–66.

[24] Feng K, Montoya B, Evans T. Discrete element method simulations of bio-cemented sands. Comput Geotech 2017;85(May):139–50.

[25] Itasca. PFC3D 4.0 User Manual. Minneapolis, MN USA; 2008.

[26] Nakata A, Hyde M, Hyodo H, Murata A. A probabilistic approach to sand particle crushing in the triaxial test. Géotechnique 1999;49(5):567–83.

[27] Potyondy D, Cundall P. A bonded-particle model for rock. Int J Rock Mech Min Sci 2004;41(8):1329–64.

[28] Wang Y-H, Leung S-C. A particulate-scale investigation of cemented sand behavior. Can Geotech J 2008;45(1):29–44.

[29] De Bono JP, McDowell GR, Wanatowski D. Discrete element modelling of a flexible membrane for triaxial testing of granular material at high pressures. Geotech Lett 2012;2(4):199–203.

[30] Coetzee C, Els D. Calibration of granular material parameters for DEM modelling and numerical verification by blade–granular material interaction. J Terramech 2009;46(1):15–26.

[31] Mota M, Teixeira J, Bowen WR, Yelshin A. Binary spherical particle mixed beds: porosity and permeability relationship measurement. Trans Filtr Soc 2001;1(4):101–6.

[32] Wang J, Dove J, Gutierrez M. Discrete-continuum analysis of shear banding in the direct shear test. Géotechnique 2007;57(6):513–26.

[33] Zhou Q, Shen HH, Helenbrook BT, Zhang H. Scale dependence of direct shear tests. Chin Sci Bull 2009;54(23):4337–48.

[34] Cundall PA, Strack OD. A discrete numerical model for granular assemblies. Géotechnique 1979;29(1):47–65.

[35] Masson S, Martinez J. Micromechanical analysis of the shear behavior of a granular material. J Eng Mech 2001;127(10):1007–16.

[36] Indraratna B, Ngo NT, Rujikiatkamjorn C, Vinod J. Behavior of fresh and fouled railway ballast subjected to direct shear testing: discrete element simulation. Int J Geomech 2012;14(1):34–44.

[37] Rao GV, Dutta R. Compressibility and strength behaviour of sand–tyre chip mixtures. Geotech Geol Eng 2006;24(3):711–24.

[38] Cui L, O'sullivan C. Exploring the macro-and micro-scale response of an idealised granular material in the direct shear apparatus. Géotechnique 2006;56(7):455–68.

1

2

# Digital Image Processing on Segregation of Rubber Sand Mixture

Can Wang[1]; An Deng[2]; and Abbas Taheri[3]

**Abstract:** The segregation of rubber sand mixtures, when they form heaps, as observed by the method of digital image processing (DIP), is presented. Through segmenting the digital images into a binary picture, the DIP method enables material ingredients identification and three-dimensional mapping of mixture segregation. This helps reach a better understanding of mixture heterogeneity when incorporating artificial material into conventional geotechnical materials. To gain an insight into the mixture heterogeneity, the DIP results were used to validate a discrete element model, and the model was then used to examine the influence of particle properties on the segregation. The discrete element simulations showed that the particle density is critical in material segregation, and the segregation becomes more noticeable when the materials density ratio increases. This trend is restricted by increasing the interparticle surface roughness. **DOI:** 10.1061/(ASCE)GM.1943-5622.0001269. © 2018 American Society of Civil Engineers.

**Author keywords:** Segregation; Digital image processing; Discrete element; Density; Roughness.

## Introduction

Waste tires create problems such as landfilling, health, and environmental challenges. The tires can go into recycling facilities for a new life. One of the new life solutions is to reuse the tires as geomaterial alternatives (Foose et al. 1996; Zornberg et al. 2004). Rubber sand mixture is an attractive alternative and has been widely used in geotechnical applications, including roadway construction (Bosscher et al. 1997; ASTM 1997), lightweight fill (Ahmed and Lovell 1993; Masad et al. 1996), backfill for retaining walls (Humphrey and Manion 1992; Garga and O'shaughnessy 2000), slope stabilization (Poh and Broms 1995), and seismic isolation system (Tsang et al. 2012). Where the mixtures are prepared, placed, or compacted, the ingredients likely segregate. Whichever induces the material segregation, a segregated profile causes heterogeneity and sometimes severe instability problems such as liquefaction (Yoshimine and Koike 2005). The sand and rubber ingredients differ at least in density and surface roughness and, when placed as a mixture, lead to flow-induced segregation as defined by Ottino and Khakhar (2000). In general, the factors causing segregation can be classified into particle sizes, densities, shapes, and particle resilience (Williams 1976). Of all the segregation mechanisms, trajectory segregation, percolation of fine particles, and the rise of coarse particles on vibration are commonly recognized (Kudrolli 2004). Other mechanisms such as rolling, sieving, water flow, soil crushing, etc., were also reported in early works (Kuerbis and Vaid 1988; Ottino and Khakhar 2000; Lőrincz et al. 2005; Watabe et al. 2014).

The first reported work on segregation mechanism came from Donald and Roseman (1962), who investigated the experiment of mixing particles of different sizes and densities in a rotating horizontal drum. The recent work to study segregation by using the discrete element method (DEM) has become popular, as the DEM is regarded as a valuable tool for studying granular flow and mixing mechanisms, e.g., free surface (Shi et al. 2007) and hopper discharge (Anand et al. 2010). These tests have shown unanimously that the particle size and density are the major factors leading to segregation. Other factors, such as shape, chute angle, liquid content, rolling friction, and magnetic fields, also contribute to material segregation (Anand et al. 2010).

While extensive studies have been performed to test material segregation, there is limited research regarding segregation phenomenon when the rubber sand mixture falls to form a heap. There is also a limited quantitative connection in terms of segregation measurements between numerical simulations and experimental observation. Studies of the sand pile by DEM simulation are limited when it comes to the angle of repose or force of percolation (Zhou et al. 1999; Yang et al. 2000; Zhou et al. 2001). And although significant achievements have been made since Zhou et al. (1999) first introduced the concept of rolling friction in studying heap formation, there is a lack of study regarding the phenomenon of segregation.

This paper presents the segregation phenomenon observed when the rubber sand forms a heap. It investigates the influence of particle properties using DEM. Since many studies have been conducted on evaluating particle sizes, this paper focused on studying segregation without size difference, e.g., a mixture with similar ingredient sizes. The results of the study are presented as a comparison between experiments and numerical simulations so that a parametric study can be performed. Also, it contains the calibration process for restitution coefficient measurements and the angle of repose tests so that important microproperties could be obtained. These examinations help quantify mixture segregation when the mixture is processed. The parametric study will examine and identify the critical material properties causing the segregation and whereby solutions can be recommended to reduce the segregation.

[1]Graduate Student, School of Civil, Environmental and Mining Engineering, Univ. of Adelaide, Adelaide, SA 5005, Australia. Email: c.wang@adelaide.edu.au

[2]Senior Lecturer, School of Civil, Environmental and Mining Engineering, Univ. of Adelaide, Adelaide, SA 5005, Australia (corresponding author). ORCID: https://orcid.org/0000-0002-3897-9803. Email: an.deng@adelaide.edu.au

[3]Senior Lecturer, School of Civil, Environmental and Mining Engineering, Univ. of Adelaide, Adelaide, SA 5005, Australia. Email: abbas.taheri@adelaide.edu.au

## Methodology

In this section, prior to investigating material segregation, a number of tests were performed to study granular behavior. DEM was adopted as a numerical method to calibrate micromechanical properties. This could be achieved through heap-forming test and repose angle studies. Serious segregation was identified in the mixture pile after the heap-forming process in both numerical simulation and tests. To accurately measure the material segregation, digital image processing (DIP) was used. Detailed discussion will be provided in the following sections.

### *Discrete Element Method*

To simulate the granular interaction, the use of DEM can provide an insight into the micromechanical properties reflecting the macroscopic phenomenon. This method simulates the material as a collection of frictional and rigid spheres so that complex problems can be addressed through observing particles' contact (Cundall and Strack 1979). The contact model, as depicted in Itasca (2009), is shown in Fig. 1. The contact model can be treated as either a linear model or as a nonlinear model (e.g., Hertz–Mindlin contact). Both models produce normal and shear forces based on normal contact and shear stiffness, respectively. A Coulomb limit is imposed on the shear force considering a friction coefficient, $u$. The dashpot component is assumed to dissipate extra energy in both normal and shear directions.

### *Damping Ratio*

As a part of an examination of the microscopic properties, it is necessary to evaluate the effect of material damping, which could have an impact on mixture segregation. The damping ratio is a dimensionless parameter that quantifies system decay during oscillations, which is an important property input in DEM. Also, for a numerical analysis on rubber sand mixture, the individual damping ratio at granular contact is not clear and lacks a calibration process (Patil et al. 2010; Evans and Valdes 2011; Lee et al. 2014). In the repose



(a)

(b)

**Fig. 3.** Maximum restitutive height captured by high resolution camera for silica beads and rubber beads.

F3 : 13

F3 : 2



F1 : 1  **Fig. 1.** Schematic of discrete element method (DEM) model.



F2 : 1  **Fig. 2.** Rubber and silica beads used in the damping ratio calibration.



**Fig. 4.** Restitution height for silica and rubber beads.

F4 : 1

F5 : 1    **Fig. 5.** The relationship between the damping coefficient and the restitution coefficient with various material properties.



(a)

(b)

F6 : 1    **Fig. 6.** Repose angle test setup: (a) experimental schematic drawing;
F6 : 2    and (b) numerical simulation.

**Table 1.** Input parameters used in simulation

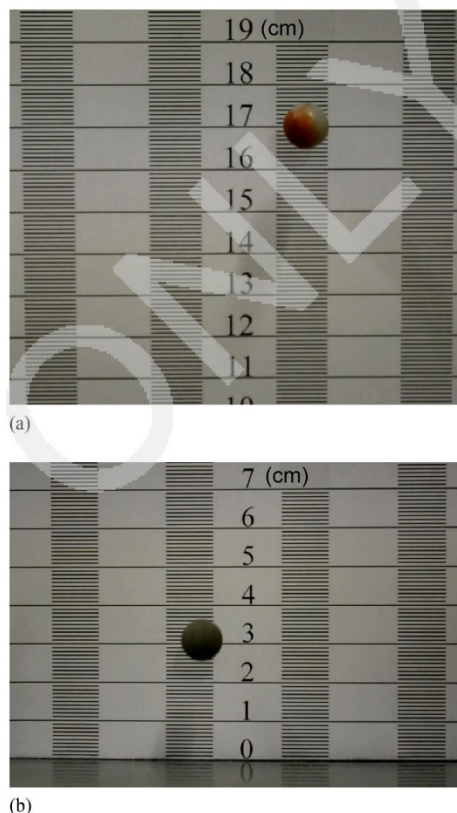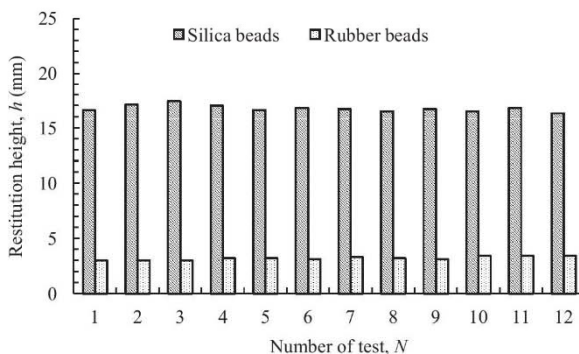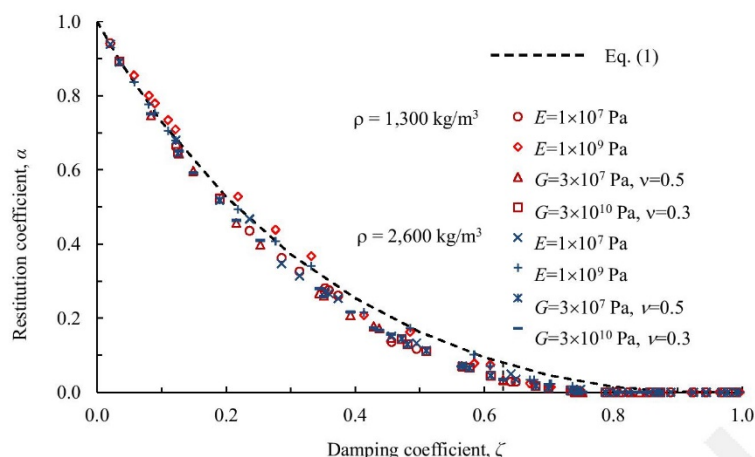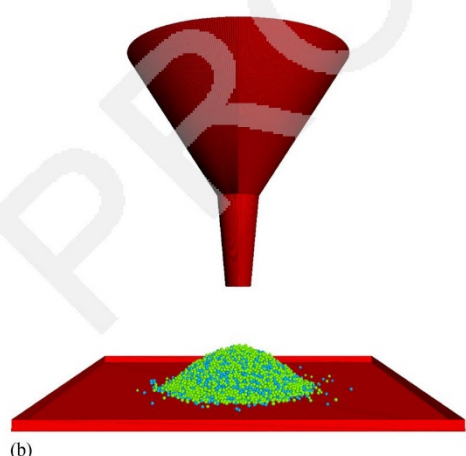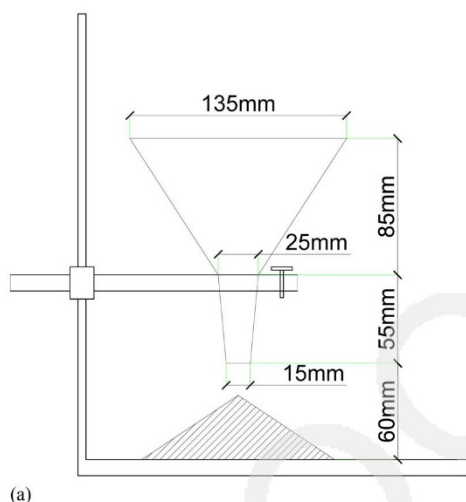| Parameter | Value | |
|---|---|---|
| Diameter of sand particle, $d_s$, mm | $1.54-2$ | T1 : 2 |
| Diameter of rubber particle, $d_r$, mm | $1.54-2$ | T1 : 3 |
| Density of sand particle, $\rho_s$, kg/m³ | 2,600 | T1 : 4 |
| Density of rubber particle, $\rho_r$, kg/m³ | 1,300 | T1 : 5 |
| Sliding friction of sand particle, $f_{s,s}$ [a] | 0.31 | T1 : 6 |
| Sliding friction of rubber particle, $f_{s,r}$ [a] | 0.6 | T1 : 7 |
| Rolling friction of sand particle, $f_{r,s}$ [b] | 0.7 | T1 : 8 |
| Rolling friction of rubber particle, $f_{r,r}$ [b] | 0.6 | T1 : 9 |
| Effective modulus of sand particle, $E_s$, Pa | $1 \times 10^7$ | T1 : 10 |
| Effective modulus of rubber particle, $E_r$, Pa | $1 \times 10^5$ | T1 : 11 |
| Particle–wall friction, $f_w$ | 0.405 | T1 : 12 |
| Particle–wall stiffness, $k_w$ | $1 \times 10^6$ | T1 : 13 |
| Damping ratio of sand particle, $\zeta_s$ [b] | 0.63 | T1 : 14 |
| Damping ratio of rubber particle, $\zeta_r$ [b] | 0.22 | T1 : 15 |

[a]Data from Patil et al. (2010).
[b]Data from calibration.

angle test, when different particles are dropped from a height, due to the difference in granular rebound height, it may generate a different heap when they are stabilized, which may greatly influence the mixture segregation at its surface. Therefore, calibrating the material damping ratio as a DEM input parameter is necessary. According to Kawaguchi et al. (1992), the restitution height is directly linked to the material properties of energy dissipation, and the relationship can be obtained by solving the motion equation for free vibration with viscous damping, as follows:

$$\alpha = \exp\left(-\frac{\zeta\,\pi}{\sqrt{1-\zeta^2}}\right) \tag{1}$$

where $\alpha$ = restitution coefficient, which is determined from the restitution height $h$; and $\zeta$ = ratio of the damping constant to the critical damping constant. For simplification, $\zeta$ is referred to as the damping ratio. It is clear that a granule's damping ratio can be calculated through its rebound height. Therefore, an experiment was designed to calibrate this parameter input.

040■■■■■-3

*Appendix*

122 The materials used for the experiment were spherical silica
123 beads and rubber beads with a radius of 5 mm, as shown in Fig. 2.
124 The two materials are identical in composition, respectively, to the
125 sand and rubber beads used for the mixture. The restitution process
126 used a glass board as a base. Silica and rubber beads were released
127 at a height of $H = 340$ mm, against a vertical scale board, and a
128 high-resolution camera of 60 frames per second (fps) was placed
129 1 m in front of the scale board. The material size and the release
130 height were determined as being proportional to the sizes of sam-
131 ples used for the tests that followed.
132 Four silica and four rubber beads were chosen at random for the
133 test, as shown in Fig. 2. Each silica and rubber bead was tested three

134 times independently. Once the beads were released, the maximum
135 rebound height was captured by using the camera to record the
136 whole process, as shown in Fig. 3. The images were analyzed at
137 each frame so that the maximum restitution height could be deter-
138 mined. The material beads at the maximum rebouncing height are
139 illustrated in Fig. 3. The final results of the repeated tests are given
140 in Fig. 4. Generally, the silica beads had a much higher height of
141 bounce, with an average of 170 mm. Rubber beads rebound to
142 31.9 mm on average.
143 For both of the silica and rubber beads, the radius of the bead, $r =$
144 5 mm, must be deducted when comparing its height of rebound.
145 Therefore, the restitution coefficient $\alpha$ is expressed as:



**Fig. 7.** The numerical measurement of the repose angle: (a) elevation view (not to scale); (b) plan view (not to scale); (c) frequency of particles intersecting the periphery; and (d) sample pile.

$$\alpha = \frac{h-r}{H-r} \qquad (2)$$

146  The corresponding restitution coefficients were 0.49 for sand
147  and 0.078 for rubber. Substituting the results to Eq. (1) to obtain the
148  damping ratio, the results were 0.22 and 0.63 for sand and rubber,
149  respectively. The standard deviation for silica beads and rubber
150  beads was found to be 0.3 and 0.16, respectively, suggesting excel-
151  lent agreement of the tests.
152  A three-dimensional simulation of the restitution test was also
153  performed by using numerical software Particle Flow Code (PFC)
154  3D. The purpose of the simulation was to evaluate the materials'
155  restitution heights under the influence of granular microproperties
156  such as the damping ratio, material density, or stiffness. For each
157  sphere, different damping ratios ranging from 0 to 1 were consid-
158  ered. Actual material densities, such as $\rho = 1,300 \, \text{kg/m}^3$ and
159  $2,600 \, \text{kg/m}^3$, respectively, were selected as input values. For each
160  density value, various contact types and contact stiffness values
161  were compared, including the linear contact model with effective
162  modulus $E = 1 \times 10^7$ Pa and $1 \times 10^9$ Pa, respectively, and the Hertz
163  contact model with shear modulus $G = 3 \times 10^7$ Pa, Poisson's ratio
164  $\nu = 0.5$, and $G = 3 \times 10^{10}$ Pa, $\nu = 0.3$, respectively. The same particle
165  size and releasing height were used in the numerical simulation. The
166  restitution coefficient $\alpha$, as defined in Eq. (2), is plotted about the
167  damping coefficient $\zeta$ and other parameters. This is shown in Fig. 5.
168  In Fig. 5, the numerical result fits well with the analytical predic-
169  tion from Eq. (1). It is thus evident that the damping ratio $\zeta$ is inde-
170  pendent from factors such as contact type, stiffness values, or den-
171  sities, and that the only influence on the damping ratio is its
172  restitution height. The numerical–analytical comparison provides
173  evidence that contact damping between particles and the base sur-
174  face can be directly obtained from the aforementioned calibration.
175  The relevant results are discussed in the DEM model results.
176  One could argue that material shape or size may create different
177  results. However, it is noted that the rebound height of silica beads
178  is around five times of that of rubber beads, as observed in the test
179  that the irregular and smaller-sized rubber and sand beads are used.
180  This can be visually observed, but is difficult to capture using the
181  camera. It is much easier to capture the restitution height of spheres
182  because the irregular ones may bounce in different directions. Also,
183  the spheres were simulated numerically in order to provide consis-
184  tency for this experiment.

### Angle of Repose

186  The repose angle test was performed in this study to investigate ma-
187  terial frictional behavior, as there is a strong correlation between

188  surface characteristics and the repose angle (Liu et al. 2012). For a
189  specific material, its frictional behavior contains two parts: slid-
190  ing friction and rolling friction, which have been well established
191  through numerical studies (Zhou et al. 1999; Yang et al. 2000;
192  Zhou et al. 2001). In the present study, sliding friction indicates
193  Mohr–Coulomb friction, resisting relative translational move-
194  ment, while rolling friction indicates the ability of particles to rotate,
195  which reflects particle irregularities. However, one test cannot deter-
196  mine two unknowns (i.e., sliding and rolling friction coefficients), so
197  this study adopted previously reported sliding frictions for sand and
198  rubber materials (Patil et al. 2010). The rolling friction coefficient
199  was determined from the repose angle accordingly.
200  The experiments used granular sand and rubber materials. Both
201  of the materials were sieved between 1.18 mm to 2.36 mm to obtain
202  the same-size material because it might have induced significant
203  differences in both the repose angle and the segregation. The mix-
204  ture was firstly mixed homogeneously and placed in a funnel with a
205  bottom diameter of 15 mm. A bottom plate was removed to allow
206  the particles to drop by force of gravity. The experiment was per-
207  formed over a glass base, and the distance from the bottom cone
208  to the base was 60 mm. The schematic drawing is shown in Fig.
209  6(a). Tests were performed for different materials: sand, rubber,
210  and sand–rubber mixture where the two ingredients were equal in
211  volume. The mixture test was conducted to confirm the individual
212  ingredient test results. Each measurement was repeated three
213  times, recording the height and diameter at two directions so that
214  the angle of repose could be determined.
215  The granular frictional properties were calibrated by using the
216  DEM simulation. The small-scale material pile [Fig. 6(b)] is
217  meaning in respect to the simulations. Firstly, a small number of
218  particles require less time to attain computation stabilization.
219  Also, owing to the granules to be displaced from the funnel, a
220  large pile may induce broader spreads, which also require a lon-
221  ger period of processing time. In addition, the pile is significantly
222  larger in scale than the greatest particle size. The pile formation is
223  not subject to a major size effect, and the pile dimension satisfies
224  the segregation purpose.
225  To simulate the shape parameter of the material granules, despite
226  making clumps of the basic shapes of 2D discs or 3D spheres
227  (Indraratna et al. 2012; Chen et al. 2014; Falagush et al. 2015), a roll-
228  ing resistance behavior at contact could be introduced, as suggested
229  by Ai (2010). It has shown great advantages in simulating a stable
230  pile with a finite angle (Zhou et al. 1999; Yang et al. 2000; Zhou et al.
231  2001). The same technique is used in this simulation. Similar to the
232  Mohr–Coulomb friction theory, the rolling resistance model imposes
233  a granular torque by introducing a rolling friction coefficient $f_r$. A
234  study of rolling resistance model can be found in Ai (2010).

**Table 2.** Measurement of repose angle

| Sample | Test | Height (mm) | Experiment Diameter (mm) X | Y | Average | Angle (°) | Average angle (°) | Simulation Angle (°) |
|---|---|---|---|---|---|---|---|---|
| Sand bead | 1 | 28 | 88 | 92 | 90 | 31.9 | 31.1 | 31.4 |
|  | 2 | 34.5 | 118 | 117 | 117.5 | 30.4 |  |  |
|  | 3 | 35 | 112 | 120 | 116 | 31.1 |  |  |
| Rubber bead | 1 | 39 | 103 | 105 | 104 | 36.9 | 36.3 | 36.5 |
|  | 2 | 40 | 108 | 108 | 108 | 36.5 |  |  |
|  | 3 | 34 | 95 | 96 | 95.5 | 35.5 |  |  |
| Mixture | 1 | 39 | 108 | 106 | 107 | 36.1 | 35.0 | 34.8 |
|  | 2 | 34 | 100 | 102 | 101 | 34.0 |  |  |
|  | 3 | 35 | 101 | 100 | 100.5 | 34.9 |  |  |

235  A calibration process is required to determine the rolling friction coefficient because very limited research has been focused on the rolling behavior of rubber and sand. The funnel was made by assembling wall plates as two cones, as shown in Fig. 6(b). More than 12,000 sphere particles were used and were first stabilized in the funnel by use of gravity. This was achieved in the simulation by allowing a long simulation time so that the particles' velocity was reduced almost to zero. The bottom plate was removed before particles settled on the base. The input micromechanical parameters are listed in Table 1.

245  The repose angle cannot be directly measured from the numerical results because there might be systematic errors. For example, the topmost particle may not rest at the center, which induces an

248  inaccurate pile height. Also, as seen in Fig. 7(d), the top of the material pile becomes flat, which underestimates the repose angle. Directly measuring the base radiuses in two directions is also problematic because many particles are scattered. Therefore, an indirect measurement method was developed. As shown in Fig. 7(d), slice the pile horizontally at two elevations: one at the pile's bottom, and the other one at 80% of its apex. The 80% plane was selected to avoid the cone altitude inaccuracy. The angle was determined by measuring the radius of the two slices and the vertical distance between the slices.

258  Specifically, the centroid of the funnel is assumed to be the center of the pile bottom rather than the projection of the highest particle at the top. At the chosen height, the upper plane in Fig.
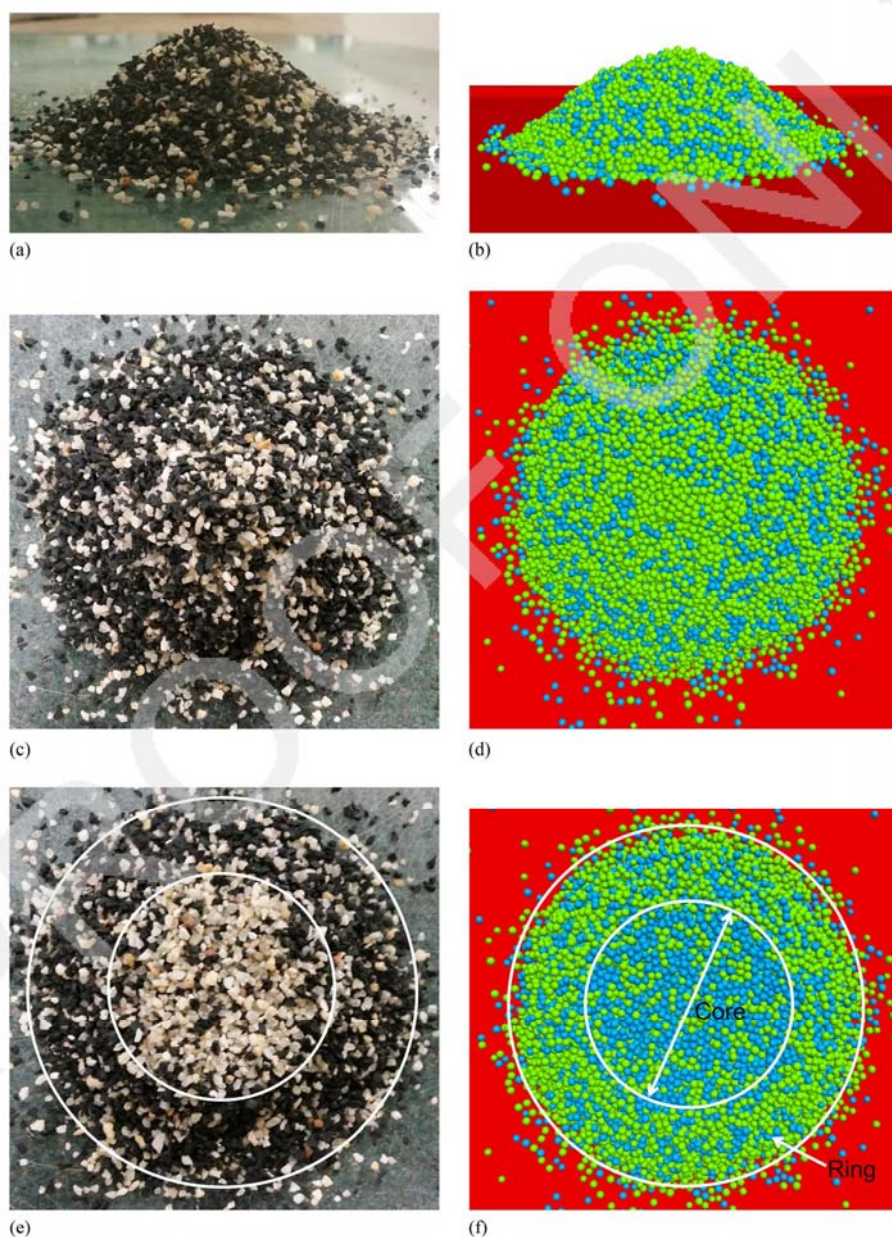


**Fig. 8.** Segregation of mixture pile.

F8 : 1

270

261 7(d) was used to slice the pile. A number of circles were plot, in
262 equally increasing radius, on the plane, as shown in Fig. 7(b), and
263 were then referred to, in sequence, from ID 1 to $N$ as the radius
264 increased. The circles were used to determine count $C_1$ of the par-
265 ticles sitting on the circular plane, as illustrated in Fig. 7(a), as
266 well as count $C_2$ of the particles intersecting the circular periph-
267 ery, as illustrated in Fig. 7(b). Define sphere-intersecting fre-
268 quency = $C_1/C_2$. The frequency vs. the sequential circles is illus-
269 trated in Fig. 7(c). The upper plane was regarded as the 14th
270 circle because it intersects the maximum number of particles.
271 Similarly, the bottom plane sat on the 43th circle. Note that some
272 particles fell outside the circle of preference, e.g., the red sphere
273 in Figs. 7 (a and b), but intersected at the top with the cut plane. In
274 this circumstance, the elevation and plan views were combined to
275 examine the preferred circle.

276 Based on the calculations and parameters described, the final
277 results of repose angle were obtained experimentally and numeri-
278 cally. The results are shown in Table 2. Through iteration, the roll-
279 ing friction coefficients were determined. Different coefficients
280 were determined for the sand and rubber, respectively, as shown in
281 Table 1. Then, when they were mixed at equal volume, the repose
282 angles were examined again, enabling verification of the coeffi-
283 cients through numerical and experimental tests. The results in
284 Table 2 suggest excellent agreement between the numerical and ex-
285 perimental tests. Specifically, for the sand heap, the repose angle is
286 31.1° in the experiment and 31.4° in the simulation. Similarly excel-
287 lent agreement is obtained for the rubber heap and rubber-sand
288 mixture heap, verifying the validity of the particle frictions of form-
289 ing the heaps. At this stage, each single microparameter had been
290 determined so that DIP could be performed.

291 As a simulation result, it is noted that different groups of mate-
292 rial stiffness were used in the simulation, but it has negligible
293 impact on the repose angle. Owing to the fact that gravity is the
294 only force considered, the load transmission is negligible at parti-
295 cle contact so that the impact on the material behavior is minor.
296 The change of material stiffness may have negligible influence to
297 granular behavior for some particular cases. For example, Chung
298 (2006) studied rod penetration and identified that scaling interpar-
299 ticle contact stiffness did not show any significant variations on
300 the simulation results, but provided considerable simulation effi-
301 ciency. It was concluded that the main reason was that reducing
302 stiffness has only minor effects on load transmission onto the
303 boundary surfaces. Ai (2010) illustrated the same finding for stiff-
304 ness scaling, but argued that if the stiffness is scaled too low, it
305 may result in unstable behavior for a granular pile. This specified
306 methodology was also adopted by Shi et al. (2007) because it has
307 no essential effect on flow mechanics.

### Segregation Observation

309 Segregation was observed in both the numerical simulation and the
310 experimental test. Figs. 8(a and b) show material piles in elevation
311 view from the experimental and numerical studies, respectively.
312 The rubber and sand beads are represented as green and blue
313 spheres, respectively, in the numerical simulations. In addition to
314 the similarity in the repose angle, it is also clear that the pile surfaces
315 are mostly covered by rubber material. A similar surface covering
316 can be seen in the plan view as well [Figs. 8(c and d)], demonstrat-
317 ing verification of the numerical results. Further quantitative com-
318 parison is provided in the subsequent sections.

319 To gain insight into the inner material distribution, the material
320 piles were sliced horizontally at their midheight, removing the re-
321 spective top cone and exposing the heap core. The midheight core
322 was assumed of representing the particle distribution inside the

323 heaps. The particles on the core were examined. For both the test
324 heap and the simulation heap, the majority of sands stayed in the
325 central area [Figs. 8(e and f)]. Close agreement exists between the
326 experimental and numerical results in respect to particles distribu-
327 tion on both the heap surface and inner core. Again, this agreement
328 is subject to further quantitative comparison, which is accomplished
329 through the DIP as follows.

### Digital Image Processing

331 One of the main objectives of this research was to present a mea-
332 surement method that could be used to quantify the segregation
333 obtained from the experiment and numerical simulation. ~~Despite~~
334 ~~another method that has been proposed to quantify the segregation,~~
335 ~~there is a size difference in the mixture. A more~~ general method was
336 developed based on visual comparison between numerical and ex-
337 perimental results (Shi et al. 2007). As an improvement of visual
338 comparison, this can be quantitatively measured by using the DIP
339 method, which has been applied in many fields, such as identifying
340 soil features (Aydemir et al. 2004; Manahiloh et al. 2016), diagnos-
341 ing soil–rock mesostructure (Kemeny et al. 1993; Villeneuve et al.
342 2011), analyzing coarse aggregate shape and size (Yue and Morin
343 1996; Altuhafi et al. 2013), and measuring saturation degree
344 (Yoshimoto et al. 2011). In this paper, as size effect is not the pri-
345 mary consideration, the DIP method was adopted to quantify and
346 compare material segregation between the numerical simulation
347 and experimental results. Based on the literature review conducted
348 in this study, it is the first time of such comparison has been con-
349 ducted in rubber–sand segregation testing.

350 DIP method refers to the process of converting a picture into a
351 digital form and then analyzing the digital image to acquire the use-
352 ful, underlying information. In the analysis, a picture is represented
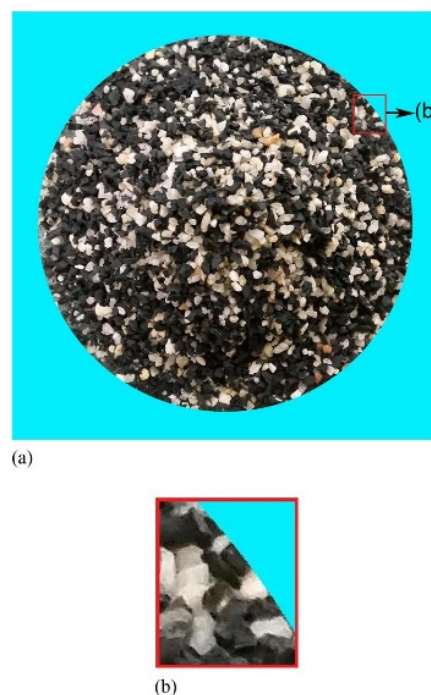353 by a number of pixels. Each pixel is a combination of primary



(a)

(b)

**Fig. 9.** Calibration of the digital image: (a) sample pile; and (b) an example image.

F9 : 1
F9 : 2

040■■■■■-7

354 colors. A standard digital picture often uses the red (R), green (G),
355 and blue (B) channels, which can be perceived by human eyes and
356 used in simple computer displays. The information extracted from a
357 digital picture can be expressed as a discrete function on a $(N \times M)$
358 grid, known as an intensity matrix in the Cartesian coordinate sys-
359 tem (Yue and Morin 1996):

$$I_k = \begin{bmatrix} I_k(1,1) & I_k(1,2) & \star & I_k(1,M) \\ I_k(2,1) & I_k(2,2) & \star & I_k(2,M) \\ M & M & & M \\ I_k(N,1) & I_k(N,2) & \star & I_k(N,M) \end{bmatrix} \quad (3)$$

360 where $I$ = a value often refers to the intensity level of a digital image
361 ranging from 1 to 255; and $k = 1$ to 3, representing red, green, and
362 blue channels, respectively; therefore, there are three separate mat-
363 rices for an image. The $I$ value extraction process is accomplished
364 by MATLAB, which is equipped to read color channel information.
The present paper briefly illustrates the method for a colored image

365 analysis in the next section. As the sample heap was formed on a
366 glass plane and the glass background color was similar to the color
367 of the sample, it was not easy to find the color difference between
368 sand and the background and rubber and the background. Some pre-
369 treatment was required to change the background color. It was cho-
370 sen to substitute a blue background for the glass background so that
371 it was easier to select the threshold value for further analysis. Fig.
372 9(a) was converted from Fig. 8(c) by changing the background
373 color. For convenience, some particles scattered on the glass base
374 were excluded because the amount of these particles are negligible
375 compared to the total granular number.
376     The threshold value was obtained by processing the pixels of an
377 image. However, a high-resolution image consists of a large number
378 of pixels (>15 million). Distinguishing color differences directly
379 from the original picture requires long processing time as a result.
380 For simplification in the detailed analysis, a small-sized picture was
381 extracted as an example so that image processing could be per-
382 formed. Fig. 9(b) picked up a small region of 35 × 43 pixels, which
383 contains all important elements of the image.
384     After selecting the small example image as shown in Fig. 9(b), a
385 detailed analysis was conducted to find threshold values between



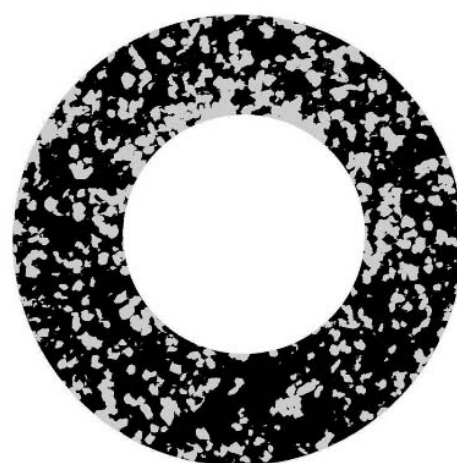(a)



(a)



(b)



(b)
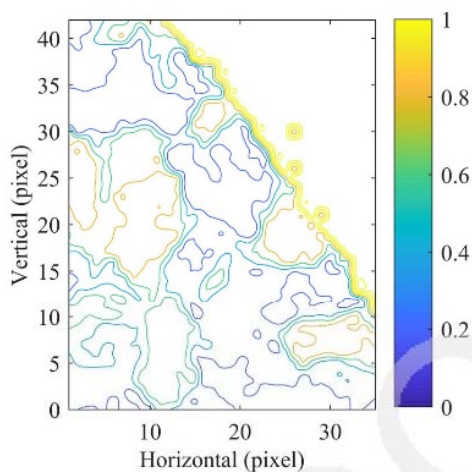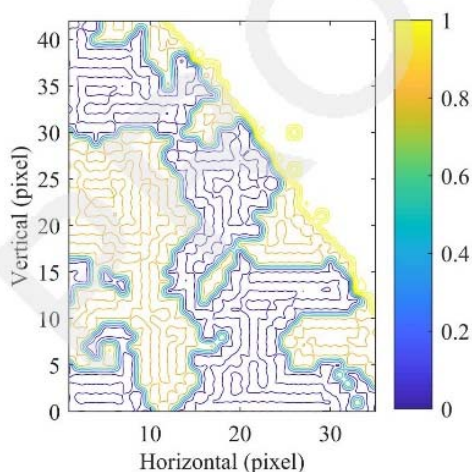
**Fig. 10.** Intensity contours expressed as: (a) the color map; and (b) the binary map.

F10 : 1
F10 : 2

**Fig. 11.** Color segmentation of sand pile at peripheral ring (experiment).

F11 : 1
F11 : 2

386 color regions. MATLAB was used to read individual pixels into $I_1$
387 for red, $I_2$ for green, and $I_3$ for blue. However, the three values can-
388 not be directly used to map the regions. A solution is to use an HSI
389 system to identify the materials more easily (Chen et al. 2004). The
390 HSI stands for *hue*, *saturation*, and *intensity*. According to Chen
391 et al. (2004), this solution combines the three intensity values based
392 on appropriate weighting, yielding a weighted intensity value, $I_w$.
393 According to NTSC standard for luminance (IBM 1990), $I_w$ is cal-
394 culated using the following algorithm:

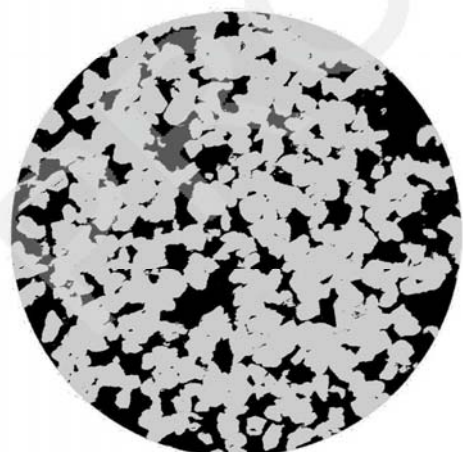$$I_w = \frac{0.2989 \times I_1 + 0.5870 \times I_2 + 0.1140 \times I_3}{255} \quad (4)$$

395 where $I_w$ has an interval of (0, 1). This $I_w$ is also known as gray-
396 level intensity in MATLAB, enabling a bicolor image. Based on the
397 $I_w$ values, contours are drawn for the small example image, as
398 shown in Fig. 10(a). Fig. 10(a) clearly identifies the color bounda-
399 ries of different materials, particularly when compared to the origi-
400 nal image [Fig. 9(b)]. However, given that there may be multiple in-
401 tensity threshold values, such as between sand and rubber, between
402 sand and the background, and between rubber and the background,
403 it was not guaranteed that all color differences have been

403 distinguished. Since the background intensity is a value in-between
404 the values of both sand and rubber, the background regions need to
405 be excluded before calculating the image intensity.
406 Recall the pretreatment that the background has been predyed to
407 blue; it is easy to find that these regions because they have very high
408 $I_3$ values (for blue channel). In this study, the background part was
409 identified by searching $I_3 > 245$ and assigning a very high constant,
410 such as 10,000. Using Eq. (4), the background intensity has a value
411 $I_w > 1$, while the other parts are not affected. In this way, the back-
412 ground is excluded, and the only intensity threshold value will be
413 the one between sand and rubber. Based on a trial-and-error method
414 suggested by Chen et al. (2004), a threshold value $I_w = 0.35$ was
415 taken to be the boundary between the partition sand and rubber after
416 comparing multiple values. To yield a clear definition of regions,
417 the pixels with $I_w < 0.35$ were reassigned as a value of 0 (i.e., rubber
418 particles), otherwise a value of 1 (i.e., sand particles). Fig. 10(b)
419 illustrates the intensity contours using the values of 0 and 1. Due to
420 noise influence, such as light intensity, the detection results may not
421 be perfectly correct. However, by comparing Figs. 10(a and b) and
422 Fig. 9(b), it is believed that $I_w = 0.35$ represents the color boundary
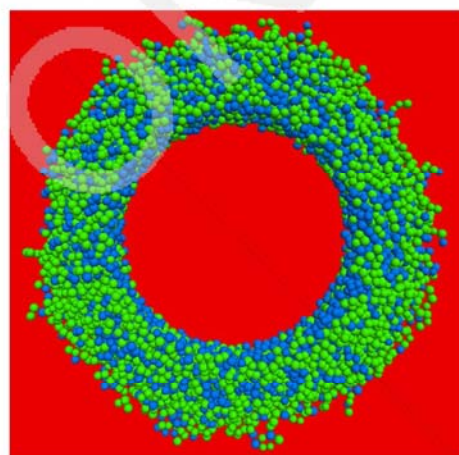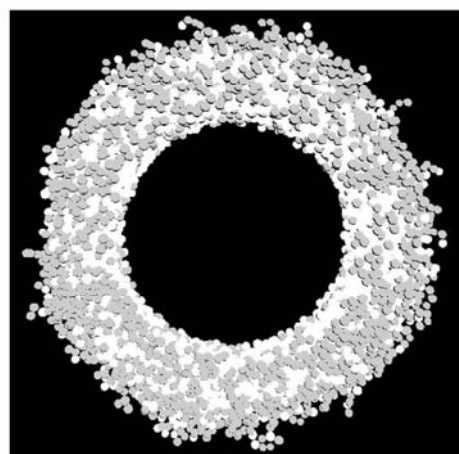


(a)

(b)

**Fig. 12.** Color segmentation of ~~sand pile at central circle (experiment).~~

F12:1



(a)

(b)

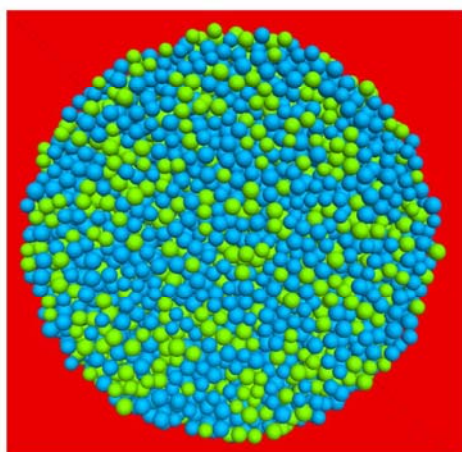**Fig. 13.** Color segmentation of ~~sand pile at peripheral ring (numerical).~~   F13:1  F13:2
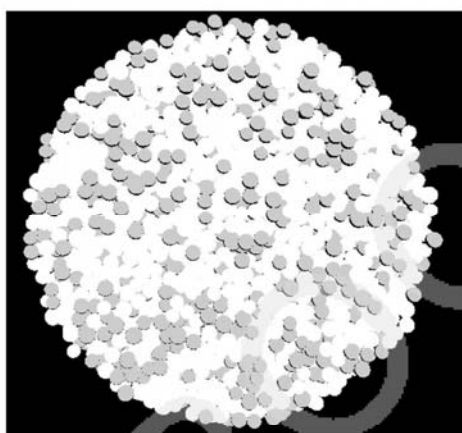
423 between sand and rubber particles and can be applied to ~~the rest part~~
724 ~~of the image~~ in Fig. 9(a).

## Results and Discussion

426 This section presents the results from a comparison of the experi-
427 mental and numerical results for the present study. The material
428 volume ratio can be expressed as the ratio of an area of color



(a)



(b)

F14 : 1    **Fig. 14.** Color segmentation of ~~sand pile at central circle (numerical)~~.

429 based on the intensity threshold outlined earlier. As segregation
430 varies significantly between the inside area and the pile surface,
431 the comparison was made after removing the pile cap, as shown
432 in Fig. 8(e).

### Segregation Ratio

434 DIP is further applied here to calculate the area ratio of different col-
435 ors. Fig. 8(e) is separated as a peripheral ring and central circle so as
436 to directly compare segregation outside and inside the pile. The
437 comparison between the experiments and simulations is shown
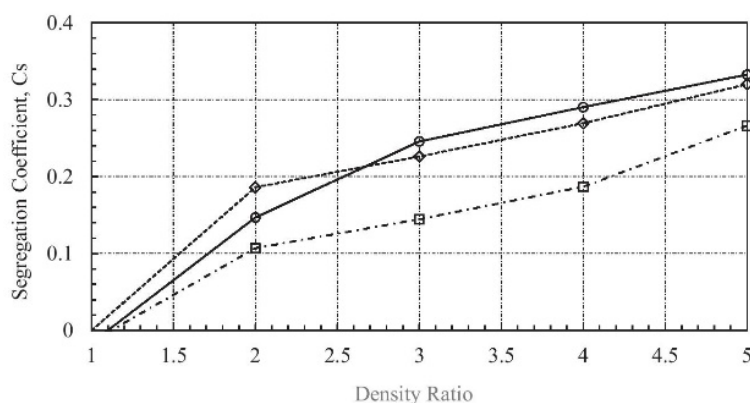438 ~~from~~ Figs. 11(a) to 14(a).
439    In the test, the radius of the central circle is half of the bottom of
440 the material heap. It is noted that in the numerical analysis, the image
441 has already been presented as basic RGB colors, which saves the in-
442 tensity threshold value selection. The RGB colors represent the three
443 primary colors of red, green, and blue. Each pixel of a digital image
444 can be made by the combinations of these primary colors. The calcu-
445 lation of the concentration of sand particles was based on color seg-
446 mentation, shown in Figs. 11(b) to 14(b). These figures present gray
447 images obtained using the aforementioned DIP method. In the
448 experiments, the percentage of sand was calculated from a color area
449 in the peripheral ring and the central circle were 32.09% and
450 69.86%, respectively, while the numerical result showed that blue
451 particles, which represent sand at peripheral ring and central circle,
452 were 39.09% and 66.00%, respectively. Excellent agreement was
453 obtained between the test and numerical results. The agreement is
454 supposed to be valid for the rest parts of the heaps, given the heap
455 surface and the core represent the outer and inner particle distribu-
456 tion profiles. The quantitative comparison based on the DIP results
457 shows a close predication of numerical simulation. This comparison
458 is more convincing than visual comparison used in previous studies.
459 Comparing the segregation in both numerical and experimental
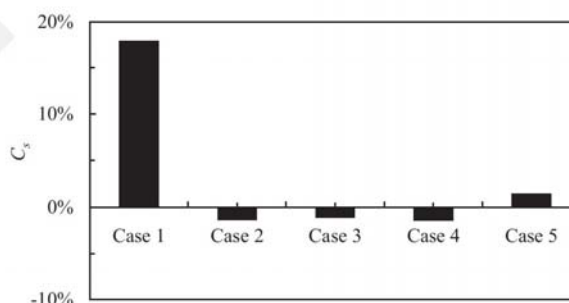


**Fig. 15.** Segregation coefficient for varying mixtures.

F15 : 1

**Table 3.** Material properties used in the parametric study

| | Case | Ingredient | Density (kg/m³) | Damping ratio | Stiffness (kPa) | Rolling friction coefficient | Sliding friction coefficient |
|---|---|---|---|---|---|---|---|
| T3 : 1 | Case 1 | $A$ | 2,600 | 0.2 | $1 \times 10^5$ | 0.6 | 0.3 |
| T3 : 2 | | $B$ | 1,300 | 0.2 | $1 \times 10^5$ | 0.6 | 0.3 |
| T3 : 3 | Case 2 | $A$ | 1,300 | 0.2 | $1 \times 10^5$ | 0.6 | 0.3 |
| T3 : 4 | | $B$ | 1,300 | 0.4 | $1 \times 10^5$ | 0.6 | 0.3 |
| T3 : 5 | Case 3 | $A$ | 1,300 | 0.2 | $1 \times 10^7$ | 0.6 | 0.3 |
| T3 : 6 | | $B$ | 1,300 | 0.2 | $1 \times 10^5$ | 0.6 | 0.3 |
| T3 : 7 | Case 4 | $A$ | 1,300 | 0.2 | $1 \times 10^5$ | 0.3 | 0.3 |
| T3 : 8 | | $B$ | 1,300 | 0.2 | $1 \times 10^5$ | 0.6 | 0.3 |
| T3 : 9 | Case 5 | $A$ | 1,300 | 0.2 | $1 \times 10^5$ | 0.6 | 0.3 |
| T3 : 10 | | $B$ | 1,300 | 0.2 | $1 \times 10^5$ | 0.6 | 0.6 |

274

F16:1

**Fig. 16.** Segregation coefficient vs. mixture density ratio under different frictions.

460 results also showed that the chosen material properties (i.e., friction,
461 material rolling friction, and damping coefficient) matched the
462 actual material properties. It is suggested that segregation tests can
463 be used as a useful calibration method.

### Parametric Study

465 Due to many input parameters, it is not clear which parameter had a
466 critical influence on particle segregation. It is necessary to evaluate
467 the impact of each parameter with other unchanged parameters.
468 Table 3 lists possible input values for parameters that potentially
469 affect the segregation. Of the parameters, the rolling and sliding
470 friction coefficients determine the particle surface roughness. Five
471 mixtures are defined, each composed of two materials, *A* and *B*, in
472 equal volume. Again, the mixture ingredients are assumed to be
473 similar in size so that size difference is not considered. In each
474 study, only one parameter was changed, while the others remained
475 the same. For example, in Case 1, the density for the two ingredients
476 is 2,600 kg/m$^3$ and 1,300 kg/m$^3$, respectively, while other parame-
477 ters, such as damping ratio or stiffness, remained the same, as listed
478 in Table 3. The input values reflect the normal range of materials
479 used as geomaterial ingredients.

480 The five cases were subjected to the segregation test. The test is
481 similar in process to the aforementioned segregation tests, including
482 forming pile through the funnel and slicing the pile at the midheight to
483 compare the inner core and the outer ring. To assess the segregation,
484 define segregation coefficient $C_s$ as suggested by Williams (1976):

$$C_s = \frac{W_I - W_O}{W_I + W_O} \times 100\% \qquad (5)$$

485 where $W_I$ = volumetric proportion of material *A* in the inner core,
486 while $W_O$ = volumetric proportion of material *A* in the outer ring.
487 Where there is no or negligible segregation, $C_s$ is equal or close to
488 zero, and vice versa. The results are provided in Fig. 15. It is clear
489 that Case 1 stands out, with $C_s$ = 17.97%, suggesting the material
490 density governs the segregation. The friction coefficients (or surface
491 roughness), however, have marginal effect on the segregation,
492 which agrees with results by Pohlman et al. (2006).

493 Even though the friction coefficients alone do not cause segrega-
494 tion of the material, it has a certain effect on the mixture once there
495 is already a density difference in the mixture. To examine this
496 density–friction combined effect, a new comparison was made
497 between the mixture density ratios $\rho_A/\rho_B$, which increase from 1 to
5, according to different sliding friction values $f_s$ = 0.3, 0.4, and 0.5,

498 respectively. The results are provided in Fig. 16. For each case, the
499 segregation coefficient $C_s$ increases with the density ratio. This rela-
500 tionship changes if the material surface roughness increases. The
501 rougher the material surface is, the less likely segregation will hap-
502 pen. Similar findings were observed by Lai et al. (1997) that frictional
503 properties sometimes dominate material segregation, such as in the
504 event of long-range transport. For the funnel discharge in the current
505 study, the density–friction correlation might be explained as follows:
506 when the surface roughness increases, the mobility of the mixture is
507 affected so that flowing from the funnel requires more kinetic energy,
508 and material granules tend to move as a whole. Consequently, the
509 mixtures are more difficult to be separated during flow.

## Conclusions

511 This study presented a DIP method used to examine material segre-
512 gation based on material color difference. The comparison between
513 the DEM simulation and experiments suggests that DIP could be
514 used as a useful method enabling verification between the DEM and
515 test results.

516 Material rolling friction and damping ratio for sand and rubber
517 were calibrated by the repose angle and rebouncing tests, respec-
518 tively. The parameter values were incorporated into the DEM
519 model for the parametric study. For a uniform mixture, from a mi-
520 croscopic perspective, the density difference had most significant
521 impact to the segregation during the funnel discharge. Other contact
522 properties, such as material stiffness, surface roughness, or damping
523 ratio, had minor to negligible impact. The higher the density differ-
524 ence is, the noticeable the segregation will be. When the segregation
525 needs to be controlled, the material density difference should be
526 considered. However, the density-induced segregation can be offset
527 by the interparticle friction. The higher the frictional properties are
528 assigned, the less likely the segregation will occur.

## Acknowledgments

## Notation

*The following symbols are used in this paper:*
533
$C_1$ = count of the particles sitting on a cutting plane;
534

535  $C_2$ = count of the particles intersecting a circular
536      periphery;
537  $C_s$ = segregation coefficient;
538  $d_r$ = diameter of rubber particle;
539  $d_s$ = diameter of sand particle;
540  $E$ = effective modulus;
541  $E_r$ = effective modulus of rubber particle;
542  $E_s$ = effective modulus of sand particle;
543  $f_r$ = rolling friction;
544  $f_s$ = sliding friction;
545  $f_{r,r}$ = rolling friction of rubber particle;
546  $f_{r,s}$ = rolling friction of sand particle;
547  $f_{s,r}$ = sliding friction of rubber particle;
548  $f_{s,s}$ = sliding friction of sand particle;
549  $f_w$ = particle–wall friction;
550  $G$ = shear modulus;
551  $h$ = bead rebound height;
552  $H$ = bead drop height;
553  $I$ = color channel intensity;
554  $I_1$ = red channel intensity;
555  $I_2$ = green channel intensity;
556  $I_3$ = blue channel intensity;
557  $I_w$ = gray level intensity;
558  $k_w$ = particle–wall stiffness;
559  $r$ = bead radius;
560  $W_I$ = volumetric proportion of material in the inner circle;
561  $W_O$ = volumetric proportion of material in the peripheral
562      ring;
563  $\alpha$ = restitution coefficient;
564  $\zeta$ = damping ratio;
565  $\zeta_r$ = damping ratio of rubber particle;
566  $\zeta_s$ = damping ratio of sand particle;
567  $\nu$ = Poisson's ratio;
568  $\rho$ = density;
569  $\rho_r$ = density of rubber particle; and
570  $\rho_s$ = density of sand particle.

571  **References**

573  Ahmed, I., and C. W. Lovell. 1993. "Rubber soils as lightweight geomaterials." *Transp. Res. Rec.* 1422: 61–70.
575  Ai, J. 2010. "Particle scale and bulk scale investigation of granular piles and silos." Ph.D. thesis, Univ. of Edinburgh.
576  Altuhafi, F., C. O'Sullivan, and I. Cavarretta. 2013. "Analysis of an image-based method to quantify the size and shape of sand particles." *J. Geotech. Geoenviron. Eng.* 139 (8): 1290–1307. https://doi.org/10.1061/(ASCE)GT.1943-5606.0000855.
580  Anand, A., J. S. Curtis, C. R. Wassgren, B. C. Hancock, and W. R. Ketterhagen. 2010. "Segregation of cohesive granular materials during discharge from a rectangular hopper." *Granular Matter* 12 (2): 193–200. https://doi.org/10.1007/s10035-010-0168-9.
584  ASTM. 1997. *An unresolved riddle: tire chips, two roadbeds, and spontaneous reactions.* STP1275. West Conshohocken, PA: ASTM.
586  Aydemir, S., S. Keskin, and L. R. Drees. 2004. "Quantification of soil features using digital image processing (DIP) techniques." *Geoderma* 119 (1-2): 1–8. https://doi.org/10.1016/S0016-7061(03)00218-0.
589  Bosscher, P. J., T. B. Edil, and S. Kuraoka. 1997. "Design of highway embankments using tire chips." *J. Geotech. Geoenviron. Eng* 123 (4): 295–304. https://doi.org/10.1061/(ASCE)1090-0241(1997)123:4(295).
592  Chen, C.,, G. R. McDowell, and N. H. Thom. 2014. "Investigating geogrid-reinforced ballast: experimental pull-out tests and discrete element modelling." *Soils Found.* 54 (1): 1–11. https://doi.org/10.1016/j.sandf.2013.12.001.
596  Chen, S., Z. Q. Yue, and L. G. Tham. 2004. "Digital image-based numerical modeling method for prediction of inhomogeneous rock failure." *Int. J.*

598  *Rock Mech. Min. Sci.* 41 (6): 939–957. https://doi.org/10.1016/j.ijrmms.2004.03.002.
600  Chung, Y.-C. 2006. "Discrete element modelling and experimental validation of a granular solid subject to different loading conditions." Ph.D. thesis, Univ. of Edinburgh.
603  Cundall, P. A., and O. D. Strack. 1979. "A discrete numerical model for granular assemblies." *Geotech.* 29 (1): 47–65. https://doi.org/10.1680/geot.1979.29.1.47.
606  Donald, M., and B. Roseman. 1962. "Mixing and demixing of solid particles. Part I: mechanisms in a horizontal drum mixer." *Br. Chem. Eng.* 7 (10): 749–752.
609  Evans, T. M., and J. R. Valdes. 2011. "The microstructure of particulate mixtures in one-dimensional compression: Numerical studies." *Granular Matter* 13 (5): 657–669. https://doi.org/10.1007/s10035-011-0278-z.
612  Falagush, O., G. R. McDowell, and H.-S. Yu. 2015. "Discrete element modeling of cone penetration tests incorporating particle shape and crushing." *Int. J. Geomech.* 15 (6): 04015003. https://doi.org/10.1061/(ASCE)GM.1943-5622.0000463.
616  Foose, G. J., C. H. Benson, and P. J. Bosscher. 1996. "Sand reinforced with shredded waste tires." *J. Geotech. Eng.* 122 (9): 760–767. https://doi.org/10.1061/(ASCE)0733-9410(1996)122:9(760).
619  Garga, V. K., and V. O'shaughnessy. 2000. "Tire-reinforced earthfill. Part 1: construction of a test fill, performance, and retaining wall design." *Can. Geotech. J.* 37 (1): 75–96. https://doi.org/10.1139/t99-084.
622  Humphrey, D. N., and W. P. Manion. 1992. "Properties of tire chips for lightweight fill." In: *Grouting, Soil Improvement and Geosynthetics,* Geotechnical Special Publication 2, 1344–1355. Reston, VA: ASCE.
625  IBM. 1990. "NTSC luminance/chrominance equation definition for digital systems." *IBM Tech. Disclosure Bull.* 32 (10A): 208–209.
627  Indraratna, B., N. T. Ngo, C. Rujikiatkamjorn, and J. S. Vinod. 2012. "Behavior of fresh and fouled railway ballast subjected to direct shear testing: discrete element simulation." *Int. J. Geomech.* 14 (1): 34–44. https://doi.org/10.1061/(ASCE)GM.1943-5622.0000264.
631  Itasca. 2009. "*PFC3D 4.0 user's manual.*" Minneapolis, MN: Itasca Consulting Group, Inc.
633  Kawaguchi, T., T. Tanaka, and Y. Tsuji. 1992. "Numerical simulation of fluidized bed using the discrete element method: the case of spouting bed." *Trans. Jpn. Soc. Mech. Eng. Ser. B* 58 (551): 2119–2125. https://doi.org/10.1299/kikaib.58.2119.
637  Kemeny, J. M., A. Devgan, R. M. Hagaman, and X. Wu. 1993. "Analysis of rock fragmentation using digital image processing." *J. Geotech. Eng.* 119 (7): 1144–1160. https://doi.org/10.1061/(ASCE)0733-9410(1993)119:7(1144).
641  Kudrolli, A. 2004. "Size separation in vibrated granular matter." *Rep. Prog. Phys.* 67 (3): 209–248. https://doi.org/10.1088/0034-4885/67/3/R01.
643  Kuerbis, R., and Y. P. Vaid. 1988. "Sand sample preparation-the slurry deposition method." *Soils Found.* 28 (4): 107–118. https://doi.org/10.3208/sandf1972.28.4_107.
646  Lai, P.-Y., L.-C. Jia, and C. Chan. 1997. "Friction induced segregation of a granular binary mixture in a rotating drum." *Phys. Rev. Lett.* 79 (25): 4994–4997. https://doi.org/10.1103/PhysRevLett.79.4994.
649  Lee, C., H. Shin, and J. S. Lee. 2014. "Behavior of sand–rubber particle mixtures: Experimental observations and numerical simulations." *Int. J. Numer. Anal. Methods Geomech.* 38 (16): 1651–1663. https://doi.org/10.1002/nag.2264.
653  Liu, J., B. Yun, and C. Zhao. 2012. "Identification and validation of rolling friction models by dynamic simulation of sandpile formation." *Int. J. Geomech.* 12 (4): 484–493. https://doi.org/10.1061/(ASCE)GM.1943-5622.0000156.
657  Lőrincz, J., E. Imre, M. Gálos, Q. Trang, K. Rajkai, S. Fityus, and G. Telekes. 2005. "Grading entropy variation due to soil crushing." *Int. J. Geomech.* 5 (4): 311–319. https://doi.org/10.1061/(ASCE)1532-3641(2005)5:4(311).
661  Manahiloh, K. N., B. Muhunthan, and W. J. Likos. 2016. "Microstructure-based effective stress formulation for unsaturated granular soils." *Int. J. Geomech.* 16 (6): D4016006. https://doi.org/10.1061/(ASCE)GM.1943-5622.0000617.
665  Masad, E., R. Taha, C. Ho, and T. Papagiannakis. 1996. "Engineering properties of tire/soil mixtures as a lightweight fill material." *Geotech. Test. J.* 19 (3): 297–304. https://doi.org/10.1520/GTJ10355J.

668  Ottino, J., and D. Khakhar. 2000. "Mixing and segregation of granular
669       materials." *Annu. Rev. Fluid Mech.* 32 (1): 55–91. https://doi.org/10
670       .1146/annurev.fluid.32.1.55.
671  Patil, U., J. R. Valdes, and T. M. Evans. 2010. "Swell mitigation with granu-
672       lated tire rubber." *J. Mater. Civ. Eng.* 23 (5): 721–727. https://doi.org/10
673       .1061/(ASCE)MT.1943-5533.0000229.
674  Poh, P. S., and B. B. Broms. 1995. "Slope stabilization using old rubber tires
675       and geotextiles." *J. Perform. Constr. Facil.* 9 (1): 76–79. https://doi.org
676       /10.1061/(ASCE)0887-3828(1995)9:1(76).
677  Pohlman, N. A., B. L. Severson, J. M. Ottino, and R. M. Lueptow. 2006.
678       "Surface roughness effects in granular matter: influence on angle of
679       repose and the absence of segregation." *Phys. Rev. E: Stat. Nonlinear
680       Soft Matter Phys.* 73 (3 Pt 1): 031304. https://doi.org/10.1103/PhysRev
681       E.73.031304.
682  Shi, D., A. A. Abatan, W. L. Vargas, and J. J. McCarthy. 2007.
683       "Eliminating segregation in free-surface flows of particles." *Phys.
684       Rev. Lett.* 99 (14): 148001. https://doi.org/10.1103/PhysRevLett.99
685       .148001.
686  Tsang, H.-H., S. H. Lo, X. Xu, and M. Neaz Sheikh. 2012. "Seismic isola-
687       tion for low-to-medium-rise buildings using granulated rubber–soil
688       mixtures: numerical study." *Earthquake Eng. Struct. Dyn.* 41 (14):
689       2009–2024. https://doi.org/10.1002/eqe.2171.
690  Villeneuve, M. C., M. S. Diederichs, and P. K. Kaiser. 2011. "Effects of
691       grain scale heterogeneity on rock strength and the chipping process."
692       *Int. J. Geomech.* 12 (6): 632–647. https://doi.org/10.1061/(ASCE)GM
693       .1943-5622.0000194.
694  Watabe, Y., H. Shinsha, H. Yoneya, and C. Ko. 2014. "Description of par-
695       tial sandy layers of dredged clay deposit using penetration resistance in
696       installation of prefabricated vertical drains." *Soils Found.* 54 (5): 1006–
697       1017. https://doi.org/10.1016/j.sandf.2014.09.006.
698  Williams, J. C. 1976. "The segregation of particulate materials. A review."
699       *Powder Technol.* 15 (2): 245–251. https://doi.org/10.1016/0032-5910(76)
700       80053-8.
701  Yang, R. Y., R. P. Zou, and A. B. Yu. 2000. "Computer simulation of the
702       packing of fine particles." *Phys. Rev. E: Stat. Phys. Plasmas Fluids
703       Relat. Interdiscip. Top.* 62 (3 Pt B): 3900–3908.
704  Yoshimine, M., and R. Koike. 2005. "Liquefaction of clean sand with
705       stratified structure due to segregation of particle size." *Soils Found.*
706       45 (4): 89–98. https://doi.org/10.3208/sandf.45.4_89.
707  Yoshimoto, N., R. P. Orense, F. Tanabe, N. Kikkawa, M. Hyodo, and Y.
708       Nakata. 2011. "Measurement of degree of saturation on model ground
709       by digital image processing." *Soils Found.* 51 (1): 167–177. https://doi
710       .org/10.3208/sandf.51.167.
711  Yue, Z. Q., and I. Morin. 1996. "Digital image processing for aggregate ori-
712       entation in asphalt concrete mixtures." *Can. J. Civ. Eng.* 23 (2): 480–
713       489. https://doi.org/10.1139/l96-052.
714  Zhou, Y. C., B. D. Wright, R. Y. Yang, B. H. Xu, and A. B. Yu. 1999. "Rolling
715       friction in the dynamic simulation of sandpile formation." *Physica A*
716       269 (2-4): 536–553. https://doi.org/10.1016/S0378-4371(99)00183-1.
717  Zhou, Y. C., B. D. Xu, A. B. Yu, and P. Zulli. 2001. "Numerical investiga-
718       tion of the angle of repose of monosized spheres." *Phys. Rev. E: Stat.
719       Nonlinear Soft Matter Phys.* 64 (2 Pt 1): 021301. https://doi.org/10.1103
720       /PhysRevE.64.021301.
721  Zornberg, J. G., A. R. Cabral, and C. Viratjandr. 2004. "Behaviour of tire
722       shred sand mixtures." *Can. Geotech. J.* 41 (2): 227–241. https://doi.org
723       /10.1139/t03-086.

277

# Energy Dissipation Due to Surface Asperity: A Micro-scale Study

Can Wang, An Deng[(✉)] and Abbas Taheri

The University of Adelaide, Adelaide, SA 5000, Australia
{c.wang,an.deng,abbas.taheri}@adelaide.edu.au

**Abstract.** A moving object on a surface slows down and eventually rests where there is no energy input to the object. In physics, the changes in state are caused by the surface asperity existed between the object and the surface, dissipating kinetic energy of the object. This interpretation is simply summative and does not reflect many micromechanics details associated with the object motion. This paper presents a study on the micromechanics of a single particle travelling on a rugged surface. The micromechanics look into the particle-surface contacting, and resulted energy dissipation of the particle. A discrete element model is developed to mimic the contacting. This model is validated against analytical exact solutions which are developed in terms of Newton's laws of motion. This study examines some important physical conditions on the contacting and the energy dissipation. An interesting example problem is examined to provide results gained from the two approaches. This research is fundamental in that it re-defines inter-particle friction from the micro-scale perspective. Therefore the research helps predict any particle-based geo-motions, e.g. particles piling, debris flow, and rock falls.

**Keywords:** Micromechanics · DEM · Asperity · Contact

## 1 Introduction

Not restricted to seismology or materials science, asperity is equally crucial to engineering problems, in particular, particle motion. A particle exhibits asperity in size, form, shape or structure and these characteristics noticeably influence the particle responding to other contacting objects [1]. An example is the sliding friction problem. A block travels at an initial velocity $v$ on a horizontal surface; the goal is to determine the time $t$ and distance $l$ until the block is at rest. Both of the unknowns are worked out based on the acceleration $a$ which is dependent on the friction or friction coefficient $\mu$, a property characterizing the block-surface contacts. Despite it being static or kinetic, the friction coefficient, from a micro-scale view, is a function of the contact surface characteristics. These characteristics are usually depicted as high-low snags or jags, as illustrated in Fig. 1, or corrugated patches. These rugged projections are extremely small in size (i.e. microns) and thus difficult to observe. In physics they are usually expressed as surface asperity or roughness. The surface asperity is measured by the friction coefficient. The more pronounced the asperity is, the larger the coefficient should be. The measure, however, is collective, ignoring the surface details. Two

surfaces that exhibit different surface asperity details (e.g., high and spaced *vs.* low and continuous) may end up with identical friction coefficient. Any extremes in asperity are amplified which leads to different answers to the travel distance *l*. There can be a way of bypassing the use of friction coefficient and encompassing specific surface asperity characteristics when examining particle motion problems.
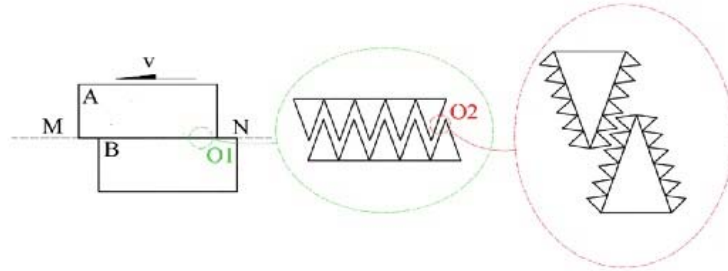


**Fig. 1.** Schematic of surface asperity drawn at different scales.

In this study, a surface with a specific asperity is developed by using the discrete element method (DEM). Using the same modeling approach, a single particle is created and allowed to move on the surface, reproducing the process of particle-surface contacting and the particle travelling. In simulating this kinetic process, the asperity is examined and linked to the particle's trajectory on the surface. Observations include particle's moving speed and thus its energy dissipation through the travel. These results help assess the particle travel distance subject to the surface asperity conditions. Further value lies in predicting granule-based geo-motions, e.g. particles piling, debris flow, and rock falls.

## 2   Model Development

### 2.1   Surface Asperity

The surface asperity is defined into a curved path, as shown in Fig. 2. The curvy surface is created by affixing $N$ discs in a row, $1, ..., j − 1, j, j + 1, ..., N$. These discs are equal in radius of $r_2$, enabling identical grooves formed between the discs. A disc with radius $r_1$ is allowed to travel at speed $v$ on the surface, with its centroid profile being a convex trajectory. The trajectory is subject to a small deviation where the moving disc bounces up when hits a base disc. For example, the new trajectory becomes curve A-B-C when the moving disc bounces up off disc $j$. The rebound results are dependent on the speed $v$, radii $r_1$ and $r_2$, and disc properties. The radii define the contact angle $\gamma$ which influences the contacting pattern. All discs are assumed having a smooth surface, eliminating secondary asperity.
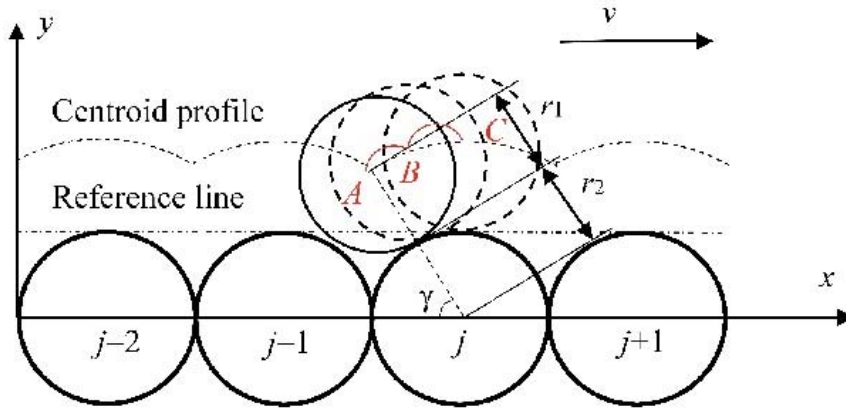
**Fig. 2.** Illustration of a disc moving on curvy surface.

## 2.2 DEM Model

The process of the disc moving on the curvy surface can be simulated by the DEM approach. This approach is able to reproduce two important disc actions: sliding and contacting. Sliding represents the disc displacing on the surface. This action is expressed into two energy forms: kinetic energy (energy of motion) and gravitational potential energy (stored energy of position). The two forms of energy amount to the total energy, i.e., the mechanical energy. The other disc action is the disc contacting (i.e. hitting by force) the surface. This contacting process is mimicked through attaching between the discs a set of physical units, i.e., springs, sliders and dashpots [2]. These units are subjected to the mechanical energy and deform (i.e., doing work). For example, the moving disc harnesses the mechanical energy to deform the springs in order to store a portion of the energy in the form of elastic potential energy. As a result of contacting, Cundall and Strack [2] defined three corresponding energy portions: the strain energy, $E_s$, slip energy, $E_\mu$, and dashpot energy, $E_\beta$. The strain energy is stored in the set of springs and remains restorable. The slip energy does not occur as this portion of energy is associated with frictional sliding which does not apply to the smooth surface (no secondary asperity). The dashpot energy $E_\beta$ arises due to material damping and becomes the unique source for energy loss when the disc moves on the surface. According to Becker et al. [3], $E_\beta$ is expressed as

$$E_\beta = -\sum \left( \dot{\delta}_n \Delta t F_n \right) \tag{1}$$

where $\delta_n$ is the relative normal displacement of the moving disc, $\Delta t$ is the time step increment, $F_n$ is the normal dashpot force and, according to Cundall [4], equal to

$$F_n = 2\dot{\delta}_n \beta_n \sqrt{k_n m_c} \tag{2}$$

where $\beta_n$ is the disc normal damping ratio, $k_n$ is the disc normal stiffness, and $m_c$ is the equivalent mass of the two contacting discs and defined as

978     C. Wang et al.

$$m_c = \frac{m_1 m_2}{m_1 + m_2} \tag{3}$$

where $m_1$ and $m_2$ are mass of two contacting discs, respectively. At each contact the dashpot energy loss uses a portion of the kinetic energy; the rest energy drives the disc forward. The total energy eventually depletes and the disc rests in a grove. These sliding-contacting actions are implemented by Particle Flow Code 2D.

### 2.3    Analytical Exact Solution

The analytical exact solution is developed in order to validate the DEM model. The solution introduces Newton's laws of motion and establishes mathematical forms for the trajectory of the moving disc. When the disc moves along the surface, the solution makes the following assumptions: (*i*) point-to-point contacting occurs; (*ii*) contacting is instantaneous. As discussed in the DEM model, the disc trajectory includes two portions: the rebound trajectory and the sliding trajectory. The two trajectory portions are determined by comparing radii sum $(r_1 + r_2)$ with $D_j^t$, the center-to-center distance $D_j^t$, at time step $t$, between the moving disc and disc $j$. The moving disc rebounds if $D_j^t > r_1 + r_2$, or slides if $D_j^t = r_1 + r_2$. Algorithm is coded to avoid $D_j^t < r_1 + r_2$. The distance $D_j^t$ is equal to

$$D_j^t = \sqrt{(x^t - x_j)^2 + (y^t - y_j)^2} \tag{4}$$

where $(x^t, y^t)$ is the moving disc center; $(x_j, y_j)$ is disc $j$ center and expressed as $x_j = -(2j - 1) \times r_2$ and $y_j = 0$, respectively.

Where the disc rebounds, the disc is subject to no force horizontally and force of gravity vertically. Then, at the next time step $(t + \Delta t)$, the velocity components in $x$- and $y$-directions, respectively, become

$$v_x^{t + \Delta t} = v_x^t \tag{5}$$

$$v_y^{t + \Delta t} = v_y^t + g \times \Delta t \tag{6}$$

The center relocates to $(x^{t + \Delta t}, y^{t + \Delta t})$ which is expressed as

$$x^{t + \Delta t} = x^t + v_x^t \times \Delta t \tag{7}$$

$$y^{t + \Delta t} = y^t + \frac{\left(v_y^{t + \Delta t} + v_y^t\right) \times \Delta t}{2} \tag{8}$$

The time step increment $\Delta t$ is set a small value for convergence purpose. Its value is dependent of the conditions set up for the disc including the radii and damping etc. and, in this study, was chosen as $\Delta t = 10^{-4}$ s.

A criterion was defined to assess if the disc re-contacts the surface in a time increment. The contacting occurs if, at time step $t$, $D_j^t > r_1 + r_2$ and, at $(t + \Delta t)$, $D_j^{t+\Delta t} < r_1 + r_2$. Define the contacting time as $t + \Delta t_0$, where $\Delta t_0$ is a dummy variable and less than $\Delta t$. As $\Delta t_0$ is a sufficiently small value, the $x$- and $y$-direction velocity components remain approximately constant. Assume a linear trajectory in $\Delta t_0$, the disc center ($x^{t+\Delta t_0}$, $y^{t+\Delta t_0}$) satisfies the discs configuration as following:

$$y^{t+\Delta t_0} = y^t + \frac{v_y^{t+\Delta t_0}}{v_x^{t+\Delta t_0}} x^{t+\Delta t_0} - \frac{v_y^{t+\Delta t_0}}{v_x^{t+\Delta t_0}} x^t \tag{9}$$

$$\left(y^{t+\Delta t_0}\right)^2 + \left(x^{t+\Delta t_0} - x_j\right)^2 = (r_1 + r_2)^2 \tag{10}$$

Equation (9) is an expression for the linear trajectory in $\Delta t_0$; Eq. (10) is the locus for the centre if in contact. Equations (9) and (10) yield roots $x^{t+\Delta t_0} = x_1$ and $x_2$ respectively. The value is set to be:

$$x^{t+\Delta t_0} = \begin{cases} x_1, & \text{if} |x_1 - x^t| < |x_2 - x^t| \\ x_2, & \text{if} |x_1 - x^t| > |x_2 - x^t| \end{cases} \tag{11}$$

Upon the discs re-contacting, the time increment $\Delta t_0$ is calculated as:

$$\Delta t_0 = \left| \frac{x^{t+\Delta t_0} - x^t}{v_x^t} \right| \tag{12}$$

Being a constant velocity in $x$-direction and doing work in $y$-direction, the velocity components are updated as

$$v_x^{t+\Delta t_0} = v_x^t \tag{13}$$

$$v_y^{t+\Delta t_0} = \lim_{\Delta t_0 \to 0} \frac{v_y^t}{|v_y^t|} \sqrt{\left(v_y^t\right)^2 - 2g\left(y^t - y^{t+\Delta t_0}\right)} \tag{14}$$

The contact angle $\gamma$ becomes:

$$\gamma = \arctan \frac{y^{t+\Delta t_0} - y_j}{x^{t+\Delta t_0} - x_j} \tag{15}$$

The tangential and normal velocity is calculated respectively as:

$$v_s^{t+\Delta t_0} = v_x^{t+\Delta t_0} \cos\gamma + v_y^{t+\Delta t_0} \sin\gamma \tag{16}$$

$$v_n^{t+\Delta t_0} = v_x^{t+\Delta t_0} \sin\gamma + v_y^{t+\Delta t_0} \cos\gamma \tag{17}$$

# References

1. Yang, J., Wei, L.: Collapse of loose sand with the addition of fines: the role of particle shape. Géotechnique **62**(12), 1111–1125 (2012)
2. Cundall, P.A., Strack, O.D.: A discrete numerical model for granular assemblies. Géotechnique **29**(1), 47–65 (1979)
3. Becker, V., Schwager, T., Pöschel, T.: Coefficient of tangential restitution for the linear dashpot model. Phys. Rev. E **77**, 011304 (2008)
4. Cundall, P.A.: Computer simulations of dense sphere assemblies. In: Satake, M., Jenkins, J.T. (eds.) Micromechanics of Granular Materials, pp. 113–123. Elsevier, Amsterdam (1988)
5. Kawaguchi, T., Tanaka, T., Tsuji, Y.: Numerical simulation of fluidized bed using the discrete element method. Trans. Jpn. Soc. Mech. Eng. Ser. B **58**, 2119–2125 (1992)